Thesis for the Degree of Doctor of Philosophy

Digital Beamforming Focal Plane Arrays for Radio Astronomy and Space-Borne Passive Remote Sensing

Oleg Iupikov

Department of Electrical Engineering
Chalmers University of Technology

Göteborg, Sweden 2017

Digital Beamforming Focal Plane Arrays for Radio Astronomy and Space-Borne Passive Remote Sensing

Oleg Iupikov

ISBN 978-91-7597-579-5

Doktorsavhandlingar vid Chalmers tekniska högskola
Ny serie nr 4260
ISSN 0346-718X

Department of Electrical Engineering
Antenna group
Chalmers University of Technology
SE–412 96 Göteborg
Sweden
Telephone: +46 (0)31 – 772 1000
Email: oleg.iupikov@chalmers.se

Typeset by the author using LaTeX.

Chalmers Reproservice
Göteborg, Sweden 2017

To my family

"Look deep into nature, and then you will understand everything better"

-Albert Einstein

Abstract

Dense Phased Array Feeds (PAFs) for reflector antennas have numerous advantages over traditional cluster feeds of horns in a one-horn-per-beam configuration, especially in RF-imaging applications which require multiple simultaneously formed and closely overlapping beams. However, the accurate analysis and design of such PAF systems represents a challenging problem, both from an EM-modeling and beamforming optimization point of view. The current work addresses some of these challenges and consists of two main parts.

In the first part the mutual interaction effects that exist between a PAF consisting of many densely packed antenna elements and an electrically large reflector antenna are investigated. For that purpose the iterative CBFM-PO method has been developed. This method not only allows one to tackle this problem in a time-efficient and accurate manner, but also provides physical insight into the feed-reflector coupling mechanism and allows to quantify its effect on the antenna impedance and radiation characteristics. Numerous numerical examples of large reflector antennas with various representative feeds (e.g. a single dipole feed and complex PAFs of hundreds of elements) are also presented and some of them are validated experimentally. In order to analyze electrically large feeds efficiently, a domain-decomposition approach to Krylov subspace iteration, where macro basis functions (or characteristic basis functions) on each subdomain are naturally constructed from the different segments of the generating vectors, is also proposed.

The second part of the thesis is devoted to the optimization of PAF beamformers and covers two application examples: (i) microwave satellite radiometers for accurate ocean surveillance; and (ii) radio telescopes for wide field-of-view sky surveys. Based on the initial requirements for future antenna systems, which are currently being formulated for these applications, we propose various figures-of-merits and describe the corresponding optimal beamforming algorithms that have been developed. Studies into these numerical examples demonstrate how optimal beamforming strategies can help to greatly improve the antenna system characteristics (e.g. beam efficiency, side-lobe level and sensitivity in the presence of the noise) as well as to reduce the complexity of the beam calibration models and overall phased array feed design.

Keywords: phased array feeds, reflector antenna feeds, beamforming, feed-reflector interaction, radio telescopes, spaceborne radiometers.

Preface

This thesis is in partial fulfillment for the degree of PhD of Engineering at Chalmers University of Technology.

The work that has resulted in this thesis was carried out between December 2011 and March 2017 and has been performed within the Antenna group at the Department of Electrical Engineering, Chalmers. Professor Marianna Ivashina has been both the examiner and main supervisor, and Associate Professor Rob Maaskant has been the co-supervisor.

The work has been supported by a project grant "System Modelering och Optimering av Gruppantenner för Digital Lobformning" from the Swedish Research Council (VR), Swedish National Space Board (SNSB) project grant 202-15 "Antenna-Array Digital-Beamforming and Calibration Methods for the Next Generation Multi-Beam Space-borne Radiometers for Ocean Observation" within the framework of the SNSB 2015-R open call for Space and Earth Observation Research, and a grant "Study on Advanced Multiple-Beam Radiometers" (contract 4000107369-12-NL-MH) from the European Space Agency (ESA).

Acknowledgments

First and foremost, I wish to thank my supervisor Prof. **Marianna Ivashina** for the opportunity to work on challenging and relevant research topics, and for her continuous guidance and encouragement during these years. I thank her for her patience and significant amount of time she spent in discussing the challenging phased-array feed problems, reviewing my research papers and technical reports. I am very thankful Prof. Ivashina for teaching me to be an independent researcher by giving me a chance to be creative in my work. I would also like to thank my co-supervisor Assoc. Prof. **Rob Maaskant** for numerous fruitful discussions related to my work, and for the infinite support in such complicated topics as numerical methods for electromagnetic modeling, electromagnetic theory, and other technical topics I could have a question on. All in all, it had been my honor to have worked with both of You. You are as much as mentors to me as are friends. I would like to thank Prof. **Per-Simon Kildal** for welcoming me to the Antenna group. Also, thanks to all of you I have met my beloved Esperanza :)

Thanks to my colleagues at the Onsala Space Observatory, especially to Prof. **John Conway** and Dr. **Miroslav Panteleev**, for providing me with interesting department service tasks related to the Square Kilometer Array (SKA) project, which was also beneficial for my PhD project as I could improve large parts of my Matlab code.

I would also like to thank Drs. **Kees van 't Klooster** and **Benedetta Fiorelli** from ESA, Drs. **Knud Pontoppidan**, **Per Heighwood Nielsen** and **Cecilia Cappellin** from TICRA, Prof. **Niels Skou** from Technical University of Denmark for the interesting and fruitful collaboration on new satellite radiometers, and Dr. **Andre Young** from Stellenbosch University for common work on calibration techniques for radio telescopes. I thank Prof. **Christophe Craeye** for inviting me to Université Catholique de Louvain and for interesting collaboration which had led to our joint journal publication on numerical methods.

I would like to acknowledge Dr. **Wim van Cappellen** from ASTRON, The Netherlands, for providing us with measurements of the Vivaldi antenna PAF (APERTIF), that were made at the Westerbork Synthesis Radio Telescope. These measurement results have been very beneficial for validating my numerical models.

My special thanks go to all the **former and current colleagues** of the Electrical Engineering Department for creating a nice and enjoyable working environment.We've had a lot of fun and enjoyable moments both at work and afterwork time.

Finally, I would like to thank the faculty opponent, Prof. **Bart Smolders**, and the committee members, Prof. **Joakim Johansson**, Prof. **Dirk de Villiers**, Dr. **Mauro Ettorre**, and Dr. **Miroslav Pantaleev**, for the time invested in reviewing my thesis. This has been a great help in improving the quality and readability of this thesis.

And of course, my most sincere gratitude to my parents, sister and my own family – **Esperanza**, **Marc** and **Tania** – for granting me a new sense of life and accompanying me in this scientific journey.

Oleg

List of Publications

This thesis is based on the work contained in the following appended papers:

Paper A

O. Iupikov, R. Maaskant, and M. Ivashina, "Towards the Understanding of the Interaction Effects Between Reflector Antennas and Phased Array Feeds", in *Proceedings of the International Conference on Electromagnetics in Advanced Applications, ICEAA 2012*, Cape Town, South Africa, September 2012, pp. 792–795.

Paper B

O. Iupikov, R. Maaskant, and M. Ivashina, "A plane wave approximation in the computation of multiscattering effects in reflector systems", in *Proceedings of the 7th European Conference on Antennas and Propagation, EUCAP 2013*, Gothenburg, Sweden, April 2013, pp. 3828–3832.

Paper C

O. Iupikov, R. Maaskant, M. Ivashina, A. Young, and P.S. Kildal, "Fast and Accurate Analysis of Reflector Antennas with Phased Array Feeds including Multiple Reflections between Feed and Reflector", *IEEE Transactions on Antennas and Propagation*, vol.62, no.7, 2014, pp. 3450–3462.

Paper D

C. Cappellin, K. Pontoppidan, P. H. Nielsen, N. Skou, S. S. Søbjærg, M. Ivashina, O. Iupikov, A. Ihle, D. Hartmann, and K. v. 't Klooster, "Novel Multi-Beam Radiometers for Accurate Ocean Surveillance", in *Proceedings of the 8th European Conference on Antennas and Propagation, EUCAP 2014*, The Hague, The Netherlands, April 2014, pp. 1–5

Paper E

O. Iupikov, M. Ivashina, K. Pontoppidan, P. H. Nielsen, C. Cappellin, N. Skou, S. S. Søbjærg, , A. Ihle, D. Hartmann, and K. v. 't Klooster, "Dense Focal Plane Arrays for Pushbroom Satellite Radiometers", in *Proceedings of the 8th European Conference on Antennas and Propagation, EUCAP 2014*, The Hague, The Netherlands, April 2014, pp. 1–5

Paper F

A. Young, M.V. Ivashina, R. Maaskant, O.A. Iupikov, D.B. Davidson, "Improving the Calibration Efficiency of an Array Fed Reflector Antenna Through Constrained Beamforming", *IEEE Transactions on Antennas and Propagation*, vol.61, no.7, July 2013, pp. 3538–3545.

Paper G

O. A. Iupikov, C. Craeye, R. Maaskant, M. V. Ivashina, "Domain-Decomposition Approach to Krylov Subspace Iteration", *EEE Antennas and Wireless Propagation Letters*, vol.15, 2016, pp. 1414–1417.

Paper H

C. Cappellin, K. Pontoppidan, P. H. Nielsen, N. Skou, S. S. Søbjærg, A. Ihle, M. V. Ivashina, O. A. Iupikov, K. v. 't Klooster, "Design of a push-broom multi-beam radiometer for future ocean observations", in *Proceedings of the 9th European Conference on Antennas and Propagation, EUCAP 2015*, Lisbon, Portugal, April 2015, pp. 1–5.

Paper I

O. A. Iupikov, M. V. Ivashina, K. Pontoppidan, P. H. Nielsen, C. Cappellin, N. Skou, S. S. Søbjærg, A. Ihle, D. Hartmann, K. v. 't Klooster, "An Optimal Beamforming Algorithm for Phased-Array Antennas Used in Multi-Beam Spaceborne Radiometers", in *Proceedings of the 9th European Conference on Antennas and Propagation, EUCAP 2015*, Lisbon, Portugal, April 2015, pp. 1–5.

Paper J

M. V. Ivashina, O. A. Iupikov, C. Cappellin, K. Pontoppidan, P. H. Nielsen, N. Skou, S. S. Søbjærg, B. Fiorelli, "Enabling High-sensitivity Near-land Radiometric Measurements With Multi-beam Conical Scanners Employing Phased Arrays", in *Proceedings of the 36th ESA Antenna Workshop on Antennas and RF Systems for Space Science*, ESA/ESTEC, The Netherlands, 6-9 October 2015, pp. 1–6.

Paper K

O. A. Iupikov, M. V. Ivashina, N. Skou, C. Cappellin, K. Pontoppidan, K. v. 't Klooster, "Multi-Beam Focal Plane Arrays with Digital Beamforming for High Precision Space-Borne Remote Sensing", Under review for *IEEE Transactions on Antennas and Propagation*, 2017.

Paper L

O. A. Iupikov, A. A. Roev, M. V. Ivashina, "Prediction of Far-Field Pattern Characteristics of Phased Array Fed Reflector Antennas by Modeling Only a Small Part of the Array – Case Study of Spaceborne Radiometer Antennas", in *Proceedings of the 11th European Conference on Antennas and Propagation, EUCAP 2017*, Paris, France, April 2017, pp. 1–4.

Contents

II Included Papers

Part I

Introductory Chapters

Chapter 1 Introduction

Since recently, several types of so-called "dense" Phased-Array Feed (PAF) systems for reflector antennas have been designed for applications in future instruments for radio astronomy, Earth surface and space observations [1–11]. The main advantage of these PAFs over conventional single-horn feeds and cluster feeds of horns is that the inter-element separation distance of such "dense" PAFs can be much smaller than one wavelength to allows the formation of multiple closely overlapping beams with high efficiency [12]. Another advantage is that these PAFs can be equipped with digital beamformers providing an individual complex excitation per array antenna element and hence can realize an optimal illumination of the reflector aperture [13–18]. These advantageous properties are of great importance both for radio astronomy and Earth observation applications requiring fast and wide field-of-view (FOV) surveys.

1.1 Next generation radio telescopes

The effectiveness of performing wide-field surveys is characterized by the telescope's survey speed, i.e., the speed at which a certain volume of space can be observed with a given sensitivity. The survey speed is proportional to the size of the instantaneous FOV and the frequency bandwidth, weighted by the sensitivity squared [19]. Present-day aperture synthesis radio telescopes have a limited observation capability due to the fact that only a small part of the sky can be observed simultaneously, which therefore results in a low survey speed. In contrast, using PAFs as a reflector antenna feed allows: (i) to increase the receiving sensitivity of the reflector antenna due to better illumination of the dish, and; (ii) to form multiple simultaneous beams, which can be closely overlapped, as a result of overlapping sub-arrays forming these beams, to provide a continuous FOV [20]. An example of such system which recently became operational is APERTIF [7], which is developed by The Netherlands Institute for Radio Astronomy (ASTRON) and illustrated in Fig. 1.1.

The FOV of conventional telescopes with single-beam feeds is limited to one half-power beamwidth, where the sensitivity takes the maximum value along the beam axis and gradually decreases from its center. To image a larger region of the sky,

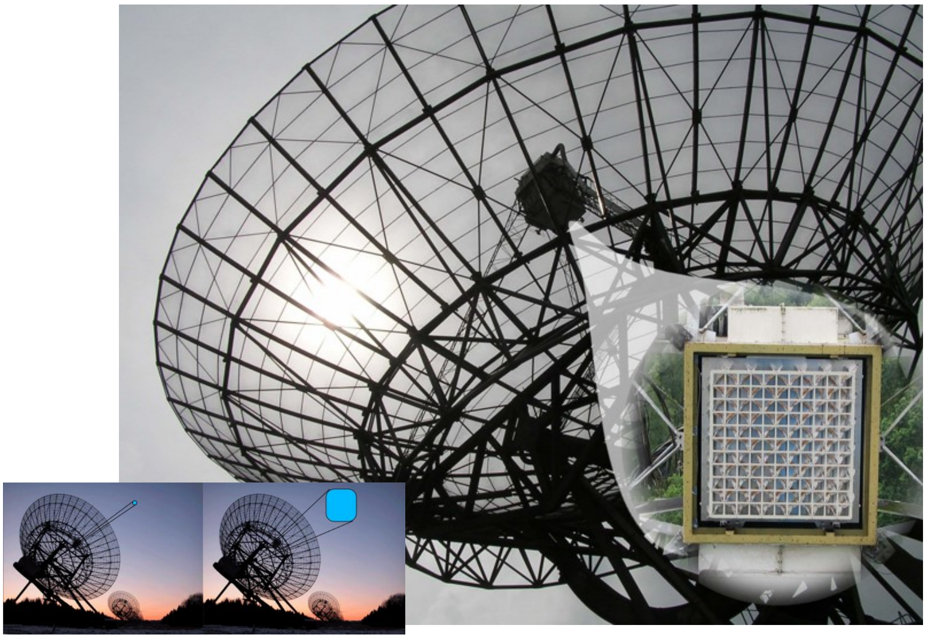

Figure 1.1: APERTIF project [7], which aims to increase the field-of-view of the Westerbork Synthesis Radio Telescope (WSRT) with a factor 25, as is illustrated in the bottom-left inset. This performance gain is achieved by placing a receiver array in the focus of each parabolic dish of the WSRT, instead of the single receiver element that the current system employs [26].

astronomers use the "mosaicing" technique [21]. With this technique, a telescope performs many observations by mechanically steering (scanning) the dish such that the main lobes of the beams generated in subsequent observations closely overlap and form an almost continuous beam envelope when superimposed. The large-field image is therefore formed by composing a mosaic of smaller sized overlapping images taken during these observations. According to Nyquist's field-sampling theorem, a uniform sensitivity of the combined image is achieved when the beam separation is equal to or smaller than one half of the half-power beamwidth [22]. A larger spacing between the observations results in a sensitivity ripple over the FOV [17, 23]. The maximum allowable ripple will depend on the particular science case.

PAFs can provide many closely overlapping beams in one snapshot, thereby greatly improving the size of the FOV. However, to meet the required field-sampling limit with a cost-effective number of PAF beams, their shapes should be optimized and the maximum achievable receiving sensitivity, as well as minimum receiver and antenna noise [24, 25], should be traded against the maximum tolerable sensitivity ripple over the FOV.

In addition to a continuous FOV and high sensitivity, high polarization discrimination is required for large-field surveys [27–29]. For this purpose, the incident field is sampled by two orthogonally polarized receptors or beams. In radio astronomy, the polarization purity of the resulting images is established after extensive offline calibration of the data. In this respect, two antenna design aspects are of particular importance: the stability (i.e. variation over time) of the co- and cross-polarized beams; and the orthogonality of the two beams in the direction of incidence. This requires that the beams are formed simultaneously and span a 2-D basis along which the incident field is decomposed. Future PAF-equipped telescopes are potentially accurate polarimeters thanks to the flexibility that digital beamforming offers. However, although the orthogonality of the beam pair in the direction of observation may be improved electronically, it is important that the intrinsic polarization characteristics of the beams are sufficiently good to minimize such corrections as they may compromise the receiving sensitivity.

Another important concern about radio telescopes is their calibration procedure. This requires accurate models of the instrumental parameters and propagation conditions, which vary over time, so that the model parameters have to be determined during the observation time through a number of calibration measurements [30]. To perform calibration of radio telescopes efficiently, the number of model parameters should be minimal. One of the instrumental parameters that needs accurate characterization is the radiation pattern of the antenna, which is especially challenging for future array based multiple beam radio telescopes due to complexity of such instruments and increased size of the FOV.

To be able to characterize all beams inside the FOV by means of a simple beam model, beamforming techniques can be used to create similarly shaped beams [31,32]. However, this leads to a loss in the receiving sensitivity requiring us to employ more advanced but still simple beam models. An attempt to develop such beam model in conjunction with constrained beamforming technique is made in this work.

1.2 Satellite radiometers for Earth observations

Besides radio astronomy applications, PAFs are used in other applications, such as remote sensing of the atmosphere and the Earth's surface [33,34]. However, there are some important differences in requirements for the instruments in these applications. For example, receivers for Earth remote sensing are typically designed to measure high brightness temperatures ($75-300$ K) along with short integration times, while in radio astronomy very low brightness temperatures are of interest and the integration time can reach many hours. Therefore, the receiving sensitivity is one of the key instrument characteristics, in particular for radio astronomy applications. On the other hand, for Earth remote sensing applications, such as the assessment of ocean parameters (salinity, sea surface temperature, ocean vector wind), additional specifications for high beam efficiency and measurement accuracy near a coast line are required [10,35].

Recent advances in phased array antenna technologies and low-cost active electronic components open up new possibilities for designing Earth observation instruments, in particular those used for radiometric measurements. Nowadays, two de-

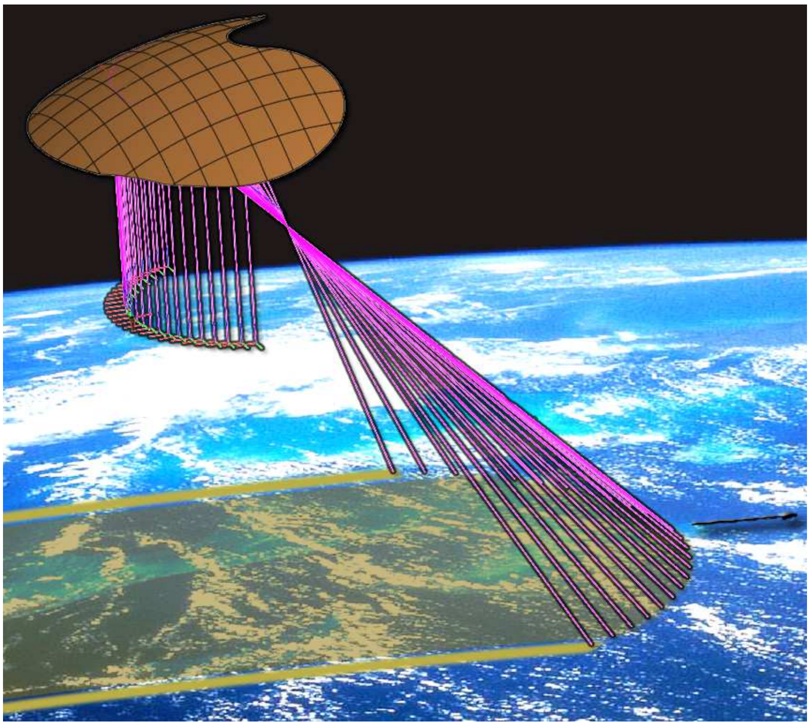

Figure 1.2: Operational principle of a push-broom microwave radiometer, which includes an off-set toroidal reflector antenna fed by a multi-beam focal plane array of horns arranged perpendicular to the flight direction of the spacecraft. Different areas of the ocean-surface are scanned as the spacecraft flies forward.

sign concepts of microwave radiometers are in use: "push-broom" and "whisk-broom" scanners [36]. Push-broom scanners have an important advantage over whisk-broom scanners in providing larger FOV with higher sensitivity, owing to the fact that these systems can observe a particular area of the ocean for a longer period of time with multiple simultaneous beams. However, the drawback of pushbroom designs – based on conventional focal plane arrays of horns in one-horn-per-beam configuration [37] or clusters with simplistic beamforming schemes [38] – is the FOV varying sensitivity. This variation occurs due to the differences between scanned beams, as these are formed by different horns or clusters, and their large beam separation distance on the oceanic surface, which is caused by a large separation distance between the horns.

This drawback may be significantly reduced by employing dense PAFs consisting of many electrically small antenna elements utilizing advanced beamforming schemes [15–17]. This technology has been extensively studied during the last decade in the radio astronomy community, and several telescopes are currently being equipped with dense PAFs [7, 39, 40]. While those systems aim at providing scan ranges of about $5-10$ beamwidths, for applications as herein considered, the desired scan range (swath range of the radiometer) is one order of magnitude larger [10]. To achieve this large scan-range performance, more complex reflector optics and PAF designs are required. For push-broom radiometers, various optics concepts have been investigated [37], and the optimum solution has been found to be an offset toroidal single reflector antenna, such as illustrated in Fig. 1.2. This reflector structure is rotationally symmetric around its vertical axis, and thus is able to cover a wide swath range. However, its aperture field exhibits significant phase errors due to the non-ideal (parabolic) surface of the reflector, which requires the use of a more complex feed system.

1.3 Antenna arrays in satellite communication and telecommunication systems

Recent developments in antenna technologies and low-cost active electronic components open a possibility to produce aperture antenna arrays and PAFs for communication applications as well, in order to improve different aspects of radio links. For example, authors in [41] suggest to use PAF for a high-gain reflector antenna to compensate pointing errors due to the unwanted movement of the antenna mast and to ease the antenna installation. A beam squint compensation in circularly polarized offset reflector antennas is proposed in [42] by employing a sequentially rotated PAF (Fig. 1.3).

Advanced PAF systems are also being considered as potential candidates for large-scale array antenna systems for 5G wireless infrastructure, as they can offer unique electronic beamforming approaches. The PAF beamformers hybridize analog and digital beamforming in an optimal manner through the combination of the best of two worlds, i.e. robustness, low-cost and design simplicity of reflector antennas with

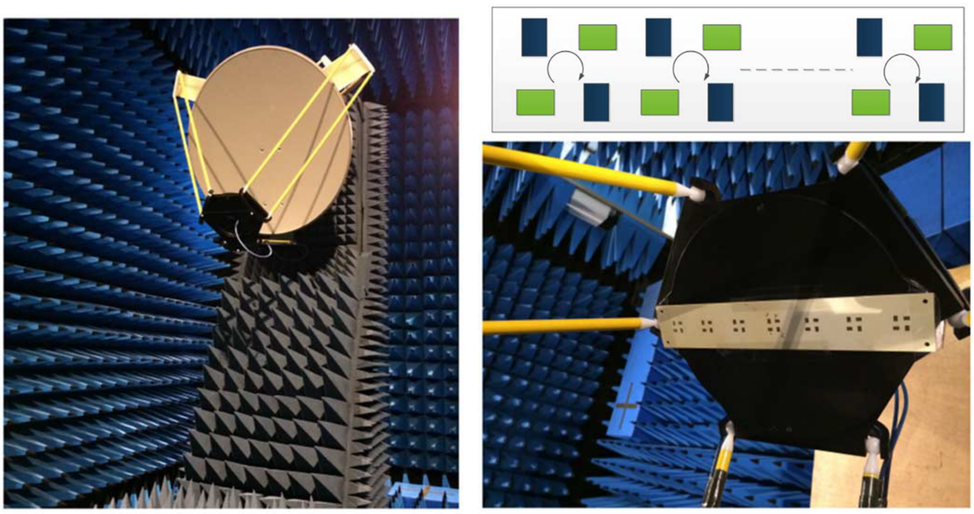

Figure 1.3: Prototype of the array-fed offset reflector antenna [42], and the array of sequentially rotated aperture-coupled microstrip antennas in the focal plane of the prototype.

the flexibility of phased arrays. The recently funded Horizon 2020 Innovative Training Network SILIKA [43] is dealing with quasi-optically beamformed array antennas such as Focal Line Arrays and Focal Plane Arrays, where each antenna element sees multiple users within a sector of the total coverage area, and where each active array element consists of a silicon integrated circuit with integrated antenna radiator.

1.4 Modeling, design and calibration challenges of novel Phased Array Feeds

The design of the above-mentioned highly complex PAF systems requires the development of accurate and efficient modeling techniques. This is a challenging task considering the size of the reflector used in radio astronomy and Earth observation applications, which can be hundreds of wavelengths in diameter, as well as the size of the PAF, which is too small to be analyzed with an infinite array simulation approach (which also has limitations on the excitation schemes), but too large for the direct usage of full-wave methods implementing plain MoM or FDTD techniques that run on standard computing platforms.

During the last decades, a number of analytical and numerical techniques have been developed to model feed-reflector interaction effects. For example, in [44], the multiscattered field between the feed and reflector is approximated by a geometric series of on-axis plane wave (PW) fields, each of which is scattered by the antenna feed due to its incident PW at each iteration, and where the amplitudes of these PWs are known in closed-form for a given reflector geometry. This method is very fast and insightful, while MoM-level accuracy can be achieved for single-horn feeds, but not for array feeds as demonstrated in Paper B. An alternative approach is to use more versatile, though more time-consuming, hybrid numerical methods combining Physical Optics or Gaussian beams for the analysis of reflectors with MoM and/or Mode Matching techniques for horn feeds [45, 46]. The recent article [47] has introduced a PO/Generalized-Scattering-Matrix approach for solving multiple domain problems, and has shown its application to a cluster of disjoint horns. This approach is generic and accurate, but may require the filling of a large scattering matrix for electrically large PAFs and/or multifrequency front-ends (MFFEs) that often includes a large extended metal structure [48]. Other hybrid methods, which are not specific for solving the present type of problems, make use of field transformations, field operators, multilevel fast multipole approaches (MLFMA), and matrix modifications [49–52]. Recently, a Krylov subspace iterative method has been combined with an MBF-PO approach for solving feed-reflector problems [53], and complementary to this, an iteration-free CBFM-PO approach has been presented by S. Hay, where a modified reduced MoM matrix for the array feed is constructed by directly accounting for the presence of the reflector [54]. However, most of these methods are either complicated or slow, or do not allow for the extraction of the feed-reflector interaction effect in a systematic manner.

Besides the efficiency and simplicity of modeling techniques, their accuracy is of great importance too. For example, present-day radio telescopes with single-beam feeds can achieve a dynamic range upward to $10^6 : 1$ along the on-axis beam direction. However, the off-axis dynamic range is severely limited by uncertainties and temporal instabilities in the beam patterns caused by gain drift in PAF channels, mispointing and mechanical deformations of the dishes, as well as by station-to-station beam patterns differences [55, 56]. A number of calibration techniques for dealing with these effects have been proposed and used in practical systems [21, 30, 57, 58]. For novel PAF-based telescopes, the beam calibration is a new challenging field and there is not yet a clear consensus on what constitutes a "good" beam pattern. Furthermore, the mutual coupling between the PAF and the dish(es) of a reflector antenna gives rise to a frequency dependent ripple in the antenna radiation and impedance characteristics [59], which exacerbates the calibration. Accurate system models can help alleviating the beam calibration problem.

In conclusion, the challenges in modeling, designing and calibrating novel PAFs, are:

- complexity to accurately model a large antenna array of complex antennas, including mutual coupling between array elements; accurate modeling of an antenna radiation efficiency can be challenging as well [24];

- cumbersomeness of analyzing a combined PAF-reflector structure due to the large size of the reflector and mutual coupling between them (multi-scale problem);

- development of optimal beamforming algorithms that provide performance requirements on multiple antenna characteristics (e.g. beam efficiency, side-lobe level, sensitivity, etc), while realizing easy-to-calibrate beam shapes and maintaining minimum complexity of the array design (minimum number of elements, similarity of sub-arrays, etc);

- Calibration of the Phased array feed (PAF) based radio telescope, which largely depends on the accuracy of the antenna beam model.

1.5 Goal and outline of the thesis

The herein presented work is devoted to address the following challenges: (i) the development of a reflector antenna model, which accounts for the feed-reflector coupling and provides physical insight in the coupling processes, and the analysis of several reflector antennas for different types of feeds and determining which of these feeds are preferred in terms of low feed-reflector coupling and overall antenna performance; (ii) the design of PAFs for an offset toroidal reflector antenna and the development of optimal beamforming algorithms for accurate radiometric measurements; (iii) improving the calibratibility of the beam shape of a radio telescope.

This thesis is organized as follows. In **Chapter 2** a general CBFM-PO model of a reflector antenna system is developed. This model is based upon the Jacobi method for solving a system of linear equations iteratively. The Characteristic Basis Function Method (CBFM) is used to model the feed, while the Physical Optics (PO) approach is used to model the current on the reflector at each iteration.

To speed-up the method, several acceleration techniques are developed: the field scattered from the reflector is expanded in a Plane Wave Spectrum (PWS), while the field radiated/scattered by the feed is computed at few near-field points only and then interpolated in order to find the PO current distribution on the reflector surface. This allows us to simulate a reflector antenna $5-100$ times faster than a pure CBFM-PO approach.

Afterwards, the developed method is used to model large reflector antennas (38λ and 118λ) fed by different types of feeds: (i) a single dipole above a ground plane; (ii) a 20-elements dipole array; (iii) a 121-element dipole array; (iv) a 121-element Vivaldi array; (v) a classical pyramidal horn with aperture size of $\sim 1\lambda$, and; (vi) the same horn with extended ground plane, which could represent a feed cabin of the reflector antenna.

Chapter 3 describes a PAF design procedure and several beamforming strategies for the application of satellite radiometers observing the sea surface, where the requirements for such radiometers are specified and translated into performance figures in terms of antenna characteristics. Two beamformer algorithms are developed to meet the tight radiometer requirements, and compared to the commonly used Conjugate-Field-Matching beamformer. An algorithm to limit the weights dynamic range keeping them optimal is also developed and numerically tested.

Next, a design procedure of an optimal PAF is presented, including analysis of the required array size and inter-element spacing, as well as trade-off study between several candidates for the array radiating element. In the later study several analysis approaches are described and compared, which allow for a time-efficient analysis of radiometers with PAFs.

Numerical results for the designed radiometer equipped with the optimal PAF are presented for each type of beamformer.

In a short **Chapter 4** it is shown how a constrained beamforming strategy can be used to improve the calibration efficiency of the PAF beam shape of a radio telescope.

The conclusions and recommendations are described in **Chapter 5**.

Chapter 2 Electromagnetic Analysis of Reflector Antennas with Phased Array Feeds Including Feed-Reflector Multiple Reflection Effects

The characterization of feeds in unblocked reflectors and on-axis beams can be handled by the traditional spillover, illumination, polarization and phase subefficiency factors defined for rotationally symmetric reflectors in [60], and be extended to include excitation-dependent decoupling efficiencies of PAFs [20, 61]. The current work investigates the effects of aperture blockage and multiple reflections on the system performance in a more generic fashion than it was done in [44] and [62] for rotationally symmetric antennas and single-pixel feeds.

2.1 Analysis method: formulation and validation of the iterative CBFM-PO approach

The herein proposed analysis method is based on the Jacobi method intended to solve a system of linear equations in an iterative manner. Suppose that the MoM matrix equation for the entire reflector antenna (including both the dish and the feed) is given by

$$\mathbf{ZI} = \mathbf{V}, \tag{2.1}$$

where $\mathbf{Z}$ is the MoM matrix of size $K \times K$ and $\mathbf{V}$ is a $K \times 1$ excitation vector.

This matrix can be decomposed into matrix blocks as

$$\begin{bmatrix} \mathbf{Z}^{\mathrm{rr}} & \mathbf{Z}^{\mathrm{rf}} \\ \mathbf{Z}^{\mathrm{fr}} & \mathbf{Z}^{\mathrm{ff}} \end{bmatrix} \begin{bmatrix} \mathbf{I}^{\mathrm{r}} \\ \mathbf{I}^{\mathrm{f}} \end{bmatrix} = \begin{bmatrix} \mathbf{V}^{\mathrm{r}} \\ \mathbf{V}^{\mathrm{f}} \end{bmatrix}, \tag{2.2}$$

where $\mathbf{Z}^{\mathrm{rr}}$ and $\mathbf{Z}^{\mathrm{ff}}$ are the MoM matrix self-blocks of the reflector and feed, respectively[1], and $\mathbf{V}^{\mathrm{r}}$ and $\mathbf{V}^{\mathrm{f}}$ are the corresponding excitation vectors. The matrix $\mathbf{Z}^{\mathrm{rf}} = (\mathbf{Z}^{\mathrm{fr}})^T$ contains the mutual reactions involving the basis functions on the feed and reflector. The unknown current expansion coefficient vectors are denoted by $\mathbf{I}^{\mathrm{r}}$ and $\mathbf{I}^{\mathrm{f}}$.

It can be shown that the solution to Eq. (2.2) can be written as an infinite geometric series (see Paper C for the derivation), which, in turn, can be represented by the recursive scheme:

Reflector		Feed	
$\mathbf{I}^{\mathrm{r}} = \sum_{n=0}^{\infty} \mathbf{I}^{\mathrm{r}}_n$	(2.3a)	$\mathbf{I}^{\mathrm{f}} = \sum_{n=0}^{\infty} \mathbf{I}^{\mathrm{f}}_n$	(2.4a)
$\mathbf{I}^{\mathrm{r}}_{n+1} = -(\mathbf{Z}^{\mathrm{rr}})^{-1}\mathbf{Z}^{\mathrm{rf}}\mathbf{I}^{\mathrm{f}}_n$	(2.3b)	$\mathbf{I}^{\mathrm{f}}_{n+1} = -(\mathbf{Z}^{\mathrm{ff}})^{-1}\mathbf{Z}^{\mathrm{fr}}\mathbf{I}^{\mathrm{r}}_n$	(2.4b)
$\mathbf{I}^{\mathrm{r}}_0 = (\mathbf{Z}^{\mathrm{rr}})^{-1}\mathbf{V}^{\mathrm{r}}$	(2.3c)	$\mathbf{I}^{\mathrm{f}}_0 = (\mathbf{Z}^{\mathrm{ff}})^{-1}\mathbf{V}^{\mathrm{f}}$	(2.4c)

The cross-coupled recursive scheme as formulated by Eqs. (2.3) and (2.4) is exemplified in Fig. 2.1 as a five-step procedure, in which the problem is first solved in isolation to obtain $\mathbf{I}^{\mathrm{r}}_0$ and $\mathbf{I}^{\mathrm{f}}_0$. Afterwards, the feed current $\mathbf{I}^{\mathrm{f}}_0$ is used to induce the reflector current $\mathbf{I}^{\mathrm{r}}_1$, which is then added up to the initial reflector current. Likewise, the initial reflector current $\mathbf{I}^{\mathrm{r}}_0$ is used to induce the feed current $\mathbf{I}^{\mathrm{f}}_1$, which is then added to the initial feed current, and so forth.

Rather than computing the reflector and feed currents through the large-size MoM matrix blocks $\mathbf{Z}^{\mathrm{rr}}$, $\mathbf{Z}^{\mathrm{rf}}$, $\mathbf{Z}^{\mathrm{fr}}$, and $\mathbf{Z}^{\mathrm{ff}}$, additional computational and memory efficient techniques can be employed for the rapid computation of these currents at each iteration. Here, the Physical Optics (PO) current is used on the reflector surface and the Characteristic Basis Function Method (CBFM, [64]) is invoked as a MoM enhancement technique for computing the current on the feed. Please see the Paper C for details on *how* this is done.

The above described approach has been validated using the MoM solver as part of the CAESAR software [64, 65] and the commercial software FEKO [66] (*c.f.* Paper C for details).

2.2 Acceleration techniques

The above-described approach allows us to simulate reflector antennas employing electrically large reflectors fed by complex feeds like PAFs of hundreds of Vivaldi antennas. However, the approach requires the field to be computed at numerous points on both the feed and the reflector surfaces, thereby rendering the field computations

[1] Here $\mathbf{Z}^{\mathrm{ff}}$ includes the effect of the antenna port terminations [63].

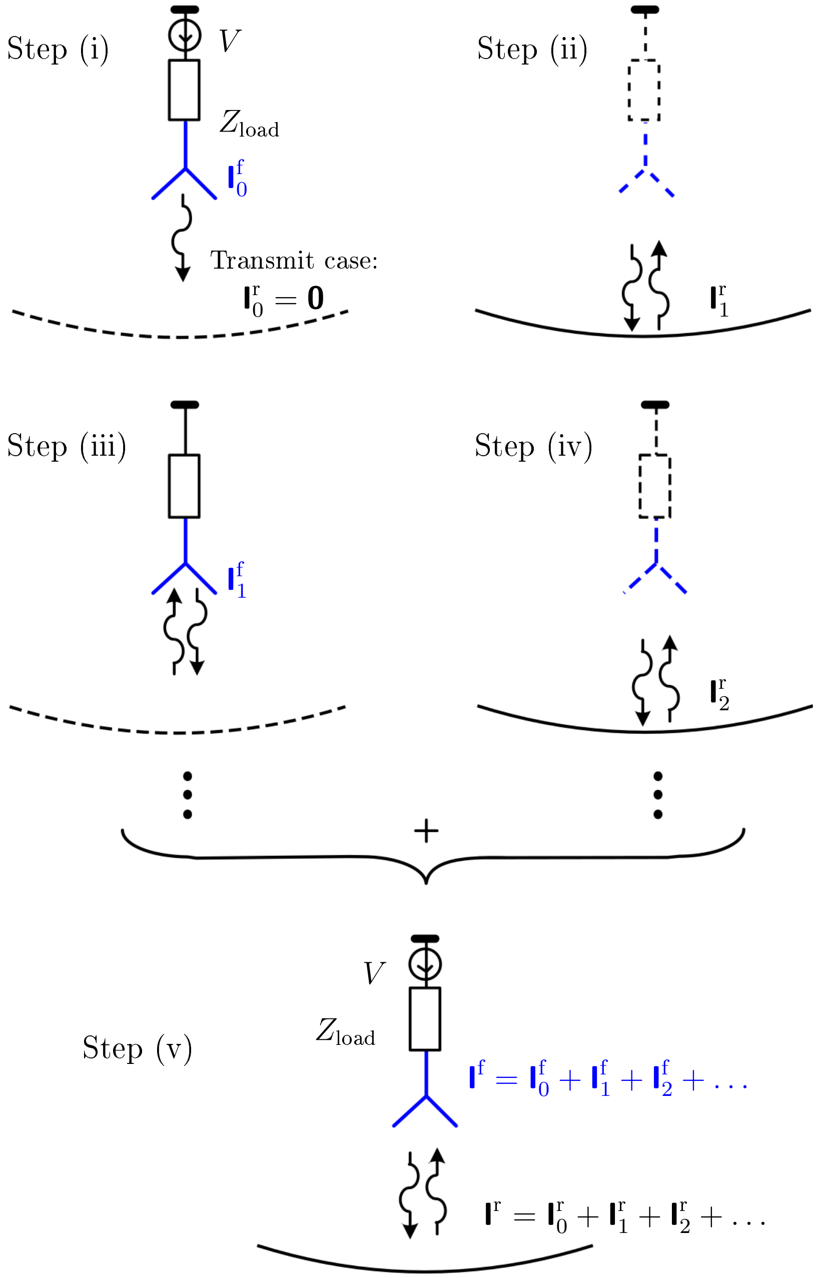

Figure 2.1: Illustration of the cross-coupled iterative scheme for the multiscattering analysis of the feed-reflector interaction effects, as formulated by Eqs. (2.3) and (2.4): (i) The antenna feed radiates in the absence of reflector; (ii) the radiated field from the feed scatters from the reflector; (iii) the scattered reflector field is incident on the terminated feed and re-scatters; (iv) the re-scattered field from the feed is incident on the reflector; etc. (v) the final solution for the current is the sum of the subsequently induced currents.

inefficient, in particular for complex-shaped electrically large feed antennas employing hundreds of thousands of low-level basis functions. Similarly, one has to cope with a computational burden when calculating the PO equivalent current on electrically large reflectors. In this section a few enhancement techniques are presented that accelerate the field computations while maintaining high accuracy.

2.2.1 Single plane wave approximation of the reflector field

The method described here relies on the fact that the field scattered from the reflector resembles a plane wave (PW), and therefore can be defined by a single PW mode amplitude. In [44] this amplitude is expressed analytically at each iteration for a given reflector geometry, and the scattered field of the feed is approximated by a geometric series of fields scattered by the antenna feed due to an incident plane wave with known amplitude. With reference to Fig. 2.2, the total radiation pattern of the feed $\boldsymbol{E}_{\mathrm{tot}}$ (including feed-reflector coupling) can be expressed as

$$\boldsymbol{E}_{\mathrm{tot}}(\theta,\phi,r) = \boldsymbol{E}_{\mathrm{r}}(\theta,\phi,r) + \frac{-\frac{1}{r_0}A(0)\exp\left(-jk2r_0\right)}{1+\frac{1}{r_0}A_{\mathrm{s}}(0)\exp\left(-jk2r_0\right)}\boldsymbol{E}_{\mathrm{s}}(\theta,\phi,r), \tag{2.5}$$

where $\boldsymbol{E}_{\mathrm{r}}$ and $\boldsymbol{E}_{\mathrm{s}}$ are the radiation and scattering far-field patterns of the feed in isolation correspondingly, and $A(0)$ and $A_{\mathrm{s}}(0)$ are values of the co-polarization component of these fields in the on-axis direction [see Fig. 2.2(a) and 2.2(b)]; r_0 is the distance between the reflector apex and the phase reference point with respect to which $\boldsymbol{E}_{\mathrm{r}}$ and $\boldsymbol{E}_{\mathrm{s}}$ are defined.

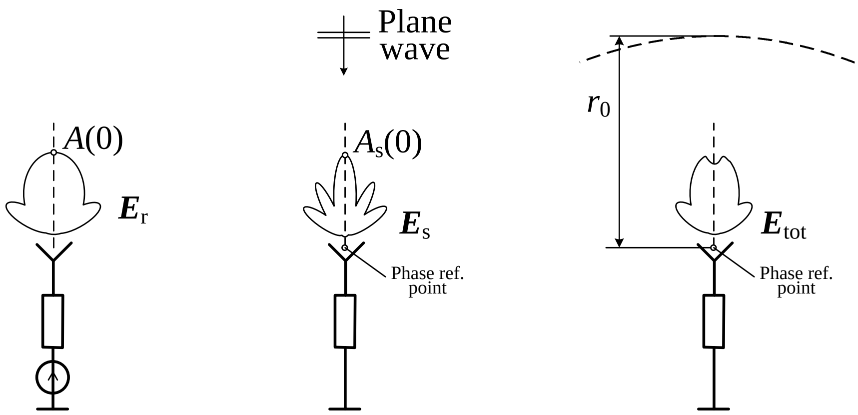

(a) The radiation pattern of the feed on transmit

(b) The scattering pattern of the feed due to an incident unit PW from the direction of the reflector

(c) The total pattern of the feed including coupling with the reflector

Figure 2.2: Semi-analytical PW approximation as described in [44].

However, as shown in Paper B, this semi-analytical approach works well only when the feed is small w.r.t. the reflector and when it has low-scattering properties. If the feed becomes electrically large and high-scattering (such as for conventional multi-frequency front-ends in radio telescopes), the accuracy of this method deteriorates. In order to improve the accuracy, the plane wave coefficient can be computed numerically at each iteration. To do so, the field scattered from the reflector is sampled in the focal plane, and the PW coefficient is computed as an average of the sampled field values on a regular grid (see Paper B for the derivation):

$$\alpha \approx \frac{1}{K} \sum_{k=1}^{K} E_p^{\mathrm{ref}}(\mathbf{r}_k), \tag{2.6}$$

where E_p^{ref} is the dominant p-component of the focal field, and the set $\{\mathbf{r}_k\}_{k=1}^{K}$ are K sample points, which are assumed to be located on a uniform grid in the focal plane.

In summary, the plane-wave-enhanced MoM/PO method consists of the following steps: (i) the antenna feed currents are computed through a method-of-moments (MoM) approach by exciting the antenna port(s) in the absence of the reflector; (ii) these currents generate an EM field which induces PO-currents on the reflector surface; (iii) the PO currents create a scattered field that is tested at only a few points in the focal plane; (iv) the field intensity at the sample points is averaged in accordance with (2.6), and the obtained value is used as the expansion coefficient for the plane wave traveling from the reflector towards the feed; (v) this incident plane wave induces a new current distribution on the feed structure. The steps (ii)–(v) are repeated until a convergence condition is met.

The following three types of feeds are used to illuminate a reflector antenna: (i) a pyramidal horn with aperture diameter in the order of one wavelength; (ii) a pyramidal horn with extended ground plane, and; (iii) an 121-element dual-polarized dipole array (see Fig. 2.3). All antennas are impedance power-matched, so that the antenna component [67] of their corresponding radar cross-section (RCS) is minimized. However, the residual component of the RCS of the horn with ground plane is still high due to the extended metal structure surrounding it, so that this feed is a high scattering antenna and strong feed-reflector coupling can be expected.

The above feeds are used to illuminate two parabolic reflectors with aperture diameters 38λ and 118λ, and the errors introduced by the PW approximation in the focal field and scalars antenna characteristics are computed as

$$\epsilon_1 = \frac{\sqrt{\sum_k |E_{p;k}^{\mathrm{ref}} - E_{p;k}^{\mathrm{mod}}|^2}}{\sqrt{\sum_k |E_{p;k}^{\mathrm{ref}}|^2}} \times 100\% \tag{2.7}$$

$$\epsilon_2 = \frac{|f^{\mathrm{ref}} - f^{\mathrm{mod}}|}{|f^{\mathrm{ref}}|} \times 100\%, \tag{2.8}$$

where $E_{p;k}^{\text{ref}}$ and $E_{p;k}^{\text{mod}}$ are the k-th sample of the discretized p-components of the actual focal E-field $\boldsymbol{E}^{\text{ref}}(x, y)$ and the focal field modeled by a plane wave $\boldsymbol{E}^{\text{mod}}(x, y)$ respectively; f^{ref} and f^{mod} is the gain or antenna input impedance, reference and modeled values, respectively. The MoM/PO results without the plane wave approximation are used as the reference solution.

Table 2.1: Errors due to the plane wave approximation

	Focal field		**Gain (on-axis)**		**Gain (@−3 dB)**		**Impedance**	
Reflector diameter D	38λ	118λ	38λ	118λ	38λ	118λ	38λ	118λ
Feed: Pyramidal horn								
Parameter variation, %	3.91	1.23	1.98	0.62	3.99	2.16	15.05	4.66
Method:	**Error, %**							
Method 1	0.3	0.05	0.28	0.05	0.36	0.14	1.37	0.18
Method 2	0.1	0.04	0.16	0.04	0.3	0.13	0.09	0.03
Feed: Pyramidal horn with extended ground plane								
Parameter variation, %	139.3	39.1	19.2	3.4	29.4	3.56	43.4	6.1
Method:	**Error, %**							
Method 1	37.7	1.29	12.7	0.1	10.1	0.17	18.5	0.2
Method 2	11.9	0.48	2.23	0.07	4.71	0.15	12.46	0.11
Feed: 121-element dual-polarized dipole array								
Parameter variation, %	8.45	3.28	1.84	0.28	3.68	0.73	5.8	1.7
Method:	**Error, %**							
Method 1	0.61	0.11	0.21	0.03	0.15	0.02	0.34	0.08
Method 2	0.44	0.1	0.12	0.03	0.08	0.03	0.58	0.05

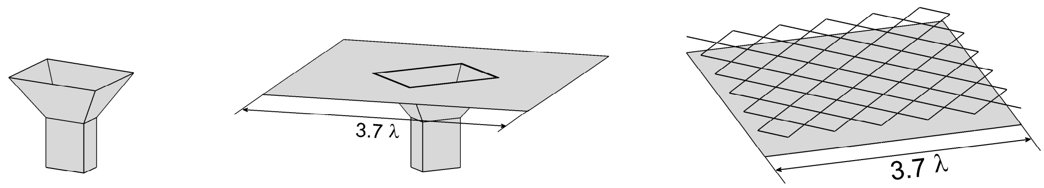

(a) Horn (b) Horn with gnd plane (c) Dipole array

Figure 2.3: Considered feed geometries (in addition to the dipole feed with PEC ground plane): (a) a classical pyramidal horn with aperture length $\sim 1\lambda$; (b) the same horn but with extended ground plane ($\sim 3.7\lambda$), where the ground plane may model the presence of a large feed cabin; (c) an antenna array consisting of 121 0.45λ-dipoles above a ground plane of the same size; (d) the same array, but with the dipoles replaced by wideband tapered slot Vivaldi antennas.

The above errors that have been computed for both the semi-analytical and the numerical PW-approximation approaches are summarized in Table 2.1. We will refer to the semi-analytical method as "Method 1", while the proposed above approach is denoted as "Method 2".

The total simulation time (10 frequency points) for the 38λ reflector fed by the considered feeds is shown in Table 2.2.

Table 2.2: Total simulation time

	Horn	**Horn with gnd plane**	**Dipole array**	**Vivaldi array**
MoM-PO, no approximations	9 min 05 sec (100%)	59 min 21 sec (100%)	71 min 09 sec (100%)	197 min 04 sec (100%)
Method 1	0 min 39 sec (7%)	1 min 12 sec (2%)	4 min 49 sec (7%)	33 min 58 sec (17%)
Method 2	2 min 32 sec (28%)	13 min 28 sec (23%)	19 min 19 sec (27%)	67 min 06 sec (34%)

By analyzing Table 2.1 and Table 2.2 the following observations can be made:

- Method 1 is numerically efficient and accurate for small feeds (whose sizes are in the order of one wavelength) and for low-scattering feeds, but fails in case of large high-scattering feeds, such as MFFEs, because the focal field produced by the feed scattering pattern has a high level and a highly tapered shape;

- Method 2 provides a better prediction of all the system parameters, since it accounts for the actual shape of the scattering pattern when fitting the plane wave to it; however, it is slower than Method 1;

- Both methods are accurate in case of large reflectors, because the multiscattering effects are less pronounced (see "Parameter variation" in Table 2.1), and the field scattered from the reflector is close to a plane wave at all iterations.

For the focal field distribution plots and more detailed discussions, see Paper B.

2.2.2 Plane wave spectrum (PWS) approach

Further improvement of the accuracy can be achieved by expanding the sampled focal field into a plane wave spectrum (PWS) [68–70].

With reference to Fig. 2.4, a grid of sampling points in the xy-plane P in front of the feed at $z = 0$ is chosen for the expansion of the PO radiated field in terms of a PWS. Each PW propagates to a specific observation point $\boldsymbol{r}$ on the feed where the field $\boldsymbol{E}^{\mathrm{i,f}}$ is tested. This process of field expansion and PW propagation is realized through the application of the truncated Fourier Transform pair [68]

$$\boldsymbol{A}(k_x, k_y) = \frac{1}{2\pi} \int_{-y_{\max}}^{y_{\max}} \int_{-x_{\max}}^{x_{\max}} \boldsymbol{E}^{\mathrm{i,f}}(x, y, z=0) e^{j(k_x x + k_y y)} \,\mathrm{d}x\,\mathrm{d}y \tag{2.9a}$$

$$\boldsymbol{E}^{\mathrm{i,f}}(\boldsymbol{r}) = \frac{1}{2\pi} \int_{-k_x^{\max}}^{k_x^{\max}} \int_{-k_y^{\max}}^{k_y^{\max}} \boldsymbol{A}(k_x, k_y) e^{-jk_z z} e^{-j(k_x x + k_y y)} \,\mathrm{d}k_x\,\mathrm{d}k_y \tag{2.9b}$$

where

$$k_z = \begin{cases} \sqrt{k^2 - k_x^2 - k_y^2} & \text{if } k^2 > k_x^2 - k_y^2 \\ -j\sqrt{k_x^2 - k_y^2 - k^2} & \text{otherwise.} \end{cases}, \tag{2.10}$$

and where the spectrum of PWs is limited to only those that are incident on the feed from directions within an angle subtended by the reflector and seen from the center of the plane P (see Fig. 2.4).

The magnitude of the co-polarized spatial frequency spectrum $|A_{\mathrm{co}}(k_x, k_y)|$ computed for small and large sampling plane sizes are shown in Fig. 2.5. It exhibits several interesting features: (i) as expected, the dominant spectral component corresponds to the on-axis PW, for which $k_x = k_y = 0$, while the second strongest set of

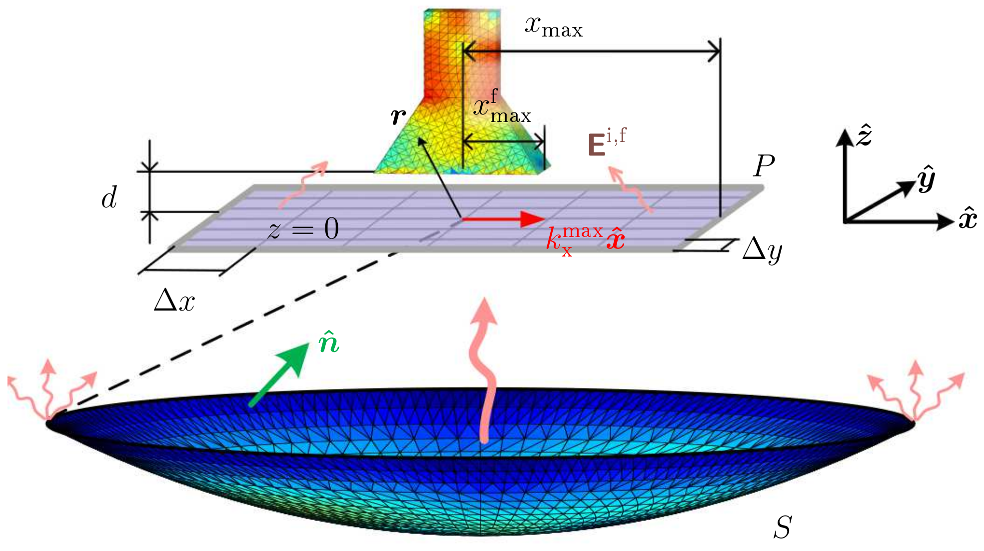

Figure 2.4: The FFT-enhanced PWS expansion method for the fast computation of the feed current due to the E-field from the reflector. Firstly, the incident field $\boldsymbol{E}^{\mathrm{i,f}}$ is sampled in the xy plane P in front of the feed in order to obtain the sampled PWS $\boldsymbol{A}(k_x, k_y)$; Secondly, each spectral PW propagates to an observation point $\boldsymbol{r}$ on the feed where $\boldsymbol{E}^{\mathrm{i,f}}$ is tested to compute the induced feed current.

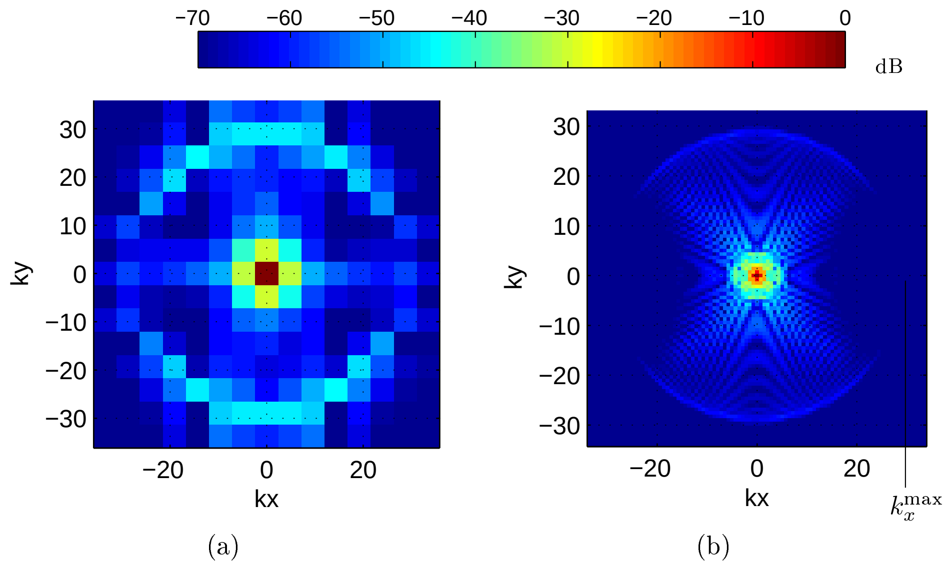

Figure 2.5: (a) The magnitude of the spatial frequency spectrum $|A_{\text{co}}(k_x, k_y)|$ (i.e. plane wave spectrum) for the 38λ reflector fed by the dipole array in case the FFT grid size is equal to size of the feed, and (b) when it is eight times the feed size.

PWs originate from the rim of the reflector, as observed by the spectral ring structure for which $k_x^2+k_y^2 = (k_x^{\max})^2 = (k_y^{\max})^2$; (ii) the magnitude of the PWs originating from the rim is polarization dependent, in fact, it is seen that, since the feed is X-polarized, the feed field interacts more at the top and bottom segments of the rim.

The approximation of the reflector field by a PWS introduces an error, ϵ_1, in the surface current of the feed. The relative error between the current expansion coefficient vectors $\mathbf{I}^{\text{approx}}$ and $\mathbf{I}^{\text{ref}}$ for the iterative CBFM-PO solution with and without field approximations, respectively – is computed as

$$\epsilon_1 = \left(\sqrt{\sum_i |I_i^{\text{ref}} - I_i^{\text{approx}}|^2} \Big/ \sqrt{\sum_i |I_i^{\text{ref}}|^2} \right) \times 100\%. \tag{2.11}$$

Fig. 2.6 illustrates the relative error computed as a function of the FFT sampling plane size P when the PWS is employed for expanding the reflector radiated field (for PWS parameters see Paper C), and when only the dominant on-axis PW term is used. As expected, the error decreases for an increasing sampling plane size, since more spectral PW terms are taken into account while the effect of the FFT-related periodic continuation of the spatial aperture field decreases. Henceforth, we choose the sampling plane size equal to that of the feed, for which the feed current error is about -35 dB for all the considered feeds, while it represents a good compromise from both a minimum number of sampling points and accuracy point of view. Conversely, if only the dominant on-axis PW term is used to approximate the reflector field, the error increases when the plane P becomes larger. This is due to the tapering of

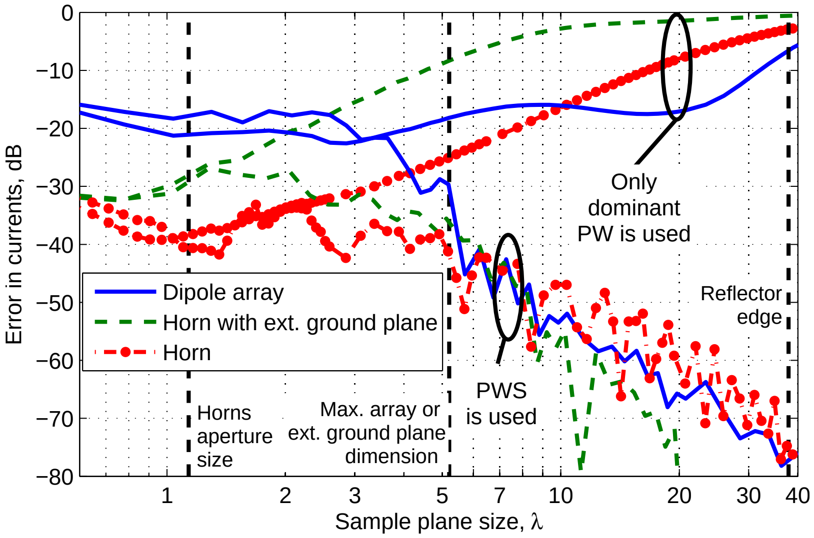

Figure 2.6: The relative error in induced feed currents [*cf.* (2.11)] as a function of the FFT sampling plane size P.

the reflector scattered field which becomes more pronounced when the plane size P increases, so that the PW amplitude $A(k_x, k_y)$ is underestimated when using the field averaging in (2.9a) for $k_x = k_y = 0$, as opposed to the direct on-axis point sampling method that has been presented in [44] and overviewed in Sec. 2.2.1.

2.2.3 Near-field interpolation (NFI) technique

While the previous section describes how the PWS-expanded E-field from the reflector accelerates the computation of the induced feed current, this section explains how the reflector incident H-field can be computed for the rapid determination of the induced PO current. For this purpose, the radiated H-field from the feed is first computed at a coarse grid on the reflector surface (white circles in Fig. 2.7), after which the field at each triangle is determined on the reflector (yellow square markers) through an interpolation technique. This interpolation technique de-embeds the initially sampled field to a reference sphere with radius R whose origin coincides with the phase center of the feed to assure that the phase of the de-embedded field will be slowly varying. Consequently, relatively few sampling points are required for the field interpolation, after which the interpolated fields are propagated back to the reflector.

In summary, and with reference to Fig. 2.7, the H-field interpolation algorithm for determining the reflector PO current

1. Defines a grid on the reflector surface (white circles) for computing the H-field.

2. De-embeds the H-field to a reference sphere around the feed phase center (green

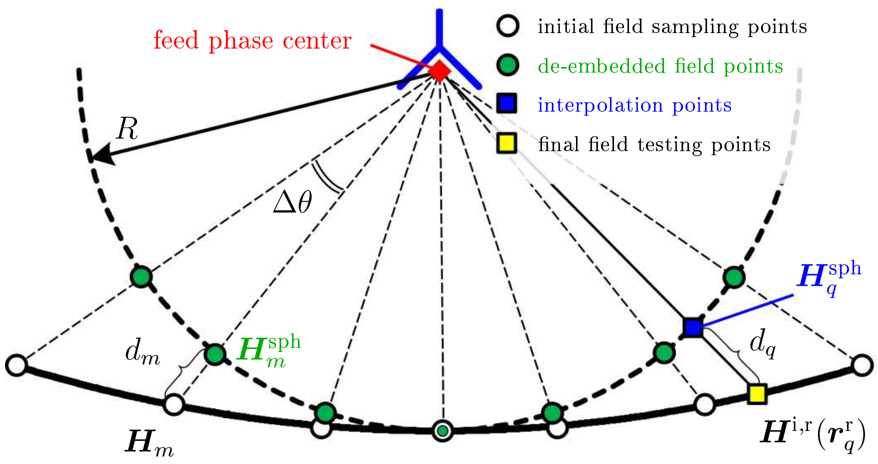

Figure 2.7: The near-field interpolation technique for the rapid determination of the induced PO current on the reflector.

points):

$$\boldsymbol{H}_m^{\mathrm{sph}} = \boldsymbol{H}_m d_m e^{jkd_m}, \tag{2.12}$$

where d_m is the distance between the reflector surface and the sphere of radius R along the line connecting the mth sample point on the reflector and the feed phase center.

3. Computes the fields on the sphere in the same directions as the reflector triangle centroids are observed (blue square markers) through interpolating the fields at the adjacent (green) points.

4. Propagates the field to the reflector surface; that is, at the qth triangle, the H-field

$$\boldsymbol{H}^{\mathrm{i,r}}(\boldsymbol{r}_q^{\mathrm{r}}) = \boldsymbol{H}_q^{\mathrm{sph}} d_q^{-1} e^{-jkd_q}. \tag{2.13}$$

5. Computes the reflector PO current (see e.g. [71, p. 343])

The error in the reflector current as a function of the sampling grid density is depicted in Fig. 2.8. It shows that the error in the resulting induced reflector current depends on the angular step size $\Delta\theta$ and $\Delta\phi$ of the initial field sampling grid (before interpolation). As expected, the error increases when the sampling grid coarsens. Furthermore, the error is larger for larger feeds, especially for high-scattering ones, for which the scattered fields (i.e. 2nd iteration and further) vary more rapidly than for smaller low-scattering antennas for which a coarser grid can be applied.

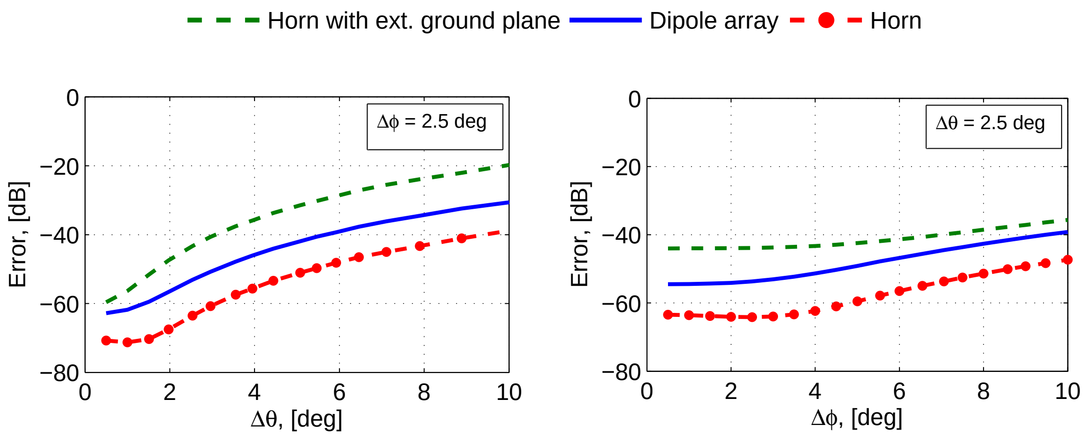

(a) (b)

Figure 2.8: The interpolation error in the 38λ reflector current as a function of (a) the sampling step $\Delta\theta$, and (b) the sampling step $\Delta\phi$ of the near fields of the feed.

2.2.4 Analysis of PWE and NFI errors and simulation times

Table 2.3 shows how the simulation time of a "plain" iterative CBFM-PO (or MoM-PO) approach reduces, and Table 2.4 summarizes the relative errors in both the currents and relevant antenna characteristics when the field approximations of Sec. 2.2.1 are used. The errors have been computed according to (2.8) and (2.11). Note that the PWS approximation leads to the small relative error of 0.28% in the surface current of the high-scattering feed for the 38λ reflector, while if only a single on-axis PW is used, the relative error is found to be two orders larger (see Sec. 2.2.1). It is also observed that, when applying the field approximations for both the reflector and feed, the relative error in the considered antenna characteristics remains less than 1%, while the computational speed advantage is significant (see Table 2.3), i.e., a factor 5 to 100, depending on the reflector size and feed complexity.

Table 2.3: Total simulation time (for $D = 118\lambda$ reflector)

	Horn	**Horn with ground plane**	**Dipole array**	**Vivaldi array**
MoM-PO, no approx.	70 min (100%)	192 min (100%)	801 min (100%)	3906 min (100%)
PWS approx.	27 min (39%)	63 min (33%)	190 min (24%)	1312 min (34%)
NFI approx.	57 min (81%)	152 min (79%)	548 min (68%)	2108 min (54%)
Both approx.	13 min (19%)	17 min (9%)	16 min (2%)	33 min (1%)

Table 2.4: Errors due to applying the field approximations, %

	Feed surface current		**Reflector surface current**		**Gain (on-axis)**		**Gain (@-3 dB)**		**Impedance**	
Reflector	**38λ**	**118λ**	**38λ**	**118λ**	**38λ**	**118λ**	**38λ**	**118λ**	**38λ**	**118λ**
Feed: Pyramidal horn										
PWS approx.	0.09	0.02	0.11	0.03	0.09	0.03	0.07	0.02	0.16	0.04
NFI approx.	0.01	<0.01	0.06	0.06	0.05	0.04	0.01	0.02	0.01	<0.01
Both approx.	0.09	0.02	0.13	0.07	0.13	0.07	0.07	0.04	0.15	0.04
Feed: Pyramidal horn with extended ground plane										
PWS approx.	0.28	0.02	0.41	0.02	0.06	0.01	0.09	0.01	0.44	0.04
NFI approx.	0.3	0.01	1.01	0.16	0.16	0.07	0.37	0.07	0.52	0.02
Both approx.	0.53	0.03	1.02	0.16	0.15	0.08	0.34	0.07	0.88	0.05
Feed: 121-element dual-polarized dipole array										
PWS approx.	0.05	0.02	0.1	0.02	0.03	0.01	0.01	0.01	0.03	0.01
NFI approx.	0.02	0.01	0.21	0.20	0.09	0.07	0.12	0.13	0.02	0.01
Both approx.	0.06	0.02	0.23	0.21	0.10	0.07	0.13	0.14	0.05	0.02

2.3 Experimental verification of the CBFM-PO approach with acceleration techniques

In addition to several cross-validations of the CBFM-PO approach using commercial software (see Paper C), a practical antenna system has been modeled and the computed illumination efficiency η_{ill} is compared to measurements. Fig. 2.9 shows η_{ill} of a 118λ reflector antenna ($D = 25$ m, $F/D = 0.35$), either fed by the Vivaldi array feed (APERTIF, [7]), or a single horn antenna. The numerically computed results are compared to measurements carried out at the Westerbork Synthesis Radio Telescope (WSRT) [7]. As one can see, the agreement is very good. The size of the simulated ground plane has been chosen equal to the size of the feed cabin ($\approx 1 \times 1$ m). The fact that η_{ill} is higher for the array feed than for the horn antenna nicely demonstrates the superior focal field sampling capabilities of dense PAFs. Furthermore, one can also observe a rather strong ripple in η_{ill} for the case of the horn feed with the extended ground plane. This ripple is caused by the relatively high feed scattering of the reflector field.

2.4 Numerical studies for different types of reflector antenna feeds

In this section several feeds are considered as part of a reflector antenna with aperture diameter 38λ. Several antenna characteristics, such as the radiation pattern, the

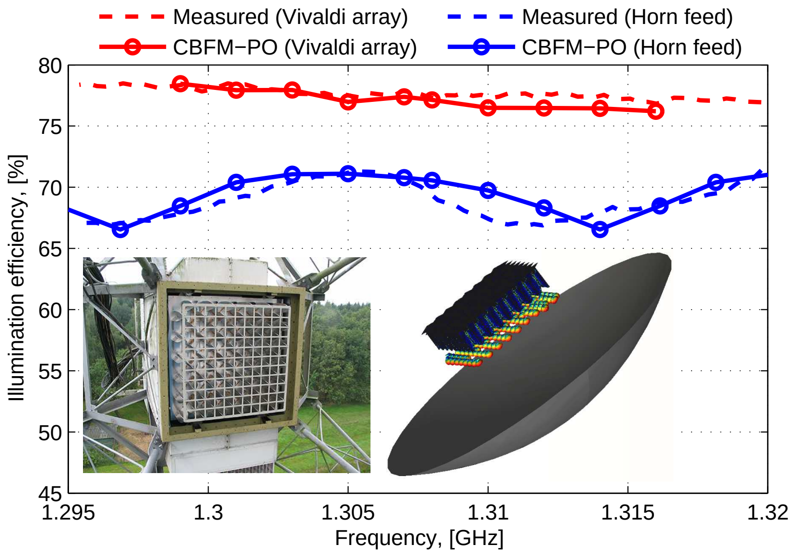

Figure 2.9: Illumination efficiencies of the 118λ reflector antenna, either fed by the 121 Vivaldi PAF, or the single-horn feed. The CBFM-PO simulated results are compared to the measured ones for a 25 m reflector antenna of the Westerbork Synthesis Radio Telescope [7]. Bottom of the figure: a photo of the experimental PAF system placed at the focal region of the reflector, and an image of a smaller-scale PAF-reflector model.

receiving sensitivity, and the aperture- and focal field distributions are analyzed using the CBFM-PO approach. First, we will show how the feed-reflector coupling affects the field distribution in the aperture of the reflector when fed by the horn with extended ground plane or the dipole antenna array of the same size [see Fig. 2.3(b) and (c)]. Afterwards, the model of the antenna system will be extended to include the spillover and antenna-LNA noise mismatch characteristics, so that the receiving sensitivity can be analyzed.

The aperture field distributions at two frequency points corresponding to the minimum and maximum aperture efficiencies are shown in Fig. 2.10 and 2.11 for the horn and the dipole array feeds, respectively. It is pointed out that the antenna elements are loaded by a complex impedance, which is accounted for directly when solving for the antenna feed currents through the CBFM. This is done through the modification of the diagonal elements of the MoM matrix corresponding to the port basis functions as described in [63, p. 223]. The impedance of the loads has been chosen to maximize the array decoupling efficiency [61], which yields the optimum load impedance of $60.88 - 8.12j$ and $147.4 + 45.6j$ Ω for the horn and array case, respectively. For the horn case this implies the ideal power-matched case.

As one can observe from the figures, the aperture field at the 2nd iteration, i.e., due to the scattered field of the feed [Fig. 2.10(c) and Fig. 2.11(c)], is about 20 dB lower for the array feed, thereby rendering the field variation negligible. On the contrary, for the horn feed, the peak and dip of the field is clearly seen in the aperture center.

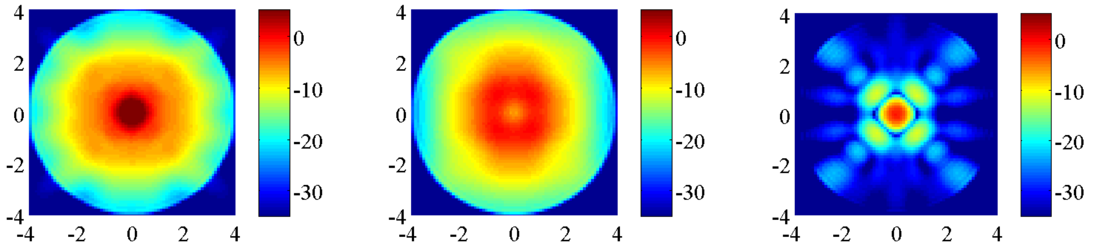

(a) Total aperture field, f @ min η_{ap} (b) Total aperture field, f @ max η_{ap} (c) Aperture field at 2nd iteration, f @ max η_{ap}

Figure 2.10: The field distribution in the aperture of a 38λ reflector fed by the horn with extended ground plane.

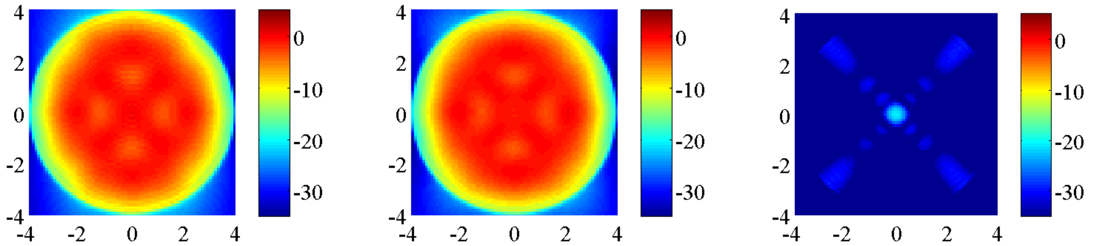

(a) Total aperture field, f @ min η_{ap} (b) Total aperture field, f @ max η_{ap} (c) Aperture field at 2nd iteration, f @ max η_{ap}

Figure 2.11: The field distribution in the aperture of a 38λ reflector fed by the array of 121 half-wavelength dipoles.

This leads to a significant variation of the aperture efficiency η_{ap} over frequency, viz. 19.6% versus 0.6% for the array.

For some applications, such as for radio astronomy, a reflector antenna works purely in receiving mode, and other system characteristics, such as the system noise temperature T_{sys} and the receiving sensitivity $A_{\mathrm{eff}}/T_{\mathrm{sys}}$, become important. The main contributors to T_{sys} that are dependent on multiscattering effects, are the spillover noise temperature T_{spill} and the noise temperature due to the noise mismatch between the antenna(s) and LNA(s)[2], T_{coup}. In order to compute T_{coup}, the equivalent one-port system representation is used as described in [72]. By using this extension to the CBFM-PO approach, the next step is to consider the two relatively small feeds shown in Fig. 2.12. The antenna array ports are connected to Low Noise Amplifiers (LNAs) which are also part of the antenna-receiver model. Two beamforming scenarios for the array are considered: (i) a singly-excited embedded element, and; (ii) a fully-excited antenna array employing the Conjugate Field Matching (CFM) beamformer for maximizing the gain of the secondary far-field beam.

The computed aperture efficiency η_{ap}, system noise temperature T_{sys}, and the

[2]in case of phased array feeds T_{coup} also takes the excitation scheme and coupling between the array elements into account.

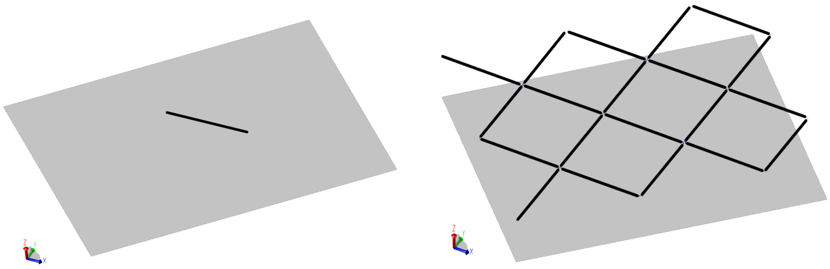

(a) A single dipole above a PEC ground plane

(b) A dual-polarized array of 20 dipole antenna elements

Figure 2.12: The considered dipole antenna feeds. The dipole length is 0.47λ and the ground plane size is $1.66\lambda \times 1.33\lambda$

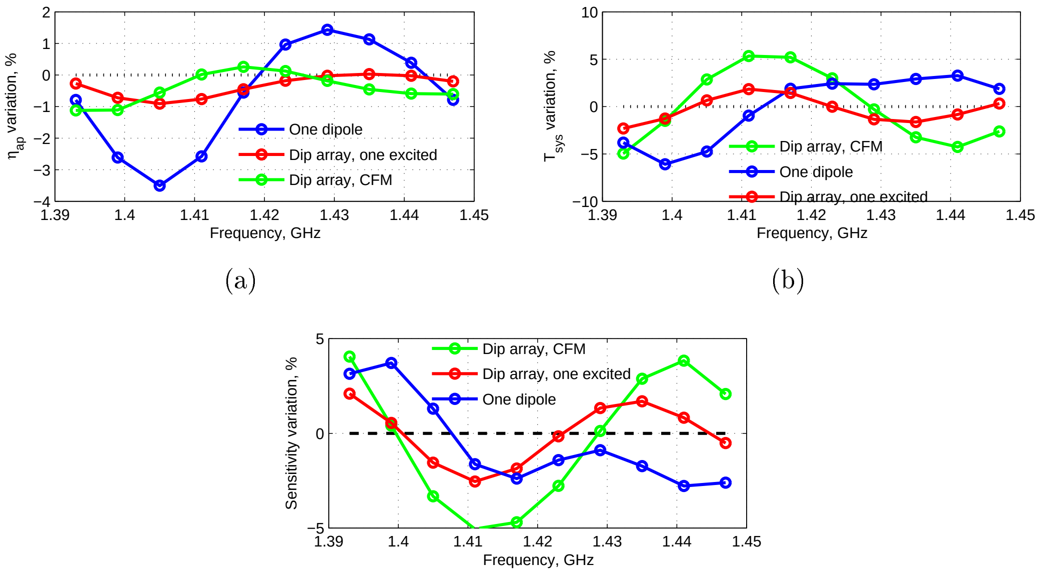

(a)

(b)

(c)

Figure 2.13: The aperture efficiency, the system noise temperature, and the resulting receiving sensitivity of the reflector antenna system as a function of frequency.

resulting receiving sensitivity $A_{\mathrm{eff}}/T_{\mathrm{sys}}$ are shown in Fig. 2.13. By analyzing these figures, one can conclude that the aperture efficiency varies with frequency much more for the case of a single element due to a fact that a lot of energy scatters from the ground plane behind the dipole.

The feed-reflector interaction phenomenon leads not only to the variation in η_{ap}, but also leads to a variation in T_{sys}. These variations are comparable for the the single dipole and array feeds, and have a major impact on the sensitivity ripple. Although T_{sys} is similar for both feeds, the mechanism of forming the ripple is different; when the reflector is fed by the feed shown in Fig. 2.12(a), the radiation pattern of the feed is "breathing" over frequency, resulting in the variation of the spillover noise temperature T_{spill}, while for the feed in Fig. 2.12(b) the main contribution to the T_{sys} variation is caused by the variation T_{coup}. See Paper A for more details.

2.5 Analysis of antenna arrays using Krylov subspace iteration with domain decomposition approach

To calculate the feed–reflector interaction the described above method involves solving for the electric current on the feed, for which CBFM method was used. There are other methods that are capable of handling electrically large antennas, such as the multilevel fast multipole method (MLFMM), the Full Orthogonalization Method (FOM), or the Generalized Minimal Residual Method (GMRES) [73]. The latter two methods are iterative in nature and make use of Krylov subspace iteration to generate so called "generating vectors", which (after orthogonalization) can be considered as macro-basis functions, the coefficients of which are determined through the GMRES approach.

In this section we propose a domain-decomposition approach to Krylov subspace iteration, where MBFs (or CBFs) on each subdomain are naturally constructed from the different segments of the generating vectors.

Formulation of the method

Consider the Method of Moments (MoM) matrix equation:

$$\mathbf{Z}\mathbf{I} = \mathbf{e}, \tag{2.14}$$

where $\mathbf{Z}$ is the $N \times N$ MoM matrix; $\mathbf{e}$ is the $N \times 1$ excitation vector and $\mathbf{I}$ is a vector containing the unknown expansion coefficients for the elementary basis functions. Accordingly, the reduced CBFM system of equations can be written as

$$\tilde{\mathbf{Z}}\tilde{\mathbf{I}} = \tilde{\mathbf{e}}, \tag{2.15a}$$

$$\tilde{\mathbf{Z}}_{i,j} = \mathbf{K}_i^H \mathbf{Z}_{i,j} \mathbf{K}_j, \tag{2.15b}$$

$$\tilde{\mathbf{e}}_i = \mathbf{K}_i^H \mathbf{e}_i, \tag{2.15c}$$

where $i, j = 1 \ldots M$ are sub-domain indices; M is the number of subdomains; H is the Hermitian operator and $\mathbf{K}_i$ is the set of MBFs. The method proposed here consists of selecting as MBFs on a given subdomain the corresponding segments of the generating vectors. Those segments correspond to entries associated to basis functions defined on the subdomain of interest. Hence, the newly proposed MBF selection reads:

$$\mathbf{K}_i = \left[\mathbf{k}_i^{(1)} = \mathbf{e}_i \mid \mathbf{k}_i^{(2)} \mid \ldots \mid \mathbf{k}_i^{(P)}\right], \tag{2.16}$$

in which the generating vector $\mathbf{k}$ is formed iteratively as

$$\mathbf{k}^{(p+1)} = \mathbf{Z}\mathbf{k}^{(p)} \quad \text{for} \quad p = 1 \ldots P-1, \tag{2.17}$$

where index i refers to the MBF vector entries related to subdomain i.

It is important to point out that the most computationally expensive part of the MoM matrix reduction (2.15b), namely the matrix-matrix product $\mathbf{Z}_{i,j}\mathbf{K}_j$, can be carried out during the subspace construction (2.17). For this purpose, (2.17) is built from M^2 smaller matrix-vector products resulting in the M^2 vectors $\mathbf{v}_{i,j}^{(p)}$, expressed as

$$\mathbf{v}_{i,j}^{(p)} = \mathbf{Z}_{i,j}\mathbf{k}_j^{(p)}. \tag{2.18}$$

Segment i of the vector $\mathbf{k}^{(p+1)}$ (at the next iteration) is obtained by a simple summation of vectors $\mathbf{v}_{i,j}^{(p)}$ as

$$\mathbf{k}_i^{(p+1)} = \sum_j \mathbf{v}_{i,j}^{(p)}. \tag{2.19}$$

If the vectors $\mathbf{v}_{i,j}^{(p)}$ are concatenated in a matrix $\mathbf{Q}$ as

$$\mathbf{Q}_{i,j} = \left[\mathbf{v}_{i,j}^{(1)} \mid \mathbf{v}_{i,j}^{(2)} \mid \ldots \mid \mathbf{v}_{i,j}^{(p)}\right], \tag{2.20}$$

then the MoM matrix reduction (2.15b) can be rewritten as

$$\tilde{\mathbf{Z}}_{i,j} = \mathbf{K}_i^H \mathbf{Z}_{i,j}\mathbf{K}_j = \mathbf{K}_i^H \mathbf{Q}_{i,j}, \tag{2.21}$$

which allows one to reduce the time involved in (2.15)-(2.17) by almost a factor two , as compared to a straight-forward implementation. The appendix in Paper G explains how (2.21) can be modified when the set of MBFs needs to be orthogonalized.

Fig. 2.14(a) visualizes the matrix $\mathbf{Q}$, which consists of vectors $\mathbf{v}$, and Fig. 2.14(b) shows the matrix segment $\mathbf{Q}_{i,j}$.

CBFM with restarts

The accuracy of the CBFM can be significantly improved down to machine precision by introducing a restart procedure similar to that used in a restarted GMRES method [73]. The main difference with GMRES is that the subspace is restarted on every subdomain. The restart algorithm is presented in Sec.III of Paper G.

Numerical results

The proposed approach is compared to the GMRES algorithm in terms of the relative error in the surface current (reference is exact MoM solution) versus the solving complexity. The complexity is herein defined as the number of elementary operations

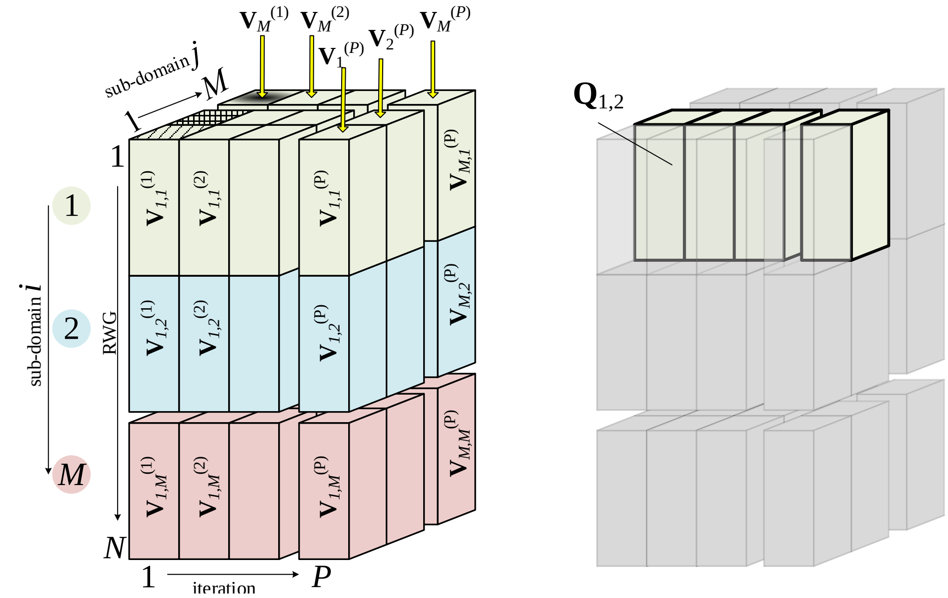

(a) (b)

Figure 2.14: (a) Matrix $\mathbf{Q}$ and its vectors, and (b) its sub-matrices $\mathbf{Q}_{i,j}$.

"$ab+$" (floating point product of complex scalar numbers and summation with another complex number), required to solve the problem.

Fig. 2.15(a) and (b) show two similar antenna arrays consisting of Vivaldi radiators, where in the first case the elements are electrically interconnected, and in second array there is a small air-gap between the elements. Different colors denote different subdomains in which the arrays are divided. First, a reference surface current distribution on each array was found using pure method-of-moments. Then, the current was computed using GMRES and the proposed CBF approach. Finally, an error between each of these and the reference solution was obtained, the result of which is depicted in Fig. 2.15(c). The round markers denote restart positions. From the figure one can see a clear advantage of the proposed CBFM approach as it takes about 1.5 to 2.6 times less of elementary operations to reach same level of the error, which was chosen to be -50 dB.

Of course, the benefit of using this approach varies depending on the type of structure under investigation. We have considered two more structures in Paper G: i) a sphere at a resonant frequency, and; ii) a rectangular plate, both of which were divided in subdomains of different sizes. It turned out that in the worst case (like for the rectangular plate) the iterative CBF approach essentially provides the same accuracy as GMRES, but for the best case (the sphere at resonant frequency), the time to reach convergence for the CBFM can be more than 3 times shorter.

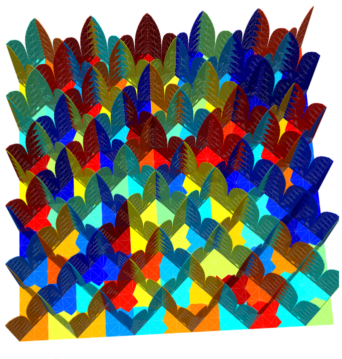

(a) connected array.

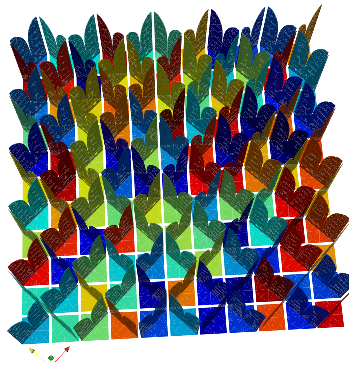

(b) disconnected array.

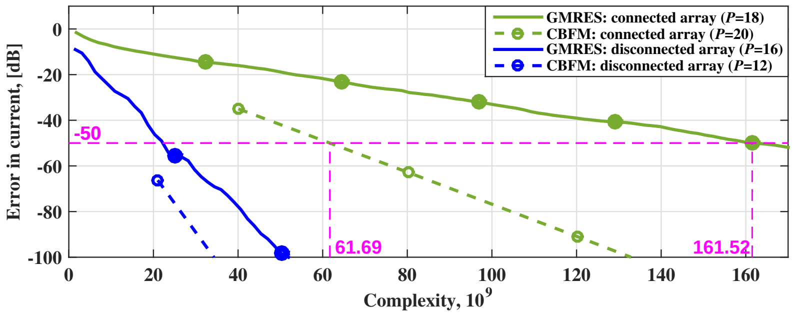

(c) GMRES and CBFM convergence.

Figure 2.15: Numerical example: (a) a connected, and; (b) disconnected 121-element dual-polarized Vivaldi array, divided into 121 subdomains and excited by a delta-gap voltage sources at each antenna element. Subfigure (c) compares the convergence rates of restarted GMRES and CBF method. The restart positions are indicated by circles.

Discussion

When well-preconditioned, GMRES converges very rapidly (i.e. within a few tens of iterations), almost irrespective of the number of unknowns. As explained in [74], GMRES amounts to solving a reduced system of equations, whose size (i.e. number of degrees of freedom, DoFs), corresponds to the number of iterations. For large problems, this solution takes a negligible time as compared to that involved in the mat-vec operations. This means that, without significant increase in the computation time, one can afford more DoFs, as is the case with the approach proposed here, since the number of DoFs now corresponds to the number of mat-vecs P multiplied by the number of subdomains. Without any specific matrix-vector multiplication, solving the reduced system of equations has a complexity $(PM)^3$ (here it is worthwhile mentioning that there exist methods to reduce this exponent, see e.g. [75]), while the complexity of the mat-vecs is PN^2. The increase in computational time is therefore small as long as $P^2M \ll N_{sd}^2$, where N_{sd}^2 is the average number of elementary basis functions per subdomain.

2.6 Conclusions

To conclude the research that has been presented in this chapter, we highlight the following observations:

- The feed-reflector interaction (standing wave) effects give rise to oscillations in the system characteristics with frequency $\Delta f = c/(2F)$, where c is speed of light and F is the reflector focal distance. This results in the "heart beating" effect – the change of the beamwidth and gain, as well as T_{sys} variation over frequency.

- An FFT-enhanced Plane Wave Spectrum (PWS) approach has been formulated in conjunction with the Characteristic Basis Function Method, a Jacobi iterative multiscattering approach, and a near-field interpolation technique for the fast and accurate analysis of electrically large array feed reflector systems. Numerical validation (presented in Paper C) has been carried out using the multilevel fast multipole algorithm method available in the commercial FEKO software.

- The scattering from the feed is minimal for power-matched antenna loads (more critical for PAFs) and when size of the surrounding metal structure is minimized (more critical for single-port feeds, especially in MFFEs).

- The electromagnetic coupling between the reflector antenna and the dipole PAFs under study have a minor impact on the antenna beam shape and aperture efficiency, as opposed to that of a single dipole feed. The finite ground plane behind the single dipole, which is part of the feed supporting structure and is often much larger than one antenna element, but comparable to the size of a PAF, is a reason for this difference.

- The (active) impedance matching of the strongly-coupled PAF elements appears to be more sensitive to the feed-reflector interaction effects, as a result of which the receiver noise temperature increases.

- The sensitivity variation is mainly driven by the variation in the system noise temperature, of which the main contribution is due to the noise mismatch of the considered PAF array elements with LNAs. Therefore, in order to reduce the sensitivity ripple of reflector antennas with PAFs, major attention should be paid to the noise matching and its stability over time in the presence of a reflector when designing a PAF system.

- The conclusion in [48] states that the Radar Cross-Section (RCS) of the feed is the determining factor in magnitude of the standing wave effect. This is true only for the aperture efficiency variation, but it does not apply to the noise characteristics (T_{spill}, T_{coup}). Other factors showing why the RCS is not a good figure of merit to quantify the standing wave effect in receiving systems are that the the RCS does not account for the relative size of the feed w.r.t. the reflector, and that it assumes a uniform PW field radiated by the reflector.

- A domain-decomposition technique into Krylov subspace iteration has been developed. This method is similar to the CBFM, here the MBFs are generated by simple segmentation of the pre-computed vectors of the Krylov subspace. The achieved convergence is faster than with GMRES by a factor ranging from 1.05 (the rectangular plate with large subdomains) to 2.6 (the connected Vivaldi array) while keeping the same accuracy.

Chapter 3 Optimum Beamforming Strategies for Earth Observations

It has been argued in Sec. 1.2 that push-broom configurations for satellite radiometers are advantageous for Earth observation systems when equipped by PAFs. Therefore, the goals of the work presented in this chapter are to determine: (i) to what extent the performance-limiting factors of push-broom radiometers can be reduced by using dense PAFs employing advanced beamforming schemes; (ii) the minimum required complexity of the PAF design (size, number of elements and their arrangement in the feed as well as the number of active receiver channels), and; (iii) what beamforming strategy to use for meeting the instrument specifications for future radiometers [10]. Finally, a trade-off analysis will be performed in order to choose the radiating antenna element for the PAF.

3.1 Performance requirements

Before describing the push-broom array design and beamforming scenarios, the requirements for such radiometers are described first and how they are related to the antenna system requirements.

In February 2013 the ESA contract 4000107369-12-NL-MH was awarded to the team consisting of TICRA, DTU-Space, HPS, and Chalmers University. The first workpackage of the contract involved the review of ocean sensing performance parameters, which in turn resulted in the requirements for future satellite radiometers as shown in Table 3.1 [10,76]. Derivation of these requirements is presented in Paper K.

The table indicates that the radiometer should operate at three narrow frequency bands: C-band (6.9 GHz), X-band (10.65 GHz) and Ku-band (18.7 GHz). The instrument must be dual-polarized and have a receiving sensitivity in the $0.22 - 0.3$ K range. The overall error of the sea temperature measurement should not exceed 0.25 K. The maximum allowed footprint size is 20 km for C- and X-band, and 10 km for the Ku-band. Under "footprint" we understand the region of the sea

Table 3.1: Radiometer requirements

Freq., [GHz]	**Bandwidth, [MHz]**	**Polarization**	**Sensitivity, [K]**	**Accuracy ΔT, [K]**	**Resolution FP, [km]**	**Dist. to land D_{L}, [km]**
6.9	300	V, H	0.30	0.25	20	5-15
10.65	100	V, H	0.22	0.25	20	5-15
18.7	200	V, H	0.25	0.25	10	5-15

that is illuminated by the antenna beam from -3 to 0 dB level with respect to the beam maximum. Additionally, the instrument should satisfy the above-described requirements even when the observation is as close as 15 km from the coast line. The latter requirement is called "distance to coast" and explained with the aid of Fig. 3.1.

The brightness temperature of the land surface is assumed to be $T_{\mathrm{L}} = 250$ K. Assume next that we wish to measure the sea at horizontal polarization for which the brightness temperature is around $T_{\mathrm{H}} = 75$ K (the brightness temperature of the vertical polarization is higher, i.e. 150 K, and therefore it is less affected by the erroneous power signal from land). It can be shown that the requirement for the maximum error $\Delta T = 0.25$ K can be satisfied only if the power of the beam in the cone with half-angle θ_{c} is 99.72 % of the total power incident on the Earth's surface [35]. This determines the distance to coast D_{c}, which is defined as the angular difference $\theta_{\mathrm{c}} - \theta_{3\mathrm{dB}}$ projected on the Earth surface, i.e.,

$$D_{\mathrm{c}} = Y \sin\theta_{\mathrm{c}} - Y \sin\theta_{3\mathrm{dB}} \approx (\theta_{\mathrm{c}} - \theta_{3\mathrm{dB}})Y, \tag{3.1}$$

where Y is the distance from the satellite to the observation point on the Earth (see Fig. 3.2 for the satellite orbit parameters). Therefore, to find the distance-to-coast

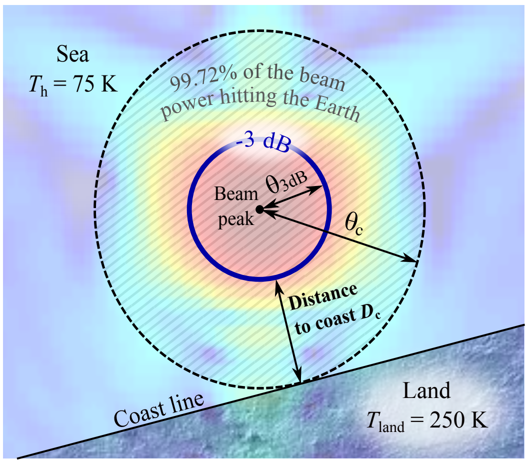

Figure 3.1: Definition of the "Distance to coast" radiometer requirement. A typical radiation pattern of the torus reflector antenna is shown as background.

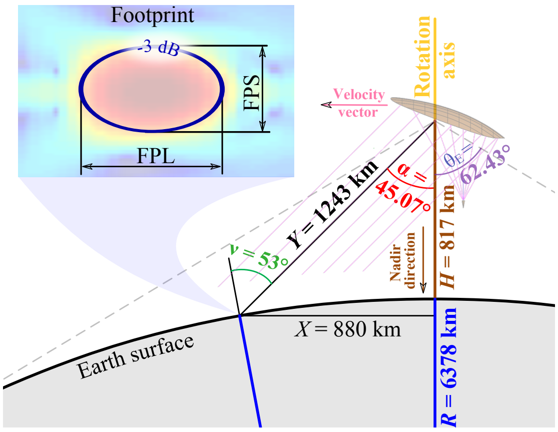

Figure 3.2: Geometrical parameters of the radiometer antenna system located on the Earth orbit. The notation of the major and minor axes of the footprint ellipse is shown in the top-left insertion.

characteristic, the angles θ_c and θ_{3dB} are found first from the antenna compound beam and Eq. (3.1) is used afterwards.

Since the radiometer must be able to measure the brightness temperature of both polarizations separately, an error is introduced due to the received power of the cross-polarized component of the incident field. It is shown in [35] that this power must not exceed 0.34 % of the co-polarized power, in order to satisfy the maximum error requirement $\Delta T = 0.25$ K. Since the brightness temperature of the sky is very low and the amount of power radiated towards the sky is small, it suffices to compute the antenna total radiation pattern only at the angular range subtended by the Earth ($\theta = 0 \ldots \theta_E$ from the Nadir direction).

Another requirement for the radiometer is the sampling resolution, which sets requirements on the maximum size of the footprint (FP). The footprint will have an elliptical shape due to oblique incidence of the radiated field on the Earth's surface as shown in the top-left insertion of Fig. 3.2. The longitudinal and transverse to the movement direction axes of the ellipse are denoted as FPL and FPS, correspondingly. The footprint size, FP, is determined as the average of FPS and FPL:

$$\mathrm{FP} = \frac{\mathrm{FPS} + \mathrm{FPL}}{2}, \tag{3.2}$$

where FPS is related to the half-power beamwidth (HPBW) as

$$\mathrm{FPS} = Y \times \mathrm{HPBW}_{\mathrm{transv}}, \tag{3.3}$$

and FPL is

$$\mathrm{FPL} = \frac{Y \times \mathrm{HPBW}_{\mathrm{long}}}{\cos \nu}, \tag{3.4}$$

where $\mathrm{HPBW}_{\mathrm{transv}}$ and $\mathrm{HPBW}_{\mathrm{long}}$ are the longitudinal and transverse beamwidths to the movement vector directions; and ν is the incidence angle.

Another characteristic of the radiometer radiation pattern is the beam efficiency, which is usually defined as the relative power within the main beam down to the −20 dB contour level. A high beam efficiency is generally synonymous with a good quality antenna. However, a low beam efficiency antenna may not necessarily represent a bad antenna. For example, for the radiometer, the feed spillover past the reflector edge reduces the beam efficiency, but it illuminates the cold sky and does no harm; it is the radiation towards the Earth that makes a significant impact, and must therefore be taken in account.

3.2 Reflector antenna design

The design procedure of the push-broom reflector is described in [37] and has been developed by TICRA. In short, and with the reference to Fig. 3.3, the surface of the reflector (blue dots) is created by rotation of the parabolic profile (black dots), defined

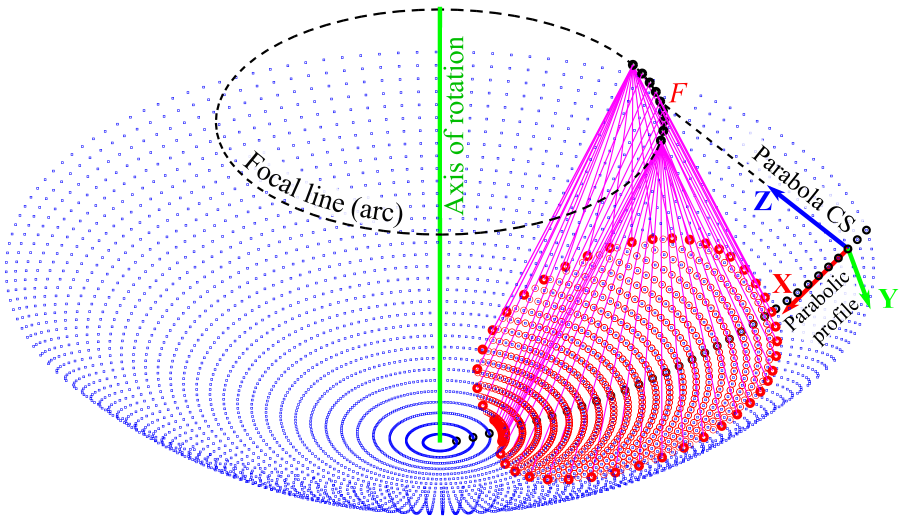

Figure 3.3: Design procedure of a parabolic torus reflector: the parabolic profile (black circles at the bottom), defined in the coordinate system "Parabola CS" and with focal point F, is rotated around the green axis of rotation which itself is tilted with respect to the parabola axis. This transforms the profile focal point F to the focal line (arc) along which a PAF will be positioned.

in the coordinate system "Parabola CS" and with focal point F, around the green axis of rotation which is tilted with respect to the parabola axis. The reflector rim (edge of the red area) is chosen based on the requirements on the projected aperture area and maximum scan angle. The latter parameter also defines the size of the PAF along the focal arc, which is created by rotating the focal point F around the axis of rotation.

Due to the rotational symmetry of the reflector, it is natural to locate the array antenna elements in a polar grid with the origin located at the point where the axis of rotation intersects the plane of the focal arc. The layout of such an array is shown in Fig. 3.4. The reflector focal arc is denoted by the black curve to show the position of the array relative to the reflector.

3.3 Optimum PAF beamformers

To outline the optimization procedure for the PAF beamformers considered in this work, we utilize the generalized system representation as shown in Fig. 3.5 for N actively beamformed PAF antennas [17]. The PAF system is subdivided into two blocks: (i) the frontend including the reflector, array feed and Low Noise Amplifiers (LNAs), and; (ii) the beamformer with complex conjugated weights $\{w_n^*\}_{n=1}^N$ and an ideal (noiseless/reflectionless) power combiner realized in software.

Here, $\mathbf{w}^H = [w_1^*, \ldots, w_N^*]$ is the beamformer weight vector, H is the Hermitian conjugate-transpose, and the asterisk denotes the complex conjugate. Furthermore,

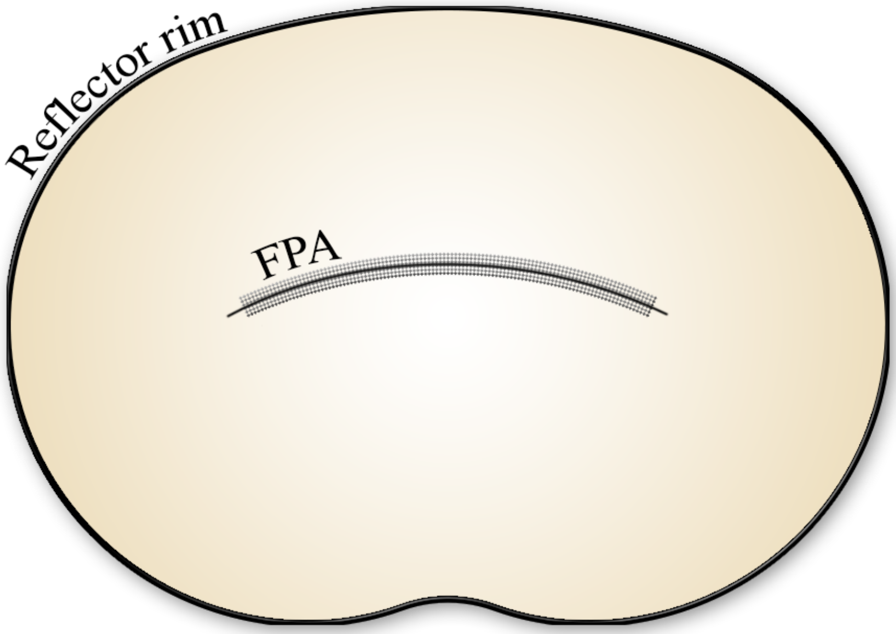

Figure 3.4: Preliminary layout of the PAF for the push-broom reflector. The black arc shows the position of the focal arc of the reflector.

$\mathbf{a} = [a_1, \ldots, a_N]^T$ is the vector holding the transmission-line voltage-wave amplitudes at the beamformer input (the N LNA outputs). Hence, the fictitious beamformer output voltage v (across Z_0) can be written as $v = \mathbf{w}^H\mathbf{a}$, and the receiver output power as $|v|^2 = vv^* = (\mathbf{w}^H\mathbf{a})(\mathbf{w}^H\mathbf{a})^* = (\mathbf{w}^H\mathbf{a})(\mathbf{a}^T\mathbf{w}^*)^* = \mathbf{w}^H\mathbf{a}\mathbf{a}^H\mathbf{w}$, where the propor-

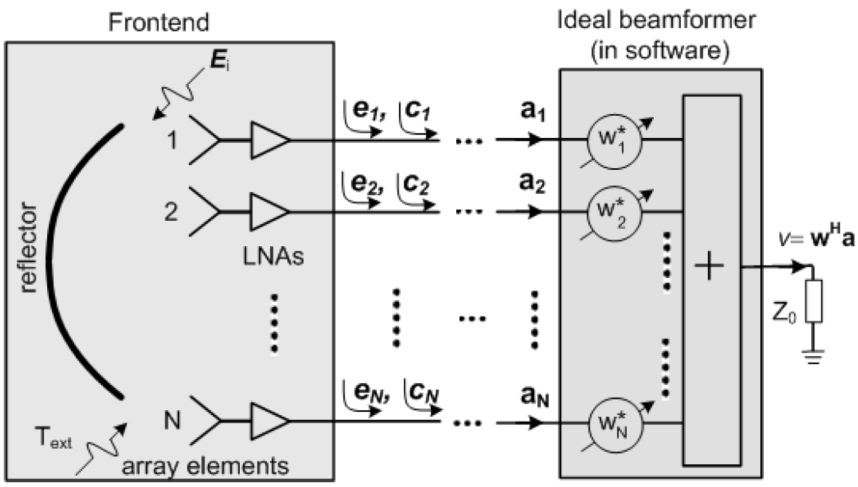

Figure 3.5: Generalized representation of the PAF reflector antenna system.

tionality constant has been dropped as this is customary in array signal processing and because we will consider only ratio of powers.

Although each subsystem can be rather complex and contain multiple internal signal/noise sources, it is characterized externally (at its accessible ports) by a scattering matrix in conjunction with a noise- and signal-wave correlation matrix. Accordingly, the signal-to-noise ratio (SNR) can be expressed as

$$\mathrm{SNR} = \frac{\mathbf{w}^H \mathbf{P} \mathbf{w}}{\mathbf{w}^H \mathbf{C} \mathbf{w}}, \tag{3.5}$$

that is, the SNR function is defined as a ratio of quadratic forms, where $\mathbf{P} = \mathbf{e}\mathbf{e}^H$ is the signal-wave correlation matrix, which is a one-rank positive semi-definite matrix for a single point source; the vector $\mathbf{e} = [e_1, \ldots, e_N]^T$ holds the signal-wave amplitudes at the receiver outputs and arises due to an externally applied electromagnetic plane wave $\boldsymbol{E}_\mathrm{i}$; and $\mathbf{C}$ is a Hermitian spectral noise-wave correlation matrix holding the correlation coefficients between the array receiver channels, i.e., $C_{mk} = \mathrm{E}\{c_m c_k^*\} = \overline{c_m c_k^*}$. Here, c_m is the complex-valued voltage amplitude of the noise wave emanating from channel m, which includes the external and internal noise contributions inside the frontend block in Fig. 3.5, and the overbar denotes time average. We consider only a narrow frequency band, and assume that the statistical noise sources are (wide-sense) stationary random processes which exhibit ergodicity, so that the statistical expectation can be replaced by a time average (as also exploited in hardware correlators).

Below, we will first discuss two standard signal processing algorithms, which are then used as the starting point to develop the two customized push-broom radiometer beamformers.

3.3.1 Standard maximum signal-to-noise ratio beamformer – MaxSNR

The well-known closed-form solution that maximizes (3.5) for the point source case, where $\mathbf{P}$ is of rank 1, is given by [77]

$$\mathbf{w}_{\mathrm{MaxSNR}} = \mathbf{C}^{-1}\mathbf{e}, \text{ with } \mathrm{SNR} = \mathbf{e}^H \mathbf{w}_{\mathrm{MaxSNR}}, \tag{3.6}$$

where the principal eigenvector $\mathbf{e}$ corresponds to the largest eigenvalue of $\mathbf{P}$. If we assume a noiseless antenna system, the matrix $\mathbf{C}$ will contain the noise correlation coefficients only due to external noise sources (received noise), and its elements can be calculated through the pattern-overlap integrals between $\boldsymbol{f}_n(\Omega)$ and $\boldsymbol{f}_m(\Omega)$, which are the nth and mth embedded element pattern of the array, respectively [17], i.e.,

$$C_{mn} = \int T_{\mathrm{ext}}(\Omega)[\boldsymbol{f}_m(\Omega) \cdot \boldsymbol{f}_n^*(\Omega)]\, \mathrm{d}\Omega, \tag{3.7}$$

where $T_{\text{ext}}(\Omega)$ is the brightness temperature distribution of the environment. The proportionality constants between the right-hand side and the noise waves on the left-hand side are omitted.

3.3.2 Standard Conjugate Field Matching beamformer – CFM

The CFM beamformer maximizes the received signal power at its output, i.e.,

$$\max_{\mathbf{w}} \left(\frac{\mathbf{w}^H \mathbf{P} \mathbf{w}}{\mathbf{w}^H \mathbf{w}} \right), \tag{3.8}$$

which is also equivalent to maximizing the directivity. The trivial solution to that is (provided that $\mathbf{P} = \mathbf{e}\mathbf{e}^H$)

$$\mathbf{w}_{\text{CFM}} = \mathbf{e}. \tag{3.9}$$

However, since this beamformer assumes a noiseless system and a uniform incident plane wave from the direction of observation, it will provide a sub-optimal solution for practical systems. In particular, it allows no control on the radiation outside of the main beam.

To overcome this issue, a slightly different CFM approach is used, in which we let a *tapered* plane wave with a Gaussian amplitude distribution be incident from the observation direction, calculate the focal field at location of the PAF elements and use the conjugate values of this field as excitation coefficients. Thus, the excitation coefficient are calculated as

$$\begin{cases} \mathbf{w}_{\text{CFM2}}^{\text{Co}} = \left[\mathbf{E}_{\text{foc}}^{\text{Co}}(\mathbf{x}^{\text{Co}}, \mathbf{y}^{\text{Co}})\right]^* \\ \mathbf{w}_{\text{CFM2}}^{\text{Xp}} = \left[\mathbf{E}_{\text{foc}}^{\text{Xp}}(\mathbf{x}^{\text{Xp}}, \mathbf{y}^{\text{Xp}})\right]^* \end{cases} \tag{3.10}$$

where $\mathbf{w}_{\text{CFM2}}^{\text{Co}}$ and $\mathbf{w}_{\text{CFM2}}^{\text{Xp}}$ are vectors holding the excitation coefficients of co- and cross-polarized components, correspondingly; $\mathbf{x}^{\{\text{Co,Xp}\}}$ and $\mathbf{y}^{\{\text{Co,Xp}\}}$ are vectors with x- and y-coordinates of the co- and cross-polarized PAF elements in the focal plane; and $\mathbf{E}_{\text{foc}}^{\text{Co}} = \left[E_{\text{foc},1}^{\text{Co}}, \dots E_{\text{foc},N}^{\text{Co}}\right]^T$ and $\mathbf{E}_{\text{foc}}^{\text{Xp}} = \left[E_{\text{foc},1}^{\text{Xp}}, \dots E_{\text{foc},N}^{\text{Xp}}\right]^T$ are vectors holding the focal field components at position of each PAF element and corresponding to their polarization.

In contrast to (3.9), the CFM approach in (3.10) assumes that the PAF elements are isotropic within the reflector subtended angle (there are no array EEPs incorporated in this beamformer, and the array radiators are just point linear/circular polarized sources), but this assumption is still good because a typical small radiator used in dense PAFs has a wide beamwidth and nearly spherical phase front of the radiated field within the reflector subtended angle ($\pm 24°$ in our case).

This CFM formulation allows us to choose the taper of the incident plane wave in order to control such beam parameters as side-lobes (related to the distance-to-coast radiometer characteristic) and beamwidth (related to the footprint size).

This beamforming approach has been used by our co-authors in Paper D, where the optimal taper value has been determined through a study how it affects the radiometer performance. Although the radiometer characteristics will then satisfy the system performance specifications, the PAF requires us to employ too many antenna elements (almost a factor 2 more as compared to the customized beamformers presented in the following subsections 3.3.3 and 3.3.4), which is not feasible for a realistic satellite system due to an excessive power consumption.

3.3.3 Maximum Sensitivity, Minimum Distance to Land beamformer – MSMDL

A major drawback of the MaxSNR and CFM beamformers is that these maximize the sensitivity/directivity without constraints imposed on the side-lobes and cross-polarization levels, or have a very limited control over them. This means that the required values of the distance-to-coast and the maximum allowable cross-polarization power cannot be guaranteed, especially not for a non-parabolic surface of the reflector.

To overcome this limitation one could consider the MaxSNR beamformer [Eq. (3.6)] which is used to maximize the beam efficiency (defined at the -20 dB level), while minimizing the power received from other directions.

For this purpose, the function $T_{\text{ext}}(\Omega)$ in Eq. (3.7) is chosen such that it has low

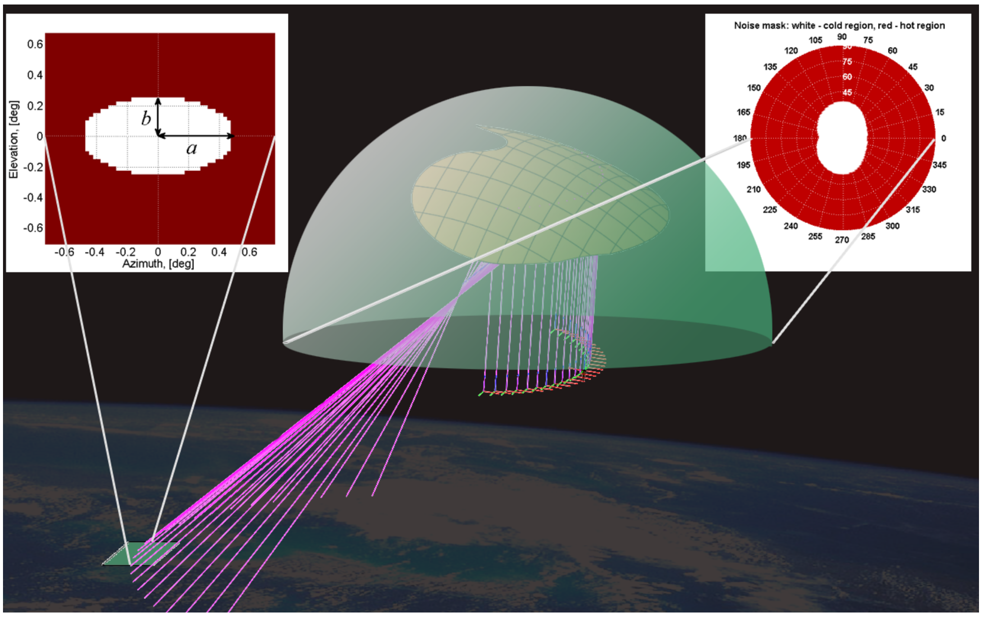

Figure 3.6: The $T_{\text{ext}}(\Omega)$ mask-constraint functions defined for the calculation of the antenna noise correlation matrices $\mathbf{C}_1$ due to the noise sources within the Earth angular region (see the inset in the left upper corner) and $\mathbf{C}_2$ due to the noise sources in the sky region (see the inset in the right upper corner). The toroidal reflector fed with a PAF is shown in the middle of the illustration, where the multiple secondary beams point to the Earth.

temperature values in the region of the expected main lobe (down to -20 dB level) and high values outside of this region. In this way, we maximize the beam efficiency – defined at the -20 dB level – while minimizing the side-lobe and cross-polarization powers outside of this region, as required for the radiometers.

The top-left insertion in Fig. 3.6 shows the function $T_{\text{ext}}(\Omega)$, where the "cold" region around the main lobe has an elliptical shape with major a and minor b semi-axes. Later in the results section we will refer to this ellipse as "mask ellipse", because it is a stepped function.

The temperature of the "hot" region is chosen to be as high as 1000 K to strongly suppress the side lobes in order to satisfy the "distance-to-coast" requirement. This value can also be a beamformer control parameter for optimization radiometer characteristics.

In order to use the beamformer to realize scanned beams (pink rays in Fig. 3.6), the noise temperature distribution function $T_{\text{ext}}(\Omega)$ can be assumed the same for each of them, but the matrix $\mathbf{C}$ needs to be recomputed.

Acceleration of the computations

When constructing the matrix $\mathbf{C}$, one should realize that its filling can be an extremely time-consuming procedure as it requires computation of all secondary EEPs over the entire sphere and evaluation of the pattern overlap integral (3.7) for all combinations of EEPs (see Tabl. 3.2). In order to speed-up the computational process, we have therefore represented the matrix $\mathbf{C}$ as a sum of two contributions, matrices $\mathbf{C}_1$ and $\mathbf{C}_2$ that can be calculated relatively quickly. The first matrix is obtained by using the secondary EEPs computed in a limited angular range around the main lobe region, while the second matrix is used for correcting for the spillover effects and is evaluated through the primary feed patterns. A similar approach has been recently published in [78] and used to calculate the antenna noise temperature of a Gregorian antenna system. The brightness temperature distribution functions $T_{\text{ext}}(\Omega)$ corresponding to $\mathbf{C}_1$ and $\mathbf{C}_2$ are illustrated in the top-left and top-right insets of Fig. 3.6, respectively.

Table 3.2 cross-compares the computation time at Ku-band (18.7 GHz) that is needed for the simulations (using GRASP10, [79]) of the secondary patterns over the entire sphere (when computing the matrix $\mathbf{C}$ through the brute-force approach) and over the reduced region with the post-correction for the spillover effect (when computing the matrices $\mathbf{C}_1$ and $\mathbf{C}_2$ through the proposed approach). There is an obvious advantage in using the latter approach, especially for systems that employ a large number of beams and operating at high frequencies.

Constraints on the dynamic range of the amplitude weights

Realistic (digital) receivers have a limit on the dynamic range of the weight coefficients due to limited resolution of analog-to-digital converters (ADC) and temporal stability

Table 3.2: Computational time of the matrix $\mathbf{C}$ at Ku-band (18.7 GHz)

Brute-force approach		Proposed approach	
Computing 156 secondary EEPs (full sphere)	Computing $\mathbf{C}$	Computing 156 secondary EEPs (small angular range)	Computing $\mathbf{C}_1$ and $\mathbf{C}_2$
$\sim$ 9 months	*no data*	3 hours	5 min/beam

of receiver channels between calibrations.

In order to account for such realistic receivers, the MSMDL beamformer, as described above, has been further extended so as to include constraints on the dynamic range of the weights. This beamforming algorithm is implemented through an iterative procedure that modifies the reference weighting coefficients (as determined by the MSMDL beamformer), while trying to maintain the shape of the PAF pattern as close as possible to the reference one. This will ensure that the radiometer parameters are as close as possible to those obtained with the reference set of weights. The corresponding algorithm is listed as follows:

- At the first iteration ($q = 1$) the sensitivity function $\frac{[\mathbf{w}^{(1)}]^H \mathbf{P} \mathbf{w}^{(1)}}{[\mathbf{w}^{(1)}]^H \mathbf{C}^{(1)} \mathbf{w}^{(1)}}$ is maximized to determine the reference weight vector $\mathbf{w}^{(1)}$. The matrix $\mathbf{C}^{(1)}$ is computed as described above for the standard MaxSNR beamformer (with no constraints on the dynamic range of the weight amplitudes).

- At iteration $q = 2, 3\ldots$ the sensitivity function $\frac{[\mathbf{w}^{(q)}]^H \mathbf{P} \mathbf{w}^{(q)}}{[\mathbf{w}^{(q)}]^H \mathbf{C}^{(q)} \mathbf{w}^{(q)}}$ is maximized to determine the new weight vector $\mathbf{w}^{(q)}$, where $\mathbf{P}$ is the signal covariance matrix (computed only once, for the 1st iteration), $\mathbf{C}^{(q)}$ is the noise covariance matrix, whose diagonal elements are a function of the weight vector $\mathbf{w}^{(q-1)}$ obtained after the previous iteration, i.e.,

$$\mathbf{C}^{(q)}(\mathbf{w}^{(q-1)}) = \begin{bmatrix} C_{11}^{(q-1)} f(|w_1^{(q-1)}|) & C_{12}^{(q-1)} & \cdots & C_{1N}^{(q-1)} \\ C_{21}^{(q-1)} & C_{22}^{(q-1)} f(|w_2^{(q-1)}|) & \cdots & C_{2N}^{(q-1)} \\ \vdots & \vdots & \ddots & \vdots \\ C_{N1}^{(q-1)} & C_{N2}^{(q-1)} & \cdots & C_{NN}^{(q-1)} f(|w_N^{(q-1)}|) \end{bmatrix}, \tag{3.11}$$

  where f is a receiver function that needs to be provided as an input to the algorithm; it should have such a behavior that the lower the weight of the array antenna element, the higher the function value is (which physically corresponds to an increase in the noise temperature of the corresponding receiver channel). In the numerical examples presented hereafter, a filter function is used whose values are close to zero when the weights magnitude $|w_i|$ are higher than w_{constr}, and which has a sharp linear increase near w_{constr}. In this way f is similar to inverse step function near w_{constr} (Fig. 3.7). Here w_{constr} is the value of the amplitude weight constraint, which is typically in the order of −30 dB to −40 dB.

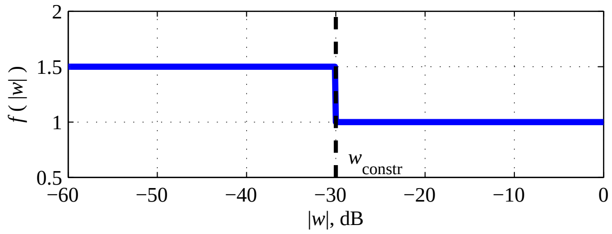

Figure 3.7: The function f used in the numerical examples presented hereafter.

- Check whether the magnitude of all weights are either higher than w_{constr} or negligibly low (i.e. −80 dB in this work). If this condition is satisfied, the iterative procedure is terminated. The channels with negligible weights are switched-off, while the resulting set of weight coefficients is considered to be the final one.

3.3.4 Advanced Maximum Beam Efficiency beamformeR – AMBER

In order to reduce the distance to coast D_{c}, we maximize the power contained in the main beam P_{mb} over the solid angle Ω_{mb} divided by the total radiated power P_{tot}. That is, our objective is to find the weights $\mathbf{w}$ such that $\max_{\mathbf{w}}(P_{\text{mb}}/P_{\text{tot}})$.

The power in the main beam of the total radiated field $\boldsymbol{E}_{\text{tot}}(\theta,\phi)$ is calculated as

$$P_{\text{mb}} = \iint\limits_{\Omega_{\text{mb}}} |\boldsymbol{E}_{\text{tot}}(\theta,\phi)|^2 \, \text{d}\Omega_{\text{mb}} = \iint\limits_{\Omega_{\text{mb}}} \left| \sum_{i=1}^{N} w_i \boldsymbol{E}_i(\theta,\phi) \right|^2 \, \text{d}\Omega_{\text{mb}}, \tag{3.12}$$

where $\boldsymbol{E}_i(\theta,\phi)$ is i-th secondary (after reflection from the dish) embedded element pattern (EEP). The proportionality constant $1/(2\eta)$ in front of the integral is omitted. It can be shown that the integrand is a quadratic form which we write in a matrix form:

$$P_{\text{mb}} = \iint\limits_{\Omega_{\text{mb}}} \mathbf{w}^H \mathbf{X} \mathbf{w} \, \text{d}\Omega_{\text{mb}} = \mathbf{w}^H \left[\iint\limits_{\Omega_{\text{mb}}} \mathbf{X} \, \text{d}\Omega_{\text{mb}} \right] \mathbf{w} = \mathbf{w}^H \mathbf{A} \mathbf{w}, \tag{3.13}$$

where $\mathbf{X}$ is a Hermitian matrix, which is function of the direction, i.e.,

$$\mathbf{X}(\theta,\phi) = \begin{bmatrix} \boldsymbol{E}_1(\theta,\phi)\cdot\boldsymbol{E}_1^*(\theta,\phi) & \dots & \boldsymbol{E}_1(\theta,\phi)\cdot\boldsymbol{E}_N^*(\theta,\phi) \\ \vdots & \ddots & \vdots \\ \boldsymbol{E}_N(\theta,\phi)\cdot\boldsymbol{E}_1^*(\theta,\phi) & \dots & \boldsymbol{E}_N(\theta,\phi)\cdot\boldsymbol{E}_N^*(\theta,\phi) \end{bmatrix}, \tag{3.14}$$

and, therefore, the elements of the matrix $\mathbf{A}$ are calculated as so-called pattern overlap integrals, i.e.,

$$A_{ij} = \iint\limits_{\Omega_{\mathrm{mb}}} \boldsymbol{E}_i \cdot \boldsymbol{E}_j^* \, \mathrm{d}\Omega_{\mathrm{mb}} = \iint\limits_{\Omega_{\mathrm{mb}}} \left(E_{i_{\mathrm{CO}}} E_{j_{\mathrm{CO}}}^* + E_{i_{\mathrm{XP}}} E_{j_{\mathrm{XP}}}^* \right) \mathrm{d}\Omega_{\mathrm{mb}}, \tag{3.15}$$

where each EEP $\boldsymbol{E}_i$ is decomposed in co- and cross-polarized components $E_{i_{\mathrm{CO}}}$ and $E_{i_{\mathrm{XP}}}$, respectively.

We aim at maximizing the beam efficiency, as well as to minimize the power in cross-polarized field component. Therefore, only the power in the co-polarized field component should be maximized. This leads to removal of the $E_{i_{\mathrm{XP}}} E_{j_{\mathrm{XP}}}^*$ term from (3.15) in the optimization process, i.e. the elements of the matrix $\mathbf{A}$ are computed now as

$$A_{ij} = \iint\limits_{\Omega_{\mathrm{mb}}} E_{i_{\mathrm{CO}}} E_{j_{\mathrm{CO}}}^* \, \mathrm{d}\Omega_{\mathrm{mb}}, \tag{3.16}$$

Following the same procedure for calculating P_{mb}, we can calculate the total radiated power P_{tot} as

$$P_{\mathrm{tot}} = \mathbf{w}^H \mathbf{B} \mathbf{w}, \tag{3.17}$$

where the elements of the matrix $\mathbf{B}$ are calculated similar to (3.15), but with integration over full sphere, i.e.,

$$B_{ij} = \iint\limits_{4\pi} \left(E_{i_{\mathrm{CO}}} E_{j_{\mathrm{CO}}}^* + E_{i_{\mathrm{XP}}} E_{j_{\mathrm{XP}}}^* \right) \mathrm{d}\Omega. \tag{3.18}$$

For a given solid angle Ω_{mb} it is thus desired to find the weight coefficients $\mathbf{w}$ that maximizes the following ratio of quadratic forms:

$$\frac{P_{\mathrm{mb}}}{P_{\mathrm{tot}}} = \frac{\mathbf{w}^H \mathbf{A} \mathbf{w}}{\mathbf{w}^H \mathbf{B} \mathbf{w}}, \tag{3.19}$$

It can be shown that the maximum value of this ratio is the maximum eigenvalue λ of the expression

$$\mathbf{A}\mathbf{w} = \lambda \mathbf{B}\mathbf{w}, \tag{3.20}$$

and that the vector holding the optimal complex-valued excitation coefficients is given by the corresponding eigenvector. In MATLAB [80] this can be coded as

```
[W,D] = eig(A,B); % generalized eigenvalue decomposition; matrix W holds
    eigenvectors
Lam = diag(D);    % extract the vector holding the eigenvalues
w = conj(W(:, Lam==max(Lam)));  % take eigenvector corresponding to the maximum
    eigenvalue
```

Note that the AMBER beamformer is parametric, i.e. the solid angle Ω_{mb} must be defined before computing the weight coefficients. Similar to the MSMDL beamformer, Ω_{mb} is defined by the *major semi-axis* and *axis ratio* of an ellipse centered around the expected main lobe. We will use them as the beamformer parameters when calculating the radiometer characteristics presented in the following sections.

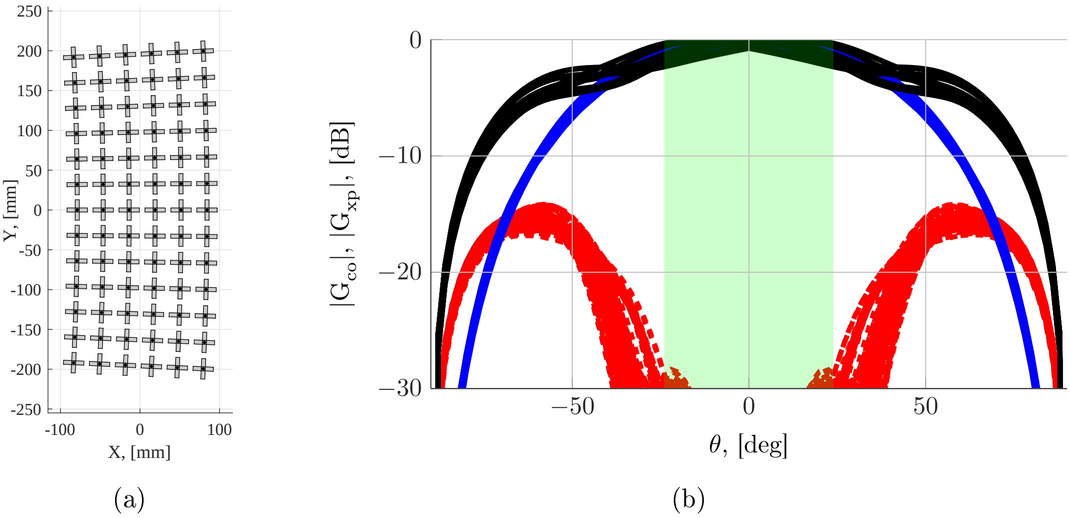

Figure 3.8: (a) The layout of the optimal (for a one beam) 6×13 array feed of the torus reflector antenna when the radiating element is a crossed half-wavelength dipole antenna, and (b) cuts of the array embedded element patterns. The cuts are shown of the co-polar patterns for E- and H-planes, as well as cross-polar pattern for diagonal plane ($\phi = 45°$), and the green area denotes the reflector subtended angle.

3.3.5 Comparison of the beamformers

In order to compare the beamformers, we analyze the push-broom radiometer equipped with the optimal PAF of crossed dipole elements (for a single beam). Details on the PAF optimization procedure will be discussed in the following sections, and for now the array is assumed to be given. The layout of such array and embedded element patterns of its elements are shown in Fig. 3.8.

The array was analyzed using the HFSS software [81] and the obtained primary EEPs were imported into GRASP software [79] to calculate the secondary EEPs (after reflection from the reflector), which in turn were used to perform the beamforming. After determining the excitation coefficients, the compound beam was computed and the radiometer characteristics as discussed in Sec. 3.1 were calculated.

As described in Sec. 3.3.2, the CFM beamformer has one parameter – the taper of the incident plane wave (PW). Fig. 3.9 shows the calculated focal field distribution, the corresponding weight coefficients and the radiation patterns of the primary and secondary compound beams when the incident PW taper is equal to -50 dB, -30 dB and -10 dB. As one can see from the figure, the focal field becomes less blurry and its side lobes increase as the PW taper decreases (the PW becomes more uniform). This results in better reflector illumination efficiency (and consequently increased directivity), narrower beamwidth ($\equiv$ footprint size), but at the same time the side lobe level of the secondary beam increases, which degrades distance-to-coast characteristic. This can be seen more clearly in Fig. 3.10 (top row), where the main radiometer

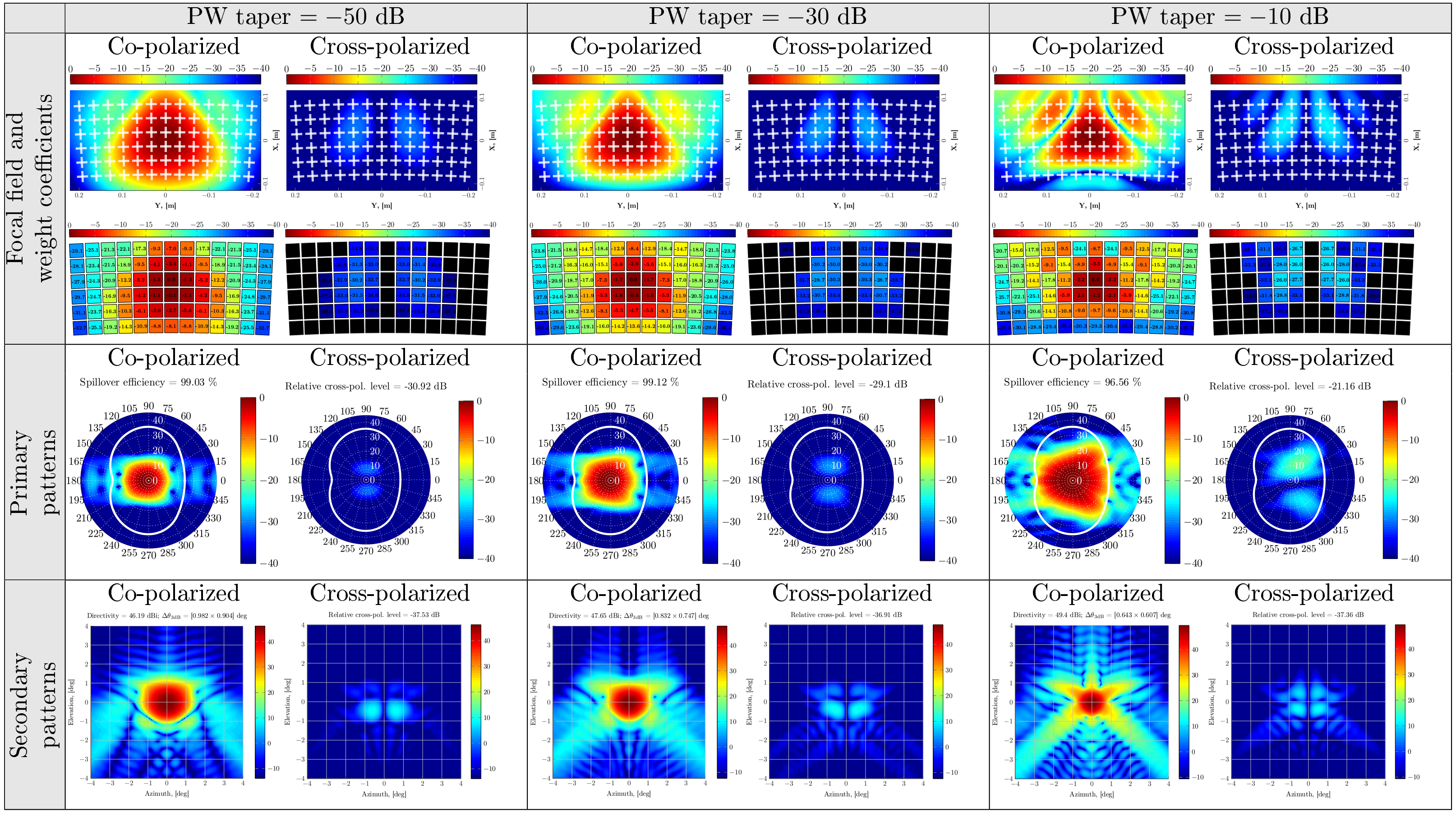

Figure 3.9: CFM beamformer results for 3 plane wave tapers: (from top to bottom) co- and cross-polarized components of the focal field (white crosses denote dipole elements); excitation coefficients of corresponding array elements; primary compound beam illuminating the reflector (white line denotes the reflector rim); secondary compound beam.

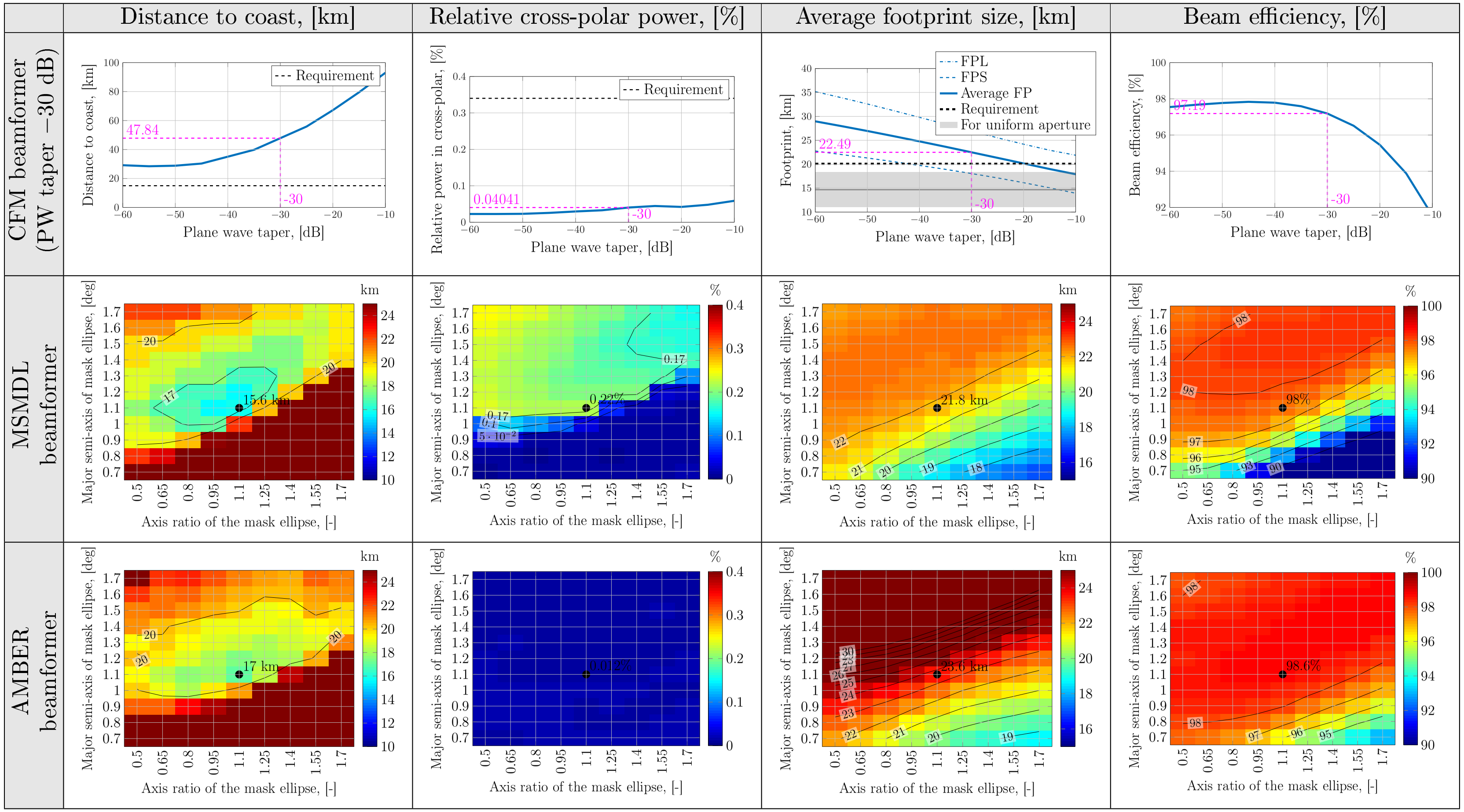

Figure 3.10: Comparison of three beamformers in terms of the main radiometer characteristics, i.e. distance to coast, relative power in cross-polarized field component; average footprint size, and beam efficiency.

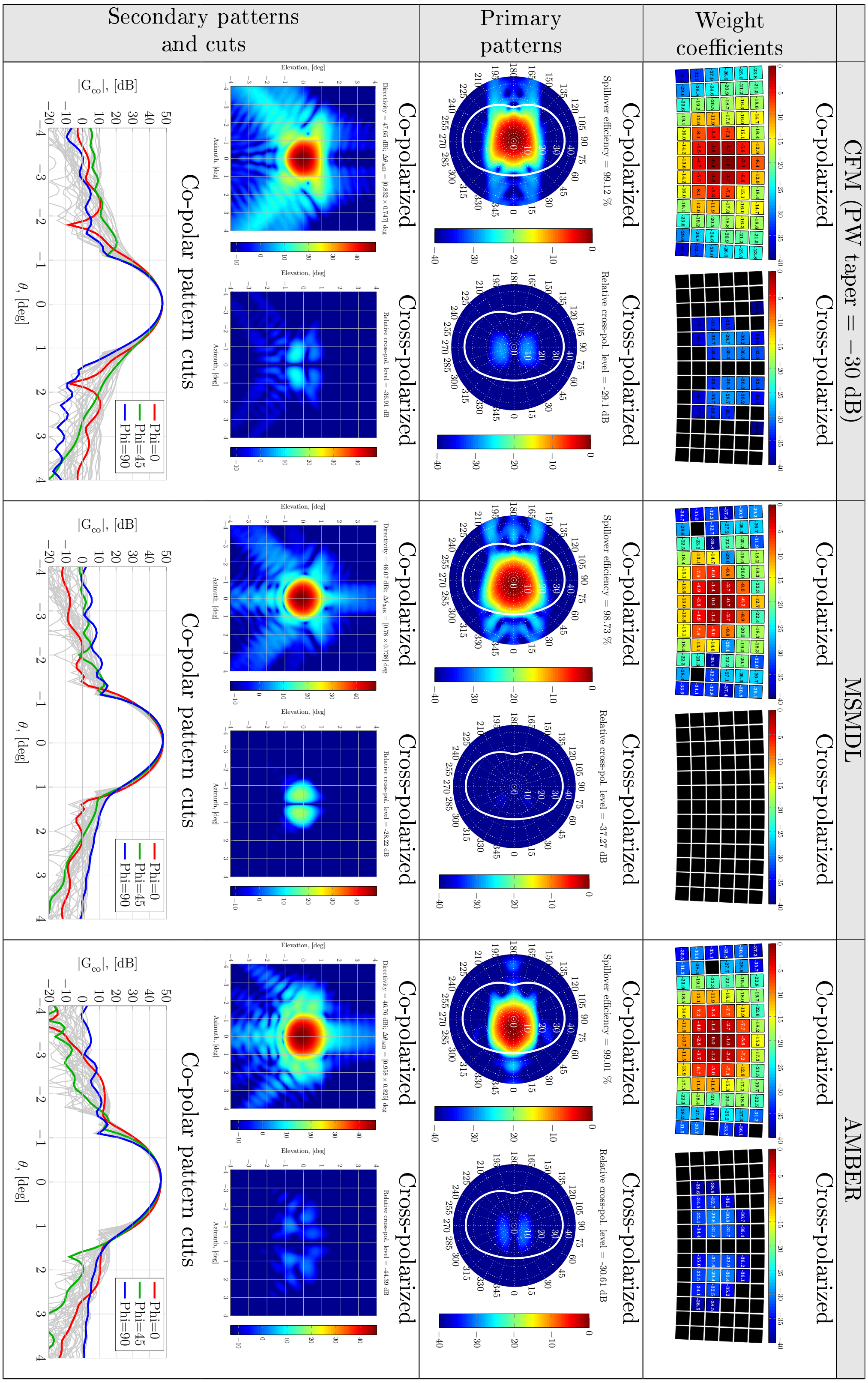

Figure 3.11: Comparison of three beamformers: (top) weight coefficients; (middle) primary radiation patterns; (bottom) secondary radiation patterns.

characteristics are shown as a function of the PW taper.

Fig. 3.10 show the main radiometer characteristics as a function of considered CFM, MSMDL and AMBER beamformer parameters, which are the PW taper for CFM beamformer and the mask ellipse parameters (major semi-axis and axis ratio) for the MSMDL and AMBER beamformers. The chosen beamformer parameters are denoted by markers in the figure, and the corresponding weight coefficients, primary and secondary radiation patterns are shown in Fig. 3.11.

Having analyzed the figures one can conclude that there is a trade-off between the distance-to-coast and the footprint characteristics, which is valid for all the beamformers. This is easy to explain from a physics point-of-view: the smaller footprint we want, the larger part of reflector should be illuminated, which results in higher side lobes and, correspondingly, a larger distance-to-coast value. From Fig. 3.10 we can see that the CFM beamformer does not allow us to satisfy both requirements at the same time, while for the MSMDL and the AMBER beamformers we can choose a point in the parametric space such that both radiometer characteristics get very close to the requirements.

Table 3.3 summarizes the radiometer performance for all three beamformers with their optimal parameters. It is pointed out that these calculations have been performed at C-band (6.9 GHz).

Table 3.3: Radiometric characteristics of the push-broom system for three types of beamformers at C-band, when the PAF consists of dipole elements, the EEPs of which are calculated using the FEM method in HFSS.

Radiometer characteristic	**Requirement**	**CFM (PW taper −30dB)**	**MSMDL**	**AMBER**
Distance to coast, [km]	<15	47.8	15.6	17.0
Rel. cross-pol. power, [%]	<0.34	0.04	0.22	0.01
Beam efficiency, [%]		97.2	98.0	98.6
Footprint, [km]	<20	22.5	21.8	23.6

For the X- and Ku-bands (10.65 GHz and 18.7 GHz) all requirements for the radiometer characteristics are fully satisfied (see Paper K) using MSMDL beamformer.

Concluding the beamformer comparison we can say that the MSMDL is more beneficial when a measurement is performed close to a coast line as it allows smaller distance-to-coast and footprint values, while measuring far from the coast line, the CFM and AMBER may be a better choice thanks to their high polarization purities.

3.4 Optimum PAF architectures

In this section we will show how the initial array layout has been chosen and optimized to minimize the required number of elements.

3.4.1 Initial PAF layout

In order to choose the initial layout of the array, we let a tapered plane wave be incident from the direction of observation on the reflector antenna, after which the vector EM field in the plane of the array is computed. The magnitude of the E-field is shown as a background color in Fig. 3.12. The initial size of the array has been chosen such that it covers an area where the field intensity exceeds $(-15\ldots-20)$ dB, while the initial inter-element spacing has been chosen to be 0.5λ. This element spacing is expected to lead to a high beam efficiency, while minimizing the spillover loss [82]. The taper of the incident plane wave has been chosen -30 dB at the reflector rim. This value is shown to be optimal from the radiometer characteristics point-of-view [Paper D], when Conjugate Field Matching (CFM) beamforming is used. Since we will use more advanced beamformers, the focal field distribution will differ from the one shown in Fig. 3.12, so that the optimal array size can be different as well. Therefore we may need different number of antenna array elements to sample this field sufficiently well in order to satisfy the radiometer requirements. Under "optimal array" we understand an array employing a minimum number of antenna elements, while all performance requirements of the radiometer equipped with a such array remain satisfied.

3.4.2 Array size and inter-element spacing

To optimize the initial array layout in conjunction with the MSMDL beamformer described in Sec. 3.3.3, the main characteristics of the radiometer are studied as a function of the inter-element spacing between the array elements and the array size in the radial direction. The array size in the azimuthal direction is not a parameter

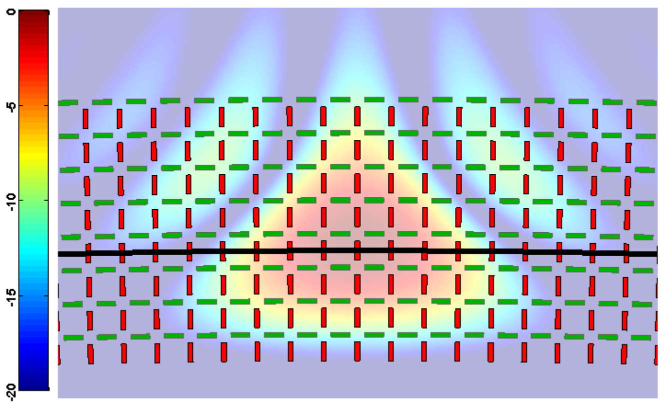

Figure 3.12: Initial layout of the PAF for the push-broom reflector: red and green lines denote the ρ- and ϕ-polarized array elements correspondingly, while the black arc shows the position of the focal arc of the reflector. The E-field distribution in the array plane (when a tapered plane wave is incident on the reflector from the direction of observation) is shown as the background color, [dB].

of interest in the optimization, since the array will need to form multiple beams in this direction and sub-arrays for the neighbouring beams will partially overlap. This work is presented in Paper E, while the performance of the radiometer at the X-band is summarized in Table 3.4. In this case the radiometer is subsequently equipped with: (i) a horn feed (its radiation pattern is modeled as a Gaussian beam), (ii) the initial array with the CFM beamformer, and (iii) the optimized array feed employing the MSMDL beamformer (unconstrained dynamic range of the beamformer weight amplitudes).

	Gaussian feed model	**PAF with CFM BF (uniform PW)** $15 \times 29 \times 2$ **elem.** $d_{\mathrm{el}} = 0.5\lambda$	**PAF with MSMDL BF** $6 \times 13 \times 2$ **elem.** $d_{\mathrm{el}} = 0.75\lambda$
PAF element excitation coefficients		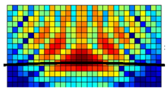	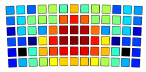
Reflector illumination patterns	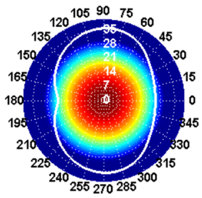	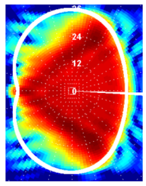	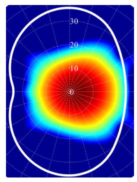
Beam efficiency [%]	84.2	85.1	98.4
XP-power, [%] (<0.34% is req.)	0.39	1.01	0.12
Dist. to land, [km] (<15 km is req.)	87.8	116.6	13.4
Beam width, [deg]	0.600	0.351	0.538
Footprint (FP), [km] (<20 km is req.)	16.9	10.5	15.9
FP ellipticity	1.38	2.14	1.21

Table 3.4: Radiometer characteristics for different PAFs and beamformers at X-band (10.65 GHz).

As expected, dense PAFs have obvious benefits in achieving the required minimum distance-to-coast and footprint roundness, while meeting all the other radiometer requirements at the same time. The minimum size of the PAF sub-array has been found to be 6×13 elements (for each polarization) with the inter-element separation distance in the order of $d_{\mathrm{el}} = 0.75\lambda$.

It generally known that for maximizing the illumination efficiency of the reflector the focal field should be sampled by an array with the element spacing $\leq 0.5\lambda$ [82]. For the considered applications, however, a reduced efficiency is acceptable as long as the primary requirements (such as distance-to-coast, cross-polar power, footprint size) are satisfied and the total number of the array elements are minimized. From the other hand, $d_{\mathrm{el}} > 0.75\lambda$ leads to the grating lobes, and hence significant drop in the antenna beam efficiency. Furthermore, the grating lobes may be directed towards a strong noise source in the sky (e.g. sun, moon) and hence increase the measurement error.

3.4.3 Dynamic range of beamformer weights

The effect of the limited dynamic range (DR) on the radiometric performance has also been investigated. It has been found that the minimum DR required to satisfy the radiometric requirements is 30 dB. If we reduce it further, first the cross-polarization power will be affected since beamforming cannot compensate it anymore. Furthermore, with the weights DR less than 20 dB the distance-to-coast characteristic will be degraded as well.

To ensure a minor effect of the DR limitation on the radiometer performance we will use a DR value equal to 40 dB, which is still realistic for receiver systems.

3.5 Radiating element trade-off study

The purpose of this section is to perform a trade-off analysis of several PAF radiator candidates and select the best one in terms of the radiometer performance and feeding/fabrication simplicity of the array. The input for this study is the requirements for the radiator as defined in Sec. 3.5.1.

Three different antenna technologies have been considered for the analysis (see Fig. 3.13): (i) a crossed-dipole antenna, (ii) a patch-excited cup antenna developed by RUAG [83], and (iii) a tapered-slot antenna (Vivaldi antenna) [Paper L].

(a) (b) (c)

Figure 3.13: Considered radiating elements for the PAF: (a) a crossed-dipole antenna (HFSS model); (b) RUAG's patch-excited cup antenna [83]; (c) Vivaldi antenna [Paper L].

3.5.1 Requirements for the array radiator

Overview of the radiating element requirements

While selecting the radiating element for the PAF, both the electrical performances and mechanical issues of the elements should be considered. These requirements are summarized in Table 3.5.

Back radiation power

The back radiation power is defined here as the power of the total radiated field of the reflector antenna system contained in the angular range subtended by the Earth, i.e., in the range of θ between $0°$ and $62°$ from the nadir, see Fig. 3.2.

Due to the high tapering of the feed pattern, the diffraction effects at the reflector edge are negligibly small, and the power of the diffracted field propagating towards the Earth is assumed to be zero. Therefore, the main contribution to the radiometer back radiation is the back radiation of the array feed. The power of the back-radiated field can be decomposed into powers containing co- and cross-polarized components of the field. Let us consider them separately.

Co-pol power in the back radiation

As it was shown in Paper K, the distance-to-coast characteristic is defined by the cone angle, inside which the radiometer beam contains at least 99.72% power of the co-polarized field component. This follows from the Eq. (4) in Paper K, which is

$$\Delta \mathrm{T} \geq (T_{\text{land}} - T_{\text{h}}) \frac{P_{\text{land}}}{P_{\text{co}}}, \tag{3.21}$$

where $\Delta \mathrm{T} = 0.25$ K is the accuracy requirement; $T_{\text{h}} = 75$ K is the brightness temperature of the sea surface (horizontal polarization); $T_{\text{land}} = 250$ K is the brightness temperature of the land surface; and P_{land} is power radiated towards the hot land, i.e.,

$$P_{\text{land}} = \frac{P_{\text{co}} - P_{\text{c}}}{2}, \tag{3.22}$$

where P_{co} is the co-polarization received power within the angular region subtended by the Earth; and P_{c} is the power contained in the beam cone with semi-angle θ_{c} (= angle between the beam center and the closest point at a coast line, see also Fig. 3.1).

If we make the same assumption as in Paper K that only half of transmitted power in reciprocal transmitting situation is outside of the beam cone (including the back radiation) and thus incident on the hot land, then we can write P_{land} as

$$P_{\text{land}} = \frac{P_{\text{co}_{\text{b}}} + P_{\text{co}_{\text{v}}} - P_{\text{c}}}{2}, \tag{3.23}$$

Table 3.5: Radiating element requirements

Electrical performance	
Frequency band	• C-band: 6.8...7.0 GHz • Dual-band operation is an advantage (+ L-band)
Matching condition	• The amplitude of the active reflection coefficient should not exceed -10dB (the reference impedance of 50 Ohm) when the element is in the final array environment and optimum beamforming coefficients are applied. For radiating elements with negligible mutual coupling effects (when they are in an array) the active reflection coefficient can be replaced by the standard passive reflection coefficient.
Beam width	• Should be wider than the reflector subtended angle ($\pm 24°$)
Cross-polarization level	• Sufficiently low in the angular range subtended by the reflector ($\pm 24°$) *
Back-radiated power	• Sufficiently low in the angular range subtended by Earth ($180 \pm 62°$) *
Mechanical considerations	
Feeding network	• Simplicity of the feeding network (feeding lines and interconnections) • Single-ended output ports of the antenna elements are preferred (no baluns) • Sufficient distance between ports of the elements in an array to connect coaxial cables
Use of dielectric	• Minimum amount of dielectric material, metal-only antenna structure is preferred in order to reduce losses and noise received while avoiding possible problems with the accommodation to space
Size of the element	• Element size must be smaller than 0.75λ in the horizontal plane (plane of the array)

* Requirements on both the cross-polarization power and back-radiated power are important for the entire array (not for a single element as in conventional non-dense arrays), since they directly affect the radiometric characteristics. It is impossible to define these requirements for a radiating element in isolation, since the resulting values will depend not only on the element type, but also on the array topology, excitation scheme and supporting structure around the array. Therefore, at this stage, we can define these requirements for the entire array with a particular array topology, excitation scheme, and no supporting structure. The calculation methodology and two case studies are in this section.

where we split the total co-polar power over the Earth P_{co} into the power in the back radiation, $P_{\mathrm{co_b}}$, and the power in the main beam vicinity, $P_{\mathrm{co_v}}$, which should have a size sufficient to capture most of the power around the main beam; we used $\theta_{\max}$ such that about 10 side-lobes are accounted for. Substituting (3.23) in (3.21) leads to

$$\frac{P_{\text{co}_\text{v}}}{P_{\text{co}}} - \frac{P_{\text{c}}}{P_{\text{co}}} \leq \frac{2\Delta T}{T_{\text{land}} - T_{\text{h}}} - \frac{P_{\text{co}_\text{b}}}{P_{\text{co}}}, \tag{3.24}$$

that is, the power outside the cone in vicinity of the main lobe, $\frac{P_{\text{out}_\text{v}}}{P_{\text{co}}} = \frac{P_{\text{co}_\text{v}}}{P_{\text{co}}} - \frac{P_{\text{c}}}{P_{\text{co}}}$, should be less than $\frac{2\Delta T}{T_{\text{land}} - T_{\text{h}}} - \frac{P_{\text{co}_\text{b}}}{P_{\text{co}}} = 0.0028 - \frac{P_{\text{co}_\text{b}}}{P_{\text{co}}}$. We can rewrite this power in percent, relative to the total power in the co-polarized component, i.e.,

$$P^{\text{rel}}_{\text{out}_\text{v}} = 0.28\% - P^{\text{rel}}_{\text{co}_\text{b}}. \tag{3.25}$$

Knowing $P^{\text{rel}}_{\text{out}_\text{v}}$, the corresponding cone angle θ_c can be found from the radiation pattern, after which the distance-to-coast is calculated using Eq. (3.1).

Fig. 3.14 shows the dependence of the distance-to-coast characteristic D_c of the relative back radiated power $P^{\text{rel}}_{\text{co}_\text{b}}$. The figure shows that if we allow for the maximum distance to coast of 20 km, the maximum acceptable co-polar back radiation power is about 0.11%. The curves on the figure were obtained using MSMDL beamformer.

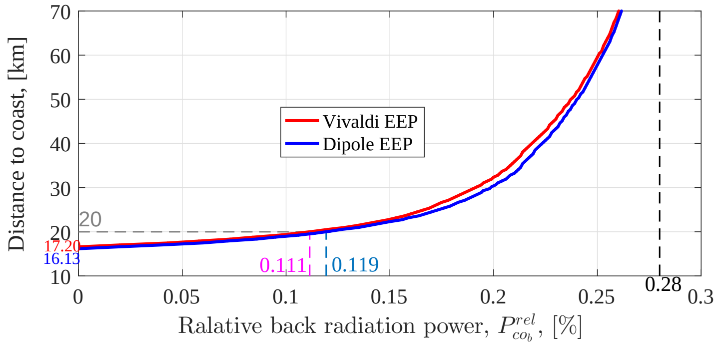

Figure 3.14: Distance-to-coast as a function of back-radiated power of the PAF feed, consisting of either Vivaldi or dipole radiating elements, excited with the weight coefficients obtained using the MSMDL beamformer.

Note that the maximum of the acceptable back-radiated power is 0.28%, otherwise the accuracy requirement of 0.25 K cannot be satisfied, even if measurements are performed far from the coast line.

Cross-pol power in the back radiation

The radiometer requirement on the temperature measurement accuracy of 0.25 K implies that the power in the cross-polar component over the entire angle subtended by the Earth must be less than 0.34% of total power within this angle. For instance, if the cross-polar power generated by the reflector antenna that is fed by a PAF of dipole or Vivaldi antennas is 0.1%, the maximum allowed cross-polar power in the array back radiation is about $0.34 - 0.1 = 0.24\%$. It is pointed out that this value depends on the beamforming algorithm used.

Therefore, *the back radiation of the radiating element* should be such that the total back radiation of the array after beamforming (both co- and cross-polar powers) satisfy the requirements described in this section.

Cross-polarization requirements

Previous studies by Chalmers and TICRA [84] show that the cross-polar power is a minor issue for the push-broom configuration. This is due to:

- The relatively low XP generated by the torus reflector itself (e.g. XP power is 0.23% when the reflector is fed by a Gaussian feed with taper -30 dB and zero cross-polar level, versus 0.87% for the conical scanner with a similar feed);
- The relatively low feed XP power inside the feed-to-reflector subtended angle.

In Sec. 3.5.3 it will be shown that the cross-polar power of the reflector fed by PAF of Vivaldi antenna elements is even better than when a PAF of dipole elements is used, despite the fact that the cross-polar level of the Vivaldi EEP is higher. This is due to the beamformer, which compensates the cross-polar component by means of exciting the orthogonal elements as well (see weight coefficients in Figs. 3.19 and A.6). Owing to this property of the beamformer, the cross-polar level of the radiating element is not an issue for the most commonly used radiators. A more detailed analysis is presented in Sec. 3.5.3.

3.5.2 Array layouts and analysis method

The torus reflector discussed in Sec. 3.2 is fed by an array feed consisting of 6×13 radiators arranged in radial type grids, as illustrated in Fig. 3.15. As shown in Sec. 3.4.2 and Paper I, 6 rows of elements are the minimum number necessary to generate one beam of the push-broom radiometer, satisfying the radiometric requirements of the instrument.

For PAF excitation scenarios, the antenna elements located at the edges of the array have significantly (-12 dB and less) lower weighting coefficients relative to the elements in the center. This implies that differences in embedded element pattern shapes, introduced by edge effects, will likely have relatively weak contribution to the total compound beam of the array when all elements are active. Hence, to speed up the simulations, one could assume that EEPs of the elements near the edges are similar to an element in the center of the array, see the "Modeling approach II" below. This approach was used in the previous radiometer project, however it was not validated (except for some initial results in Paper L for the conical radiometer). Hence,

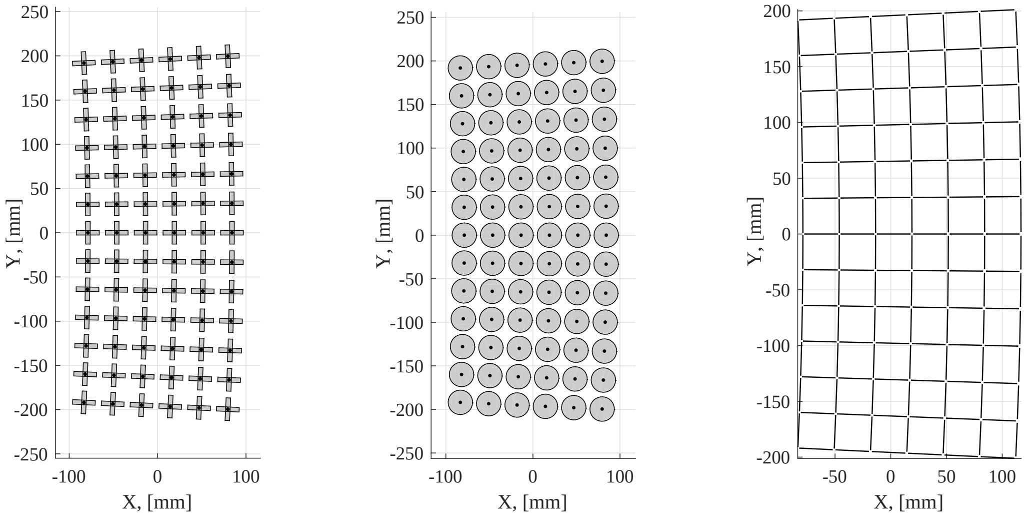

(a) (b) (c)

Figure 3.15: The layouts of the 6×13 array feed of the torus reflector when the radiating antenna element is: (a) a crossed half-wavelength dipole antenna; (b) a dual-polarized patch-excited cup antenna, and; (c) a Vivaldi antenna (the Y-polarized elements in the 7th column are passive).

here we perform validation tests for the push-broom radiometer, and in particular consider three modeling approaches for the computation of the EEPs of the array elements (see also Fig. 3.16):

1. **Modeling approach I:** All EEPs are identical, obtained from an infinite array simulation and shifted to the positions of array elements in the layout;

2. **Modeling approach II:** The same as Modeling approach I, but where the EEPs are obtained from the central element of a finite 5×5 rectangular array, which allows for better estimation of the EEPs (especially its cross-polarization component);

3. **Modeling approach III (Reference):** All individual EEPs are obtained from a full-wave simulation of the full 6×13 array of dual-polarized elements.

The first approach is the fastest one, however, as can be seen from the EEPs (see e.g. Fig. 3.17), its accuracy is limited. On the other hand, and as expected, the full-wave full-array approach is very time-consuming.

In next section we show the results for all radiators using the above described approaches.

Identical EEPs from an infinite array (Approach I)	Identical EEPs equal to the central EEP of a 5x5 finite rectangular array (Approach II)	Individual EEPs from a full-wave array (Approach III)
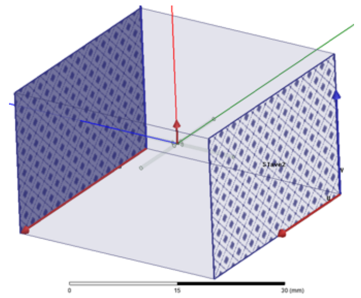	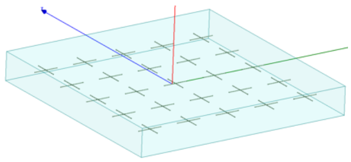	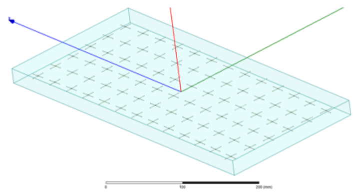

Figure 3.16: HFSS models to calculate EEPs for the 6x13 array: (a) Infinite array simulations (Approach I); (b) a small-scale finite array simulation and phase-shifted versions of the central element EEP (Approach II), and; (c) a complete large-scale array simulation (Approach III).

3.5.3 Comparison of the dipole, patch and Vivaldi elements

In this section we present the numerical results for the dipole-element arrays. The results for patch- and Vivaldi antenna arrays are given in the Appendix A. The set of results is composed of the following figures:

1. (Fig. 3.17) EEPs of the array including: (i) the co- and cross-polarization component contour plots of the central element, and; (ii) the E- and H-plane cuts of co-polarized E-field component, as well as D-plane cuts of cross-polarized E-field component. In case of the small-scale array (Modeling approach II) the cuts are shown for the central element only, while in case of the full-scale array model (Modeling approach III) the cuts are shown for every array element.

2. (Fig. 3.18) Contour plots of the main radiometer characteristics (distance to coast, relative cross-polar power, beam efficiency and average footprint) as a function of two beamformer parameters, i.e., the major semi-axis and axis ratio of the reflector antenna beamwidth at the -20 dB level. The optimum set of the beamformer parameters are chosen such that all the above mentioned characteristics are within the required specifications, and is indicated by black marker, along with its corresponding value.

3. (Fig. 3.19) The amplitude of the optimal weighting coefficients corresponding to the above chosen beamformer parameters. They are shown for both the co- and cross-polarized antenna elements.

Additionally, in Fig. 3.20, the resultant radiation patterns of the PAF are shown for the dipole array, when the antenna array elements are excited using optimal beamforming weights, as well as the corresponding radiation pattern of the whole antenna system that is used to evaluate the radiometer characteristics. Radiation patterns for the patch and Vivaldi arrays are visually very similar and therefore not shown.

Table 3.6 summarizes achieved radiometer performance for the three arrays with the EEPs computed by three methods described above. The results for the full-wave Vivaldi array are not available due to limited computational resources.

Table 3.6: Radiometric characteristics of the push-broom system for three types of PAF with EEPs each calculated using three methods.

Radiometer characteristic	**Requirement**	**Approach I: Inf.array**	**Approach II: Small array**	**Approach III: Full-wave**
Dipole array				
Distance-to-coast, [km]	<15	15.3	15.5	16.5
Rel. cross-pol. power, [%]	<0.34	0.20	0.18	0.19
Beam efficiency, [%]		98.5	98.3	98.1
Footprint, [km]	<20	22.6	22.2	22.2
Footprint ellipticity		1.54	1.57	1.54
Patch-excited cup array				
Distance-to-coast, [km]	<15	15.3	15.2	16.1
Rel. cross-pol. power, [%]	<0.34	0.20	0.16	0.15
Beam efficiency, [%]		98.3	98.3	98.1
Footprint, [km]	<20	22.5	22.7	23.1
Footprint ellipticity		1.54	1.53	1.42
Vivaldi array				
Distance-to-coast, [km]	<15	16.6	16.6	N/A
Rel. cross-pol. power, [%]	<0.34	0.17	0.10	N/A
Beam efficiency, [%]		98.0	98.3	N/A
Footprint, [km]	<20	22.0	22.2	N/A
Footprint ellipticity		1.51	1.59	N/A

As one can see, the power of the cross-polarized component is not an issue regardless of the radiating element type and analysis approach. The distance-to-coast and footprint size exceed a little the requirement, but is still much better than if a horn feed is used (see Papers K and E for the push-broom radiometer results with a horn feed). From Fig. 3.18 it follows that we could reduce the footprint size, but this would result in a unacceptably large distance-to-coast characteristic and reduced beam efficiency. This trade-off effect is expected because in order to achieve a smaller footprint we need to over-illuminate the reflector (reduce the illumination taper at the reflector edge), which leads also to increased side-lobe and spillover levels, which in turn affect the distance-to-coast and the beam efficiency, respectively.

Another interesting observation can be made about the cross-polarization power for each radiating element. Despite the cross-polarization level within the reflector subtended angle is the lowest for the PAF of dipole elements and the largest for the Vivaldi PAF (see 2$^{\text{nd}}$ column in Figs. 3.17, A.1 and A.4), the power contained in the cross-polarized field component after beamforming behaves in opposite way, i.e.,

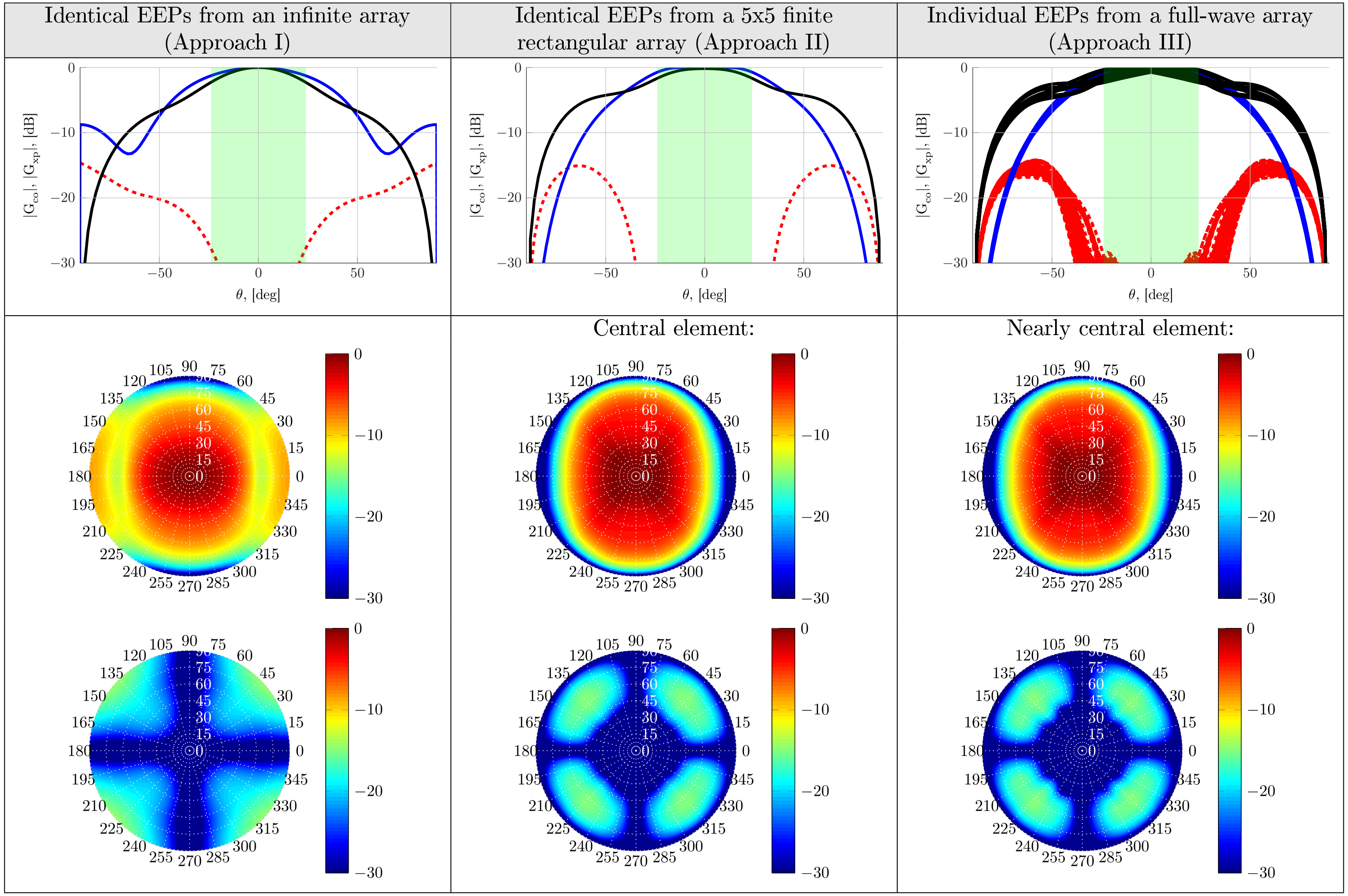

Figure 3.17: Embedded element patterns of the **dipole array**. Cuts of the co-polar patterns for E- and H-planes, as well as cross-polar pattern for diagonal plane ($\phi = 45°$) are shown on top, and the green area denotes the reflector subtended angle.

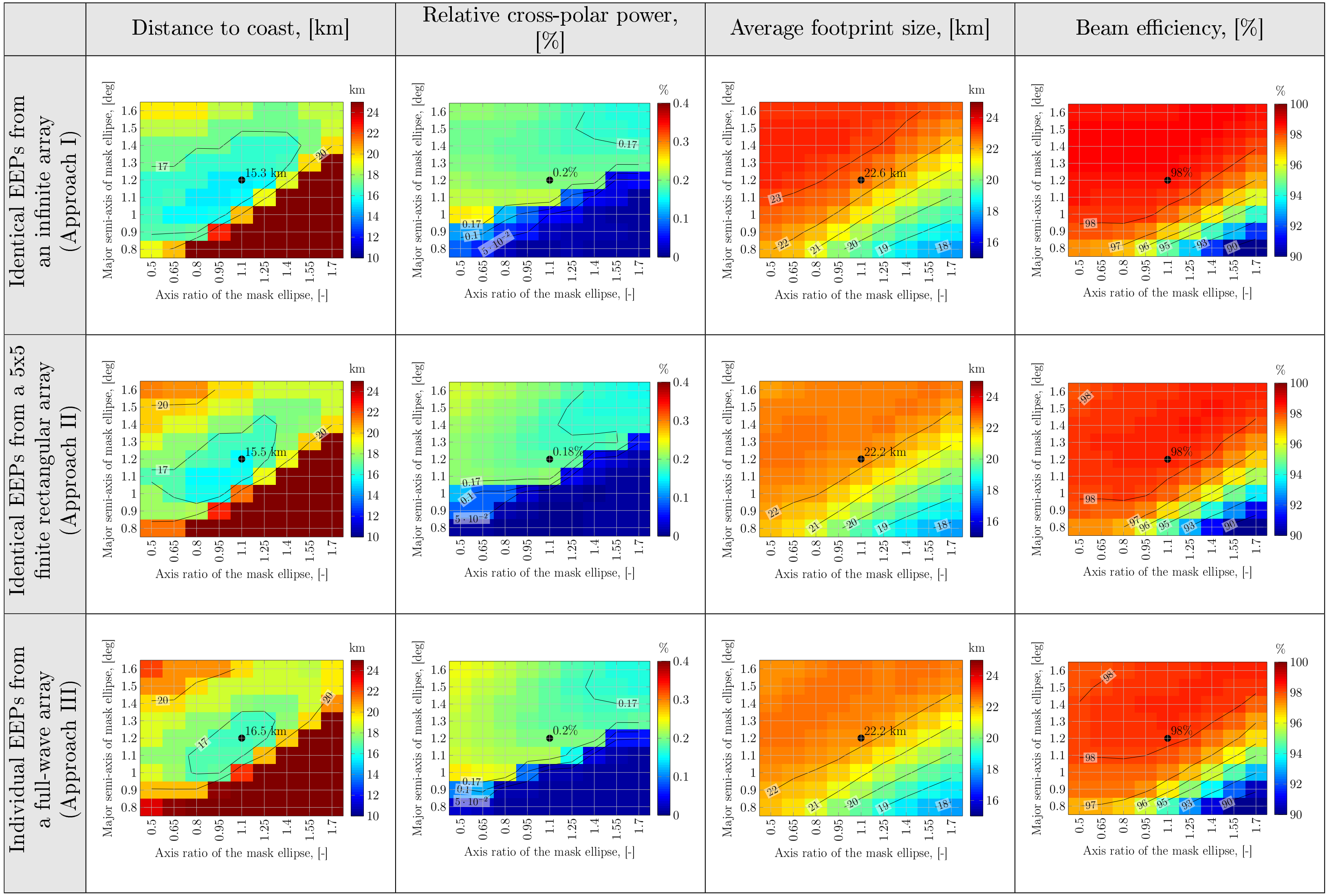

Figure 3.18: Radiometer characteristics as function of two beamformer parameters, i.e. major semi-axis and axis ratio of the antenna main lobe. The black marker shows the chosen optimum parameters and corresponding characteristic's value.

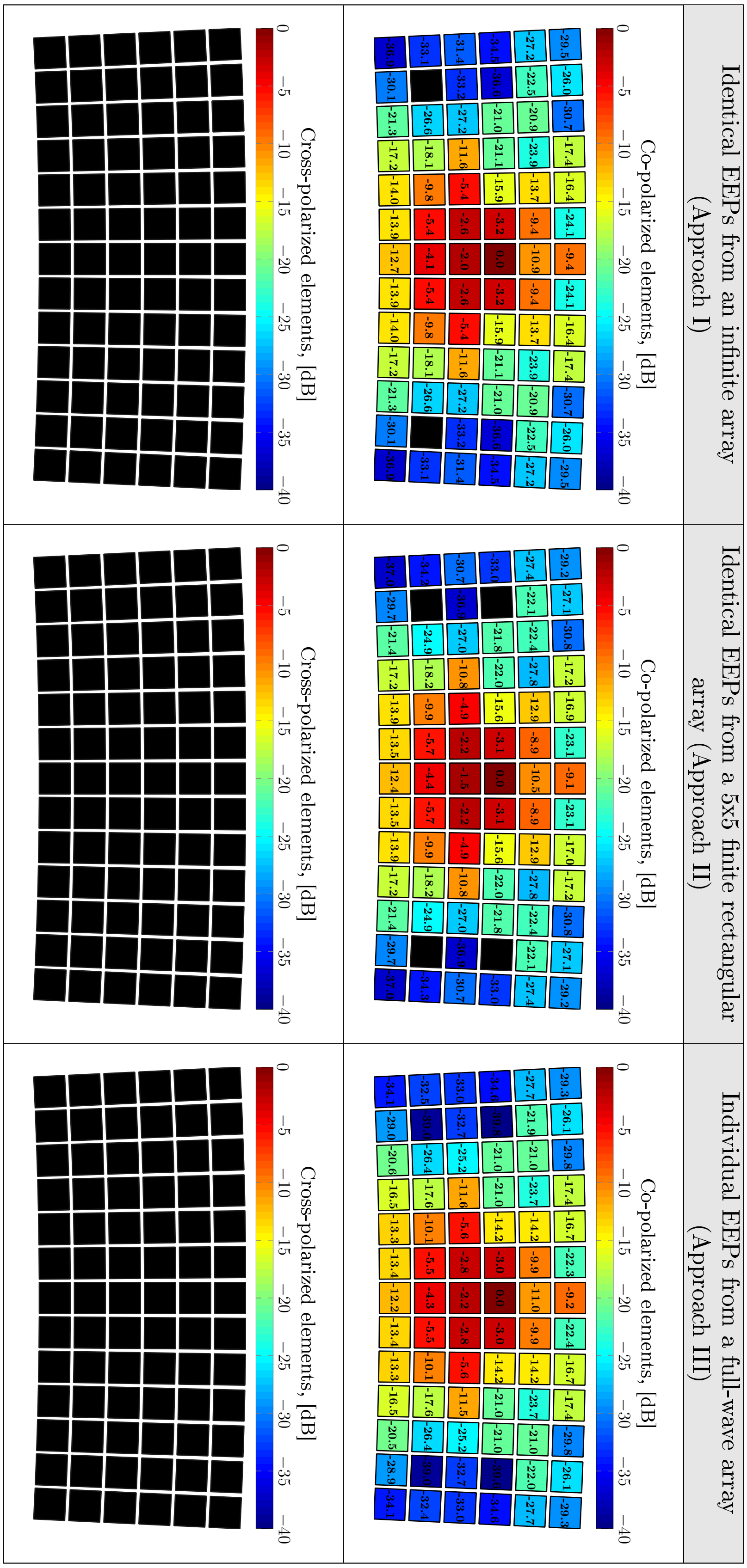

Figure 3.19: Amplitude of the weighting coefficients, [dB], of the 6 × 13 elements for the chosen beamformer parameters (black color indicates passive elements): (top) co-polarized and (bottom) cross-polarized elements

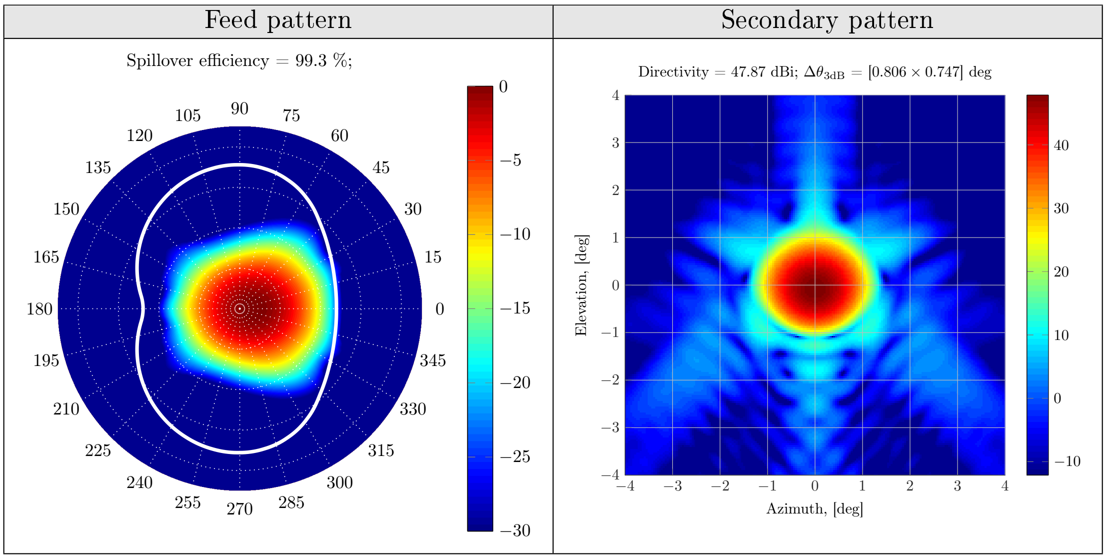

Figure 3.20: (left) PAF radiation pattern, illuminating the reflector aperture, where the white line denotes the reflector rim, and; (right) radiation pattern of the reflector antenna illuminated by the PAF (central beam). The patterns are for the full-wave dipole array. Radiation patterns for other arrays and calculation approaches are visually very similar.

it is the smallest for the Vivaldi PAF (see the "Approach II" column in Table 3.6). This can be explained by the capability of the beamformer to use orthogonal array elements to compensate for the cross-polarized component of the secondary field. This can be seen from Figs. 3.19, A.3 and A.6, where the cross-polarized elements are most strongly excited for the Vivaldi array.

In summary, we can say that the numerical results demonstrate that all considered radiating elements perform well in the array environment and meet the radiometer specifications when excited according to the optimum beamforming strategy (MSMDL, [Paper I]). They weakly depend on the modeling approach for the array antenna element, in the sense that the final beams of the PAF-fed reflector antenna are almost identical, though the primary embedded element patterns and their excitations derived by the three approaches differ. The three approaches require very different computation times, as well as the time for setting up the array geometry in software.

Since all elements were found to meet the radiometer requirements, the final choice of the final array element should be mainly based on the mass and cost figures, as well as possible multi-band considerations for future potential ocean missions.

3.6 Conclusions

Existing space-borne microwave radiometers that are used for the assessment of ocean parameters like salinity, temperature, and wind can provide valid observations only up to $\sim$ 100 km from the coastline, and hence do not allow for monitoring of the coastal areas and ice-edge polar seas, or for measuring under extreme wind and weather conditions. To achieve the desired precision, as required for future missions, we propose digitally-beamforming phased array feeds (PAFs) – previously not used in space-borne applications – employed either in a traditional conical-scan offset parabolic reflector antenna or in a wide-scan torus reflector system.

When synthesized and excited according to the proposed optimum beamforming procedure – aiming at minimizing the signal contamination given by the side-lobe and cross-polarization levels of antenna beams over the land – the number of PAF antenna elements and associated receivers can be kept to a minimum. In this procedure, the input parameters include the number of array elements, their positions and the secondary embedded element patterns (EEPs), which are computed after illuminating the reflector antenna. The output parameters are the optimal complex-valued element excitations. Although the primary EEPs are generally not identical due to the array antenna mutual coupling and edge truncation effects, for the considered PAFs with more than 100 dipole antenna elements and inter-element spacing of 0.75λ, it has been found sufficient to use a single primary EEP. That is, the one for a central element of the array as the source for each secondary EEP to accurately predict the achievable radiometric characteristics.

For both types of radiometers[1], the realized resolutions are at least twice higher than those realized by present-day systems; the distance-to-coast is as short as 6-16 km, depending on the frequency band. This excellent performance was shown to be impossible with traditional multi-frequency PAFs of horns in one-horn-per-beam configurations, as these cannot compensate for the high cross-polarization levels of off-axis beams in conical-scanners and lead to unacceptably high side-lobes due to severe focal-field under-sampling effects in torus reflector systems.

[1]results for the conical scanner see in Paper K

Chapter 4 Beamforming Strategy for Beam Shape Calibration of PAF-equipped Radio Telescope

In this chapter we will come back to the radio astronomy application of phased array feeds and show how a constrained beamformer may simplify the calibration of a beam shape.

Calibration of radio telescopes requires accurate models of the instrumental parameters and propagation conditions that affect the reception of radio waves [30]. These effects vary over time and the model parameters have to be determined at the time of observation through a number of calibration measurements. Furthermore, the calibration measurements should complete in a relatively short time and may be repeated often over the course of an observation during which the instrumental and atmospheric conditions can change significantly. One of the instrumental parameters that needs accurate characterization is the radiation pattern of the antenna, which is especially challenging in the arena of future array based multiple beam radio telescopes [85–87], both due to the complexity of these instruments, as well as the increased size of the Field-of-View (FoV). Calibrating for the radiation pattern of a multi-beam PAF-based radio telescope largely depends on the accuracy of the pattern model, and the availability of suitable reference sources to solve for the unknown parameters in the pattern model.

The proposed idea on improving the calibration efficiency of a radio telescope radiation pattern is to conform the beamformed far-field patterns to a two-parameter physics-based analytic reference model through the use of a linearly constrained minimum variance (LCMV) beamformer. Through this approach, which requires only a few calibration measurements, an accurate and simple pattern model is obtained.

The first term of the Jacobi-Bessel (JB) series solution of reflector antenna far field patterns [88, 89] is used as a reference pattern:

$$F_A(\theta,\phi) \propto \frac{J_1(ka\sin\theta)}{ka\sin\theta} \equiv \mathrm{jinc}(ka\sin\theta), \tag{4.1}$$

where a is the reflector aperture radius; k is the free space wavenumber. This model has been extended to account for a beam width (parameter s in the equation below) and the phase gradient of a scanned beam (parameter Ψ):

$$F(s,\Psi;\theta,\phi) = \mathrm{jinc}(ksa\sin\theta)e^{j\Psi\sin\theta\cos(\phi-\phi_0)}, \tag{4.2}$$

in which s and Ψ control the the amplitude and phase distributions of the reference pattern, respectively.

The reference pattern (4.2) is used to define directional constraints in a LCMV beamformed PAF, for which the weights applied to the elements of the PAF are calculated according to [90] [77, p. 526]

$$\mathbf{w}^H_{\mathrm{LCMV}} = \mathbf{g}^H \left[\mathbf{G}^H\mathbf{C}^{-1}\mathbf{G}\right]^{-1}\mathbf{G}^H\mathbf{C}^{-1} \tag{4.3}$$

in which $\mathbf{x}^H$ means the complex conjugate transpose of $\mathbf{x}$, $\mathbf{C}$ is the noise covariance matrix, $\mathbf{g}$ is the constraints vector, and $\mathbf{G}$ is the directional constraint matrix. For L elements in the array and constraints enforced in the K different directions $\{\Omega_1, \Omega_2, \ldots, \Omega_K\}$, $\mathbf{G}$ is an $L \times K$ matrix in which the ith column contains the signal response vector of the array due to a plane wave incident from direction Ω_i, and the corresponding element g_i in the vector $\mathbf{g}$ is the constraint value enforced on the pattern in that direction. The choice of these constraint parameters comes from the reference pattern (4.2).

An effect of the model parameters s and Ψ on the resulting beam characteristics (directivity, side-lobes level) and the error between the actual LCMV beamformed pattern and its model (4.2) are presented in Paper F, where the APERTIF PAF [7] has been used to feed an offset Gregorian reflector based on the MeerKAT radio telescope reflector antenna [91].

It is shown in Paper F that this beamforming approach has several performance benefits including circularly symmetric scanned beams over a wide FoV, even for non-symmetric reflector antennas. For the example of the MeerKAT offset Gregorian antenna, this strategy resulted in multiple beams with aperture efficiency above 70 % that could be approximated down to the 10 dB level as a single analytic function with an error of less than 5 %. In comparison with a conventional MaxDir beamformer, this would reduce the average pattern calibration model error by more than 50 %.

Chapter 5 Conclusions and recommendations for future work

During last decades phased array feeds (PAFs) for reflector antennas have been proven to have numerous advantages over single-pixel feeds or clusters of them. However, many unsolved questions remain, among them: "What is the mechanism governing the PAF-reflector interaction and how does it affect the reflector antenna characteristics, such as its radiation pattern, directivity, receiving sensitivity, etc?" In the first part of the current work an attempt to answer this question is made. For this purpose a CBFM-PO Jacobi-iterative approach has been developed to model a large reflector antenna (with a diameter exceeding 100 wavelengths) that is fed by a complex PAF. This approach, in combination with the proposed acceleration techniques, not only allows one to solve electrically large antenna systems accurately and time-efficiently, but it also provides a physical insight in the feed-reflector mutual coupling mechanism. Several numerical computations have been performed – including for a real-world PAF system (i.e. a prototype of “APERTIF” system of the Westerbork Synthesis Radio Telescope located in The Netherlands) – and demonstrated excellent agreement with the measurements. As a part of this study on PAFs for radio astronomy, it has been shown how advanced beamforming algorithms can be used to reduce the calibration complexity of the beam shape, while maintaining high receiving sensitivity of radio telescopes equipped with PAFs.

The second part of the thesis is devoted to a feasibility study of PAFs in satellite radiometers for remote sensing of the sea surface. In the current work the push-broom radiometer with a toroidal reflector has been considered and the following questions have been addressed:

- to what extent can the performance of push-broom radiometers be enhanced by using dense PAFs and what are their performance-limiting factors?
- what beamforming algorithms should be used to approach a certain optimality criterion on the receiving characteristics of the radiometer?
- what is the minimum complexity of the PAF design (size, number of elements and their arrangement in the feed as well as the number of active receiver

channels) that is required for meeting the instrument specifications at which future radiometers aim?

- what radiating element types are most suitable for such radiometer applications?

To answer these questions several optimum beamforming methods have been considered, including a conventional Conjugate Field Matching (CFM) method and two new methods which have been developed in this work: Maximum-radiometric Sensitivity-to Minimum-Distance-to-Land (MSMDL) beamformer; and Advanced Maximum Beam Efficiency beamformer (AMBER). The latter are specialized optimum beamforming algorithms aiming at minimizing the signal contamination caused by the side-lobes and cross-polarization of antenna beams covering the land, when measuring the brightness temperature of the sea with a certain footprint.

The proposed beamforming solutions have been evaluated for the torus reflector antenna, which has the projected aperture of 5×7.5 m and the focal length of 5 m. It has been found that the MSMDL beamformer has the best performance in terms of minimum distance-to-coast for the required footprint size, which is given by the reflector antenna aperture. The CFM and AMBER beamformers are preferred when high polarization purity is required (e.g. the relative cross-polar power was found to be in order of 0.01% for the AMBER and 0.2% for MSMDL beamformers, respectively); with the difference that AMBER leads to a more compact array with almost twice fewer active antenna elements as compared to CFM in order to achieve similar distance-to-coast.

Furthermore, it has been shown that when the PAF antenna elements are located along the focal line of the torus reflector (i.e. synthesize a "moon-shaped" array layout), the optimum beamforming coefficients are virtually identical for all subarrays generating multiple beams over a wide scanning range ($\pm 20°$ for the present study case, and potentially up to $\pm 180°$). This is an advantage of the torus geometry over conventional parabolic reflectors, though this wide scanning range can be realized only in a single dimension. A drawback of the torus configuration is that it requires a very large number of the PAF antenna elements and associated receivers – in the present case 1332, 1836 and 3060 elements for 58, 89, and 156 beams at C-, X- and Ku-bands, respectively. (In comparison, the L-band PAF illuminating a prime-focus parabolic reflector of the APERTIF radio telescope has $\sim$ 100 Vivaldi antenna elements producing 37 beams.) Therefore, a modified torus reflector geometry can be further considered that has shorter focal length, and hence more compact focal field distribution.

Several types of PAF elements have been studied, including a crossed-dipole antenna, patch-excited cup antenna, and tapered-slot antenna elements. To cross-compare these elements, we used the above array layout synthesis procedure and beamforming algorithms optimizing the radiometer characteristics while minimizing the numbers of array elements. It was found that for dense PAFs (where the inter-element-separation distance is $\sim 0.75\lambda$ and the total number of elements is large) the type of the antenna element has a minor impact on the radiometer characteristics, as opposed to the array beamforming method. Thanks to the large number of degrees of freedom in beamforming (i.e. the fact that all array elements are excited with their individual complex-valued coefficients), the relative difference between the array embedded element patterns are compensated for in the beam forming process.

At present, a research project funded by the European Space Agency, is manufacturing a test $7 \times 5 \times 2$ element PAF breadboard, that has been designed by using the proposed array synthesis methodology and optimum beamforming algorithms. This project is carried out in collaboration with TICRA and DTU-Space (Denmark).

Appendix

A Radiometer characteristics for the PAFs of the patch-excited cups and Vivaldi elements

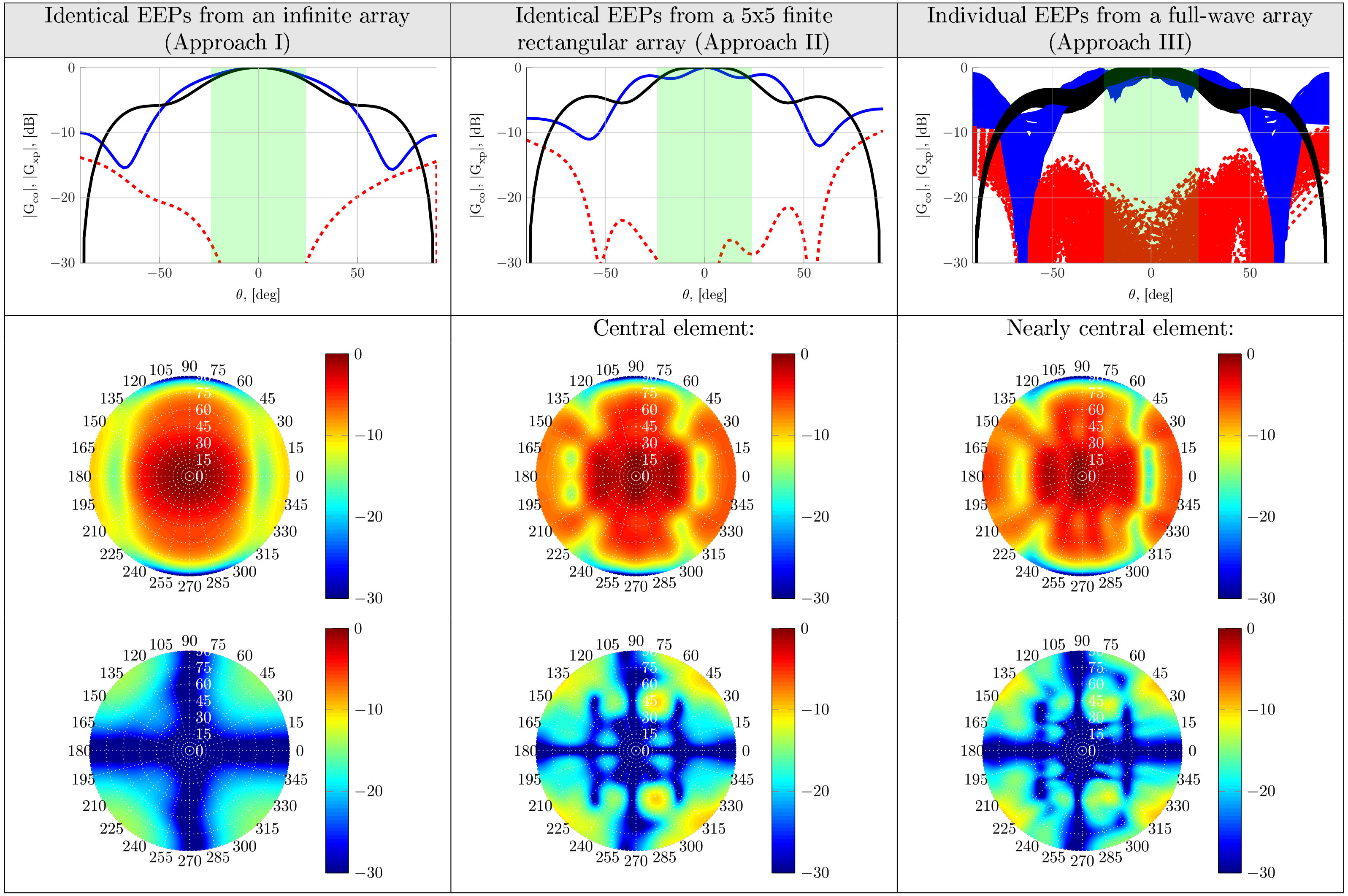

Figure A.1: **Patch array:** Embedded element patterns. Cuts of the co-polar patterns for E- and H-planes, as well as cross-polar pattern for diagonal plane ($\phi = 45°$) are shown on top, and the green area denotes the reflector subtended angle.

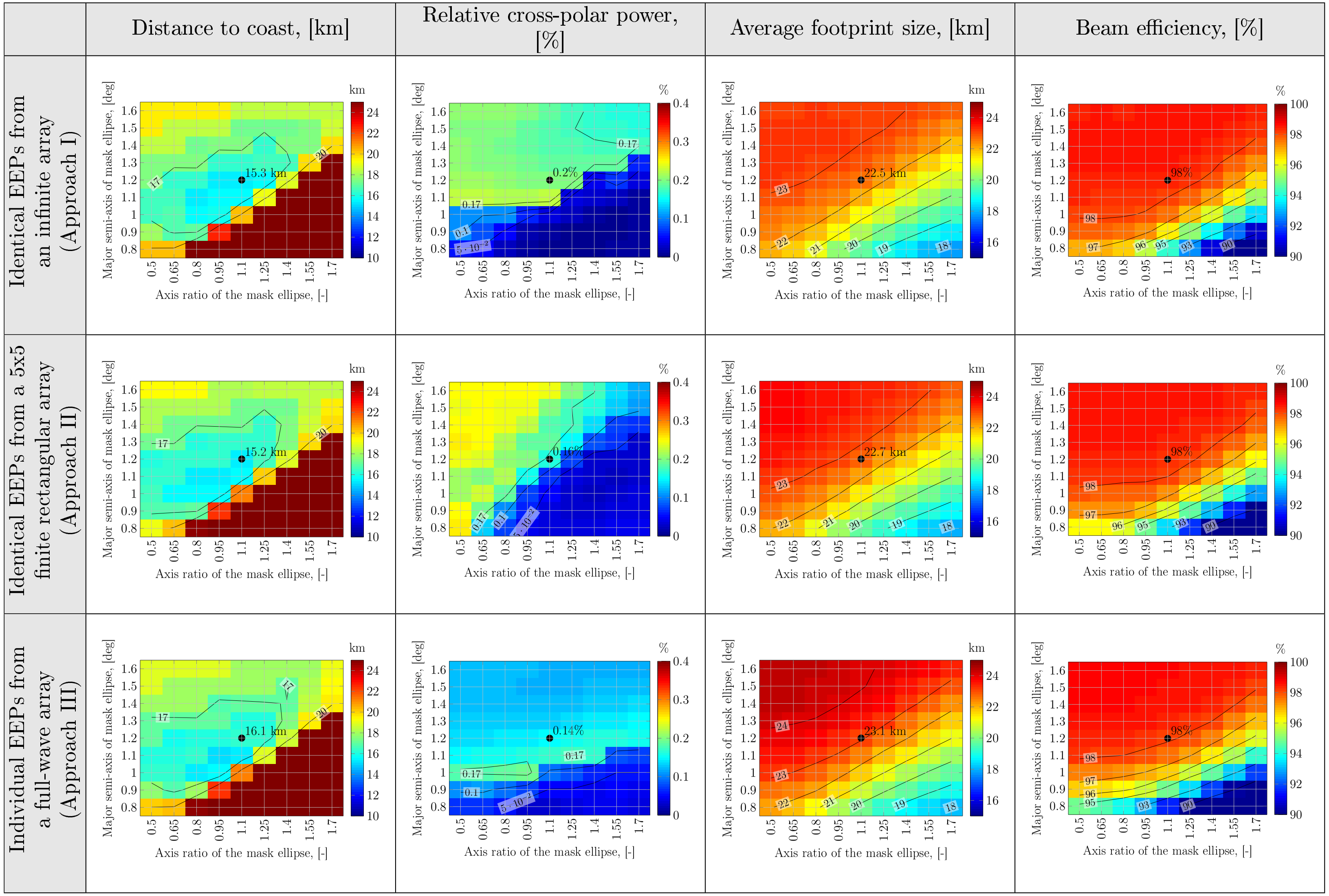

Figure A.2: **Patch array:** Radiometer characteristics as function of two beamformer parameters, i.e. major semi-axis and axis ratio of the antenna main lobe. The black marker shows the chosen optimum parameters and corresponding characteristic's value.

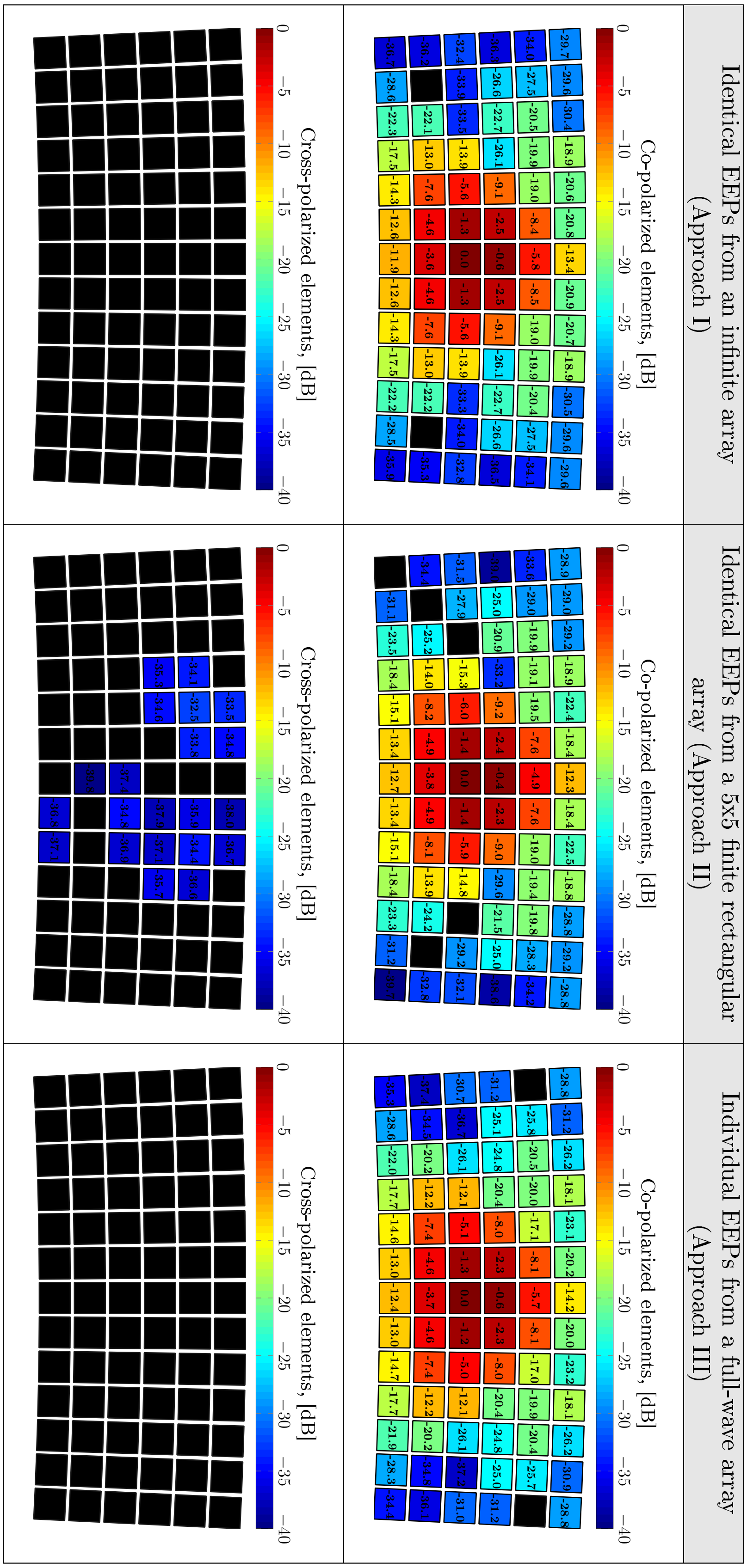

Figure A.3: **Patch array:** Amplitude of the weighting coefficients, [dB], of the 6 × 13 elements for the chosen beamformer parameters (black color indicates passive elements): (top) co-polarized and (bottom) cross-polarized elements

Identical EEPs from an infinite array (Approach I)	Identical EEPs from a 5x5 finite rectangular array (Approach II)	Individual EEPs from a full-wave array (Approach III)
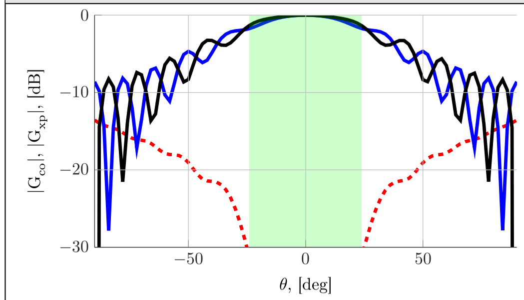	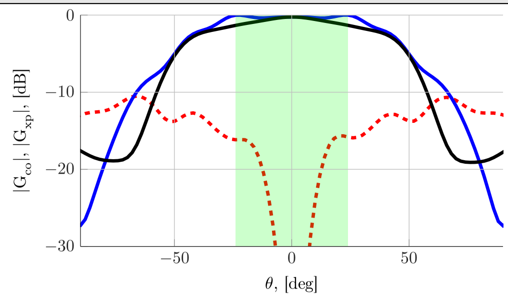	N/A
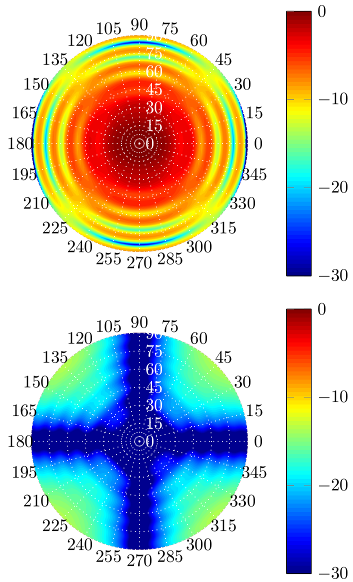	Central element: 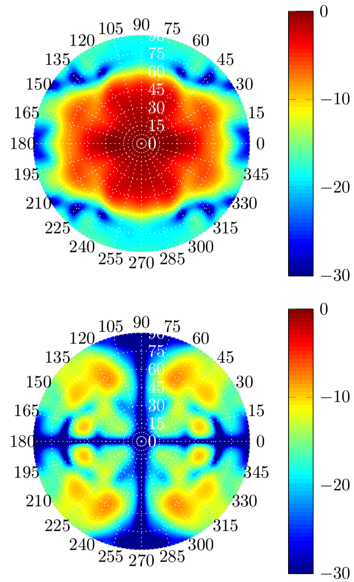	N/A N/A

Figure A.4: **Vivaldi array:** Embedded element patterns. Cuts of the co-polar patterns for E- and H-planes, as well as cross-polar pattern for diagonal plane ($\phi = 45°$) are shown on top, and the green area denotes the reflector subtended angle.

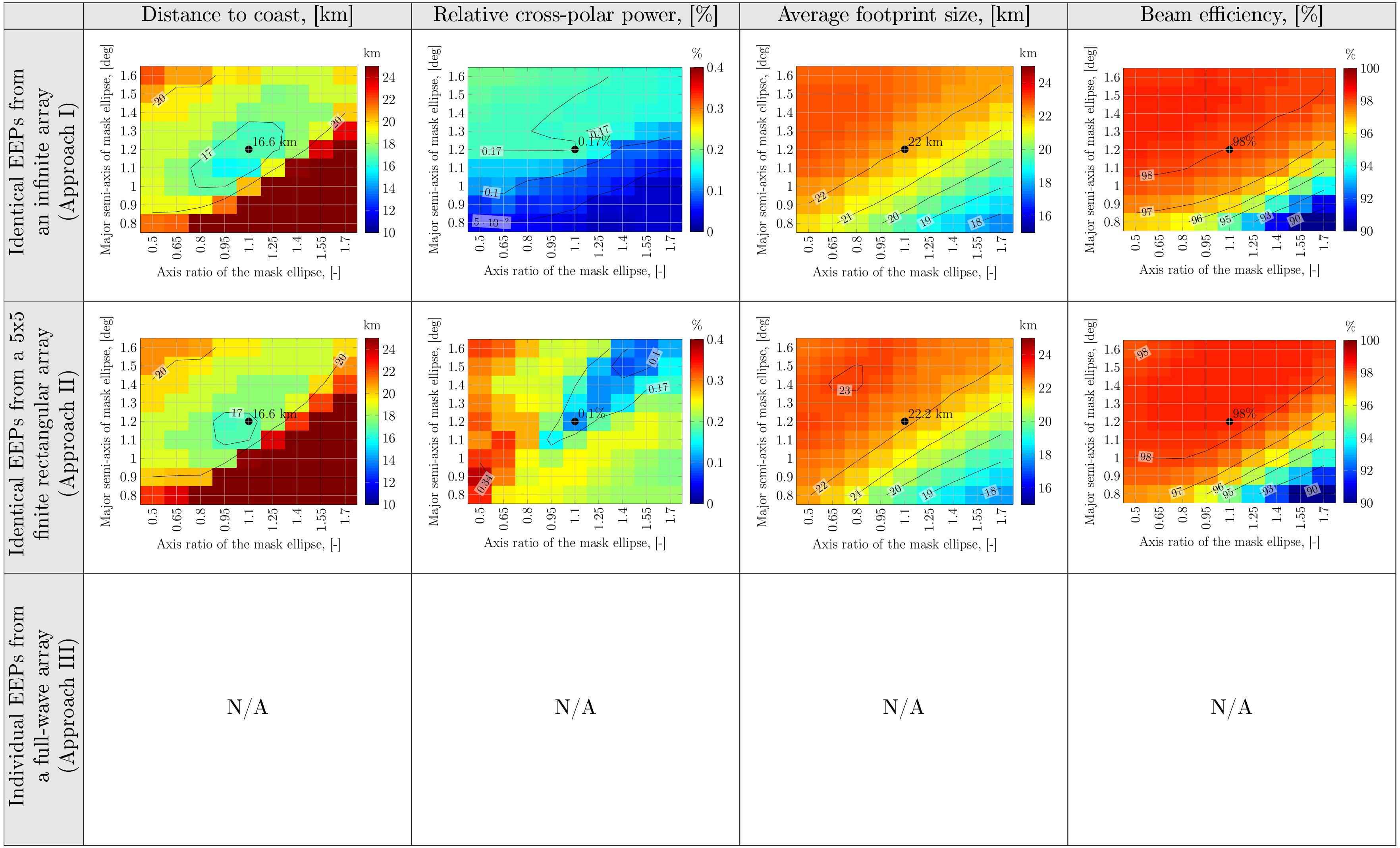

Figure A.5: **Vivaldi array:** Radiometer characteristics as function of two beamformer parameters, i.e. major semi-axis and axis ratio of the antenna main lobe. The black marker shows the chosen optimum parameters and corresponding characteristic's value.

<table>
<tr><th>Identical EEPs from an infinite array (Approach I)</th><th>Identical EEPs from a 5x5 finite rectangular array (Approach II)</th><th>Individual EEPs from a full-wave array (Approach III)</th></tr>
<tr><td>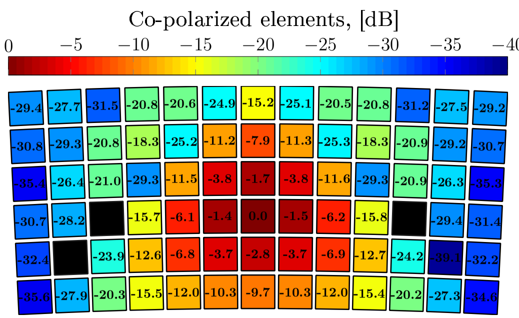
</td><td>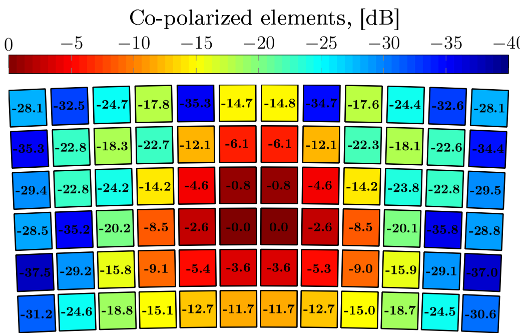
</td><td>N/A</td></tr>
<tr><td>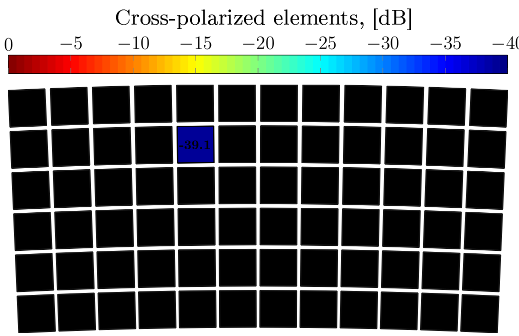
</td><td>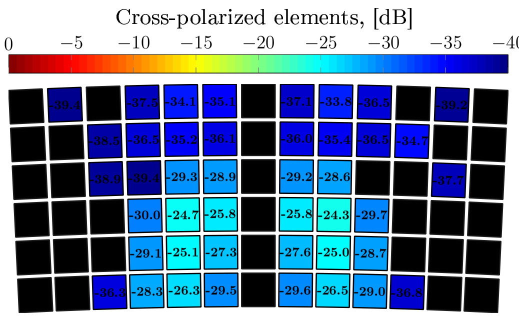
</td><td>N/A</td></tr>
</table>

Figure A.6: **Vivaldi array:** Amplitude of the weighting coefficients, [dB], of the 6×13 elements for the chosen beamformer parameters (black color indicates passive elements): (top) co-polarized and (bottom) cross-polarized elements

References

[1] W. V. Cappellen, J. G. B. de Vaate, K. Warnick, B. Veidt, R. Gough, C. Jackson, and N. Roddis, “Phased array feeds for the square kilometre array,” in *General Assembly and Scientific Symposium, 2011 XXXth URSI*, Istanbul, Turkey, Aug. 2011, pp. 1–4.

[2] J. Fisher and R. Bradley, “Full-sampling array feeds for radio telescopes,” in *Proc. SPIE, Radio Telescopes*, vol. 4015, Munich, Germany, Jul. 2000, pp. 308–318.

[3] M. Ivashina, J. bij de Vaate, R. Braun, and J. Bregman, “Focal plane arrays for large reflector antennas: First results of a demonstrator project,” in *Proc. of the SPIE, Astronomical Telescopes and Instrumentation*, vol. 5489, Glasgow, UK, Jun. 2004, pp. 1129–1138.

[4] D. Cavallo, A. Neto, G. Gerini, and G. Toso, “On the potentials of connected slots and dipoles in the presence of a backing reflector,” in *Proc. of 30th ESA Antenna Workshop on Antennas for Earth Observation, Science, Telecommunication and Navigation Space Missions*, Noordwijk, The Netherlands, May 2008, pp. 407–410.

[5] D. R. DeBoer, R. G. Gough, J. D. Bunton, T. J. Cornwell, R. J. Beresford, S. Johnston, I. J. Feain, A. E. Schinckel, C. A. Jackson, M. J. Kesteven, A. Chippendale, G. A. Hampson, J. D. O’Sullivan, S. G. Hay, C. E. Jacka, T. W. Sweetnam, M. C. Storey, L. Ball, and B. J. Boyle, “Australian SKA pathfinder: A high-dynamic range wide-field of view survey telescope,” *Proc. IEEE*, vol. 97, no. 8, pp. 1507–1521, Aug. 2009.

[6] B. Veidt, T. Burgess, R. Messing, G. Hovey, and R. Smegal, “The DRAO phased array feed demonstrator: Recent results,” in *13th Int. Symp. on Antenna Technology and Applied Electromagnetics and the Canadian Radio Science Meeting, ANTEM/URSI 2009*, Banff, Canada, Feb. 2009, pp. 1–4.

[7] W. A. van Cappellen and L. Bakker, “APERTIF: Phased array feeds for the Westerbork synthesis radio telescope,” in *IEEE International Symposium on Proc. Phased Array Systems and Technology (ARRAY)*, Boston, Oct. 2010, pp. 640–647.

[8] M. Arts, M. Ivashina, O. Iupikov, L. Bakker, and R. van den Brink, "Design of a low-loss low-noise tapered slot phased array feed for reflector antennas," in *Proc. European Conference on Antennas and Propag. (EuCAP)*, Barcelona, Spain, Apr. 2010, pp. 1–5.

[9] X. Bosch-Lluis, I. Ramos-Perez, A. Camps, J. F. Marchan-Hernandez, N. Rodriguez-Alvarez, E. Valencia, M. A. Guerrero, and J. M. Nieto, "Initial results of a digital radiometer with digital beamforming," in *IEEE International Geoscience and Remote Sensing Symposium, IGARSS 2008*, vol. 2, Boston, Massachusetts, U.S.A., Jul. 2008, pp. II–485–II–488.

[10] C. Cappellin, K. Pontoppidan, P. Nielsen, N. Skou, S. S. Søbjærg, A. Ihle, D. Hartmann, M. Ivashina, O.Iupikov, and K. v. t Klooster, "Novel multi-beam radiometers for accurate ocean surveillance," in *Proc. European Conference on Antennas and Propag. (EuCAP)*, The Hague, The Netherlands, Apr. 2014, pp. 1–4.

[11] O. A. Iupikov, M. V. Ivashina, K. Pontoppidan, P. H. Nielsen, C. Cappellin, N. Skou, S. S. Søbjærg, A. Ihle, D. Hartmann, and K. v. t Klooster, "Dense focal plane arrays for pushbroom satellite radiometers," in *Proc. European Conference on Antennas and Propag. (EuCAP)*, Hague, The Netherlands, Apr. 2014, pp. 1–5.

[12] M. Ivashina and C. G. M. van 't Klooster, "Focal fields in reflector antennas and associated array feed synthesis for high efficiency multi-beam performances," *TIJDSCHRIFT-NERG*, vol. 68, no. 1, pp. 11–19, 2003.

[13] W. Brisken and C. Craeye. (2004, Jan.) Focal-plane array beam-forming and spill-over cancellation using vivaldi antennas. EVLA memo 69. [Online]. Available: http://http://www.aoc.nrao.edu/evla/geninfo/memoseries/evlamemo69.pdf

[14] C. Craeye, W. Brisken, and X. Dardenne, "Simulated radiation characteristics of wideband focal-plane arrays and their impact on the system gain-to-temperature ratio," in *Proc. of the JINA 2004 Conference*, Nice, France, Nov. 2004.

[15] B. D. Jeffs, K. F. Warnick, J. Landon, J. Waldron, D. Jones, J. R. Fisher, and R. Norrod, "Signal processing for phased array feeds in radio astronomical telescopes," *IEEE J. Selected Topics in Signal Processing*, vol. 2, no. 5, pp. 635–646, Oct. 2008.

[16] D. Hayman, T. Bird, K. Esselle, and P. Hall, "Experimental demonstration of focal plane array beamforming in a prototype radiotelescope," *IEEE Trans. Antennas Propag.*, vol. 58, no. 6, pp. 1922–1934, Jun. 2010.

[17] M. V. Ivashina, O. Iupikov, R. Maaskant, W. A. van Cappellen, and T. Oosterloo, "An optimal beamforming strategy for wide-field surveys with phased-array-fed reflector antennas," *IEEE Trans. Antennas Propag.*, vol. 59, no. 6, pp. 1864–1875, Jun. 2011.

[18] M. Elmer, B. Jeffs, K. F. Warnick, J. Fisher, and R. Norrod, "Beamformer design methods for radio astronomical phased array feeds," *IEEE Trans. Antennas Propag.*, vol. 60, no. 2, pp. 930–914, Feb. 2012.

[19] (2003, Sep.) Ska memo 40: Figure of merit for ska survey speed. [Online]. Available: https://www.skatelescope.org/uploaded/51368_40_memo_Bunton.pdf

[20] M. V. Ivashina, M. Kehn, P.-S. Kildal, and R. Maaskant, "Decoupling efficiency of a wideband Vivaldi focal plane array feeding a reflector antenna," *IEEE Trans. Antennas Propag.*, vol. 57, no. 2, pp. 373–382, Feb. 2009.

[21] A. Thompson, J. Moran, and G. Swenson, *Interferometry and Synthesis in Radio Astronomy.* New York: Wiley, 2001.

[22] J. F. Johansson, "Theoretical limits for aperture efficiency in multi-beam antenna systems," Chalmers University of Technology (Sweden), Dept. of Radio Space Sciences, Technical Report 161, May 1988.

[23] M. V. Ivashina and C. G. M. van't Klooster, "Focal fields in reflector antennas and associated array feed synthesis for high efficiency multi-beam performances," in *Proc. 25th ESA Workshop on Satellite Antenna Technologies*, Noordwijk, The Netherlands, Sep. 2002, pp. 339–346.

[24] R. Maaskant, D. J. Bekers, M. J. Arts, W. A. van Cappellen, and M. V. Ivashina, "Evaluation of the radiation efficiency and the noise temperature of low-loss antennas," *IEEE Antennas Wireless Propag. Lett.*, vol. 8, no. 8, pp. 1536–1225, Jan. 2009.

[25] E. E. M. Woestenburg, L. Bakker, and M. V. Ivashina, "Experimental results for the sensitivity of a low noise aperture array tile for the SKA," *IEEE Trans. Antennas Propag.*, vol. 60, no. 2, pp. 915–921, Feb. 2012.

[26] (2017) APERTIF project (ASTRON) – Official website. [Online]. Available: https://www.astron.nl/general/apertif/apertif

[27] K. F. Warnick, M. V. Ivashina, S. J. Wijnholds, and R. Maaskant, "Polarimetry with phased array antennas: theoretical framework and definitions," *IEEE Trans. Antennas Propag.*, vol. 60, no. 1, pp. 184–196, Jan. 2012.

[28] S. Wijnholds, M. Ivashina, R. Maaskant, and K. F. Warnick, "Polarimetry with phased array antennas: Sensitivity and polarimetric performance using unpolarized sources for calibration," *IEEE Trans. Antennas Propag.*, vol. 60, no. 10, pp. 4688–4698, Oct. 2012.

[29] T. Carozzi and G. Woan, "A fundamental figure of merit for radio polarimeters," *IEEE Trans. Antennas Propag.*, vol. 59, no. 6, pp. 2058–2065, Jun. 2011.

[30] O. Smirnov, "Revisiting the radio interferometer measurement equation. ii. calibration and direction-dependent effects," *Astronomy and Astrophysics*, vol. 527, Feb. 2011. [Online]. Available: http://arxiv.org/pdf/1101.1765v3.pdf

[31] O. A. Iupikov, M. V. Ivashina, and O. M. Smirnov, "Reducing the complexity of the beam calibration models of phased-array radio telescopes," in *Proc. European Conference on Antennas and Propag. (EuCAP)*, Rome, Italy, Apr. 2011, pp. 930–933.

[32] A. Young, R. Maaskant, M. V. Ivashina, and D. B. Davidson, "Performance evaluation of far field paterns for radio astronomy application through the use of the Jacobi-Bessel series," in *Proc. Int. Conf. on Electromagn. in Adv. Applicat. (ICEAA)*, Cape Town, Sep. 2012, pp. 884–887.

[33] P. Valle, G. Orlando, R. Mizzoni, F. Heliere, and K. van 't Klooster, "P-band feedarray for biomass," in *Proc. European Conference on Antennas and Propag. (EuCAP)*, Prague, Czech Republic, Mar. 2012, pp. 3426–3430.

[34] P. Cecchini, R. Mizzoni, G. Orlando, F. Heliere, and K. van 't Klooster, "A dual band array-fed reflector scansar antenna," in *Proc. European Conference on Antennas and Propag. (EuCAP)*, Prague, Czech Republic, Mar. 2012, pp. 3431–3435.

[35] "Antenna requirements document," TICRA (Denmark), Technical Report S-1580-03, Jul. 2013.

[36] (2013, Sep.). [Online]. Available: http://earthobservatory.nasa.gov/Features/EO1/eo1_2.php

[37] P. Nielsen, K. Pontoppidan, J. Heeboell, and B. L. Stradic, "Design, manufacture and test of a pushbroom radiometer," in *Antennas and Propagation, 1989. ICAP 89., Sixth International Conference on (Conf. Publ. No.301)*, Coventry, United Kingdom, Apr. 1989, pp. 126–130.

[38] R. Hoferer and Y. Rahmat-Samii, "RF characterization of an inflatable parabolic torus reflector antenna for space-borne applications," *IEEE Trans. Antennas Propag.*, vol. 46, no. 10, pp. 1449–1457, Oct. 1998.

[39] S. G. Hay, J. D. O'Sullivan, J. S. Kot, C. Granet, A. Grancea, A. R. Forsyth, and D. H. Hayman, "Focal plane array development for ASKAP (australian SKA pathfinder)," in *Proc. European Conference on Antennas and Propag. (EuCAP)*, Edinburgh, UK, Nov. 2007, pp. 1–5.

[40] K. F. Warnick, "High efficiency phased array feed antennas for large radio telescopes and small satellite communication terminals," in *Proc. European Conference on Antennas and Propag. (EuCAP)*, Gothenburg, Sweden, Apr. 2013, pp. 448–449.

[41] A. N. H. Al-Rawi, A. Dubok, M. H. A. J. Herben, and A. B. Smolders, "Point-to-point radio link variation at e-band and its effect on antenna design," in *in Proc. of Progress In Electromagnetics Research Symposium (PIERS)*, Prague, Czech Republic, Jul. 2015, pp. 913–917.

[42] A. Zamanifekri and A. B. Smolders, "Beam squint compensation in circularly polarized offset reflector antennas using a sequentially rotated focal-plane array," *IEEE Antennas and Wireless Propagation Letters (AWPL)*, vol. 14, pp. 815–818, Dec. 2015.

[43] (2017, May) Silicon-based Ka-band massive MIMO antenna systems for new telecommunication services. [Online]. Available: http://cordis.europa.eu/project/rcn/205533_en.html

[44] A. Moldsvor and P.-S. Kildal, "Systematic approach to control feed scattering and multiple reflections in symmetrical primary-fed reflector antennas," *IEEE Trans. Antennas Propag.*, vol. 139, no. 1, pp. 65–71, Sep. 1992.

[45] P. Bolli, G. Gentili, L. Lucci, R. Nesti, G. Pelosi, and G. Toso, "A hybrid perturbative technique to characterize the coupling between a corrugated horn and a reflector dish," *IEEE Trans. Antennas Propag.*, vol. 54, no. 2, pp. 595–603, Sep. 2006.

[46] M. Bandinelli, F. Milani, G. Guida, M. Bercigli, P. Frandsen, S. Sorensen, B. Bencivenga, and M. Sabbadini, "Feed-array design in presence of strong scattering from reflectors," in *Proc. European Conference on Antennas and Propag. (EuCAP)*, Rome, Italy, Apr. 2011, pp. 3844–3848.

[47] C. D. Giovampaola, E. Martini, A. Toccafondi, and S. Maci, "A hybrid PO/generalized-scattering-matrix approach for estimating the reflector induced mismatch," *IEEE Trans. Antennas Propag.*, vol. 60, no. 9, pp. 4316–4325, Sep. 2012.

[48] W. A. van Cappellen and L. Bakker. (2010) Eliminating sensitivity ripples in prime focus reflectors with low-scattering phased array feeds. [Online]. Available: http://csas.ee.byu.edu/docs/Workshop/BYU_StandingWaves_Cappellen.pdf

[49] R. E. Hodges and Y. Rahmat-Samii, "An iterative current-based hybrid method for complex structures," *IEEE Trans. Antennas Propag.*, vol. 45, no. 2, pp. 265–276, Feb. 1997.

[50] C. S. Kim and Y. Rahmat-Samii, "Low profile antenna study using the physical optics hybrid method (POHM)," in *Proc. IEEE AP-S International Symposium*, Ontario, Canada, Jun. 1991, pp. 1350–1353.

[51] J. M. Taboada and F. Obelleiro, "Including multibounce effects in the moment-method physical-optics (MMPO) method," *Micr. Opt. Technol.*, vol. 32, no. 6, pp. 435–439, 2002.

[52] U. Jakobus and F. M. Landstorfer, "Improved PO-MM hybrid formulation for scattering from three-dimensional perfectly conducting bodies of arbitrary shape," *IEEE Trans. Antennas Propag.*, vol. 43, no. 2, pp. 162–169, Feb. 1995.

[53] B. Andrés-Garciá, D. Gonzalez-Ovejero, C. Craeye, L. Garciá-Muñoz, and D. Segovia-Vargas, "An iterative MoM-PO method based on a MBF/Krylov approach," in *Proc. European Conference on Antennas and Propag. (EuCAP)*, Barcelona, Spain, Apr. 2010, pp. 1–4.

[54] S. Hay, R. Mittra, and N. Huang. (2010) Analysis of reflector and feed scattering and coupling effects on the sensitivity of phased array feeds. [Online]. Available: http://csas.ee.byu.edu/docs/Workshop/BYUSGH.pdf

[55] G. Harp, R. F. Ackermann, Z. J. Nadler, S. Blair, M. Davis, M. C. H. Wright, J. R. Forster, D. DeBoer, W. J. Welch, S. Atkinson, D. Backer, P. R. Backus, W. Barott, A. Bauermeister, L. Blitz, D. C. J. Bock, G. Bower, T. Bradford, C. Cheng, S. Croft, M. Dexter, J. Dreher, G. Engargiola, E. D. Fields, C. Heiles, T. Helfer, J. Jordan, S. Jorgensen, T. Kilsdonk, C. Gutierrez-Kraybill, G. Keating, C. Law, J. Lugten, D. H. E. MacMahon, P. McMahon, O. Milgrome, A. Siemion, K. Smolek, D. Thornton, T. Pierson, K. Randall, J. Ross, S. Shostak, J. Tarter, L. Urry, D. Werthimer, P. Williams, and D. Whysong, "Primary beam and dish surface characterization at the Allen telescope array by radio holography," *IEEE Trans. Antennas Propag.*, vol. 59, no. 6, pp. 2004–2021, Jun. 2011.

[56] W. Van Cappellen and M. Ivashina, "Temporal beam pattern stability of a radio astronomy phased array feed," in *Proc. European Conference on Antennas and Propag. (EuCAP)*, Rome, Italy, Apr. 2011, pp. 926–929.

[57] R. Maaskant, M. V. Ivashina, S. J. Wijnholds, and K. F. Warnick, "Efficient prediction of array element patterns using physics-based expansions and a single far-field measurement," *IEEE Trans. Antennas Propag.*, accepted for publication.

[58] A. Young, R. Maaskant, M. V. Ivashina, D. I. L. de Villiers, and D. B. Davidson, "Accurate beam prediction through characteristic basis function patterns for the MeerKAT/SKA radio telescope antenna," *IEEE Trans. Antennas Propag.*, vol. 61, no. 5, pp. 2466–2473, May 2013.

[59] O. A. Iupikov, R. Maaskant, M. Ivashina, A. Young, and P. Kildal, "Fast and accurate analysis of reflector antennas with phased array feeds including multiple reflections between feed and reflector," *IEEE Trans. Antennas Propag.*, vol. 62, no. 7, Jul. 2014.

[60] P.-S. Kildal, "Factorization of the feed efficiency of paraboloids and cassegrain antennas," *IEEE Trans. Antennas Propag.*, vol. 33, no. 8, pp. 903–908, Aug. 1985.

[61] N. M. Kehn, M. V. Ivashina, P.-S. Kildal, and R. Maaskant, "Definition of unifying decoupling efficiency of different array antennas – case study of dense focal plane array feed for parabolic reflector," *Int. Journal of Electronics and Communications (AEU)*, vol. 64, no. 5, pp. 403–412, May 2010.

[62] P.-S. Kildal, S. Skyttemyr, and A. Kishk, "G/T maximization of a paraboloidal reflector fed by a dipole-disk antenna with ring by using the multiple-reflection approach and the moment method," *IEEE Trans. Antennas Propag.*, vol. 45, no. 7, pp. 1130–1139, Jul. 1997.

[63] S. N. Makarov, *Antenna and EM Modeling With MATLAB*. New York: John Wiley and Sons, Inc., 2002.

[64] R. Maaskant, "Analysis of large antenna systems," Ph.D. dissertation, Electrical engineering, Eindhoven University of Technology, Eindhoven, 2010. [Online]. Available: http://alexandria.tue.nl/extra2/201010409.pdf

[65] R. Maaskant, M. V. Ivashina, O. Iupikov, E. A. Redkina, S. Kasturi, and D. H. Schaubert, "Analysis of large microstrip-fed tapered slot antenna arrays by combining electrodynamic and quasi-static field models," *IEEE Trans. Antennas Propag.*, vol. 56, no. 6, pp. 1798–1807, Jun. 2011.

[66] (2007) EM Software & Systems – S.A. (Pty) Ltd, Stellenbosch, South Africa, FEKO, Suite 6.0. [Online]. Available: http://www.feko.info

[67] B. A. Munk, *Finite Antenna Arrays and FSS.* Danvers, Massachusetts: John Wiley & Sons, Inc., 2003.

[68] J. J. H. Wang, "An examination of the theory and practices of planar near-field measurement," *IEEE Trans. Antennas Propag.*, vol. 36, no. 6, pp. 746–753, Jun. 1988.

[69] J. P. McKay and Y. Rahmat-Samii, "Compact range reflector analysis using the plane wave spectrum approach with an adjustable sampling rate," *IEEE Trans. Antennas Propag.*, vol. 39, no. 6, pp. 746–753, Jun. 1991.

[70] R. C. Rudduck, D. C. Wu, and M. Intihar, "Near-field analysis by the plane-wave spectrum approach," *IEEE Trans. Antennas Propag.*, vol. 21, no. 2, pp. 231–234, Mar. 1973.

[71] C. A. Balanis, *Advanced Engineering Electromagnetics.* New York: John Wiley and Sons, Inc., 1989.

[72] M. V. Ivashina, R. Maaskant, and B. Woestenburg, "Equivalent system representation to model the beam sensitivity of receiving antenna arrays," *IEEE Antennas Wireless Propag. Lett.*, vol. 7, no. 1, pp. 733–737, Jan. 2008.

[73] Y. Saad and M. H. Schultz, "GMRES: a generalized minimal residual algorithm for solving nonsymmetric linear systems," *SIAM Journal on Scientific and Statistical Computing*, vol. 7, no. 3, pp. 856–869, Jul. 1986.

[74] C. Craeye, J. Laviada, R. Maaskant, and R. Mittra, "Macro Basis Function framework for solving Maxwell's equations in surface integral equation form," *The FERMAT Journal*, vol. 3, pp. 1–16, 2014.

[75] A. Bojańczyk, "Complexity of solving linear systems in different models of computation," *SIAM Journal on Numerical Analysis*, vol. 21, no. 3, pp. 591–603, Jun. 1984.

[76] "Technical note 1," TICRA (Denmark), DTU-Space (Denmark), Technical Report S-1580-02, Mar. 2013.

[77] H. L. van Trees, *Optimum Array Processing – Part IV of Detection, Estimation, and Modulation Theory.* New York: Wiley, 2002.

[78] D. I. L. de Villiers and R. Lehmensiek, "Rapid calculation of antenna noise temperature in offset gregorian reflector systems," *IEEE Trans. Antennas Propag.*, vol. 63, no. 4, pp. 1564–1571, Apr. 2015.

[79] (2017) General Reflector Antenna Software Package (GRASP) – Official website. [Online]. Available: http://www.ticra.com/products/software/grasp

[80] (2017) Mathworks MATLAB – Official website. [Online]. Available: https://mathworks.com/products/matlab.html

[81] (2017) High Frequency Structural Simulator (HFSS) – official website. [Online]. Available: http://www.ansys.com/products/electronics/ansys-hfss

[82] M. Ivashina, M. Kehn, and P.-S. Kildal, "Optimal number of elements and element spacing of wide-band focal plane arrays for a new generation radio telescope," in *IEEE Trans. Antennas Propag.*, Edinburgh, UK, Nov. 2007, pp. 1–7.

[83] J. Johansson and P. Ingvarson, "Array antenna activities at RUAG space: An overview," in *Proc. European Conference on Antennas and Propag. (EuCAP)*, Gothenburg, Sweden, Apr. 2013, pp. 666–669.

[84] "Study on advanced multiple-beam radiometers, ESA contract No 4000107369/12/NL/MH, Final report," TICRA (Denmark), DTU-Space (Denmark), Chalmers (Sweden), HPS (Germany), Technical Report S-1580-D2, Sep. 2014.

[85] S. Ellingson, T. Clarke, A. Cohen, J. Craig, N. Kassim, Y. Pihlstrom, L. Rickard, and G. Taylor, "The long wavelength array," *IEEE Trans. Antennas Propag.*, vol. 97, no. 8, pp. 1421–1430, Aug. 2009.

[86] M. D. Vos, A. Gunst, and R. Nijboer, "The lofar telescope: System architecture and signal processing," *IEEE Trans. Antennas Propag.*, vol. 97, no. 8, pp. 1431–1437, Aug. 2009.

[87] The SKA website. [Online]. Available: http://www.skatelescope.org/

[88] V. Galindo-Israel and R. Mittra, "A new series representation for the radiation integral with application to reflector antennas," *IEEE Trans. Antennas Propag.*, vol. 55, no. 5, pp. 631–641, Sep. 1977.

[89] Y. Rahmat-Samii and V. Galindo-Israel, "Shaped reflector antenna analysis using the Jacobi-Bessel series," *IEEE Trans. Antennas Propag.*, vol. 28, no. 4, pp. 425–435, Jul. 1980.

[90] O. I. Frost, "An algorithm for linearly constrained adaptive array processing," *Proceedings of the IEEE*, vol. 60, no. 8, pp. 926–935, Aug. 1972.

[91] I. Theron, R. Lehmensiek, and D. de Villiers, "The design of the meerkat dish optics," in *Proc. Int. Conf. on Electromagn. in Adv. Applicat. (ICEAA)*, Cape Town, Sep. 2012, pp. 539–542.

Part II

Included Papers

Paper A

Towards the Understanding of the Interaction Effects Between Reflector Antennas and Phased Array Feeds

O. A. Iupikov, R. Maaskant, and M. Ivashina

in *Proceedings of the International Conference on Electromagnetics in Advanced Applications,* Cape Town, WP, South Africa, September 2012.

The layout of this paper has been revised in order to comply with the rest of the thesis.

Towards the Understanding of the Interaction Effects Between Reflector Antennas and Phased Array Feeds

O. A. Iupikov, R. Maaskant, and M. Ivashina

Abstract

A computationally efficient numerical procedure has been developed and used to analyze the mutual interaction effects between an electrically large reflector antenna and a phased array feed (PAF). The complex electromagnetic behavior for such PAF systems is studied through a few simple and didactical examples, among which a single dipole antenna feed, a singly-excited antenna in an array of 20 dipoles, and a fully-excited array. These examples account for the effects of the ground plane, active loading (low noise amplifiers), and beamforming scenario, and are used to illustrate the differences between single-port feeds and PAFs.

1 Introduction

For many practical applications it is required to accurately model the beam patterns of reflector antennas. Several factors can cause the actual beam to differ from the ideally designed one due to inaccuracies of the antenna system model. For instance, one often neglects – or only partly takes into account – the effects of the feed supporting structure and reflector-feed interactions. A rigorous analysis of such electrically large antenna structures represents a challenging electromagnetic problem, especially when the reflector is fed with a phased array feed (PAF) consisting of many strongly coupled antenna elements. During the last few years a number of pioneering studies have been carried out towards the development of more complete numerical models [1–4] while, at the same time, knowledge has been acquired through experimental studies [5,6]. For example, in [6] it has been observed that the magnitude of the receiving sensitivity ripple as a function of frequency caused by the feed-reflector interactions is significantly smaller for a PAF of wideband Vivaldi antennas than it is for a horn feed. It has been suggested that the smaller radar cross section (RCS) of Vivaldi PAFs is a reason for this improvement. However, the fact that there exist differences in the EM coupling mechanisms for different phased-array and single-element feeds, and how this affects the system design procedure, is not yet fully understood. The objective of the present work is therefore to investigate this phenomenon in more detail.

2 Analysis methodology

First, we examine a single dipole antenna feed above a finite ground plane, after which an array of dipole elements is considered, as shown in Fig. 1(a) and (b), respectively. The antenna array ports are connected to Low Noise Amplifiers (LNAs) which are also part of the antenna-receiver model. Two beamforming scenarios are considered: (i) a singly-excited embedded element, and; (ii) a fully-excited antenna array employing the Conjugate Field Matching (CFM) beamformer for maximizing the gain of the secondary far-field beam. This beamforming array system is analyzed in combination with a parabolic reflector of 8 m in diameter ($\sim 38\lambda$ @ $f = 1.42$ GHz), $F/D = 0.35$.

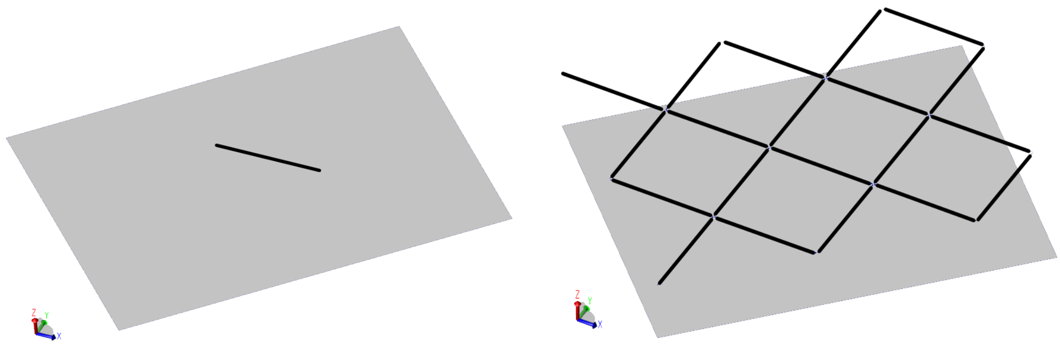

(a) (b)

Figure 1: The considered dipole antenna feeds: (a) a single dipole; and (b) a dual-polarized array of 20 dipole antenna elements. The dipole length is (0.47λ) and the ground plane size is ($3.3\lambda \times 2.65\lambda$)

To account for the mutual coupling between the feed and reflector antenna in the described system, a rapidly converging iterative procedure has been developed. It consists of the following steps: (i) the antenna feed currents are computed through a method-of-moments (MoM) approach by exciting the antenna port(s) in the absence of the reflector; (ii) these currents generate an EM field which induces PO-currents on the reflector surface; (iii) the PO currents create a scattered field that, in turn, induces currents on the feed structure. The steps (ii) and (iii) are repeated until the multiply induced currents – which form the total current when summed – has converged. Afterwards, the antenna radiation pattern, the input impedance (matrix) and derived antenna parameters affecting the receiving sensitivity can be computed.

It is worthwhile to mention that the antenna elements in our study are loaded by LNAs, so that we will account for this loading when solving for the antenna feed currents through the MoM. This is done through the modification of the diagonal elements of the MoM matrix corresponding to the port basis functions as described in [7, p. 223]. The impedance of the loads, and thus the input impedance of the LNAs, has been chosen real-valued. Next, the (passive) reflection coefficient of the antenna was minimized, which yielded the optimum load resistance of 80 and 140 Ω for the single dipole and array case, respectively.

To quantify the performance degradation of the antenna system – due to the interaction effects – we analyze the antenna efficiencies as well as the system noise temperature contributions, both of which affect the receiving sensitivity $A_{\mathrm{eff}}/T_{\mathrm{sys}}$ [8], i.e.,

$$\frac{A_{\mathrm{eff}}}{T_{\mathrm{sys}}} = \frac{A_{\mathrm{ph}}\eta_{\mathrm{ap}}\eta_{\mathrm{rad}}}{\eta_{\mathrm{rad}}T_{\mathrm{spil}} + (1-\eta_{\mathrm{rad}})\,T_{\mathrm{amb}} + T_{\mathrm{Eq}}^{\mathrm{LNA}}} \tag{1}$$

where A_{ph} and A_{eff} are the physical and effective areas of the reflector antenna, respectively; T_{sys} – the system noise temperature; η_{ap} – the aperture efficiency; T_{spil} – the spillover noise temperature contribution; η_{rad} – the antenna radiation efficiency (herein assumed 100%); $T_{\mathrm{amb}} = 290$ K – the ambient temperature; $T_{\mathrm{Eq}}^{\mathrm{LNA}}$ – the receiver noise temperature due to LNAs with minimum noise temperature T_{min}, a component which is independent from the antenna, and the noise coupling component T_{coup}, due to the impedance noise mismatch between the LNAs and the antenna elements [8].

In the next section it will be shown which of the above contributions are most affected by the feed-reflector interaction effects.

3 Numerical Results

The frequency-varying receiving sensitivity, which is caused by the interaction effects, gives rise to a standing wave component between feed and reflector with oscillation period $\Delta f = 2F/c$, where c is the speed of light [3]. Fig. 2 presents the computed current distributions on the ground plane of the three feeds at two frequency points leading to the minimum and maximum antenna aperture efficiency within one period of the oscillation. For the case of the single dipole [see Fig. 2(a)], one can clearly see a significant difference between the areas supporting large currents on the ground plane at these frequencies, as a result of which the corresponding far-field patterns of the feed differ in shape and beamwidth [see Fig. 3(a)].

Upon comparing the left- and right-hand-side subfigures in Fig. 2, one observes that the groundplane for the single-dipole case has a predominant effect on the scattering mechanism. On the contrary, when the field from the reflector illuminates the antenna array (the physical area of which is comparable to the size of the ground plane), part of this field is blocked by the dipoles. Therefore, the differences between the feed patterns for the dipole arrays in Fig. 3(b) and (c) are less pronounced, regardless of the beamforming scenario.

Next, we present the results for the system sensitivity and its subefficiencies for the three considered antenna feeds.

Fig. 4(a)–(c) shows the aperture efficiency and its dominant contributions, i.e., the spillover efficiency η_{spil} and the taper illumination efficiency η_{tap}; and Fig. 4(d) compares the respective frequency variations of η_{ap} due to the standing wave phenomenon. It is readily seen that the aperture efficiency variation is less than 1% for

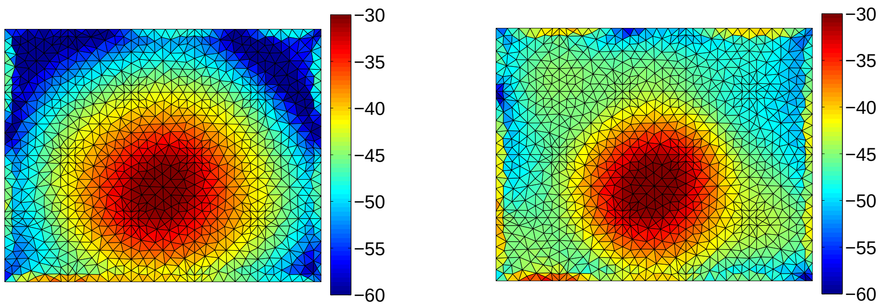

(a) Isolated dipole

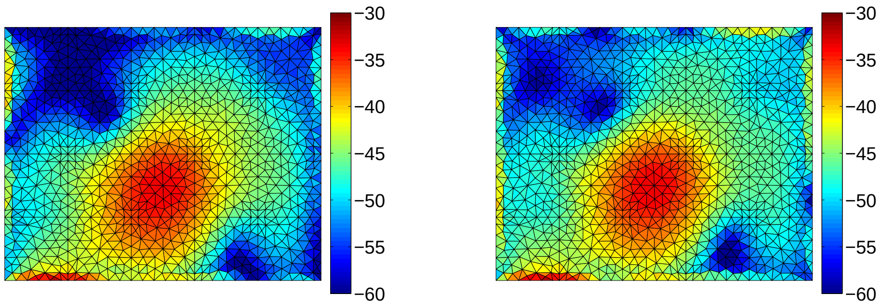

(b) Embedded dipole

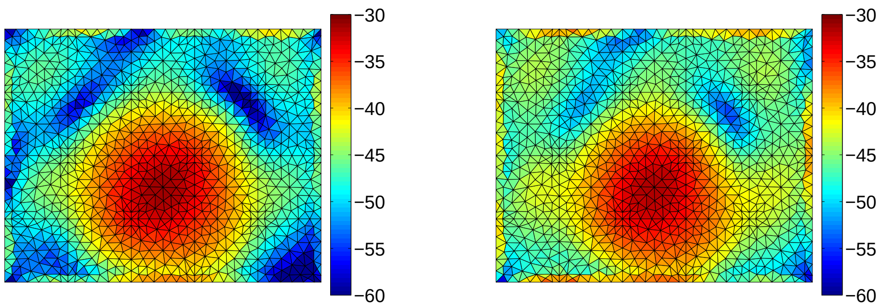

(c) Fully-excited array (CFM)

Figure 2: Current distributions on the ground plane of the feeds for two frequency points corresponding to the minimum (left column) and maximum (right column) of the aperture efficiency.

the two PAF cases, since the illumination pattern remains almost constant, whereas this variation is approximately three times larger for the single dipole case, due to the scattering mechanism differences as described above.

A similar analysis has been performed for the system noise temperature T_{sys} (see Fig. 5). Note that, for the embedded element case, T_{sys} is not affected much by the standing wave phenomenon, since the input impedance of a centralized dipole array element varies only little with frequency and is therefore well-matched (after optimally loading the array elements), as opposed to the single dipole antenna. Also,

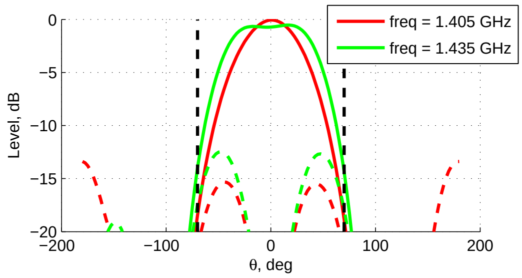

(a) Isolated dipole

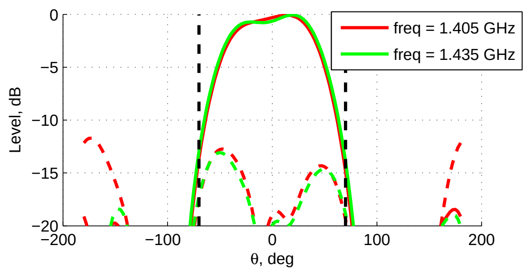

(b) Embedded dipole

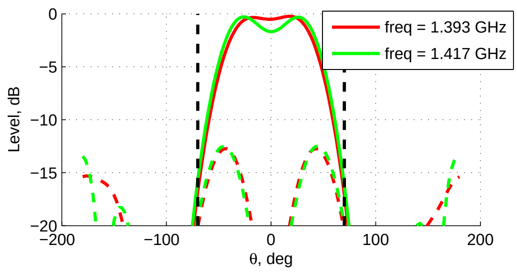

(c) Fully-excited array (CFM)

Figure 3: Primary patterns in $\phi = 45°$ cross-section.

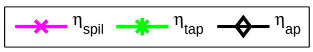

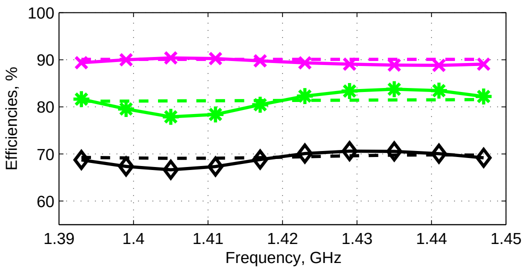

(a) Isolated dipole

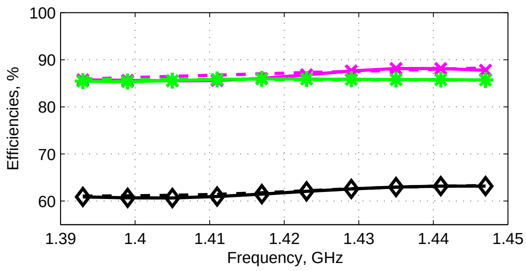

(b) Embedded dipole

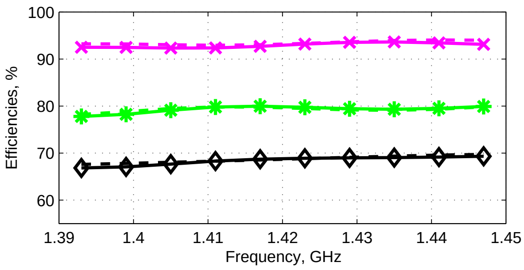

(c) Fully-excited array (CFM)

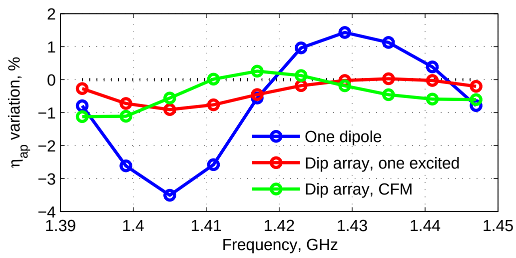

(d) Comparison of the η_{ap} variation

Figure 4: The aperture efficiency and its dominant contributions. The solid and dotted lines are for with and without accounting for feed-reflector interactions, respectively.

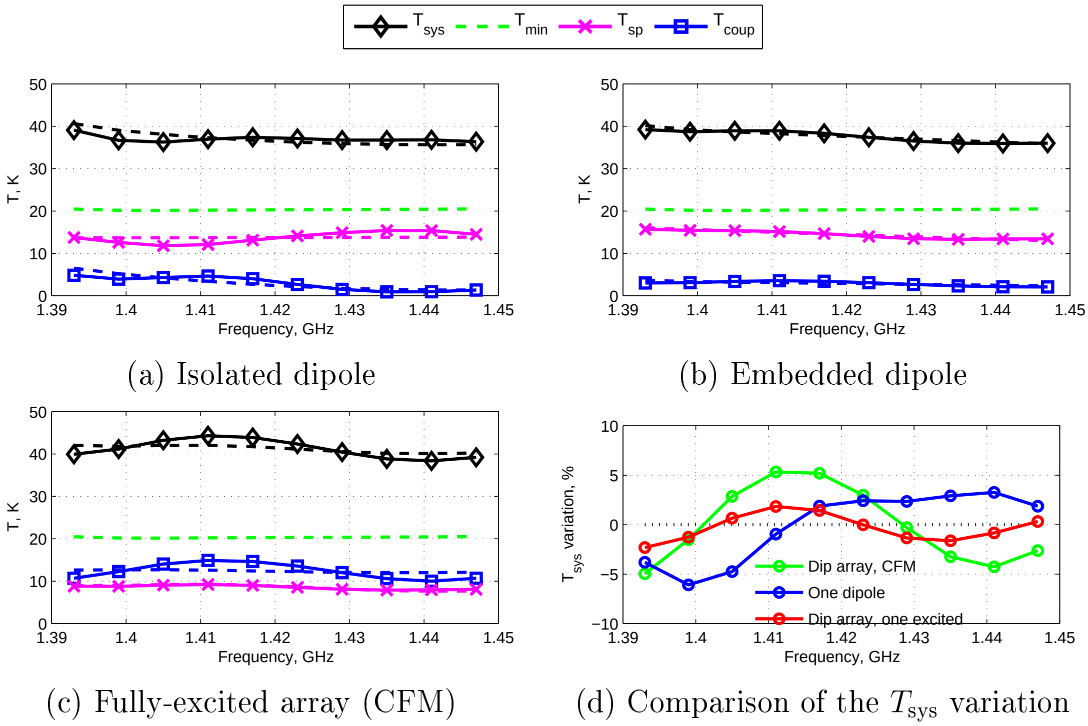

(a) Isolated dipole (b) Embedded dipole

(c) Fully-excited array (CFM) (d) Comparison of the T_{sys} variation

Figure 5: System noise temperature and its dominant contributions.

when beamforming is performed, the input impedance of each antenna array element (scan impedance) will differ from its optimal noise-match impedance, and therefore becomes more sensitive to the feed-reflector coupling. This results to higher T_{coup} and a stronger frequency variation. Hence, and in contrast to the systems employing single antenna feeds, the noise temperature due to mismatch effects, T_{coup}, is the dominant contribution to T_{sys} in case of PAF systems.

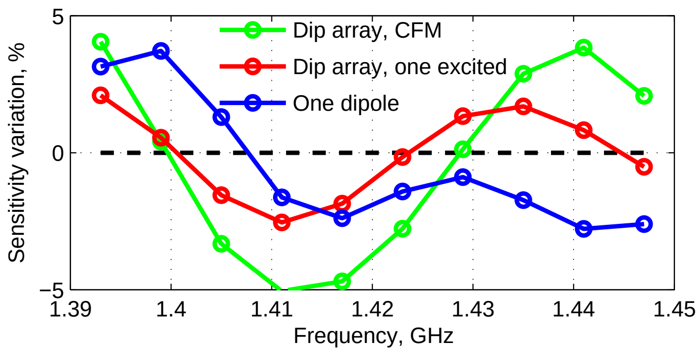

Figure 6: System sensitivity variation.

The sensitivity variation for all three cases is shown in Fig. 6. Although both η_{ap} and T_{sys} vary significantly for the system with a single dipole (i.e. -4% to

1.5%; and −5.5% to 3%, respectively), they partly compensate each other, leading to approximately the same sensitivity variation for all three feeding schemes.

4 Conclusions

The electromagnetic coupling between the reflector antenna and a single dipole feed was found to have a significant effect on the antenna beam shape and aperture efficiency, as opposed to the dipole PAFs. Our study indicates that the finite ground plane behind the single dipole, which is part of the feed supporting structure and often much larger than one antenna element, but comparable to the size of a PAF, is a reason for this difference. However, the (active) impedance matching of the strongly-coupled PAF elements appears to be more sensitive to the feed-reflector interaction, which has an impact on the receiver noise temperature. Similar conclusions were drawn from the numerical analysis of the checkerboard PAF of patch antennas [4], whereas these effects were found to be much smaller for the larger experimentally characterized array of 121 tapered-slot antenna elements [6]. The latter difference will be examined in more detail in future studies.

References

[1] N.-T. Huang, R. Mittra, M. Ivashina, and R. Maaskant, "Numerical study of a dual-polarized focal plane array (FPA) with vivaldi elements in the vicinity of a large feed box using the parallelized FDTD code GEMS," in *Proc. IEEE AP-S International Symposium*, Charleston, South Carolina, Jun. 2009, pp. 1–4.

[2] C. Craeye, "Analysis of complex phased array feeds and their interaction with a cylindrical reflector," in *Proc. IEEE AP-S International Symposium*, San Diego, California, Jul. 2008, pp. 1–4.

[3] M. A. Apeldoorn, "Characterizing reflector-feed interaction for parabolic reflector antennas," Master's thesis, International Research Centre for Telecommunications and Radar (IRCTR), Delft University of Technology, Delft, The Netherlands, 2011. [Online]. Available: http://repository.tudelft.nl/assets/uuid:d6605869-37e0-49a6-8bc4-817855ab3710/MSc-Thesis-MAApeldoorn.pdf

[4] S. Hay, R. Mittra, and N. Huang. (2010) Analysis of reflector and feed scattering and coupling effects on the sensitivity of phased array feeds. [Online]. Available: http://csas.ee.byu.edu/docs/Workshop/BYUSGH.pdf

[5] M. Ivashina. (2008) Dutch FPA progress – characterization of efficiency, system noise temperature and sensitivity of focal plane arrays. [Online]. Available: http://ska2008.ivec.org/www/Marianna_Ivashina.pdf

[6] W. A. van Cappellen and L. Bakker. (2010) Eliminating sensitivity ripples in prime focus reflectors with low-scattering phased array feeds. [Online]. Available: http://csas.ee.byu.edu/docs/Workshop/BYU_StandingWaves_Cappellen.pdf

[7] S. N. Makarov, *Antenna and EM Modeling With MATLAB.* New York: John Wiley and Sons, Inc., 2002.

[8] M. V. Ivashina, R. Maaskant, and B. Woestenburg, "Equivalent system representation to model the beam sensitivity of receiving antenna arrays," *IEEE Antennas Wireless Propag. Lett.*, vol. 7, no. 1, pp. 733–737, Jan. 2008.

Paper B

A Plane Wave Approximation In The Computation Of Multiscattering Effects In Reflector Systems

O. A. Iupikov, R. Maaskant, and M. Ivashina

in *Proceedings of the 7th European Conference on Antennas and Propagation, EUCAP 2013,* Gothenburg, Sweden, April 2013.

The layout of this paper has been revised in order to comply with the rest of the thesis.

A Plane Wave Approximation In The Computation Of Multiscattering Effects In Reflector Systems

O. A. Iupikov, R. Maaskant, and M. Ivashina

Abstract

A hybrid MoM/PO method for the analysis of multiple scattering effects between reflector and large feeds, such as dense multibeam phased array feeds or multifrequency front-ends (MFFEs) in which higher frequency feeds operate in the vicinity of an extended metal structure, has been presented and studied. This paper evaluates the accuracy and computational efficiency for the MoM/PO method with and without using a uniform plane wave approximation of the reflector scattered field.

1 Introduction

Prime-focus reflector antennas are widely used for radio astronomy, satellite and radio link communication thanks to their relatively low cost as compared to that of more complex offset- and multi-reflector systems. When designing these antennas, one focuses on the optimization of the antenna feed to realize high gain, low sidelobes, and low spillover loss for the selected reflector, often under stringent dimensional constraints to minimize the aperture blockage and frequency variation of the antenna characteristics due to multiple scattering effects of electromagnetic waves traveling between the feed and reflector antenna.

During the last decades, a number of analytic and numerical techniques have been developed to model feed-reflector interaction effects. For example, in [1] the scattered field of the feed is approximated by a geometric series of fields scattered by the antenna feed due to an incident plane wave at each iteration, where the amplitudes of these plane waves are expressed analytically for a given reflector geometry. This method is very fast and, for the case of a horn feed with an aperture diameter in the order of one wavelength, has been demonstrated to have an accuracy comparable to that of a MoM approach. An alternative to this method is the use of more rigorous (though more time-consuming) hybrid numerical methods combining Physical Optics or Gaussian beams for the analysis of reflectors with the Method of Moments and/or Mode Matching techniques for radiating horns feeds [2, 3]. The recent article [4] has introduced the PO/Generalized-Scattering-Matrix approach for solving multiple domain problems, and has shown its application to a cluster of a few horns. This approach is generic and accurate, but requires the filling of a large scattering matrix that can be time consuming especially for more complex feed systems, such as (i) multifrequency front-ends (MFFEs) in which higher frequency feeds operate in the vicinity of an extended metal structure, or (ii) dense multibeam phased array feeds (PAFs [5, 6]). On the other hand, the above-mentioned analytic method may be inaccurate for these systems, due to a much larger physical area and higher complexity of radiation/scattering mechanisms (the plane wave approximation may not hold). To examine this multiple domain problem with MFFEs and PAFs, we propose to use a hybrid MoM/PO approach as described in [7]. While in [7] the field is computed at each mesh cell of the feed and reflector structure, herein we investigate the approximation of the field scattered by the reflector with a (single) uniform plane wave defined over the area of the feed. As will be shown in this paper, the scattered field computed through integration of the reflector PO currents needs to be known only at a few points in the focal plane region in order to determine the plane wave expansion coefficient in an accurate manner. This significantly reduces the simulation time relative to a direct MoM/PO solution.

2 Modeling procedure and numerical results

The MoM/PO method [7] consists of the following steps: (i) the antenna feed currents are computed through a method-of-moments (MoM) approach by exciting the antenna port(s) in the absence of the reflector; (ii) these currents generate an EM field which induces PO-currents on the reflector surface; (iii) the PO currents create a scattered field that, in turn, induces currents on the feed structure. The steps (ii) and (iii) are repeated until the sum of the multiply induced currents – which forms the total current – has converged (typically, for low-scattering feeds, 2-3 iterations are enough to achieve an error less than 1% relative to a MoM solution). Afterwards, we can determine the antenna radiation pattern, the input impedance (matrix), and derived antenna parameters affecting the receiving sensitivity.

The third step of this procedure is the most time-consuming since it requires the field computation (integrating of PO currents) at each mesh cell of the feed. To alleviate this computational burden, the field scattered from the reflector can be expanded into a plane wave spectrum, each spectral component of which induces a current on the feed. This approach is much faster since it does not require the integration of the reflector currents at each basis function of the feed; the smoothly-varying field has to be tested at a few points only to find the expansion coefficients of the corresponding plane wave modes. The incident field on the feed is then tested through these plane wave modes.

The model $\mathbf{E}^{\text{mod}}$ of the actual focal field $\mathbf{E}^{\text{ref}}$ of the reflector antenna, due to a radiating PO current on the reflector, can be expanded into a set of plane wave modes

$\{\mathbf{E}_n\}$ as

$$\mathbf{E}^{\text{mod}} = \sum_{n=1}^{N} \alpha_n \mathbf{E}_n. \tag{1}$$

The least squares error ϵ between the actual field $\mathbf{E}^{\text{ref}}$ and the modeled field (1) can be expressed as

$$\epsilon(\boldsymbol{\alpha}) = \langle \mathbf{E}^{\text{ref}} - \mathbf{E}^{\text{mod}}(\boldsymbol{\alpha}), \mathbf{E}^{\text{ref}} - \mathbf{E}^{\text{mod}}(\boldsymbol{\alpha}) \rangle \tag{2}$$

where

$$\langle \mathbf{a}, \mathbf{b} \rangle = \iint_{S_a} \mathbf{a}^H \mathbf{b} \, \mathrm{d}S; \tag{3}$$

$(\ldots)^H$ is the Hermitian operator; and S_a is the area constituting the support of the vector function $\mathbf{a}$.

It can be shown that, the solution that minimizes ϵ is obtained through solving the matrix expression

$$\mathbf{A}\boldsymbol{\alpha} = \mathbf{b} \tag{4}$$

where $\boldsymbol{\alpha} = [\alpha_1, \alpha_2, \ldots, \alpha_N]^T$;

$$\mathbf{A}_{mn} = \langle \mathbf{E}_m, \mathbf{E}_n \rangle \quad \text{and} \quad \mathbf{b}_m = \langle \mathbf{E}_m, \mathbf{E}^{\text{ref}} \rangle \tag{5}$$

for $m, n = 1, 2, ..., N$.

Since the scattered field from large parabolic reflectors resembles a plane wave in the vicinity of the antenna feed, it is sufficient to employ only a single plane wave expansion function [1]. Hence, we can solve Eq. (4) analytically for the coefficient α_1:

$$\alpha_1 = \frac{\langle \mathbf{E}_1, \mathbf{E}^{\text{ref}} \rangle}{\langle \mathbf{E}_1, \mathbf{E}_1 \rangle}. \tag{6}$$

If we choose the plane wave expansion function to have unit amplitude, the coefficient α_1 will be equal to

$$\alpha_1 = \frac{1}{A_{\text{f}}} \iint_{A_{\text{f}}} E_p^{\text{ref}} \, \mathrm{d}S \tag{7}$$

where the subscript p denotes the dominant component of the field $\mathbf{E}^{\text{ref}}$; A_{f} is the area in the focal plane occupied by the feed. Eq. (7) can be evaluated numerically using the midpoint integration rule, i.e.,

$$\alpha_1 \approx \frac{1}{K} \sum_{k=1}^{K} E_p^{\text{ref}}(\mathbf{r}_k), \tag{8}$$

where the set $\{\mathbf{r}_k\}_{k=1}^K$ are K sample points, which are assumed to be located on a uniform grid.

In summary, the plane-wave-enhanced MoM/PO method consists of the following steps: (i) the antenna feed currents are computed through a method-of-moments (MoM) approach by exciting the antenna port(s) in the absence of the reflector; (ii) these currents generate an EM field which induces PO-currents on the reflector surface; (iii) the PO currents create a scattered field that is tested at only a few points in the focal plane; (iv) the field intensity at the sample points is averaged in accordence with (8), and the obtained value is used as the expansion coefficient for the plane wave traveling from the reflector towards the feed; (v) this incident plane wave induces a new current distribution on the feed structure. The steps (ii)–(v) are repeated until a convergence condition is met.

The following three types of feeds were used to illuminate a reflector antenna: (i) a pyramidal horn with aperture diameter in the order of one wavelength, (ii) a pyramidal horn with extended ground plane, and (iii) an 121-element dual-polarized dipole array [see Fig. 1(a)]. All antennas are impedance power-matched, so that antenna component [8] of their corresponding radar cross-section (RCS) is minimized. However, the residual component of the RCS of the horn with ground plane is still high due to the extended metal structure surrounding it, so that this feed is a high scattering antenna and strong feed-reflector coupling can be expected.

The corresponding E- and H-plane focal field distribution cuts at the 1st and 2nd iterations are shown in Figs. 2(b) and (c), respectively, each for the reflector antenna with the semi-subtended angle of 70 deg and a respective diameter of 38λ and 118λ. This result clearly demonstrates that the field scattered by the reflector differs slightly from a uniform plane wave, where the largest variation in amplitude is about 0.8–1.5 dB (and 4–6 degrees in phase) over the area occupied by the feed (the vertical dashed line). The ripples in the focal plane field at the 1st iteration are due to diffraction effects from the reflector edges when it is illuminated by the primary feed pattern and, as expected, are more pronounced for the electrically smaller reflector, regardless of the type of the feed. It is also observed that, at the 2nd iteration, when the scattered field component of the feed is incident on the reflector, the focal field distribution due to the horn feed remains rather uniform, but becomes more tapered for the case of the electrically larger feeds (the PAF and horn with the extended ground plane) because of the much narrower scattered patterns of these feeds [see Fig. 1(b)]. Thus, larger errors due to the plane wave approximation can be expected for these feed structures. Another important observation is that the shapes of the scattered patterns and the corresponding focal fields at the 2nd iteration are rather similar in case of the PAF and horn with the extended ground plane, as the result of the equal aperture areas. This similarity, however, does not imply that modeling errors due to the plane wave approximation will be close as well. This can be readily seen from Table 1, where the errors in the total focal field and several antenna characteristics such as the gain, the gain at -3 dB level, and the antenna input impedance (in case of an array – the input impedance of the most excited antenna element) are summarized.

The errors in focal field and scalars antenna characteristics are computed as

$$\epsilon_1 = \frac{\sqrt{\sum_k |E^{\text{ref}}_{p;k} - E^{\text{mod}}_{p;k}|^2}}{\sqrt{\sum_k |E^{\text{ref}}_{p;k}|^2}} \times 100\% \tag{9}$$

$$\epsilon_2 = \frac{|f^{\text{ref}} - f^{\text{mod}}|}{|f^{\text{ref}}|} \times 100\%, \tag{10}$$

where $E^{\text{ref}}_{p;k}$ and $E^{\text{mod}}_{p;k}$ are the k-th sample of the discretized p-components of the focal E-field $\mathbf{E}^{\text{ref}}$ and $\mathbf{E}^{\text{mod}}$ respectively; f^{ref} and f^{mod} is the gain or antenna input impedance, reference and modeled values respectively. The MoM/PO results without the plane wave approximation are used as the reference solution.

Table 1: Errors due to a plane wave approximation

	Focal field		**Gain (on-axis)**		**Gain (@−3 dB)**		**Impedance**	
Reflector diameter D	38λ	118λ	38λ	118λ	38λ	118λ	38λ	118λ

Feed: Pyramidal horn

Parameter variation, %	3.91	1.23	1.98	0.62	3.99	2.16	15.05	4.66
Method:	**Error, %**							
Method 1	0.3	0.05	0.28	0.05	0.36	0.14	1.37	0.18
Method 2	0.1	0.04	0.16	0.04	0.3	0.13	0.09	0.03

Feed: Pyramidal horn with extended ground plane

Parameter variation, %	139.3	39.1	19.2	3.4	29.4	3.56	43.4	6.1
Method:	**Error, %**							
Method 1	37.7	1.29	12.7	0.1	10.1	0.17	18.5	0.2
Method 2	11.9	0.48	2.23	0.07	4.71	0.15	12.46	0.11

Feed: 121-element dual-polarized dipole array

Parameter variation, %	8.45	3.28	1.84	0.28	3.68	0.73	5.8	1.7
Method:	**Error, %**							
Method 1	0.61	0.11	0.21	0.03	0.15	0.02	0.34	0.08
Method 2	0.44	0.1	0.12	0.03	0.08	0.03	0.58	0.05

Table 2: Total simulation time

	Horn	**Horn with gnd plane**	**Dipole array**	**Vivaldi array**
MoM-PO, no approximations	9 min 05 sec (100%)	59 min 21 sec (100%)	71 min 09 sec (100%)	197 min 04 sec (100%)
Method 1	0 min 39 sec (7%)	1 min 12 sec (2%)	4 min 49 sec (7%)	33 min 58 sec (17%)
Method 2	2 min 32 sec (28%)	13 min 28 sec (23%)	19 min 19 sec (27%)	67 min 06 sec (34%)

The above values were also computed using the method described in [1], where the plane wave coefficient α_1 is computed analytically from the field intensity in the on-axis direction of both the original and the scattered feed pattern due to an incident plane wave. We will refer to this method as "Method 1" while the herein proposed approach is denoted as "Method 2".

The total simulation time (10 frequency points) for the 38λ reflector fed by the considered feeds is shown in table 2. Virtually all simulation time is consumed by the field computation on the reflector surface for obtaining its PO currents, while the computation of the currents on the feed due to the currents on the reflector is more than 1000 times faster when a plane wave approximation is used.

By analyzing Table 1 and Table 2 the following observations can be made:

- Method 1 is numerically efficient and accurate for small feeds (whose size is in the order of one wavelength) and for low-scattering feeds, but fails in case of large high-scattering feeds, such as MFFEs, because the focal field produced by the feed scattering pattern has a high level and a highly tapered shape;

- Method 2 provides a better prediction of all the system parameters, since it accounts for the actual shape of the scattered pattern when fitting the plane wave to it; however, it is slower than Method 1;

- Both methods are accurate in case of large reflectors because (i) the multiscattering effects are less pronounced (see "Parameter variation" in Table 1), and (ii) the field scattered from the reflector is close to a plane wave at all iterations.

3 Conclusions

A hybrid MoM/PO method for the analysis of multiple scattering effects between the reflector and large feeds, such as PAFs and MFFEs, has been presented and studied. It has been shown that, although the field scattered by the parabolic reflector differs slightly from that of a uniform plane wave, the plane wave approximation can be used to predict the main antenna parameters with an error less than a few percent relative

3. Conclusions

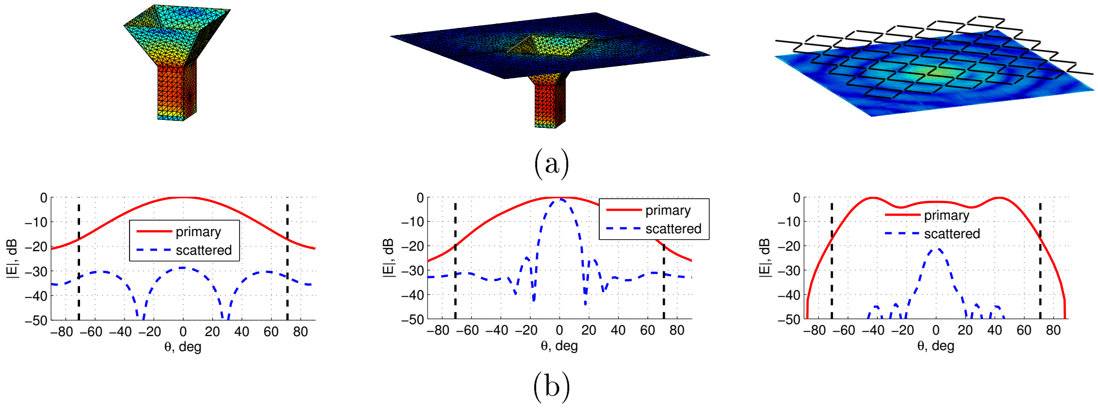

Figure 1: (a) EM models of the reflector antenna feeds, including (when viewing from left to right) the pyramidal horn feed (with the aperture diameter of one wavelength) without and with the extended ground plane and the phased array feed of 121 half wavelength dipole antenna elements; and (b) the corresponding primary field patterns of the feeds and their scattered field patterns due to the field incident from the reflector at the 1st iteration.

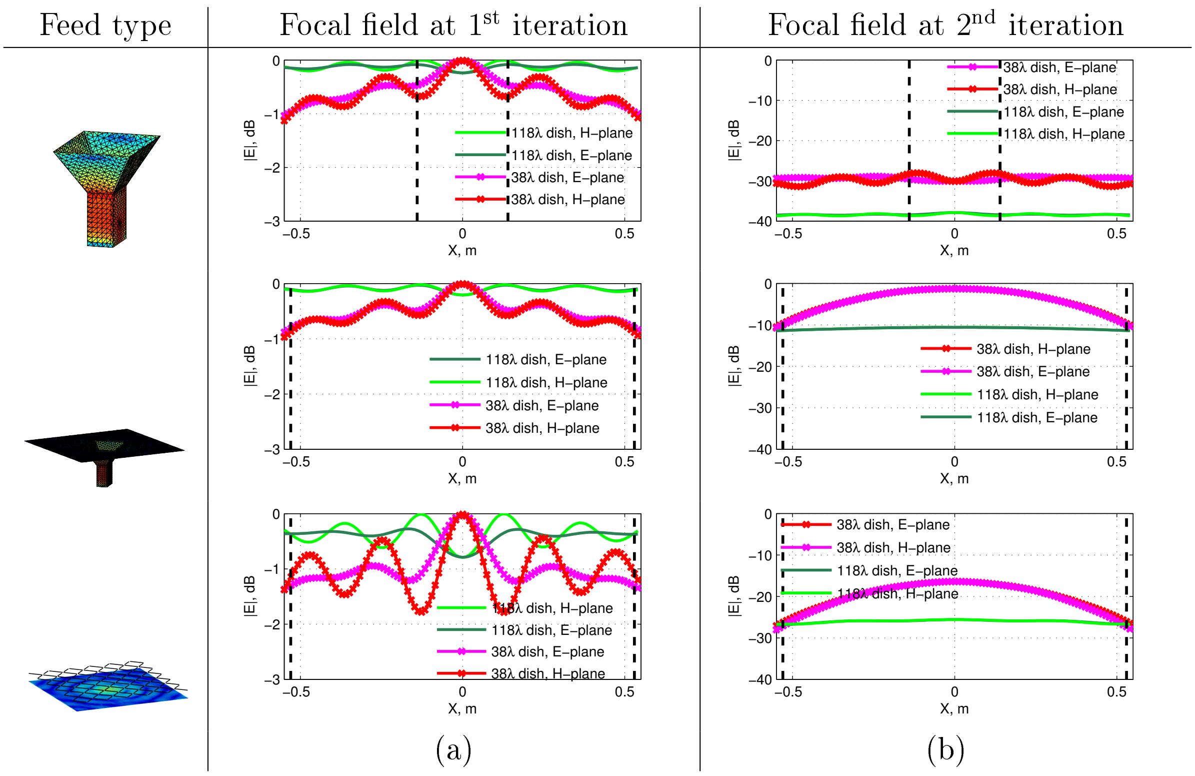

Figure 2: (a)-(b) The focal plane fields of the reflector antenna on transmit for the feeds shown in Fig. 1(a). The plots in Fig. 2(a) are for the fields computed at the 1st iteration, when the reflector is illuminated by the primary field of each of the considered feeds, and the results in Fig. 2(b) are for the fields obtained at the 2nd iteration, when the illumination source is the scattering field component of the feed due to the scattered field from the reflector at the 1st iteration.

to a direct MoM/PO approach, while reducing the computational time significantly. It has also been shown that, for electrically large high-scattering feeds (exceeding 2–3 λ in diameter), the plane wave approximation gives rise to an increased error, since the scattered field from a reflector at the 2nd iteration is tapered and has a large amplitude. In the latter a spectrum of plane waves can be considered, which is planned as future work. Among the antenna characteristics, the input impedance is found to be the most sensitive to errors.

References

[1] A. Moldsvor and P.-S. Kildal, "Systematic approach to control feed scattering and multiple reflections in symmetrical primary-fed reflector antennas," *IEEE Trans. Antennas Propag.*, vol. 139, no. 1, pp. 65–71, Sep. 1992.

[2] P. Bolli, G. Gentili, L. Lucci, R. Nesti, G. Pelosi, and G. Toso, "A hybrid perturbative technique to characterize the coupling between a corrugated horn and a reflector dish," *IEEE Trans. Antennas Propag.*, vol. 54, no. 2, pp. 595–603, Sep. 2006.

[3] M. Bandinelli, F. Milani, G. Guida, M. Bercigli, P. Frandsen, S. Sorensen, B. Bencivenga, and M. Sabbadini, "Feed-array design in presence of strong scattering from reflectors," in *Proc. European Conference on Antennas and Propag. (EuCAP)*, Rome, Italy, Apr. 2011, pp. 3844–3848.

[4] C. D. Giovampaola, E. Martini, A. Toccafondi, and S. Maci, "A hybrid PO/generalized-scattering-matrix approach for estimating the reflector induced mismatch," *IEEE Trans. Antennas Propag.*, vol. 60, no. 9, pp. 4316–4325, Sep. 2012.

[5] S. Hay, R. Mittra, and N. Huang. (2010) Analysis of reflector and feed scattering and coupling effects on the sensitivity of phased array feeds. [Online]. Available: http://csas.ee.byu.edu/docs/Workshop/BYUSGH.pdf

[6] M. V. Ivashina, O. Iupikov, R. Maaskant, W. A. van Cappellen, and T. Oosterloo, "An optimal beamforming strategy for wide-field surveys with phased-array-fed reflector antennas," *IEEE Trans. Antennas Propag.*, vol. 59, no. 6, pp. 1864–1875, Jun. 2011.

[7] O. Iupikov, R. Maaskant, and M. Ivashina, "Towards the understanding of the interaction effects between reflector antennas and phased array feeds," in *Proc. Int. Conf. on Electromagn. in Adv. Applicat. (ICEAA)*, Cape Town, Sep. 2012, pp. 792–795.

[8] B. A. Munk, *Finite Antenna Arrays and FSS.* Danvers, Massachusetts: John Wiley & Sons, Inc., 2003.

Paper C

Fast and Accurate Analysis of Reflector Antennas with Phased Array Feeds including Multiple Reflections between Feed and Reflector

O. A. Iupikov, R. Maaskant, M. Ivashina, A. Young, and P.S. Kildal

IEEE Transactions on Antennas and Propagation, vol.62, no.7, 2014

The layout of this paper has been revised in order to comply with the rest of the thesis.

Fast and Accurate Analysis of Reflector Antennas with Phased Array Feeds including Multiple Reflections between Feed and Reflector

O. A. Iupikov, R. Maaskant, M. Ivashina, A. Young, and P.S. Kildal

Abstract

Several electrically large Phased Array Feed (PAF) reflector systems are modeled to examine the mechanism of multiple reflections between parabolic reflectors and low- and high-scattering feeds giving rise to frequency-dependent patterns and impedance ripples. The PAF current is expanded in physics-based macro domain basis functions (CBFs), while the reflector employs the Physical Optics (PO) equivalent current. The reflector-feed coupling is systematically accounted for through a multiscattering Jacobi approach. An FFT expands the reflector radiated field in only a few plane waves, and the reflector PO current is computed rapidly through a near-field interpolation technique. The FEKO software is used for several cross validations, and the convergence properties of the hybrid method are studied for several representative examples showing excellent numerical performance. The measured and simulated results for a 121-element Vivaldi PAF, which is installed on the Westerbork Synthesis Radio Telescope, are in very good agreement.

1 Introduction

Focal plane arrays can be used to form multiple reflector beams covering a wide field-of-view (FoV) and large bandwidth. Among these feeds, one can distinguish between a cluster of horns yielding one beam per feed [1, 2], and the more densely packed beamforming array antennas commonly referred to as Phased Array Feeds (PAFs) capable of providing a continuous FoV of simultaneous beams. Examples that benefit from these technologies are radars and terrestrial communications; while since recently, PAFs have also been developed for astronomical and geoscientific instruments, as well as for commercial satellite communication terminals [3–6]. Thanks to their electronic beamforming capabilities, these new systems potentially enable much faster studies of the Earth and Space than currently possible and are an attractive alternative to bulky mechanically beam steered antennas.

The characterization of feeds in unblocked reflectors and on-axis beams can be handled by the traditional spillover, illumination, polarization and phase subefficiency factors defined for rotationally symmetric reflectors in [7], and be extended to

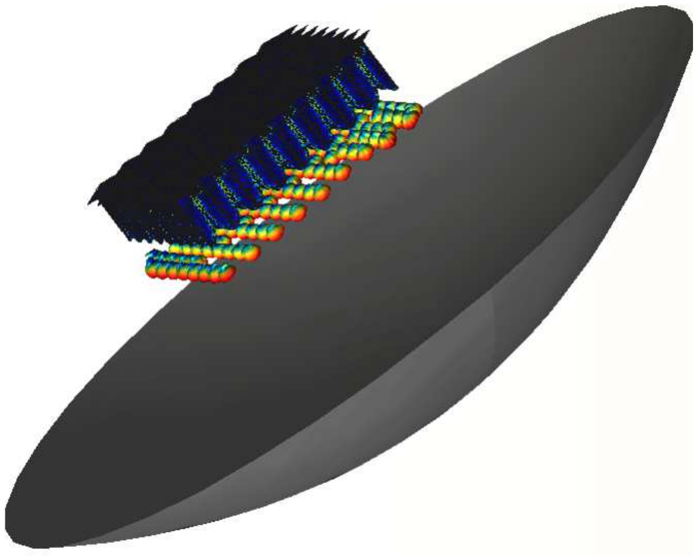

Figure 1: Reflector antenna and a Phased Array Feed (PAF) system.

include excitation-dependent decoupling efficiencies of PAFs [8,9]. The present paper investigates the effects of aperture blockage and multiple reflections on the system performance in a more generic fashion than in [10] and [11] for rotationally symmetric antennas.

An accurate analysis of these PAF systems, which include an array of many closely-spaced antenna elements and an electrically large reflector (see e.g. Fig. 1), requires a modeling approach for the entire feed-reflector structure accounting for the array mutual coupling and the multiple scattering effects between the reflector and the feed, whose aperture diameter can be in the order of several wavelengths for multi-beam applications [12, 13]. These effects give rise to a ripple in the antenna impedance and radiation characteristics over frequency leading to impedance mismatch effects and a periodically perturbed beam shape [14–18]. The level of these variations depends on several factors related to the reflector geometry and feed design, among which the blockage area of the reflector aperture caused by the feed, the antenna array scattering characteristics [19, Sec. 2.2], the weighting coefficients of the beamforming network, and the presence of the (metal) structure in the vicinity of the feed [20]. In order to solve these challenging problems, a method is needed that is fast and physically-insightful for understanding how the EM coupling mechanism between the PAF and reflector antenna impacts the overall system performance.

During the last decades, a number of analytical and numerical techniques have been developed to model feed-reflector interaction effects. For example, in [10] the multiscattered field is approximated by a geometric series of on-axis plane wave (PW) field scattered by the antenna feed due to an incident PW at each iteration, where the amplitudes of these PWs are expressed analytically for a given reflector geometry. This method is very fast and insightful, while MoM-level accuracy can be achieved for single-horn feeds, but not for array feeds as demonstrated in this paper. An alternative approach is to use more versatile, though more time-consuming, hybrid numerical methods combining Physical Optics or Gaussian beams for the analysis of reflectors with MoM and/or Mode Matching techniques for horn feeds [21, 22]. The recent article [23] has introduced the PO/Generalized-Scattering-Matrix approach for solving multiple domain problems, and has shown its application to a cluster of a few horns. This approach is generic and accurate, but may require the filling of a large scattering matrix for electrically large PAFs and/or multifrequency front-ends (MFFEs) that often have an extended metal structure [17]. Other hybrid methods, which are not specific for solving the present type of problems, make use of field transformations, field operators, multilevel fast multipole approaches (MLFMA), and matrix modifications [24–27].

Recently, a Krylov subspace iterative method has been combined with an MBF-PO approach for solving feed-reflector problems [28], and complementary to this, an iteration-free CBFM-PO approach has been presented by Hay, where a modified reduced MoM matrix for the array feed is constructed by directly accounting for the reflector [16].

Among the above methods, the iterative methods have shown to be most useful for gaining insight in the feed-reflector multiscattering effects. In the present paper, we therefore employ the Jacobi iterative approach as a simplified version of the full orthogonalization method (FOM [28]), and combine it with an CBFM-PO approach enhanced by field expansion (see also [18]) and interpolation techniques. The method is shown to converge within a few iterations.

The paper is arranged as follows: first, the numerical approach is formulated and then validated through a few representative examples, after which the field expansion and interpolation techniques are described along with a numerical accuracy and efficiency assessment; second, the performance and the multiscattering mechanism between electrically large reflector antennas and several fundamentally different types of feeds, including single-pixel horn feeds as in practical MFFEs, and 121-element PAFs of dipoles and tapered slot Vivaldi antennas are studied for different port termination schemes. The predicted system sensitivity is in very good agreement with the measurements of a single horn and Vivaldi PAF system feeding one of the 25-m Westerbork Synthesis Radio Telescope reflector antennas [29].

2 Iterative CBFM-PO Formulation

The below proposed iterative CBFM-PO approach is based upon the Jacobi method for solving a system of linear equations in an iterative manner [30, 31].

Suppose the Method of Moments (MoM) matrix equation of the entire antenna system comprised of both the parabolic reflector and the antenna feed is given by

$$\mathbf{ZI} = \mathbf{V}, \tag{1}$$

where the elements of the $K \times K$ MoM matrix $\mathbf{Z}$ and $K \times 1$ excitation vector $\mathbf{V}$ are computed as

$$Z_{pq} = \langle \boldsymbol{f}_p, \boldsymbol{E}^{\mathrm{s}}(\boldsymbol{f}_q)\rangle, \qquad\qquad V_p = -\langle \boldsymbol{f}_p, \boldsymbol{E}^{\mathrm{i}}\rangle \tag{2}$$

for $p, q = 1, 2, \ldots K$. Furthermore, $\boldsymbol{f}_{p,q}$ are the K basis/test functions for the current/field (Galerkin method); $\boldsymbol{E}^{\mathrm{i,s}}$ is the incident/scattered electric field, and $\langle \boldsymbol{a}, \boldsymbol{b}\rangle = \iint_{S_a \cap S_b} [\boldsymbol{a} \cdot \boldsymbol{b}]\, \mathrm{d}S$ is the symmetric product, where S_a and S_b are the supports of the vector functions $\boldsymbol{a}$ and $\boldsymbol{b}$, respectively. The expansion coefficient vector is given by $\mathbf{I} = [I_1, \ldots I_K]^T$, where T denotes the transposition operator.

To allow for a multiscattering analysis between the feed and reflector, the MoM matrix equation in (1) is first partitioned into matrix blocks as

$$\begin{bmatrix} \mathbf{Z}^{\mathrm{rr}} & \mathbf{Z}^{\mathrm{rf}} \\ \mathbf{Z}^{\mathrm{fr}} & \mathbf{Z}^{\mathrm{ff}} \end{bmatrix} \begin{bmatrix} \mathbf{I}^{\mathrm{r}} \\ \mathbf{I}^{\mathrm{f}} \end{bmatrix} = \begin{bmatrix} \mathbf{V}^{\mathrm{r}} \\ \mathbf{V}^{\mathrm{f}} \end{bmatrix} \tag{3}$$

where $\mathbf{Z}^{\mathrm{rr}}$ and $\mathbf{Z}^{\mathrm{ff}}$ are the MoM matrix self-blocks of the reflector and feed, respectively[1], and $\mathbf{V}^{\mathrm{r}}$ and $\mathbf{V}^{\mathrm{f}}$ are the corresponding excitation vectors. The matrix $\mathbf{Z}^{\mathrm{rf}} = (\mathbf{Z}^{\mathrm{fr}})^T$ contains the mutual reactions involving the basis functions on the feed and reflector. The unknown current expansion coefficient vectors are denoted by $\mathbf{I}^{\mathrm{r}}$ and $\mathbf{I}^{\mathrm{f}}$. Next, Eq. (3) is written as

$$\left(\begin{bmatrix} \mathbf{Z}^{\mathrm{rr}} & \mathbf{0} \\ \mathbf{0} & \mathbf{Z}^{\mathrm{ff}} \end{bmatrix} + \begin{bmatrix} \mathbf{0} & \mathbf{Z}^{\mathrm{rf}} \\ \mathbf{Z}^{\mathrm{fr}} & \mathbf{0} \end{bmatrix} \right) \begin{bmatrix} \mathbf{I}^{\mathrm{r}} \\ \mathbf{I}^{\mathrm{f}} \end{bmatrix} = \begin{bmatrix} \mathbf{V}^{\mathrm{r}} \\ \mathbf{V}^{\mathrm{f}} \end{bmatrix}. \tag{4}$$

Upon multiplying both sides by $[\mathbf{Z}^{\mathrm{rr}}, \mathbf{0}; \mathbf{0}, \mathbf{Z}^{\mathrm{ff}}]^{-1}$, the final solution for the combined problem can be obtained as

$$\begin{bmatrix} \mathbf{I}^{\mathrm{r}} \\ \mathbf{I}^{\mathrm{f}} \end{bmatrix} = \left(\begin{bmatrix} \mathbf{1} & \mathbf{0} \\ \mathbf{0} & \mathbf{1} \end{bmatrix} + \begin{bmatrix} \mathbf{Z}^{\mathrm{rr}} & \mathbf{0} \\ \mathbf{0} & \mathbf{Z}^{\mathrm{ff}} \end{bmatrix}^{-1} \begin{bmatrix} \mathbf{0} & \mathbf{Z}^{\mathrm{rf}} \\ \mathbf{Z}^{\mathrm{fr}} & \mathbf{0} \end{bmatrix} \right)^{-1} \begin{bmatrix} \mathbf{I}_0^{\mathrm{r}} \\ \mathbf{I}_0^{\mathrm{f}} \end{bmatrix}. \tag{5}$$

where $\mathbf{1}$ is the identity matrix, and where the initial expansion coefficient vector for the reflector current $\mathbf{I}_0^{\mathrm{r}} = (\mathbf{Z}^{\mathrm{rr}})^{-1}\mathbf{V}^{\mathrm{r}}$, while for the feed current $\mathbf{I}_0^{\mathrm{f}} = (\mathbf{Z}^{\mathrm{ff}})^{-1}\mathbf{V}^{\mathrm{f}}$. These initial currents are obtained by solving the reflector and antenna feed problems in isolation. It is observed that Eq. (5) is of the form

$$\mathbf{I} = \left(\mathbf{1} + (\mathbf{Z}^{\mathrm{d}})^{-1}\mathbf{Z}^{\mathrm{o}}\right)^{-1}\mathbf{I}_0 \tag{6}$$

[1]Here $\mathbf{Z}^{\mathrm{ff}}$ includes the effect of the antenna port terminations [32].

where

$$\mathbf{Z}^{\mathrm{d}} = \begin{bmatrix} \mathbf{Z}^{\mathrm{rr}} & \mathbf{0} \\ \mathbf{0} & \mathbf{Z}^{\mathrm{ff}} \end{bmatrix} \quad \text{and} \quad \mathbf{Z}^{\mathrm{o}} = \begin{bmatrix} \mathbf{0} & \mathbf{Z}^{\mathrm{rf}} \\ \mathbf{Z}^{\mathrm{fr}} & \mathbf{0} \end{bmatrix}. \tag{7}$$

Upon using the matrix equivalent of the scalar infinite geometric series $\sum_{n=0}^{\infty} r^n = (1-r)^{-1}$, where $|r| < 1$ for the series to converge, Eq. (6) can be rewritten in terms of the infinite series

$$\mathbf{I} = \sum_{n=0}^{\infty} \left(-(\mathbf{Z}^{\mathrm{d}})^{-1}\mathbf{Z}^{\mathrm{o}}\right)^n \mathbf{I}_0 \tag{8}$$

where the spectral radius $\rho((\mathbf{Z}^{\mathrm{d}})^{-1}\mathbf{Z}^{\mathrm{o}}) \stackrel{\mathrm{def}}{=} \max_i(|\lambda_i|)$ of the matrix $(\mathbf{Z}^{\mathrm{d}})^{-1}\mathbf{Z}^{\mathrm{o}}$ with eigenvalues $\{\lambda_i\}$ must be smaller than unity for the series to converge. The physical multiscattering interpretation of the geometric series in (8) is apparent when expanding it as:

$$\mathbf{I} = \mathbf{I}_0 - (\mathbf{Z}^{\mathrm{d}})^{-1}\mathbf{Z}^{\mathrm{o}}\mathbf{I}_0 + \left((\mathbf{Z}^{\mathrm{d}})^{-1}\mathbf{Z}^{\mathrm{o}}\right)^2\mathbf{I}_0 + \ldots = \sum_{n=0}^{\infty} \mathbf{I}_n \tag{9}$$

where the last summation is supposed to add up successively smaller contributions for the currents on the reflector and antenna feed in order to converge. It is conjectured that $\rho((\mathbf{Z}^{\mathrm{d}})^{-1}\mathbf{Z}^{\mathrm{o}}) \ll 1$ for the practical reflector antenna systems that we consider, since most of the energy is radiated out after each iteration and where the feeds have relatively small aperture areas (weak reflector-feed coupling), so that the sum converges within a few iterations (*cf.* Sec. 4.1 and 4.3). Finally, using (7), the infinite series summation in Eq. (9) can be written in the cross-coupled recursive scheme

Reflector	Feed
$\mathbf{I}^{\mathrm{r}} = \sum_{n=0}^{\infty} \mathbf{I}^{\mathrm{r}}_n$ (10a)	$\mathbf{I}^{\mathrm{f}} = \sum_{n=0}^{\infty} \mathbf{I}^{\mathrm{f}}_n$ (11a)
$\mathbf{I}^{\mathrm{r}}_{n+1} = -(\mathbf{Z}^{\mathrm{rr}})^{-1}\mathbf{Z}^{\mathrm{rf}}\mathbf{I}^{\mathrm{f}}_n$ (10b)	$\mathbf{I}^{\mathrm{f}}_{n+1} = -(\mathbf{Z}^{\mathrm{ff}})^{-1}\mathbf{Z}^{\mathrm{fr}}\mathbf{I}^{\mathrm{r}}_n$ (11b)
$\mathbf{I}^{\mathrm{r}}_0 = (\mathbf{Z}^{\mathrm{rr}})^{-1}\mathbf{V}^{\mathrm{r}}_0$ (10c)	$\mathbf{I}^{\mathrm{f}}_0 = (\mathbf{Z}^{\mathrm{ff}})^{-1}\mathbf{V}^{\mathrm{f}}_0$ (11c)

where $\mathbf{V}^{\mathrm{r}}_0 = \mathbf{V}^{\mathrm{r}}$ and $\mathbf{V}^{\mathrm{f}}_0 = \mathbf{V}^{\mathrm{f}}$ are the initial excitation voltage vectors of the reflector and the feed, respectively (in transmit situation $\mathbf{V}^{\mathrm{r}}_0 = \mathbf{0}$).

The cross-coupled recursive scheme as formulated by Eqs. (10) and (11) is exemplified in Fig. 2 as a five-step procedure, in which the problem is first solved in isolation to obtain $\mathbf{I}^{\mathrm{r}}_0$ and $\mathbf{I}^{\mathrm{f}}_0$. Afterwards, the feed current $\mathbf{I}^{\mathrm{f}}_0$ is used to induce the reflector current $\mathbf{I}^{\mathrm{r}}_1$, which is then added up to the initial reflector current. Likewise, the initial reflector current $\mathbf{I}^{\mathrm{r}}_0$ is used to induce the feed current $\mathbf{I}^{\mathrm{f}}_1$, which is then

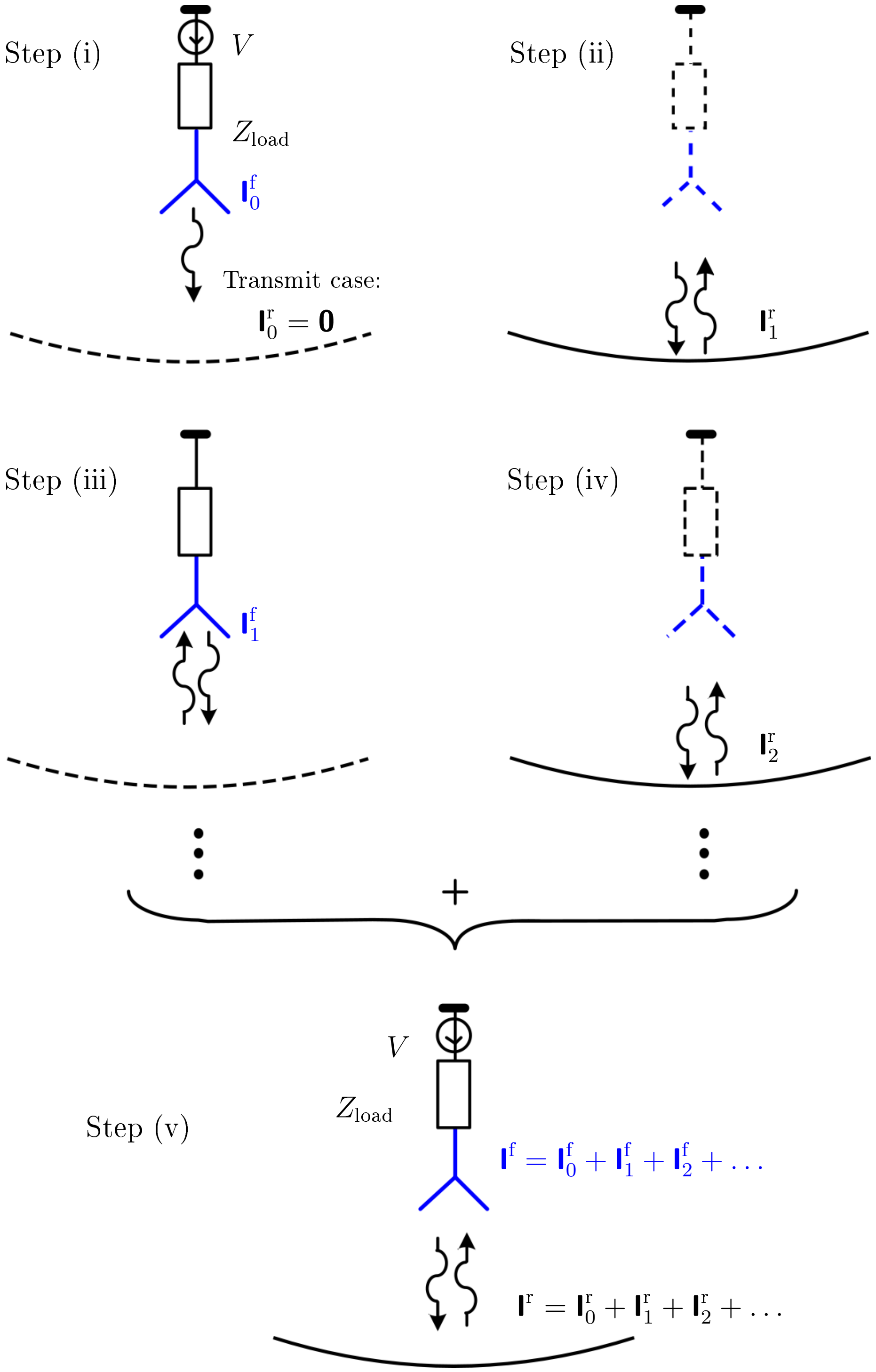

Figure 2: Illustration of the cross-coupled iterative scheme for multiscattering analysis of the feed-reflector interaction effects, as formulated by Eqs. (10) and (11): (i) The antenna feed radiates in the absence of reflector; (ii) the radiated field from feed scatters from the reflector; (iii) the scattered reflector field is incident on the terminated feed and re-scatters; (iv) the re-scattered field from the feed is incident on the reflector; etc. (v) the final solution for the current is the sum of the induced currents.

added to the initial feed current, and so forth. It is pointed out that this recursive scheme can be used for any pair of radiating and/or scattering objects, provided that the system is weakly coupled – due to radiation and/or dissipation losses – in order to obtain a convergent solution.

Rather than computing the reflector and feed currents through the large-size MoM matrix blocks $\mathbf{Z}^{\mathrm{rr}}$, $\mathbf{Z}^{\mathrm{rf}}$, $\mathbf{Z}^{\mathrm{fr}}$, and $\mathbf{Z}^{\mathrm{ff}}$, additional computational and memory efficient techniques can be used for the rapid computation of these currents at each iteration; we propose to employ the Physical Optics (PO) current on the reflector and invoke the Characteristic Basis Function Method (CBFM, [33]) as a MoM enhancement technique for computing the current on the feed.

Note that (11b) represents the MoM matrix solution $\mathbf{I}^{\mathrm{f}}_{n+1} = (\mathbf{Z}^{\mathrm{ff}})^{-1}\mathbf{V}^{\mathrm{f}}_{n}$, where $\mathbf{V}^{\mathrm{f}}_{n} = -\mathbf{Z}^{\mathrm{fr}}\mathbf{I}^{\mathrm{r}}_{n}$ is the voltage excitation vector of the feed at iteration n. Hence, one can obviate the construction of the large matrix $\mathbf{Z}^{\mathrm{fr}}$ by directly computing $\mathbf{V}^{\mathrm{f}}_{n}$. This is done through testing the incident electric field $\boldsymbol{E}^{\mathrm{i,f}}_{n}(\boldsymbol{r})$ by the P basis functions $\{\boldsymbol{f}^{\mathrm{f}}_{p}\}_{p=1}^{P}$ supported by the feed, i.e.,

$$\mathbf{I}^{\mathrm{f}}_{n+1} = -\left(\mathbf{Z}^{\mathrm{ff}}\right)^{-1}\left[\langle \boldsymbol{E}^{\mathrm{i,f}}_{n}, \boldsymbol{f}^{\mathrm{f}}_{1}\rangle, \langle \boldsymbol{E}^{\mathrm{i,f}}_{n}, \boldsymbol{f}^{\mathrm{f}}_{2}\rangle, \ldots, \langle \boldsymbol{E}^{\mathrm{i,f}}_{n}, \boldsymbol{f}^{\mathrm{f}}_{P}\rangle\right]^{T} \tag{12}$$

where $\boldsymbol{E}^{\mathrm{i,f}}_{n}$ is taken equal to the E-field radiated by the PO current $\mathbf{J}^{\mathrm{r}}_{n}$ on the reflector, which is directly known through the reflector incident H-field $\mathbf{H}^{\mathrm{i,r}}_{n}$, so that there is no need to compute the basis function coefficients $\mathbf{I}^{\mathrm{r}}_{n}$ explicitly.

For electrically small triangular cells on the reflector surface (with edge length $< 0.2\lambda$), the smoothly-varying PO current can be considered constant over each cell, so that the electric field produced by the qth reflector triangle at the pth observation point, $\boldsymbol{E}^{\mathrm{i,f}}_{n,pq}$, can be computed through the near-field formula for an incremental electric current source, i.e. [34, p. 102],

$$\boldsymbol{E}^{\mathrm{i,f}}_{n,pq} = \frac{-j\eta k}{4\pi}\left[C_{1;pq}\boldsymbol{\ell}_{n,q} - C_{2;pq}(\boldsymbol{\ell}_{n,q}\cdot\hat{\boldsymbol{r}}_{pq})\hat{\boldsymbol{r}}_{pq}\right]\frac{e^{-jkr_{pq}}}{r_{pq}} \tag{13}$$

where

$$C_{1;pq} = 1 + \frac{1}{jkr_{pq}} - \frac{1}{(kr_{pq})^2}, \quad C_{2;pq} = 3C_{1;pq} - 2, \tag{14}$$

and where the dipole moment is computed as $\boldsymbol{\ell}_{n,q} = \boldsymbol{J}^{\mathrm{r}}_{n,q}A_q$, with A_q the area of qth reflector triangle ($q = 1, 2, \ldots, Q$). Hence, by using the expression for the PO current for $\boldsymbol{J}^{\mathrm{r}}_{n,q}$ [35, p. 343], we find that

$$\boldsymbol{\ell}_{n,q} = 2A_q\hat{\boldsymbol{n}}_q \times \boldsymbol{H}^{\mathrm{i,r}}_{n}(\boldsymbol{r}^{\mathrm{r}}_{q}), \tag{15}$$

where $\boldsymbol{r}^{\mathrm{r}}_{q} \in S$ is the centroid of the qth triangle on the reflector surface S (*cf.* Fig. 3); $\hat{\boldsymbol{n}}_q$ is the normal to the reflector surface of the qth triangle, and $\boldsymbol{H}^{\mathrm{i,r}}_{n}$ is the incident H-field generated by the feed current at iteration n. Using (15) and (13), the incident

E-field in (12) is readily computed as $\boldsymbol{E}_{n,p}^{\mathrm{i,f}} = \sum_{q=1}^{Q} \boldsymbol{E}_{n,pq}^{\mathrm{i,f}}$. The computation of (11b) can be further accelerated as explained in Sec. 3.1.

Once $\mathbf{V}_n^{\mathrm{f}}$ is known, the current on the feed $\mathbf{I}_{n+1}^{\mathrm{f}}$ at the next iteration can be computed through solving the linear system of equations $\mathbf{Z}^{\mathrm{ff}}\mathbf{I}_{n+1}^{\mathrm{f}} = \mathbf{V}_n^{\mathrm{f}}$. For complex-shaped and electrically large antennas, such as the wideband tapered slot antenna array feeds [13], it becomes necessary to use both memory- and time-efficient methods, such as the CBFM. The CBFM solves the current $\mathbf{I}_{n+1}^{\mathrm{f}}$ through the following set of equations:

$$\begin{cases} \mathbf{I}_{n+1}^{\mathrm{f}} &= \mathbf{J}^{\mathrm{CBF}}\mathbf{I}_{n+1}^{\mathrm{CBF}} \\ \mathbf{I}_{n+1}^{\mathrm{CBF}} &= \mathbf{Z}^{\mathrm{CBF}}\mathbf{V}_n^{\mathrm{CBF}} \\ \mathbf{V}_n^{\mathrm{CBF}} &= (\mathbf{J}^{\mathrm{CBF}})^T\mathbf{V}_n^{\mathrm{f}} \end{cases}, \tag{16}$$

where $\mathbf{Z}^{\mathrm{CBF}} = (\mathbf{J}^{\mathrm{CBF}})^T\mathbf{Z}^{\mathrm{ff}}\mathbf{J}^{\mathrm{CBF}}$ is the CBFM-reduced MoM matrix of the feed; $\mathbf{J}^{\mathrm{CBF}} = [\mathbf{J}_1^{\mathrm{CBF}}|\mathbf{J}_2^{\mathrm{CBF}}|\ldots|\mathbf{J}_L^{\mathrm{CBF}}]$ is the column-augmented matrix of Characteristic Basis Functions (CBFs), i.e., $\mathbf{J}_l^{\mathrm{CBF}}$ is the set of CBFs (pre-defined expansion coefficient vectors) on the lth macro domain of the feed, and $l = 1\ldots L$, where L is number of macro domains on the feed. Specific details on the generation of CBFs can be found in [33], where the feed is analyzed as a phased array antenna in the absence of the reflector. Also, it is worth pointing out that the computation of $\mathbf{Z}^{\mathrm{CBF}}$ (i.e. the CBF coupling terms) is performed in a time-efficient manner through utilizing the Adaptive Cross Approximation (ACA) algorithm [36].

3 Acceleration of the Field Computations

The above-described iterative CBFM-PO approach requires the field to be computed at numerous points on both the feed and the reflector surfaces, thereby rendering the field computations inefficient, in particular for complex-shaped electrically large feed antennas employing hundreds of thousands of low-level basis functions. Similarly, one has to cope with a computational burden when calculating the PO equivalent current on electrically large reflectors.

However, it has been shown that the PO radiated field for on-axis beams can be approximated rather accurately through a single plane wave (PW) field [10, 37]. This observation opts for employing a Plane Wave Spectrum (PWS) to speed up the field computations [38–40]. In fact, the on-axis PW corresponds to the Geometrical Optics (GO) contribution of the PO-radiated field (originating from the stationary phase point), as will be demonstrated in Sec. 3.1, while the higher-order PWs are needed to model the edge-diffracted fields from the rim of the reflector, which are associated with the end-point contributions of the PO current in the radiation integral.

Furthermore, one can accelerate the computation of the PO current itself by using an interpolation technique of the near-field antenna feed pattern as detailed below.

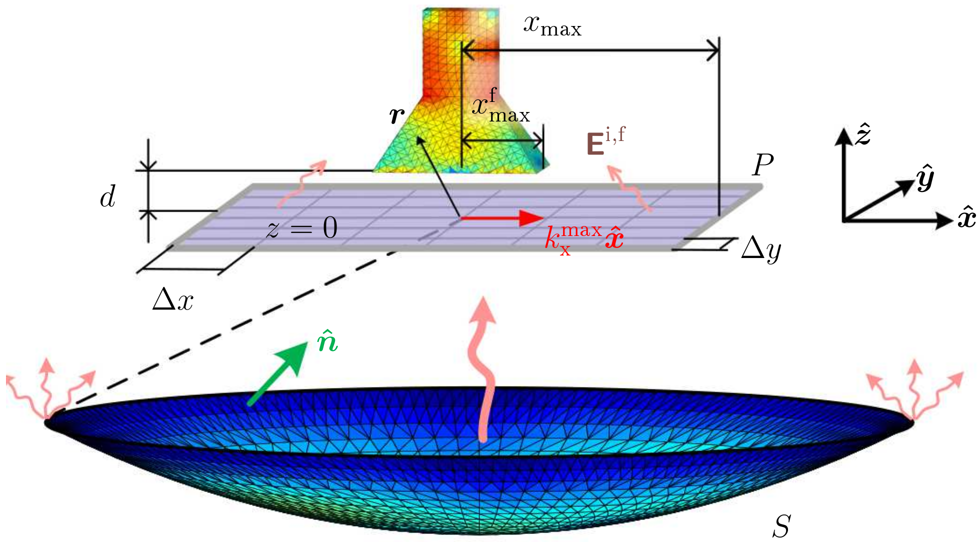

Figure 3: The FFT-enhanced PWS expansion method for the fast computation of the feed current due to the E-field from the reflector. Firstly, the incident field $\boldsymbol{E}^{\mathrm{i,f}}$ is sampled in the xy plane P in front of the feed in order to obtain the sampled PWS $\boldsymbol{A}(k_x, k_y)$; Secondly, each spectral PW propagates to an observation point $\boldsymbol{r}$ on the feed where $\boldsymbol{E}^{\mathrm{i,f}}$ is tested to compute the induced feed current.

3.1 Plane Wave Spectrum Expansion – FFT

With reference to Fig. 3, a grid of sampling points in the xy-plane P in front of the feed at $z=0$ is chosen for the expansion of the PO radiated field in terms of a PWS. Each PW propagates to a specific observation point $\boldsymbol{r}$ on the feed where the field $\boldsymbol{E}^{\mathrm{i,f}}$ is tested. This process of field expansion and PW propagation is realized through the application of the truncated Fourier Transform pair [38]

$$\boldsymbol{A}(k_x, k_y) = \frac{1}{2\pi} \int\limits_{-y_{\mathrm{max}}}^{y_{\mathrm{max}}} \int\limits_{-x_{\mathrm{max}}}^{x_{\mathrm{max}}} \boldsymbol{E}^{\mathrm{i,f}}(x, y, z=0) e^{j(k_x x + k_y y)} \, \mathrm{d}x \, \mathrm{d}y \tag{17a}$$

$$\boldsymbol{E}^{\mathrm{i,f}}(\boldsymbol{r}) = \frac{1}{2\pi} \int\limits_{-k_x^{\mathrm{max}}}^{k_x^{\mathrm{max}}} \int\limits_{-k_y^{\mathrm{max}}}^{k_y^{\mathrm{max}}} \boldsymbol{A}(k_x, k_y) e^{-jk_z z} e^{-j(k_x x + k_y y)} \, \mathrm{d}k_x \, \mathrm{d}k_y \tag{17b}$$

where

$$k_z = \begin{cases} \sqrt{k^2 - k_x^2 - k_y^2} & \text{if } k^2 > k_x^2 - k_y^2 \\ -j\sqrt{k_x^2 - k_y^2 - k^2} & \text{otherwise.} \end{cases}, \tag{18}$$

and where the spectrum of PWs is limited to only those that are incident on the feed from directions within an angle subtended by the reflector and seen from the center of the plane P (see Fig. 3); hence, the maximum wavenumbers $k_x^{\max}$ and $k_y^{\max}$ in (17b) are chosen to be equal to

$$k_x^{\max} = k_y^{\max} = k \sin \left[\tan^{-1} \left(\frac{8 \left(\frac{F}{D} \right)}{16 \left(\frac{F}{D} \right)^2 \left[1 - \left(\frac{F}{d} \right)^{-1} \right] - 1} \right) \right] \tag{19}$$

where $k = 2\pi/\lambda$ is the free-space wavenumber; F and D are the focal distance and diameter of the parabolic reflector, respectively; and d is the distance between the plane P and the geometrical focal plane of the reflector. Since the maximum spectral components $k_x^{\max}$ and $k_y^{\max}$ are known, the minimum step size Δx and Δy for the spatial sampling of the field is found from Nyquist's sampling theorem:

$$\Delta x = \pi / k_x^{\max}, \qquad \Delta y = \pi / k_y^{\max}. \tag{20}$$

Furthermore, if (17) is evaluated through a Fast Fourier Transform (FFT), the discretely sampled field functions are periodic in both the spatial and frequency domains. To minimize the field artifacts that are associated with this periodicity, $x_{\max}$ and $y_{\max}$ must be chosen sufficiently large, that is, at least equal to the maximum size $x_{\max}^{\mathrm{f}}$ and $y_{\max}^{\mathrm{f}}$ of the feed coordinates. The examination of how the error of the feed current depends on $x_{\max}$ and $y_{\max}$ is presented in Sec. 4.2.

As a result, the total number of sampling points in the x and y directions are $N_x = 2x_{\max}/\Delta x$ and $N_y = 2y_{\max}/\Delta y$, respectively, and the spectral spacings and the spatial extents are related through $\Delta k_x = 2k_x^{\max}/N_x = \pi/x_{\max}$ and $\Delta k_y = 2k_y^{\max}/N_y = \pi/y_{\max}$.

3.2 Near-Field Interpolation

While the previous section describes how the PWS-expanded E-field from the reflector accelerates the computation of the induced feed current, this section explains how the reflector incident H-field can be computed for the rapid determination of the induced PO current. For this purpose, the radiated H-field from the feed is first computed at a coarse grid on the reflector surface (white circles in Fig. 4), after which the field at each triangle is determined on the reflector (yellow square markers) through an interpolation technique. This interpolation technique de-embeds the initially sampled field to a reference sphere with radius R whose origin coincides with the phase center of the feed to assure that the phase of the de-embedded field will be slowly varying. Consequently, relatively few sampling points are required for the field interpolation, after which the interpolated fields are propagated back to the reflector.

In summary, and with reference to Fig. 4, the H-field interpolation algorithm for determining the reflector PO current

1. Defines a grid on the reflector surface (white circles) for computing the H-field.

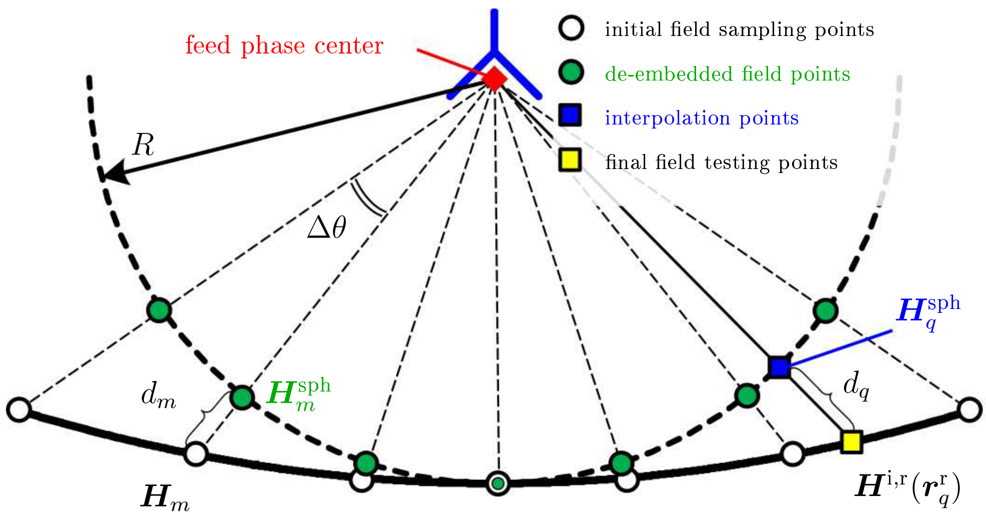

Figure 4: The near-field interpolation technique for the rapid determination of the induced PO current on the reflector.

2. De-embeds the H-field to a reference sphere around the feed phase center (green points):

$$\boldsymbol{H}_m^{\mathrm{sph}} = \boldsymbol{H}_m d_m e^{jkd_m}, \tag{21}$$

where d_m is the distance between the reflector surface and the sphere of radius R along the line connecting the mth sample point on the reflector and the feed phase center.

3. Computes the fields on the sphere in the same directions as the reflector triangle centroids are observed (blue square markers) through interpolating the fields at the adjacent (green) points.

4. Propagates the field to the reflector surface; that is, at the qth triangle, the H-field

$$\boldsymbol{H}^{\mathrm{i,r}}(\boldsymbol{r}_q^{\mathrm{r}}) = \boldsymbol{H}_q^{\mathrm{sph}} d_q^{-1} e^{-jkd_q}. \tag{22}$$

5. Computes the reflector PO current by using (15).

Sec. 4.2 examines the error in the reflector current as a function of the sample grid density, in addition to the improvement in computation time that this method offers.

4 Numerical Results

In this section, we start with the validation of the proposed iterative MoM-PO approach for a relatively strongly coupled feed-reflector system, comprised of a small

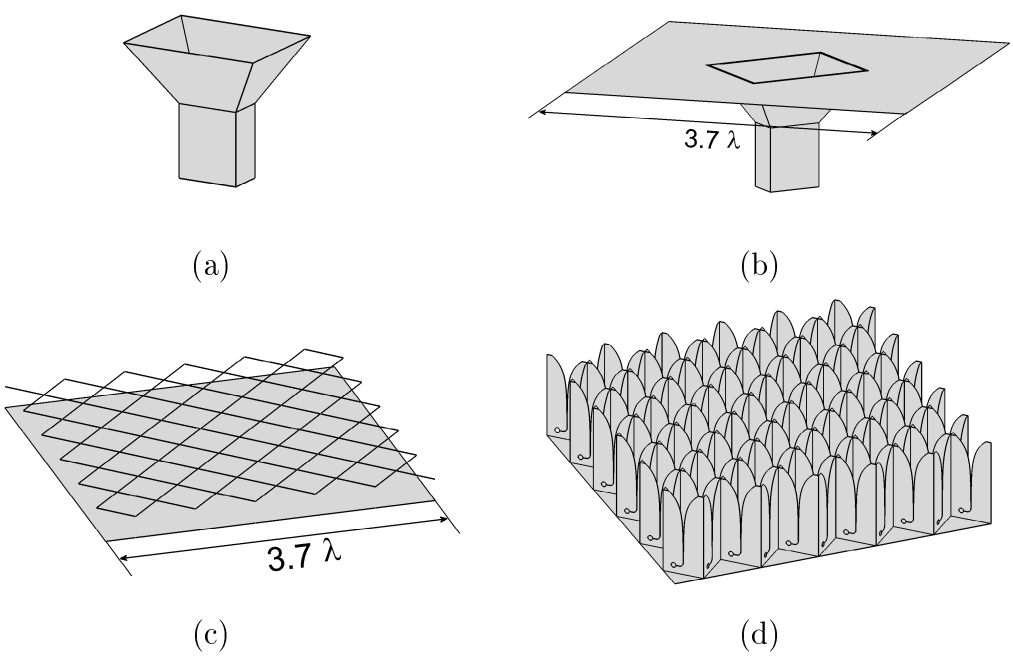

Figure 5: Considered feed geometries (in addition to the dipole feed with PEC ground plane): (a) a classical pyramidal horn with aperture length $\sim 1\lambda$; (b) the same horn but with extended ground plane ($\sim 3.7\lambda$), where the ground plane may model the presence of a large feed cabin; (c) an antenna array consisting of 121 0.45λ-dipoles above a ground plane of the same size; (d) the same array, but with the dipoles replaced by wideband tapered slot Vivaldi antennas.

reflector ($D = 14\lambda$) fed by a dipole antenna over a ground plane for which we examine the convergence rate of the solution for the antenna input impedance. Furthermore, we validate the frequency-dependent radiation characteristics of a dipole array feed through the commercially available software FEKO [41]. Afterwards, a relative error analysis of the antenna transmit characteristics is performed when the acceleration techniques in Sec. 3 are utilized. Finally, a more practical study is carried out, where the impact of the feed-reflector coupling on the performance of the antenna reflector system for different types of low- and high-scattering feeds is analyzed and discussed. For the latter study, two parabolic reflectors with diameters $D = 38\lambda$ and 118λ are considered, in conjunction with the four types of feeds that are shown in Fig. 5. It is shown that the measured and simulated results for a 121-element Vivaldi PAF, which is installed on the Westerbork Synthesis Radio Telescope, are in very good agreement.

The MoM computations have been carried out on a 64-bit openSUSE Linux server (kernel version: 2.6.37.6-0.20-desktop), equipped with 144 GB of RAM and two quad-core Intel(R) Xeon(R) E5640 CPUs, each operating at 2.67 GHz. The FEKO Suite 6.0 EM solver runs on an Ubuntu Linux server (kernel-release: 2.6.32-21-server), equipped with a Dual Core AMD Opteron Processor 275 at 2.2 GHz with 16 GB of

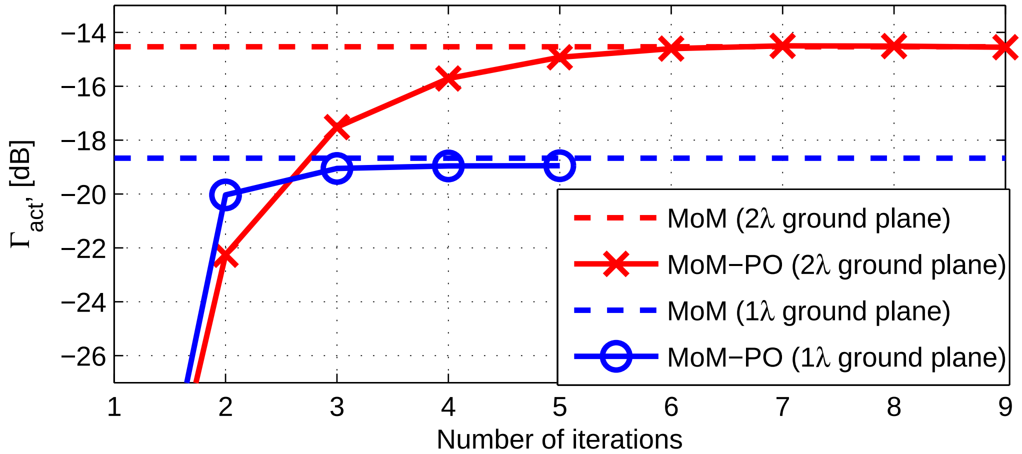

(a)

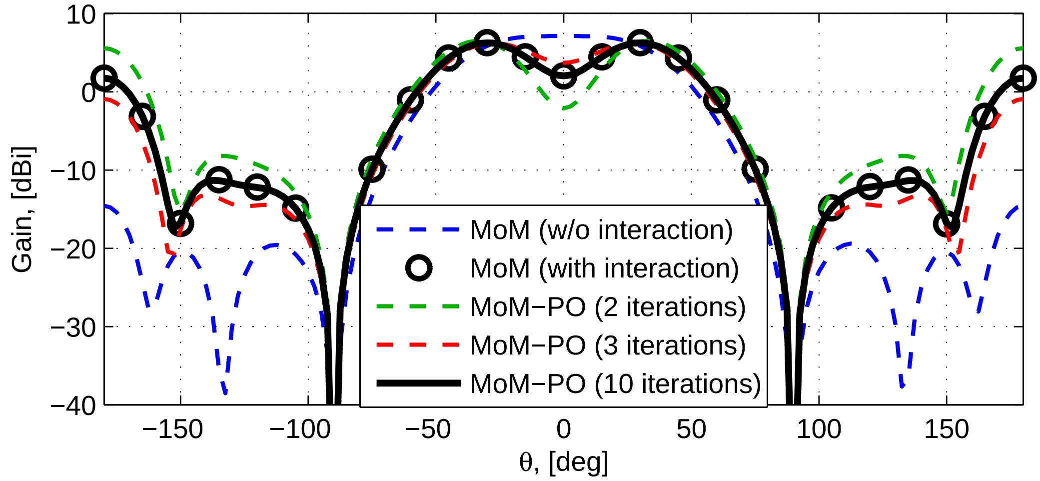

(b)

Figure 6: The convergence of the feed radiation characteristics in the presence of the reflector as a function of the number of Jacobi iterations, in terms of: (a) the dipole input reflection coefficient, and; (b) the dipole illumination pattern at 1 GHz (ground plane size is $2\lambda \times 2\lambda$). The convergence as a function of the dipole load impedance is analyzed for a dipole antenna array feeding a 38λ reflector.

RAM.

4.1 Validation of the Iterative Approach

For validating the implemented iterative MoM-PO approach, a relatively small reflector ($D = 14\lambda$, $F/D = 0.35$) fed by a 0.5λ-dipole spaced 0.25λ above an $1\lambda \times 1\lambda$ and a $2\lambda \times 2\lambda$ PEC ground plane has been simulated, both by the proposed iterative and plain MoM approach. The dipole reflection coefficient as a function of the iteration

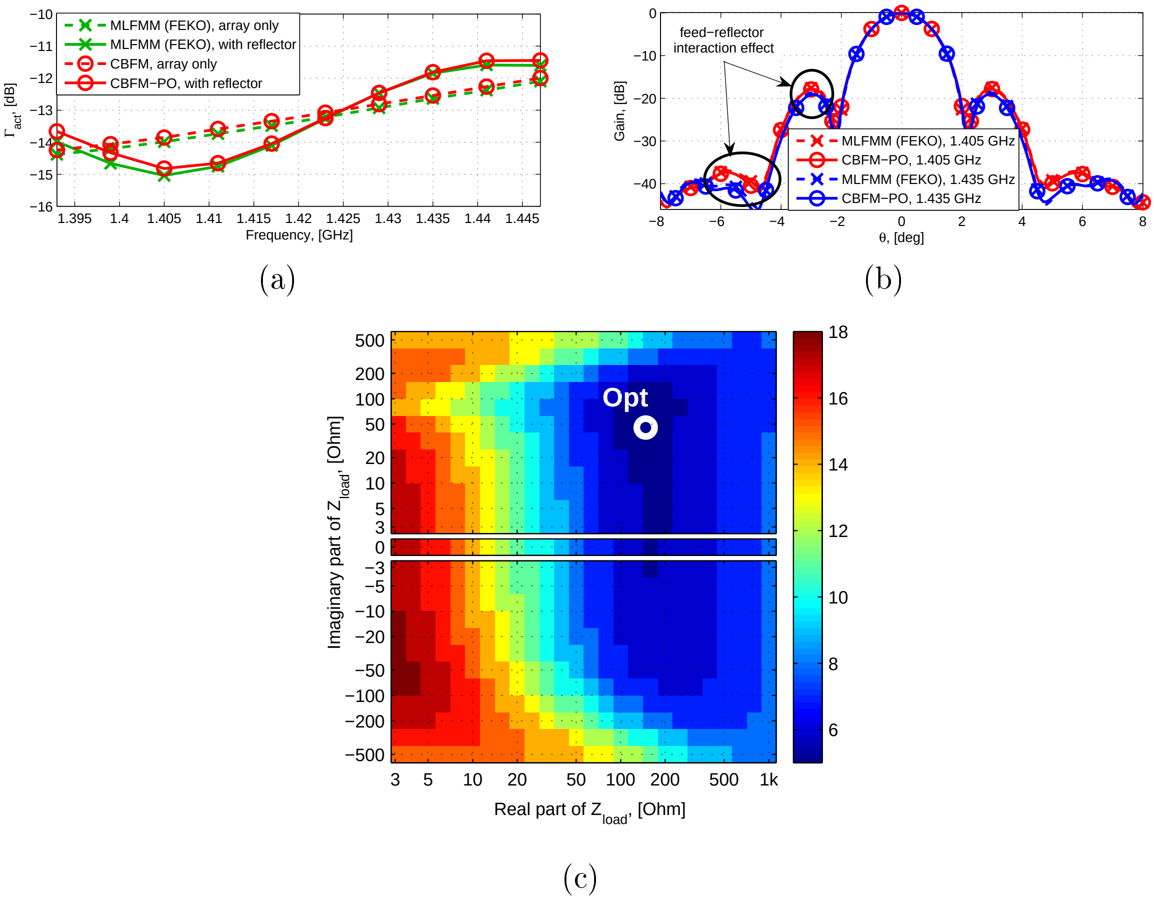

Figure 7: (a) The magnitude of the active reflection coefficient of the most excited antenna array dipole element feeding a 38λ reflector as a function of frequency, and; (b) reflector antenna radiation pattern, simulated in FEKO (MLFMM) and using the described iterative CBFM-PO approach; (c) the number of required iterations for reaching convergence (error in feed current less than 0.5%). Interesting fact: the round marker indicates the impedance that maximizes the decoupling efficiency (=power-matched case) when the array feed is used as a broadside-scanned aperture array, which also happens to coincide with the minimum number of iterations (=low multiscattering effect).

count is shown in Fig. 6(a). Even though the feed-reflector coupling is relatively large due to a relatively large blockage area of the high-scattering feed, convergence of the impedance down to 0.1% relative error level, measured as a change between the last two iterations, is seen to occur within 5 and 9 iterations for the $1\lambda \times 1\lambda$ and $2\lambda \times 2\lambda$ PEC ground planes, respectively. This error ϵ_n at iteration n is computed as

$$\epsilon_n = \left(\sqrt{\sum_i |I_i^n - I_i^{n-1}|^2} \Big/ \sqrt{\sum_i |I_i^n|^2} \right) \times 100\%. \tag{23}$$

The small residual error of order 1% is a result of the PO-approximated reflector current. Fig. 6(b) shows how the forward gain of the dipole illumination pattern changes due to the feed-reflector coupling as the number of iterations increases.

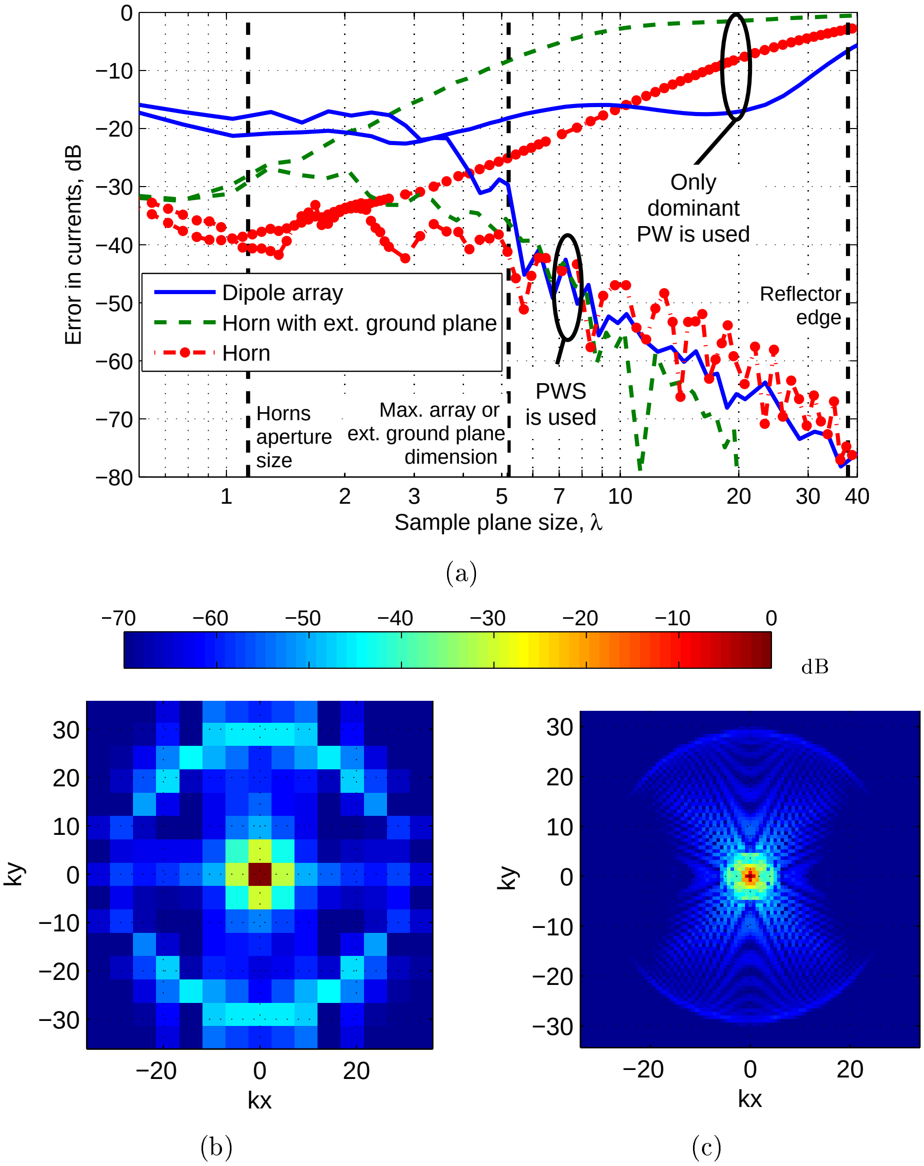

Figure 8: (a) The relative error in induced feed currents [*cf.* (24)] as a function of the FFT sampling plane size P; (b) the magnitude of the spatial frequency spectrum $|A_{\text{co}}(k_x, k_y)|$ (i.e. plane wave spectrum) for the 38λ reflector fed by the dipole array in case the FFT grid size is equal to size of the feed, and (c) when it is eight times the feed size.

For cross-code validation purposes, a larger and more complex 38λ reflector ($F/D = 0.35$) fed by an 121-dipole array feed has been analyzed [*cf.* Fig. 5(c)], both by the proposed iterative approach and the commercial FEKO software. Fig. 7(a,b) demonstrates a good agreement between the reflector antenna radiation patterns (includes the feed blockage effect) and the magnitudes of the computed active reflection coefficients as a function of frequency, where the frequency interval Δf of the oscillation period is consistent with the electrical distance between the feed and the reflector vertex, i.e., $\Delta f = c/2F$. Here, the optimal port termination that maximizes the array decoupling efficiency [8] was found through Matlab's "fminsearch" unconstrained nonlinear optimization routine (Nelder-Mead simplex direct search method) and was found to be $147 + 45.6j\ \Omega$. Thus far, practical PAF antenna elements have been optimized in phased array mode, broadside scan, using periodic boundary conditions in EM simulation software [42], hence, here too, the co-polarized elements of the array feed are excited in-phase to determine the optimal port loading. This optimal impedance is marked on Fig. 7(c) (and Fig. 11), where its plot shows the number of iterations – required to obtain an error in the dipole array feed current between the two last iterations less than 0.5% – as a function of the array loading. Note the interesting fact that the minimum number of iterations (=lowest multiscattering effect) occurs when the array is optimally loaded (=power matched), which is in accordance with our expectations, and this applies even though the antenna load impedance has been found for the aperture-array-excited case.

4.2 Field Approximation Errors

Sec. 3.1 and 3.2 describe a field expansion and interpolation technique for accelerating the feed-reflector interaction computations, respectively. In this section, we analyze the reflector induced feed current when the field from the reflector is expanded in terms of a truncated spectrum of plane waves, and compute the error in the feed current relative to a direct "full-wave" solution where the number of field modes radiated by the reflector equals the number of reflector triangles (=number of incremental dipole sources on the reflector). The distance d between the feed and the sampling plane P (*cf.* Fig. 3) has been chosen equal to 0.5λ in all PWS computations; in fact, our study shows that the selection of d in the range of $0.1 \ldots 5\lambda$ has a negligible ($< 0.7\%$) effect on the antenna characteristics, such as the aperture efficiency, even when the size of the plane P is kept the same. Both the relative error of the feed induced PO-reflector current and how the near-field interpolation grid density affects this error will be analyzed afterwards. Furthermore, the errors in the feed and reflector currents, as well as those in the gain of the antenna reflector system and the input impedance of the feed, will be summarized in a table.

The relative error between vector (or matrix) quantities – such as between the current expansion coefficient vectors $\mathbf{I}^{\text{approx}}$ and $\mathbf{I}^{\text{ref}}$ for the iterative CBFM-PO solution with and without field approximations, respectively – is computed as

$$\epsilon_1 = \left(\sqrt{\sum_i |I_i^{\text{ref}} - I_i^{\text{approx}}|^2} \Big/ \sqrt{\sum_i |I_i^{\text{ref}}|^2} \right) \times 100\%, \tag{24}$$

while the relative error for scalar functions (antenna gain, impedance characteristics,

Table 1: Errors due to applying the field approximations, %

	Feed surface current		**Reflector surface current**		**Gain (on-axis)**		**Gain (@−3 dB)**		**Impedance**	
Reflector	**38λ**	**118λ**	**38λ**	**118λ**	**38λ**	**118λ**	**38λ**	**118λ**	**38λ**	**118λ**
Feed: Pyramidal horn										
PWS approx.	0.09	0.02	0.11	0.03	0.09	0.03	0.07	0.02	0.16	0.04
NFI approx.	0.01	<0.01	0.06	0.06	0.05	0.04	0.01	0.02	0.01	<0.01
Both approx.	0.09	0.02	0.13	0.07	0.13	0.07	0.07	0.04	0.15	0.04
Feed: Pyramidal horn with extended ground plane										
PWS approx.	0.28	0.02	0.41	0.02	0.06	0.01	0.09	0.01	0.44	0.04
NFI approx.	0.3	0.01	1.01	0.16	0.16	0.07	0.37	0.07	0.52	0.02
Both approx.	0.53	0.03	1.02	0.16	0.15	0.08	0.34	0.07	0.88	0.05
Feed: 121-element dual-polarized dipole array										
PWS approx.	0.05	0.02	0.1	0.02	0.03	0.01	0.01	0.01	0.03	0.01
NFI approx.	0.02	0.01	0.21	0.20	0.09	0.07	0.12	0.13	0.02	0.01
Both approx.	0.06	0.02	0.23	0.21	0.10	0.07	0.13	0.14	0.05	0.02

Table 2: Total simulation time (for $D = 118\lambda$ reflector)

	Horn	**Horn with gnd plane**	**Dipole array**	**Vivaldi array**
MoM-PO, no approx.	70 min (100%)	192 min (100%)	801 min (100%)	3906 min (100%)
PWS approx.	27 min (39.0%)	63 min (32.9%)	190 min (23.8%)	1312 min (33.6%)
NFI approx.	57 min (81.3%)	152 min (79.4%)	548 min (68.5%)	2108 min (54.0%)
Both approx.	13 min (19.2%)	17 min (9.0%)	16 min (2.0%)	33 min (0.9%)

etc.), is computed as

$$\epsilon_2 = \left(|A^{\text{ref}} - A^{\text{approx}}|/|A^{\text{ref}}|\right) \times 100\%. \tag{25}$$

Fig. C.8(a) illustrates the relative error in the feed surface current as a function of the FFT sampling plane size when the PWS is employed for expanding the reflector

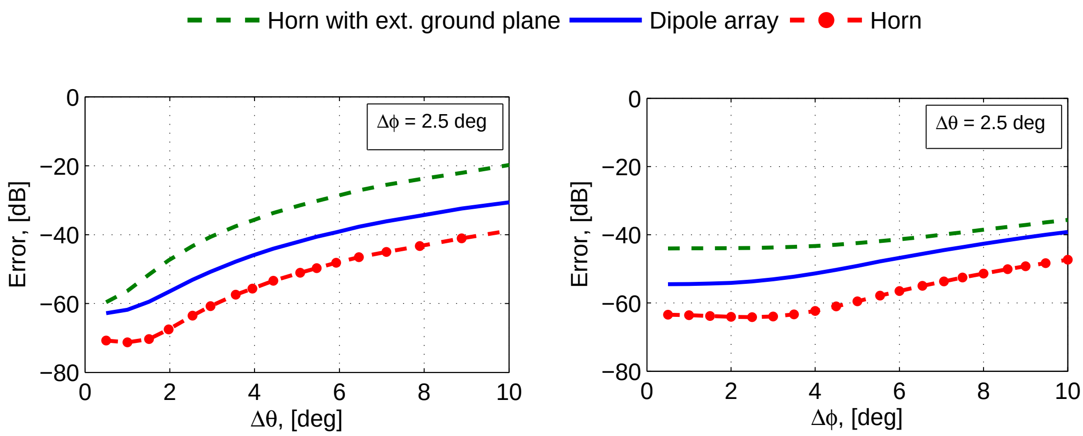

(a) (b)

Figure 9: The interpolation error in the 38λ reflector current as a function of (a) the sampling step $\Delta\theta$, and (b) the sampling step $\Delta\phi$ of the near fields of the feed.

radiated field (for PWS parameters see Sec. 3.1), and when only the dominant on-axis PW term is used. As expected, the error decreases for an increasing sampling plane size, since more spectral PW terms are taken into account while the effect of the FFT-related periodic continuation of the spatial aperture field decreases. Henceforth, we choose the sampling plane size equal to that of the feed, for which the feed current error is about -35 dB for all the considered feeds, while it represents a good compromise from both a minimum number of sampling points and accuracy point of view. Conversely, if only the dominant on-axis PW term is used to approximate the reflector field, the error increases when the plane P becomes larger. This is due to the tapering of the reflector scattered field which becomes more pronounced when the plane size P increases, so that the PW amplitude $A(k_x, k_y)$ is underestimated when using the field averaging in (17a) for $k_x = k_y = 0$, as opposed to the direct on-axis point sampling method that has been presented in [10].

Note that the magnitude of the co-polarized spatial frequency spectrum $|A_{\mathrm{co}}(k_x, k_y)|$ in Figs. 8(b) and (c) exhibit several interesting features; as expected, the dominant spectral component corresponds to the on-axis PW, for which $k_x = k_y = 0$, while the second strongest set of PWs originate from the rim of the reflector, as observed by the spectral ring structure for which $k_x^2 + k_y^2 = (k_x^{\max})^2 = (k_y^{\max})^2$.

Regarding the interpolation method for the radiated near-fields of the feed (Sec. 3.2), Figs. C.9(a) and (b) show that the error in the resulting induced reflector current depends on the angular step size $\Delta\theta$ and $\Delta\phi$ of the initial field sampling grid (before interpolation). As expected, the error increases when the sampling grid coarsens. Furthermore, the error is larger for larger feeds, especially for high-scattering ones, for which the scattered fields (i.e. 2nd iteration and further) vary more rapidly than for smaller low-scattering antennas for which a coarser grid can be applied.

Table 1 summarizes the relative errors in both the currents and relevant antenna characteristics, while Table 2 shows how the simulation time of a "plain" iterative CBFM-PO (or MoM-PO) approach reduces when the field approximations of Sec. 2 are used. Note that the PWS approximation leads to a small relative error in the surface current of the high-scattering feed for the 38λ reflector, i.e. 0.28%, while if only a single on-axis PW is used, the relative error is found to be two orders larger [37]. It is also observed that, when applying the field approximations for both the reflector and feed, the error in the considered antenna characteristics remains less than 1%, while the computational speed advantage is significant, i.e., a factor 5 to 100, depending on the reflector size and feed complexity.

4.3 Feed-Reflector Antenna System Performance Study

The performance of several reflectors fed by low- and high-scattering feeds is studied in detail in this section. It is shown how the frequency ripple in the antenna radiation characteristics is formed and how the feed termination affects the magnitude of this ripple. The system performance and pros and cons of the different feeds are summarized in a table and discussed from a multiscattering point of view.

Fig. 10 illustrates the level of the total (including feed-reflector interaction) and the scattered field distributions in the aperture of a 38λ reflector fed by the horn with an extended ground plane, the dipole array, and the Vivaldi array, for both the short-circuited (left column) and the power-matched (right column) loading schemes. Although the short-circuited case is not very practical, it does showcase how two very different loading scenarios affect the aperture field variation, and how it depends on the type of the feed. The two solid lines in each sub-figure show the extrema that the aperture field distribution attains within one period of the ripple's frequency interval $\Delta f = c/2F$. The dashed lines show the aperture field due to the scattered field of the feeds. Clearly, for array feeds, the aperture field distribution is strongly dependent on the antenna port termination; the re-scattered fields from the array feeds affect the aperture field distribution significantly when the antenna ports are short-circuited, as opposed to the power-matched array feeds, whose scattered fields are significantly weaker. Note the differences in results for the horn with extended ground plane, for which the dominant part of the scattered field is primarily attributed to the metallic ground plane, while the impedance mismatch of the horn itself has only a minor effect (i.e. the residual component of the Radar Cross Section is large, but the antenna component is small [19]).

From the above analysis, one concludes that more Jacobi iterations are required to reach convergence for feeds that are poorly impedance matched as they tend to scatter a larger portion of the incident field (stronger multiscattering effects). It is therefore likely that the number of Jacobi iterations is closely related to the magnitude

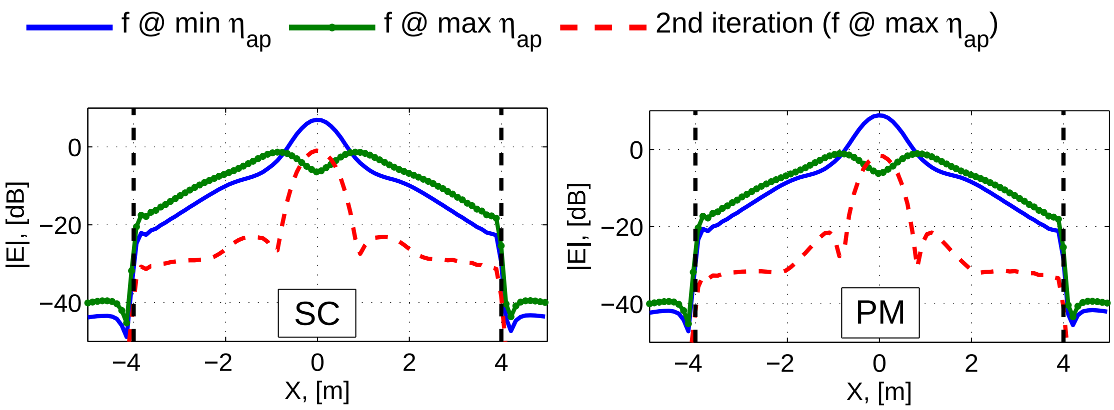

(a) Horn with ground plane

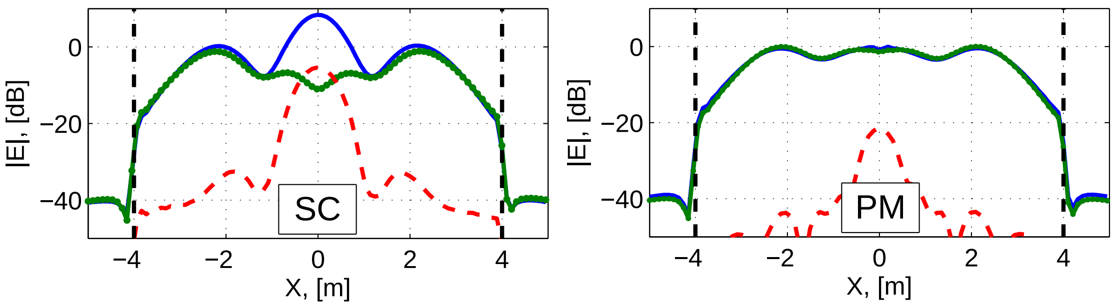

(b) Dipole array

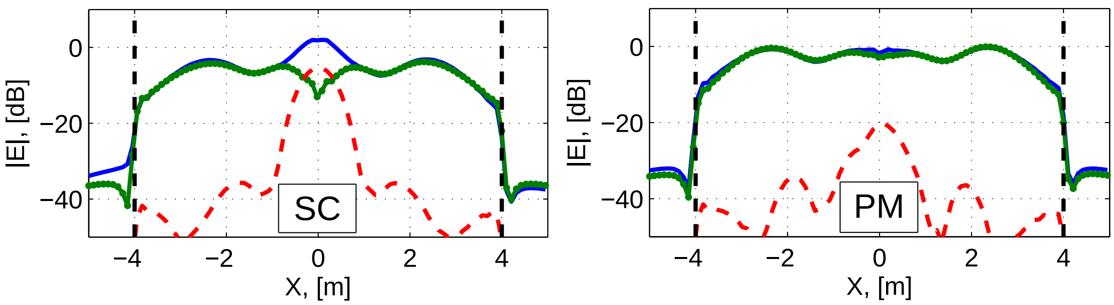

(c) Vivaldi array

Figure 10: Distribution of the field in the aperture of a 38λ reflector fed by: (a) horn with extended ground plane; (b) dipole array, and; (c) Vivaldi array. Left and right columns correspond to the short-circuited (SC) and average power-matched (PM) feeds, respectively.

of the ripple on the antenna radiation characteristics; this fact is demonstrated in Fig. 11, which shows the aperture efficiency, mismatch factor [8, 43] and their ripples as a function of the port termination impedance. The ripple R_ν for a frequency-dependent parameter $\nu(f)$ is herein defined as

$$R_\nu = \frac{\max_f [\Delta\nu(f)] - \min_f [\Delta\nu(f)]}{\mathrm{mean}_f \left[\nu_{\mathrm{with\_coup}}(f)\right]} \times 100\%, \tag{26}$$

where $\Delta\nu(f) = \nu_{\mathrm{with\_coup}}(f) - \nu_{\mathrm{no\_coup}}(f)$ is the difference between the considered parameter ν, with and without accounting for the feed-reflector coupling. The considered frequency band is herein taken relatively narrow as it corresponds to one period of the ripple only, i.e., $\Delta f = c/2F$. We further point out that these results apply to a feed that is excited at all its ports such as to realize a maximum gain pattern of the combined feed-reflector system, hereafter referred to as the Conjugate Field Match (CFM) beamformer. Furthermore, to be able to compare the results with the commonly employed uniformly excited array case analyzed above, the CFM excitations are fixed and determined only once for the optimal antenna port loading, i.e., pertaining to the uniformly excited array.

Table 3: Maximum parameter difference due to feed-reflector coupling effect w.r.t. the cases when no coupling is taken in account, %

	Feed surface current		**Reflector surface current**		**Gain (on-axis)**		**Gain (@−3 dB)**		**Impedance**	
Reflector	**38λ**	**118λ**	**38λ**	**118λ**	**38λ**	**118λ**	**38λ**	**118λ**	**38λ**	**118λ**
Pyramidal horn	7.9	2.5	4.2	1.3	2.0	0.6	4.0	2.2	15.1	4.7
Horn with ext. ground plane	23.2	3.5	65.1	11.9	19.2	3.4	29.4	3.6	43.4	6.1
Dipole array	13.8	4.2	3.2	0.8	1.8	0.3	3.7	0.7	5.8	1.7
Vivaldi array	14.1	4.1	3.4	1.0	1.9	0.3	3.4	0.4	4.6	1.4

One concludes from Fig. C.11(a) that the aperture efficiency is a function of the antenna port loading, and that the impedance for which η_{ap} attains a maximum is close to the optimal power-match impedance found in Sec. 4.1 for the uniformly excited array case. This apparently even holds in the absence of the feed-reflector interactions, in which case the array illumination pattern has changed slightly due to perturbed array embedded element patterns while the CFM excitation coefficients remain unaltered. In Sec. 4.1 we maximized the decoupling efficiency to find the optimal port loading. For the present CFM all-excited array case the decoupling efficiency reduces to the mismatch factor η_{mis}. The maximum of η_{mis} does, however, not coincide with the earlier optimal load impedance primarily due to the difference

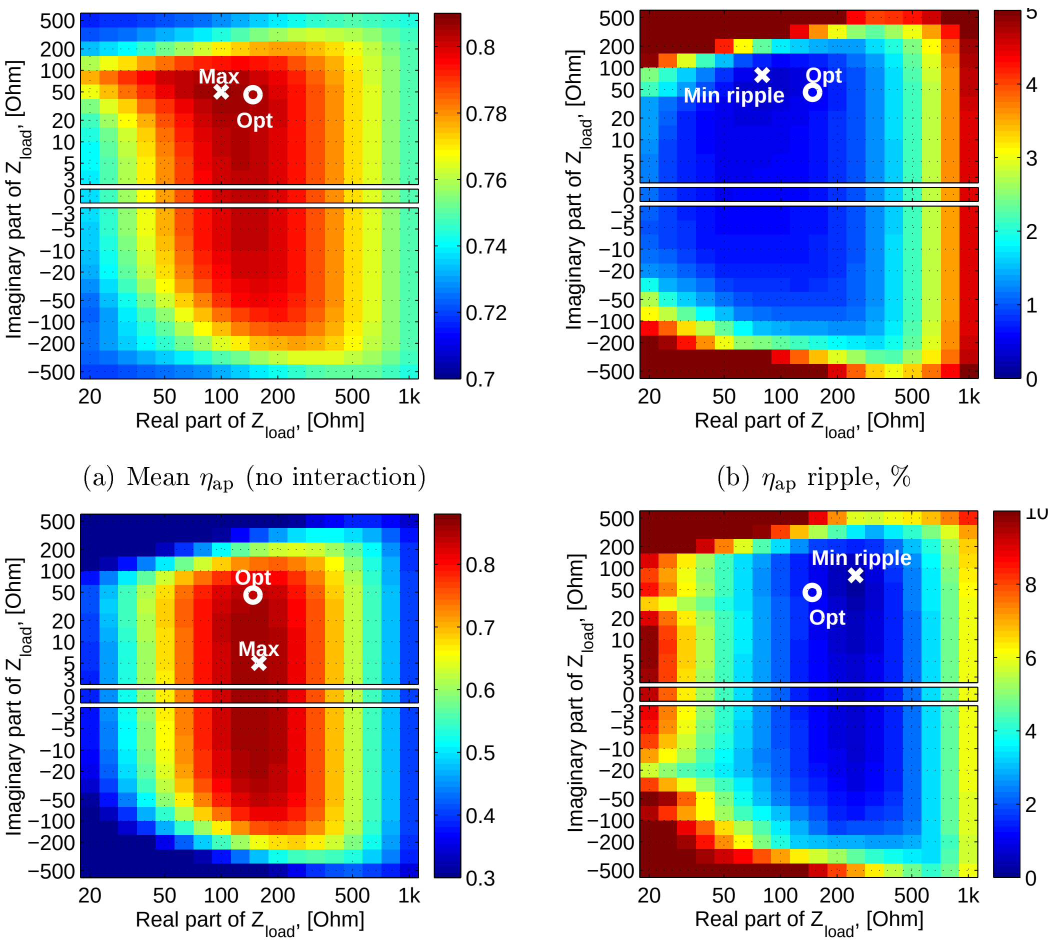

(a) Mean η_{ap} (no interaction)

(b) η_{ap} ripple, %

(c) Mean η_{mis} (no interaction)

(d) η_{mis} ripple, %

Figure 11: Effect of the antenna port loading on (a) the aperture efficiency without feed-reflector coupling, and (b) aperture efficiency ripple when the feed-reflector coupling is present; (c),(d) the same for the mismatch efficiency. A 38λ reflector is fed by the 121-element dipole array. The round marker denotes the optimal load impedance that maximizes the decoupling efficiency (*cf.* Sec. 4.1).

in array excitation schemes. Nonetheless, the observed quantities are only weakly dependent on impedance variations around their maximums. As for the feed-reflector-induced ripple of η_{ap} and η_{mis} [Fig. C.11(b) and Fig. C.11(d)], we can conclude that the η_{mis} ripple is more sensitive to variations in the array loading relative to the ripple in η_{ap}. In practice, however, when the amplifier/LNA impedance changes up to 10-20%, this only weakly affect η_{ap} and η_{mis} and their ripple.

Table 3 and 4 summarize the maximum difference in mean values and ripple, respectively, of several other relevant antenna radiation characteristics when the feed-reflector coupling is taken into account. For the computation of this difference Eq. (24) is used, where the superscripts “ref” and “approx” denote in this case the considered antenna parameter after the 1st (no coupling) and final iteration,

Table 4: System characteristics (and their ripple) over frequency band

38λ reflector				
	Horn	**Horn + gnd**	**Dipole array**	**Vivaldi array**
η_{ill}	0.71 (7.2%)	0.67 (34.1%)	0.86 (1.0%)	0.92 (0.6%)
η_{mis}	0.992 (1.0%)	0.987 (5.1%)	0.830 (1.2%)	0.910 (0.9%)
T_{sp}	7.7 K (18%)	6.8 K (39%)	4.2 K (16.8%)	8.8 K (9.6%)
118λ reflector				
	Horn	**Horn + gnd**	**Dipole array**	**Vivaldi array**
η_{ill}	0.71 (2.2%)	0.72 (4.1%)	0.85 (0.4%)	0.92 (0.2%)
η_{mis}	0.999 (0.2%)	0.999 (0.2%)	0.853 (0.5%)	0.926 (0.4%)
T_{sp}	7.7 K (6.0%)	7.2 K (6.8%)	3.8 K (5.7%)	8.7 K (3.4%)

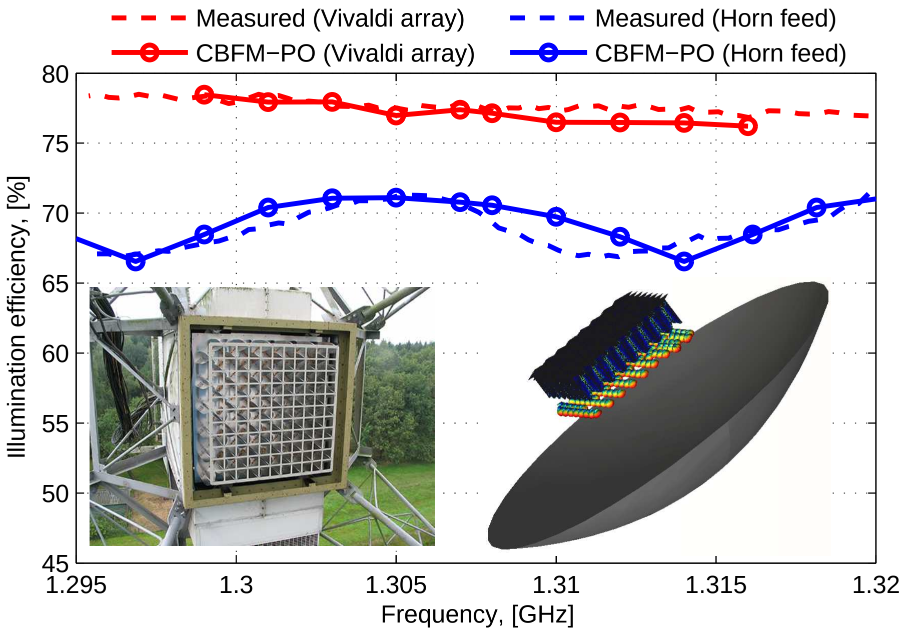

Figure 12: Illumination efficiencies of the 118λ reflector antenna, either fed by the 121 Vivaldi PAF, or the single-horn feed. The CBFM-PO simulated results are compared to the measured ones for a 25 m reflector antenna of the Westerbork Synthesis Radio Telescope [4]. Bottom of the figure: a photo of the experimental PAF system placed at the focal region of the reflector, and an image of a smaller-scale PAF-reflector model.

respectively, and where the summations are taken over frequency samples. Hence, this table allows us to estimate how strong the feed-reflector coupling is and how it affects the antenna characteristics. As expected, the high-scattering horn feeds cause stronger multiscattering effects, which is further excercebated for smaller dishes due to the larger relative blockage area. The difference in the antenna characteristics and their ripples are largest for the case of the 38λ reflector fed by the horn with extended ground plane, while these values are comparable and weakly dependent on the antenna element type in case of the array feeds.

Table 4 shows the mean values of various antenna radiation characteristics as well as their ripple caused by the multiscattering phenomenon, where the reflector antenna is assumed to be pointed at zenith for the computation of the spillover noise temperature T_{sp}. Upon comparing the values in the table, one conludes that the spillover noise temperature T_{sp} is most sensitive to the feed-reflector coupling, which may be of importance in radio astronomy applications where high receiving sensitivity is required.

Fig. 12 shows the illumination efficiencies η_{ill} of a 118λ reflector antenna ($D = 25$ m, $F/D = 0.35$), either fed by the Vivaldi array feed, or a single horn antenna. The numerically computed results are compared to measurements at the Westerbork Synthesis Radio Telescope (WSRT) [4]. As one can see, the agreement is very good. In the simulations, the size of the ground plane has been chosen equal to the size of the feed cabin ($\approx 1 \times 1$ m). The fact that η_{ill} is higher for the array feed than for the horn antenna nicely demonstrates the superior focal field sampling capabilities of dense phased array feeds. Furthermore, one can also observe a rather strong ripple in η_{ill} for the case of the horn feed with extended ground plane. This ripple is caused by the relatively high feed scattering of the reflector field.

5 Conclusions

An FFT-enhanced Plane Wave Spectrum (PWS) approach has been formulated in conjunction with the Characteristic Basis Function Method, a Jacobi iterative multi-scattering approach, and a near-field interpolation technique for the fast and accurate analysis of electrically large array feed reflector systems. Numerical validation has been carried out using the multilevel fast multipole algorithm method available in the commercially available FEKO software.

This physics-based numerical modeling offers the possibility to pull the feed-reflector interaction effects apart in a systematic manner and has demonstrated that: (i) a relation exists between the number of Jacobi iterations and the magnitude of the ripple on the frequency-dependent antenna radiation characteristics introduced by the feed-reflector coupling; (ii) the on-axis plane wave of the reflector field and the ones originating from the reflector rim are the strongest PWS components; (iii) the reflector-feed-induced ripple reduces when the array port termination is near a power-matched situation; (iv) the array feeds demonstrate a higher illumination efficiency than a single-horn feed with extended ground plane as a result of a better synthesized illumination pattern, and; (v) the level of the ripple as a function of frequency is smaller due to a smaller fraction of the scattered field from the array feed. The latter two findings have also been observed in measurements [4] for a horn feed and a 121-element Vivaldi PAF system installed at the Westerbork Synthesis Radio

Telescope (118λ-diameter), where we have shown that the relative difference between the simulated and measured antenna efficiencies is only in the order of a few percent.

Acknowledgment

The authors thank Wim van Cappellen from ASTRON for providing the measurement data of the APERTIF PAF system.

References

[1] B. Veidt. (2006) SKA memo 71: Focal-plane array architectures: Horn clusters vs. phased array techniques. [Online]. Available: http://www.skatelescope.org/uploaded/29162_71_Veidt.pdf

[2] M. V. Ivashina and C. G. M. van't Klooster, "Focal fields in reflector antennas and associated array feed synthesis for high efficiency multi-beam performances," in *Proc. 25th ESA Workshop on Satellite Antenna Technologies*, Noordwijk, The Netherlands, Sep. 2002, pp. 339–346.

[3] D. R. DeBoer, R. G. Gough, J. D. Bunton, T. J. Cornwell, R. J. Beresford, S. Johnston, I. J. Feain, A. E. Schinckel, C. A. Jackson, M. J. Kesteven, A. Chippendale, G. A. Hampson, J. D. O'Sullivan, S. G. Hay, C. E. Jacka, T. W. Sweetnam, M. C. Storey, L. Ball, and B. J. Boyle, "Australian SKA pathfinder: A high-dynamic range wide-field of view survey telescope," *Proc. IEEE*, vol. 97, no. 8, pp. 1507–1521, Aug. 2009.

[4] W. A. van Cappellen and L. Bakker, "APERTIF: Phased array feeds for the Westerbork synthesis radio telescope," in *IEEE International Symposium on Proc. Phased Array Systems and Technology (ARRAY)*, Boston, Oct. 2010, pp. 640–647.

[5] K. F. Warnick, "High efficiency phased array feed antennas for large radio telescopes and small satellite communication terminals," in *Proc. European Conference on Antennas and Propag. (EuCAP)*, Gothenburg, Sweden, Apr. 2013, pp. 448–449.

[6] O. A. Iupikov, M. V. Ivashina, K. Pontoppidan, P. H. Nielsen, C. Cappellin, N. Skou, S. S. Søbjærg, A. Ihle, D. Hartmann, and K. v. t Klooster, "Dense focal plane arrays for pushbroom satellite radiometers," in *Proc. European Conference on Antennas and Propag. (EuCAP)*, Hague, The Netherlands, Apr. 2014, pp. 1–5.

[7] P.-S. Kildal, "Factorization of the feed efficiency of paraboloids and cassegrain antennas," *IEEE Trans. Antennas Propag.*, vol. 33, no. 8, pp. 903–908, Aug. 1985.

[8] N. M. Kehn, M. V. Ivashina, P.-S. Kildal, and R. Maaskant, "Definition of unifying decoupling efficiency of different array antennas – case study of dense focal plane array feed for parabolic reflector," *Int. Journal of Electronics and Communications (AEU)*, vol. 64, no. 5, pp. 403–412, May 2010.

[9] M. V. Ivashina, M. Kehn, P.-S. Kildal, and R. Maaskant, "Decoupling efficiency of a wideband Vivaldi focal plane array feeding a reflector antenna," *IEEE Trans. Antennas Propag.*, vol. 57, no. 2, pp. 373–382, Feb. 2009.

[10] A. Moldsvor and P.-S. Kildal, "Systematic approach to control feed scattering and multiple reflections in symmetrical primary-fed reflector antennas," *IEEE Trans. Antennas Propag.*, vol. 139, no. 1, pp. 65–71, Sep. 1992.

[11] P.-S. Kildal, S. Skyttemyr, and A. Kishk, "G/T maximization of a paraboloidal reflector fed by a dipole-disk antenna with ring by using the multiple-reflection approach and the moment method," *IEEE Trans. Antennas Propag.*, vol. 45, no. 7, pp. 1130–1139, Jul. 1997.

[12] S. G. Hay, J. D. O'Sullivan, and R. Mittra, "Connected patch array analysis using the characteristic basis function method," *IEEE Trans. Antennas Propag.*, vol. 59, no. 6, pp. 1828–1837, Jun. 2011.

[13] R. Maaskant, M. V. Ivashina, O. Iupikov, E. A. Redkina, S. Kasturi, and D. H. Schaubert, "Analysis of large microstrip-fed tapered slot antenna arrays by combining electrodynamic and quasi-static field models," *IEEE Trans. Antennas Propag.*, vol. 56, no. 6, pp. 1798–1807, Jun. 2011.

[14] A. Popping and R. Braun, "The standing wave phenomenon in radio telescopes, frequency modulation of the wsrt primary beam," *Astronomy and Astrophysics*, vol. 479, no. 3, pp. 903–913, Mar. 2008.

[15] M. A. Apeldoorn, "Characterizing reflector-feed interaction for parabolic reflector antennas," Master's thesis, International Research Centre for Telecommunications and Radar (IRCTR), Delft University of Technology, Delft, The Netherlands, 2011. [Online]. Available: http://repository.tudelft.nl/assets/uuid:d6605869-37e0-49a6-8bc4-817855ab3710/MSc-Thesis-MAApeldoorn.pdf

[16] S. Hay, R. Mittra, and N. Huang. (2010) Analysis of reflector and feed scattering and coupling effects on the sensitivity of phased array feeds. [Online]. Available: http://csas.ee.byu.edu/docs/Workshop/BYUSGH.pdf

[17] W. A. van Cappellen and L. Bakker. (2010) Eliminating sensitivity ripples in prime focus reflectors with low-scattering phased array feeds. [Online]. Available: http://csas.ee.byu.edu/docs/Workshop/BYU_StandingWaves_Cappellen.pdf

[18] O. Iupikov, R. Maaskant, and M. Ivashina, "Towards the understanding of the interaction effects between reflector antennas and phased array feeds," in *Proc. Int. Conf. on Electromagn. in Adv. Applicat. (ICEAA)*, Cape Town, Sep. 2012, pp. 792–795.

[19] B. A. Munk, *Finite Antenna Arrays and FSS.* Danvers, Massachusetts: John Wiley & Sons, Inc., 2003.

[20] N.-T. Huang, R. Mittra, M. V. Ivashina, and R. Maaskant, "Numerical study of a dual-polarized focal plane array (FPA) with vivaldi elements in the vicinity of a large feed box using the parallelized FDTD code GEMS." in *Proc. IEEE AP-S International Symposium*, Charleston, USA, Jun. 2009, pp. 1522–3965.

[21] P. Bolli, G. Gentili, L. Lucci, R. Nesti, G. Pelosi, and G. Toso, "A hybrid perturbative technique to characterize the coupling between a corrugated horn and a reflector dish," *IEEE Trans. Antennas Propag.*, vol. 54, no. 2, pp. 595–603, Sep. 2006.

[22] M. Bandinelli, F. Milani, G. Guida, M. Bercigli, P. Frandsen, S. Sorensen, B. Bencivenga, and M. Sabbadini, "Feed-array design in presence of strong scattering from reflectors," in *Proc. European Conference on Antennas and Propag. (EuCAP)*, Rome, Italy, Apr. 2011, pp. 3844–3848.

[23] C. D. Giovampaola, E. Martini, A. Toccafondi, and S. Maci, "A hybrid PO/generalized-scattering-matrix approach for estimating the reflector induced mismatch," *IEEE Trans. Antennas Propag.*, vol. 60, no. 9, pp. 4316–4325, Sep. 2012.

[24] R. E. Hodges and Y. Rahmat-Samii, "An iterative current-based hybrid method for complex structures," *IEEE Trans. Antennas Propag.*, vol. 45, no. 2, pp. 265–276, Feb. 1997.

[25] C. S. Kim and Y. Rahmat-Samii, "Low profile antenna study using the physical optics hybrid method (POHM)," in *Proc. IEEE AP-S International Symposium*, Ontario, Canada, Jun. 1991, pp. 1350–1353.

[26] J. M. Taboada and F. Obelleiro, "Including multibounce effects in the moment-method physical-optics (MMPO) method," *Micr. Opt. Technol.*, vol. 32, no. 6, pp. 435–439, 2002.

[27] U. Jakobus and F. M. Landstorfer, "Improved PO-MM hybrid formulation for scattering from three-dimensional perfectly conducting bodies of arbitrary shape," *IEEE Trans. Antennas Propag.*, vol. 43, no. 2, pp. 162–169, Feb. 1995.

[28] B. Andrés-Garciá, D. Gonzalez-Ovejero, C. Craeye, L. Garciá-Muñoz, and D. Segovia-Vargas, "An iterative MoM-PO method based on a MBF/Krylov approach," in *Proc. European Conference on Antennas and Propag. (EuCAP)*, Barcelona, Spain, Apr. 2010, pp. 1–4.

[29] W. A. van Cappellen, L. Bakker, and T. A. Oosterloo, "Experimental results of the APERTIF phased array feed," in *General Assembly and Scientific Symposium, 2011 XXXth URSI*, Istanbul, Turkey, Aug. 2011, pp. 1–4.

[30] Y. Brand, A. K. Skrivervik, J. R. Mosig, and F. E. Gardiol, "New iterative integral equation technique for multilayered printed array antennas," in *Mathematical Methods in Electromagnetic Theory*, Kharkov, Ukraine, Jun. 1998, pp. 615–617.

[31] A. C. Polycarpou, "Evaluation of stationary block iterative techniques for the solution of finite arrays using the FE-BI method and domain decomposition," in *Proc. European Conference on Antennas and Propag. (EuCAP)*, Nice, France, Nov. 2006, pp. 1–6.

[32] S. N. Makarov, *Antenna and EM Modeling With MATLAB.* New York: John Wiley and Sons, Inc., 2002.

[33] R. Maaskant, "Analysis of large antenna systems," Ph.D. dissertation, Electrical engineering, Eindhoven University of Technology, Eindhoven, 2010. [Online]. Available: http://alexandria.tue.nl/extra2/201010409.pdf

[34] P.-S. Kildal, *Foundations of Antennas: a Unified Approach.* Lund: Studentlitteratur, 2000.

[35] C. A. Balanis, *Advanced Engineering Electromagnetics.* New York: John Wiley and Sons, Inc., 1989.

[36] R. Maaskant, R. Mittra, and A. G. Tijhuis, "Fast analysis of large antenna arrays using the characteristic basis function method and the adaptive cross approximation algorithm," *IEEE Trans. Antennas Propag.*, vol. 56, no. 11, pp. 3440–3451, Nov. 2008.

[37] O. A. Iupikov, R. Maaskant, and M. V. Ivashina, "A plane wave approximation in the computation of multiscattering effects in reflector systems," in *Proc. European Conference on Antennas and Propag. (EuCAP)*, Gothenburg, Sweden, Apr. 2013, pp. 3828–3832.

[38] J. J. H. Wang, "An examination of the theory and practices of planar near-field measurement," *IEEE Trans. Antennas Propag.*, vol. 36, no. 6, pp. 746–753, Jun. 1988.

[39] J. P. McKay and Y. Rahmat-Samii, "Compact range reflector analysis using the plane wave spectrum approach with an adjustable sampling rate," *IEEE Trans. Antennas Propag.*, vol. 39, no. 6, pp. 746–753, Jun. 1991.

[40] R. C. Rudduck, D. C. Wu, and M. Intihar, "Near-field analysis by the plane-wave spectrum approach," *IEEE Trans. Antennas Propag.*, vol. 21, no. 2, pp. 231–234, Mar. 1973.

[41] (2007) EM Software & Systems – S.A. (Pty) Ltd, Stellenbosch, South Africa, FEKO, Suite 6.0. [Online]. Available: http://www.feko.info

[42] M. Arts, M. Ivashina, O. Iupikov, L. Bakker, and R. van den Brink, "Design of a low-loss low-noise tapered slot phased array feed for reflector antennas," in *Proc. European Conference on Antennas and Propag. (EuCAP)*, Barcelona, Spain, Apr. 2010, pp. 1–5.

[43] M. V. Ivashina, R. Maaskant, and B. Woestenburg, "Equivalent system representation to model the beam sensitivity of receiving antenna arrays," *IEEE Antennas Wireless Propag. Lett.*, vol. 7, no. 1, pp. 733–737, Jan. 2008.

Paper D

Novel Multi-Beam Radiometers for Accurate Ocean Surveillance

C. Cappellin, K. Pontoppidan, P. H. Nielsen, N. Skou, S. S. Søbjærg, M. Ivashina, O. Iupikov, A. Ihle, D. Hartmann, and K. v. 't Klooster

in *Proceedings of the 8th European Conference on Antennas and Propagation, EUCAP 2014,* The Hague, The Netherlands, April 2014.

The layout of this paper has been revised in order to comply with the rest of the thesis.

Novel Multi-Beam Radiometers for Accurate Ocean Surveillance

C. Cappellin, K. Pontoppidan, P. H. Nielsen, N. Skou, S. S. Søbjærg, M. Ivashina, O. Iupikov, A. Ihle, D. Hartmann, and K. v. 't Klooster

Abstract

Novel antenna architectures for real aperture multi-beam radiometers providing high resolution and high sensitivity for accurate sea surface temperature (SST) and ocean vector wind (OVW) measurements are investigated. On the basis of the radiometer requirements set for future SST/OVW missions, conical scanners and push-broom antennas are compared. The comparison will cover reflector optics and focal plane array configuration.

1 Introduction

The assessment of ocean parameters like salinity, sea surface temperature and ocean vector wind based on spaceborne microwave radiometer measurements is an important and challenging task, not only concerning geophysical algorithms but also concerning technical aspects. A thorough and very recent review of ocean sensing was carried out by ESTEC and leading oceanography expert groups worldwide, producing the instrument requirements that future radiometers shall aim at, according to Table 1. The satellite height above the Earth and the incidence angle are assumed equal to 817 km and 53 deg, respectively.

Table 1: Radiometer characteristics for the conical scan antenna at C-, X- and Ku-band.

Freq., [GHz]	**Bandwidth, [MHz]**	**Polarization**	**Sensitivity, [K]**	**Bias, [K]**	**Resolution, [km]**	**Dist. to coast, [km]**
6.9	300	V, H	0.30	0.25	20	5-15
10.65	100	V, H	0.22	0.25	20	5-15
		S_3, S_4	0.22	0.25	20	5-15
18.7	200	V, H	0.25	0.25	10	5-15
		S_3, S_4	0.25	0.25	10	5-15

It is seen that SST and OVW are measured from C to Ku band, with a desired ground resolution of around 20 km at C- and X-band, and 10 km at Ku-band. The desired sensitivity is around 0.22 K. It is easily derived, see the procedure described

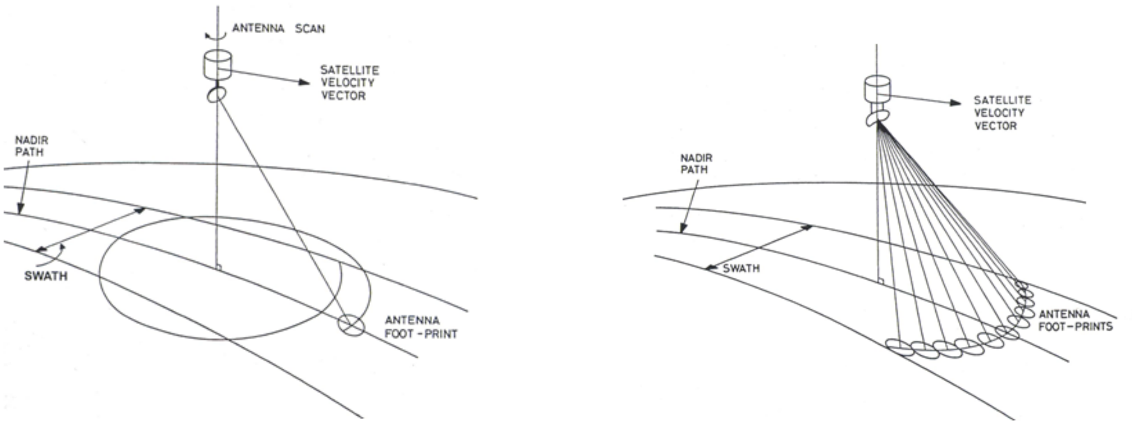

Figure 1: Conical scan (left) and push-broom (right) scenario.

in [1], that a radiometer with antenna aperture of around 5 m provides the required ground resolution but cannot achieve the desired sensitivity in a traditional single radiometer channel/beam concept, even with the state-of-the-art noise performance of receivers available in the market. The required sensitivity can only be met by considering several simultaneous beams in the along- and across-track, in either a push-broom system, or in a multi-beam scanning system, as depicted in Fig. 1.

The push-broom system achieves very high sensitivity since all across track footprints are measured simultaneously by their own receivers [2]. The antenna has the clear advantage of being stationary, but the number of beams and receivers is very high. An advanced feed design and reflector are necessary, and its light-weight mechanical realization is challenging. The multi-beam scanning system achieves high sensitivity by measuring each footprint several times followed by integration. The antenna is mechanically smaller than an equivalent torus, but presents numerous challenges in order to achieve a well-balanced rotation at satellite level [3]. Again, an advanced feed design is necessary.

In February 2013 the ESA contract 4000107369-12-NL-MH was awarded the team consisting of TICRA, DTU-Space, HPS and Chalmers University. The purpose of the activity is to identify the antenna requirements for a conical scanning and a push-broom radiometer for accurate SST and OVW measurements, and to make a trade-off of such two antennas, with respect to reflector optics, focal plane array configuration, ultra-light mesh reflector technology, mechanical stability, and calibration and RFI mitigation techniques. The purpose of the present paper is to describe the reflector optics and feed array design used for the trade-off, for a conical scanning and a push-broom radiometer antenna satisfying the requirements of Table 1. The paper is organized as follows: In Section 2 the optical design is described, while in Section 3 the antenna requirements derived from the radiometer requirements are highlighted. The feed array design is finally given in Section 4.

2 Optical Design

Following the procedure described in [1] it was found that a reflector antenna with projected aperture of around 5 m provides the required ground resolution. A conical scanning and a torus-push-broom antenna implementation were then considered. They are described in more detail in the following subsections.

2.1 Conical scanning radiometer antenna

The conical scanning antenna is an offset paraboloid with projected aperture D of 5 m. The clearance is set to 1 meter in order to provide space for the feed cluster and the focal length f is set to 3 m in order to make the design more compact. For a swath of 1500 km, the sensitivity of Table 1 can be achieved by:

- 2 beams along track at 6.9 GHz;
- 3 beams along track and 7 beams across track at 10.65 GHz;
- 5 beams along track and 6 beams across track at 18.7 GHz.

The number of beams in the along track direction is selected such that they cover the same strip width on the Earth. The antenna rotates at 11.5 RPM and the radiometer has a for-and-aft look.

2.2 Torus push-brom radiometer antenna

The push-broom antenna is a torus reflector with projected aperture D of 5 m. The torus is obtained by rotating a section of a parabolic arc around a rotation axis. The focal length of the parabolic generator is also 5 m. A possible way of obtaining the torus is shown in Fig. 2: the feed axis is selected parallel to the rotation axis, implying that all feed element axes are parallel and orthogonal to the focal plane. The feed array becomes therefore planar, simplifying the mechanical and electrical design. The reflector rim is found by the illuminated rotated aperture up to the outmost scan positions, see Fig.3.

The antenna shall be able to provide a scan of $\pm 20°$ corresponding to a swath width of 600 km. The final design is shown in Fig. 4, where the projected reflector aperture is 5 m by 7.5 m. It is recalled that the swath of the torus push-broom was reduced from 1500 km to 600 km in order to decrease the horizontal size of the reflector from 11 m to 7.5 m. This also reduces the feed array size and simplifies the electrical and mechanical realization.

It is noted that the sensitivity provided by the torus push-broom is always one degree of magnitude higher than the one provided by the conical scanner. This is at the expenses of a very large number of beams, and correspondingly large number of receivers. For a swath of 600 km we need:

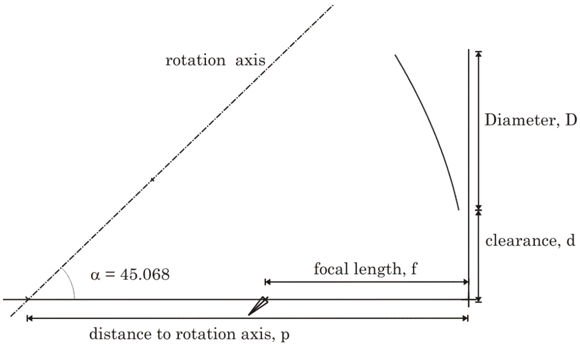

Figure 2: Torus design.

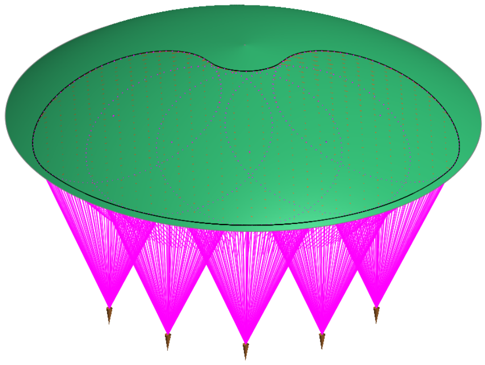

Figure 3: Rim trace for toroidal push-broom antenna design.

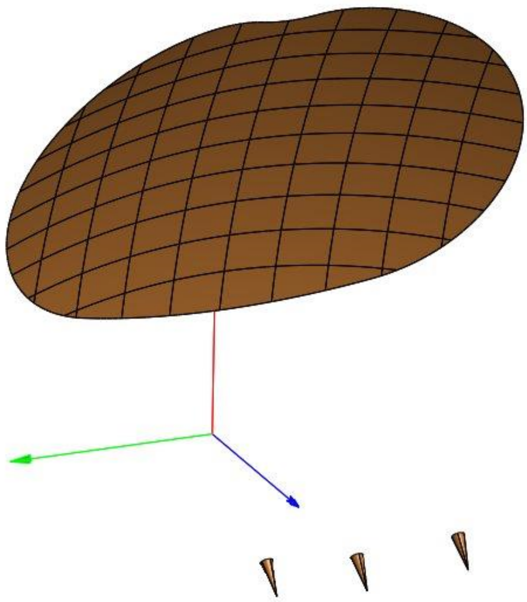

Figure 4: Torus push-broom antenna with projected aperture D of 5 m, three feeds located at $0°$ and $\pm 20°$, $f/D = 1$, and swath of 600 km.

- 58 beams across track at 6.9 GHz;
- 89 beams across track at 10.65 GHz;
- 156 beams across track at 18.7 GHz.

The antenna is stationary in contrast to the conical scan antenna.

3 Antenna Requirements

3.1 Acceptable cross-polarization

The requirement for the cross polarisation is not given directly in Table 1. We know, however, that the radiometer shall operate with two linear polarisations, vertical and horizontal, and that the accuracy indicated in the column "Bias" in Table 1 shall be achieved. It can be shown that the required $\Delta T \leq 0.25$ K implies that the cross polar power must not exceed 0.33 % of the total power on the Earth.

3.2 Acceptable side lobes and distance to coast

Table 1 states that the radiometer shall operate satisfactorily within $5 - 15$ km from the coast. It is assumed that this distance D_c is measured from the 3 dB footprint of the beam. The reason behind the requirement is that the brightness temperature of land areas is much higher than the brightness temperature of the sea, which is what we want to measure. Assume that the coast is located at the angle θ_c from boresight. It turns out, with $\Delta T \leq 0.25$ K, that the power from boresight up to θ_c shall contain 99.71 % of the total power on the Earth. The value of θ_c is determined by integration of the power pattern.

4 Feed Array Design

4.1 Conical scanning radiometer antenna

To design a feed array for the conical scanning radiometer antenna of Section 2.1, and at the same time compensate for the cross-polar component generated by the small f/D, a single feed per beam approach is not possible. A feed array with many closely spaced elements is a good candidate. A "feed" is here understood as the collection of the elements used to generate a particular beam. In the following, we will assume that:

- The feed array element is a half wave dipole above an infinite ground plane;
- The feed array elements are arranged in a square grid with a spacing of 0.75 wavelengths;
- Each feed can be represented by a sub array of 5 by 5 elements.

We wish to design the feed arrays for the three frequencies and to calculate the properties of the least scanned and the most scanned beams. This will require the following steps:

1. Determine the necessary feed array size for each of the bands C, X and Ku;

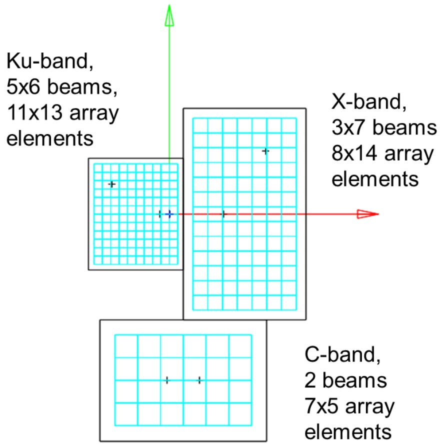

Figure 5: Feed arrays located in the focal plane.

2. Position the feed arrays in the focal plane.

The conical scan antenna is a focusing system and the half power beam width is inversely proportional to the frequency. With this in mind, and the previously mentioned required number of beams, it is a simple task to determine the size of the feed arrays for the three frequencies. The result is shown in Fig. 5. The layout is selected such that the scan, measured in beam widths, for the most scanned beam has been minimized. It is noted that the required number of beams is obtained by assuming that the beams overlap at the −3 dB cross-over points.

To calculate the performance of the conical scan antenna we select the least scanned and the most scanned beam for each frequency. The feed positions corresponding to these beams are indicated by small black crosses in Fig. 5. In order to find the feed array excitations necessary to generate these beams, the following procedure is used:

1. Illuminate the reflector with a Gaussian beam with correct direction and orientation;
2. Calculate the focal plane field;
3. Determine the top 30 dB co- and cross-polar element excitations.

The direction of the Gaussian beam in step 1 is given directly by the selected beam. The orientation of the beam is especially important for the scanned beams: it must be such that the beam on the Earth is vertically and horizontally polarized. The Gaussian beam incident on the reflector has a taper of 20 dB. The focal plane field is calculated in step 2. This field is used to calculate the excitation of the array elements in step 3 applying the Conjugate Field Matching (CFM) method. Only the elements with excitations from the maximum value and down to 30 dB below the maximum value are included, in order to account for realistic receivers.

The radiometer characteristics for the six beams of the conical scan antenna are summarized in Table 2. It is seen that the X and Ku band beams satisfy the requirements of Table 1, relative to distance to coast, footprint and cross-polar power. The performances for the C-band beams are not acceptable with respect to cross polarization, while the distance to coast is around 20 km, slightly more than the required 15 km. The design and performances of the above feed array was obtained both by TICRA and Chalmers, following the same procedure.

Table 2: Radiometer characteristics for the conical scan antenna at C-, X- and Ku-band.

Beam	**Number of active elements**		**cross-polar power**	**Peak directivity**	**Footprint**	**Dist. to coast**
	x-dir	**y-dir**	**%**	**dBi**	**km**	**km**
C_1	52	23	0.72	48.13	21.34	20.7
C_2	52	23	0.74	48.15	21.29	19.14
X_1	26	10	0.18	52.08	13.79	10.03
X_2	40	16	0.30	51.98	13.76	15.45
Ku_1	21	12	0.11	56.96	7.87	5.73
Ku_2	31	16	0.24	56.57	7.93	13.28

4.2 Torus push-brom radiometer antenna

To design the feed array for the torus push-broom antenna, a slightly different procedure than the one described in Section 4.1 is necessary. This is due to the fact that the push broom reflector is not a paraboloid and the antenna is not a focusing system for which results obtained at one frequency can easily be scaled to another frequency.

As a starting point, the influence of the taper of the Gaussian beam incident on the reflector is investigated at 10 GHz. The center beam is considered. The taper is varied from 20 dB to 60 dB in steps of 10 dB. The associated focal plane fields are shown to the left in Fig. 6 for the 20 dB and the 60 dB cases. It is seen that the extent of the field decreases as the taper of the incident beam increases. This means that if we can use a higher taper of the incident Gaussian beam we can apparently reduce the size of the feed array.

A large feed array covering the same part of the focal plane as Fig. 6 is now generated. The element spacing is 0.75 wavelengths = 22.5 mm and the number of elements is 73 in both directions. The total number of elements is actually $2 \times 73 \times 73 = 10658$ because there are two orthogonal dipoles at each element location.

The focal plane fields in Fig. 6 are used to determine, again with the Conjugate Field Matching (CFM) method, the excitations of all the 10658 dipole elements,

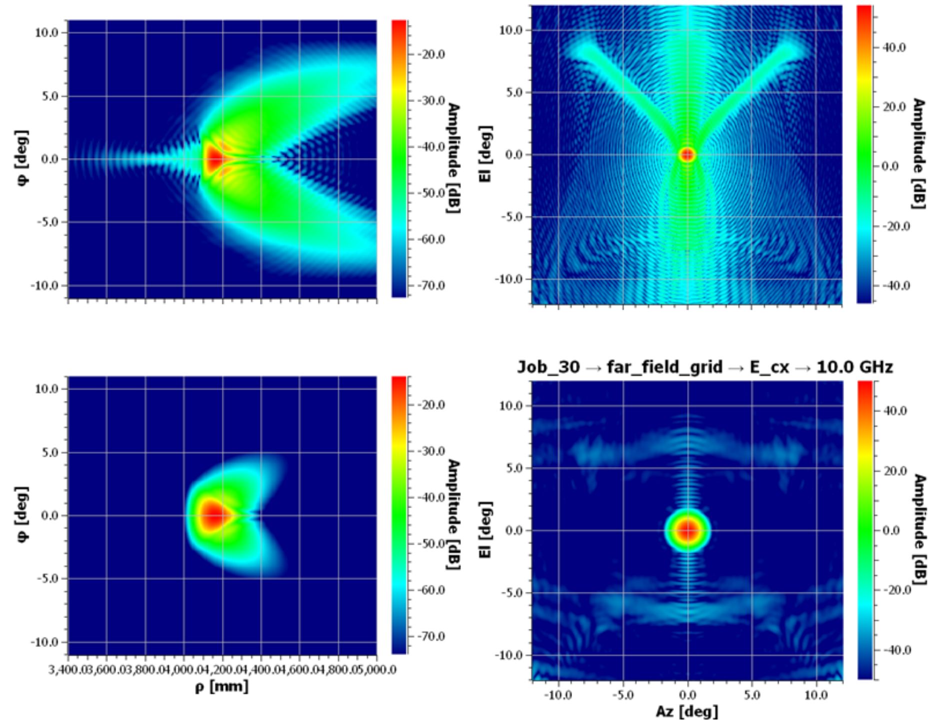

Figure 6: Focal plane field (left) and far field (right) for incident beam tapers of −20 dB (top) and −60 dB (bottom). The center beam is considered.

which then are used to generate the radiated center beam. The co polar component of the calculated far fields is shown to the right in Fig. 6 and it is seen, as expected, that the beam becomes broader as the taper increases, and, at the same time, the side lobes become smaller.

The radiometer characteristics for the center beams of Fig. 6 are shown in Table 3. We see that the cross polarisation requirement is always perfectly met. The footprint and the distance to coast increase as the taper increases. The results here are for 10 GHz which is close to the X-band frequency, where the requirement to footprint and distance to coast is 20 km and 15 km, respectively.

The results in Table 3 include all the elements in the feed array. It is of course of interest to reduce the number of active elements. Fig. 6 shows that the extent of the field in the focal plane decreases as the incident beam taper increases so from a feed array size point of view it is better to use a high input taper. Table 3 shows that with an incident taper of 50 dB a very acceptable beam is obtained. It is therefore attempted to use this focal plane field but only use those elements in the feed array with an excitation larger than a certain value below the maximum. Table 4 shows the results obtained when this limit is set to 40, 30 and 20 dB below the maximum.

It is seen that with a 30 dB limit both the cross polarisation, the footprint and the distance to coast meet the requirements and the number of active elements are

Table 3: Radiometer characteristics for the toroidal push broom antenna at 10 GHz for varying taper of the incident beam.

Taper of incident field	**Number of active elements**		**co-polar power**	**cross-polar power**	**Peak directivity**	**Foot-print**	**Dist. to coast**
dB	**ρ-dir**	**ϕ-dir**	**%**	**%**	**dBi**	**km**	**km**
20	5329	5329	98.83	0.07	53.27	12.08	7.93
30	5329	5329	99.74	0.03	51.84	14.16	9.89
40	5329	5329	99.93	0.02	50.68	16.12	11.51
50	5329	5329	99.98	0.01	49.74	17.93	12.89
60	5329	5329	99.99	0.01	48.96	19.60	14.11

Table 4: Radiometer characteristics for an incident field taper of 50 dB and excitation limits of 40, 30 and 20 dB.

Taper of incident field	**Number of active elements**		**co-polar power**	**cross-polar power**	**Peak directivity**	**Foot-print**	**Dist. to coast**
dB	**ρ-dir**	**ϕ-dir**	**%**	**%**	**dBi**	**km**	**km**
40	292	56	98.96	0.02	49.63	18.31	12.77
30	155	2	99.79	0.12	49.46	18.66	13.60
20	69	0	99.35	0.14	49.09	19.49	40.18

reduced from 10658 to 157, i.e. 155 in the radial direction and 2 in the azimuthal direction.

The experience gained at 10 GHz is used to design the feed array in the three bands, following pretty much the same procedure. It is recalled that it is necessary to tilt the direction of the incident beams such that the focal plane fields for the different frequencies are located side by side, leading to the feed array parameters shown in Table 5. Again, it is assumed that beams overlap at the -3 dB cross-over points. The feed arrays are shown in Fig. 7 and the radiometer characteristics for the center beam are presented in Table 6. It is seen that the performance meet the requirements except for the distance to coast at C-band.

Table 5: Table used to determine the necessary size of the feed arrays for the push broom torus reflector antenna.

Freq.	**Wave-length**	**Distance between elements**	**Element $\rho_{\max}$**	**Element $\rho_{\min}$**	N_ρ	N_ϕ	**Total element number**
GHz	**mm**	**mm**	**mm**	**mm**			
6.90	43.48	32.61	4078	3732	11	93	1023
10.65	28.17	21.13	4566	4314	12	163	1956
18.70	16.04	12.03	4292	4108	16	271	4336

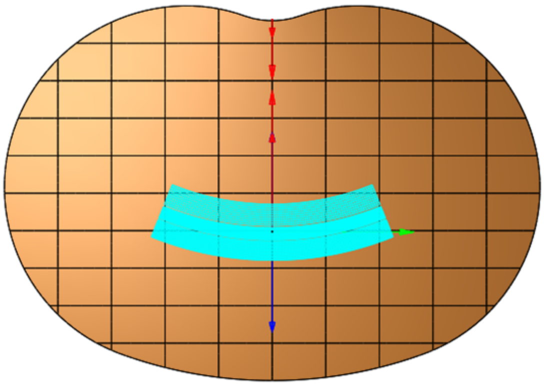

Figure 7: The three feed arrays for the push broom torus reflector antenna.

Table 6: Radiometer characteristics for the three frequency bands.

Freq.	**Input taper**	**Exci-tation limit**	**Number of active elements**		**co-polar power**	**cross-polar power**	**Peak direc-tivity**	**Foot-print**	**Dist. to coast**
GHz	**dB**	**dB**	**x-dir**	**y-dir**	**%**	**%**	**dBi**	**km**	**km**
6.90	30	30	133	4	99.56	0.20	48.13	21.82	27.59
10.65	50	30	161	2	99.68	0.10	49.96	17.61	13.29
18.70	40	30	351	0	99.73	0.17	55.56	9.28	13.00

The feed array designed by Chalmers for the torus push-broom antenna is described in detail in [4]. The feed array element is a Vivaldi antenna and the element spacing is 0.7 wavelength. The number of active elements and their weight coefficients is found with a customized beam former that aims to realize the best trade-off between the maximum beam efficiency and the minimum sidelobe and cross-polarization power. To include constraints on the dynamic range of the beamformer in the course of optimization, the customized beamforming algorithm proposed in [4] has been further extended through the use of an iterative procedure. This procedure modifies the reference weights, as determined for the beamformer without constraints, while aiming to maintain the radiometer characteristics as close as possible to the references ones for a specified value of the dynamic range. The performances obtained by Chalmers coincided with Table 6, except for the distance to land at C-band which was 16.9 Km, and thus met the requirements. The total number of elements of the complete feed array for one polarization was 888, 1224 and 2184, for the C- X- and Ku-band respectively, thus smaller than the number of elements obtained by TICRA and reported in the last column of Table 5.

5 Conclusions

The reflector optics and feed array designs of a conical scanning and push-broom radiometer antenna for future SST/OVW missions were described. The conical scanning is a traditional offset paraboloid with reduced f/D rotating at 11.5 RPM, while the push-broom is a stationary torus reflector, with projected aperture of 5 m by 7.5 m. The feed array of the conical scan antenna was obtained by considering half wave dipoles above an infinite ground plane, with a spacing of 0.75 wavelengths. The array excitations were obtained by CFM, considering a Gaussian beam with taper of 20 dB impinging on the reflector. The performances of the least and most scanned beams met all the requirements at X- and Ku-band. The performances for the C-band beams were not acceptable with respect to cross polarization, and the distance to coast was slightly more than the required 15 km. The feed array of the torus push-broom antenna was derived by TICRA in a way similar to the one used for the conical scan, while Chalmers developed a customized beam former to optimize the maximum beam efficiency and the minimum sidelobe and cross-polarization power, including constraints on the dynamic range of the beamformer. The performances of the center beam obtained by Chalmers met all the requirements at all three frequency bands, while TICRA obtained a slightly larger distance to coast at C-band and used more antenna elements. The present results must be considered preliminary.

References

[1] N. Skou and D. L. Vine, *Microwave Radiometer Systems: Design & Analysis.* Artech House, 2006.

[2] P. Nielsen, K. Pontoppidan, J. Heeboell, and B. L. Stradic, "Design, manufacture and test of a pushbroom radiometer," in *Antennas and Propagation, 1989. ICAP 89., Sixth International Conference on (Conf. Publ. No.301)*, Coventry, United Kingdom, Apr. 1989, pp. 126–130.

[3] M. Mobrem, E. Keay, G. Marks, and E. Slimko, "Development of the large aperture reflector/boom assembly for the SMAP spacecraft," in *ESA/ESTEC Workshop on Large Deployable Antennas*, Noordwijk, The Netherlands, Oct. 2012.

[4] O. A. Iupikov, M. V. Ivashina, K. Pontoppidan, P. H. Nielsen, C. Cappellin, N. Skou, S. S. Søbjærg, A. Ihle, D. Hartmann, and K. v. t Klooster, "Dense focal plane arrays for pushbroom satellite radiometers," in *Proc. European Conference on Antennas and Propag. (EuCAP)*, Hague, The Netherlands, Apr. 2014, pp. 1–5.

Paper E

Dense Focal Plane Arrays for Pushbroom Satellite Radiometers

O. Iupikov, M. Ivashina, K. Pontoppidan, P. H. Nielsen, C. Cappellin, N. Skou, S. S. Søbjærg, , A. Ihle, D. Hartmann, and K. v. 't Klooster

in *Proceedings of the 8th European Conference on Antennas and Propagation, EUCAP 2014,* The Hague, The Netherlands, April 2014.

The layout of this paper has been revised in order to comply with the rest of the thesis.

Dense Focal Plane Arrays for Pushbroom Satellite Radiometers

O. Iupikov, M. Ivashina, K. Pontoppidan, P. H. Nielsen, C. Cappellin, N. Skou, S. S. Søbjærg, , A. Ihle, D. Hartmann, and K. v. 't Klooster

Abstract

Performance of a dense focal plane array feeding an offset toroidal reflector antenna system is studied and discussed in the context of a potential application in multi-beam radiometers for ocean surveillance. We present a preliminary design of the array feed for the 5-m diameter antenna at X-band. This array is optimized to realize high antenna beam efficiency ($\sim 95\%$) over a wide scan range ($\pm 20°$) with very low side-lobe and cross-polarization levels.

1 Introduction

Recent advances in phased-array antenna technologies and low-cost active electronic components open up new possibilities for designing Earth observation instruments, in particular those used for radiometric measurements. Nowadays, two design concepts of microwave radiometers are in use: "push-broom" and "whisk-broom" scanners [1]. Push-broom scanners have an important advantage over whisk-broom scanner in providing larger field-of-view with higher sensitivity, owing to the fact that these systems can look at a particular area of the ocean for a longer time with multiple simultaneous beams. This concept is illustrated on Fig. 1, where one can see several beams, arranged perpendicular to the flight direction of the spacecraft. However, the drawback of pushbroom designs – based on conventional focal plane arrays (FPAs) of horns in one-horn-per-beam configuration [2] or clusters with simplistic beamforming [3] – is the varying sensitivity. This variation occurs due to the difference between the scanned beams (as these are formed by different horns/clusters) and their large separation on the ocean surface, as the result of the large separation between the horns.

This drawback may be significantly reduced by employing dense FPAs, i.e. phased-array feeds consisting of many electrically small antenna elements, with advanced beamforming [4]. This technology has been extensively studied during the last decade in the radio astronomy community, and several telescopes are currently being equipted with dense FPAs [5–7]. While those systems aim to provide the scan range of about $5-10$ beamwidths, for applications as herein considered, the desired scan range (swath range of the radiometer) is one order of magnitude larger [8]. Therefore, to achieve this performance, more complex designs of the reflector optics and FPA are required. For push-broom radiometers, various optics concepts have been investigated [2], and the optimum solution has been found to be an offset toroidal single reflector antenna, such as illustrated on Fig. 1. This reflector structure is rotationally symmetric around a vertical axis, and thus is able to cover a wide swath range. However, its aperture field exhibits significant phase errors due to the non-ideal (paraboloid) surface of the reflector – as compared to that of classical paraboloids. The phase errors cause degradation of the antenna beam efficiency and increase the side-lobe and cross-polarization levels. These degradations, in turn, limit the radiometer characteristics (such as the minimum distance to coast at which the measurement data remains usable) as well as worsen the situation with Radio Frequency Interference (RFI) that is problematic at many radiometer bands [9].

The purpose of this work is, therefore, (i) to determine to what extent the performance-limiting factors of push-broom radiometers can be reduced by using dense FPAs with advanced beamforming; and (ii) what is the minimum complexity of the FPA design (size, number of elements) that is required for meeting the instru-

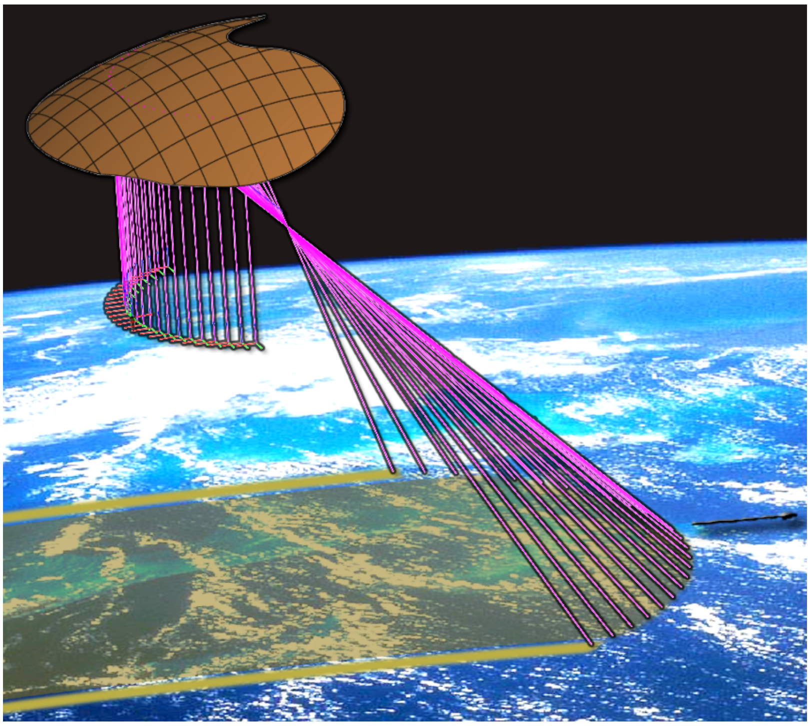

Figure 1: Operational principle of a push-broom microwave radiometer, which includes an off-set toroidal reflector antenna fed with a multi-beam focal plane array of horns arranged perpendicular to the flight direction of the spacecraft. Different areas of the ocean-surface are scanned as the spacecraft flies forward.

ment specifications at which future radiometers aim [8]. To address these questions, we have created an initial numerical model of the array that is based on the MoM-CBFM-model in [4]; the elements of this array represent tapered-slot antennas, as designed for the FPA system in [5]. To perform the parametric study, we have implemented this model for different array sizes and inter-element separation distances varying from 0.5 to 1 wavelength. For the evaluation of the radiometer characteristics, two beamforming methods have been considered that aim to optimize the beam efficiency with the minimum distance to land and cross-polarization loss.

2 Antenna Requirements

In February 2013 the ESA contract 4000107369-12-NLMH was awarded the team consisting of TICRA, DTU-Space, HPS and Chalmers University. The group comprises experts in reflector antennas design and analysis, passive microwave radiometry, mechanical and thermal analysis of ultra-light mesh reflector technology, and radio astronomy with the knowledge of dense focal plane arrays designs. As a part of this activity, we perform a preliminary design study of a pushbroom antenna, as shown on Fig. 1 with conventional FPAs of horns, as well as novel dense FPAs with active beamforming.

To identify the best design for the targeted application, we use the list of antenna system requirements that has been derived in [8], based on the the instrument specifications for accurate sea surface temperature and ocean vector wind measurements. This list includes the values for the required half-power beamwidth (and corresponding footprint on the sea-surface), acceptable cross-polarization power, as well as the minimum distance to coast at which the radiometer stops working correctly. It can be shown that in order to meet the requirements for radiometer characteristics (maximum allowed error of the measured sea brightness temperature $\Delta T < 0.25$K and the distance to coast < 15km) the power incident on the land must be less than 0.14% of the total power hitting the Earth. This requirement leads to stringent constraints on both the side-lobe and cross-polarization levels of the antenna beams.

At present, the pushbroom antenna which can satisfy these requirements is a torus antenna with projected aperture of 5 m, ($\pm 20°$) scan, the focal length to diameter ratio f/D=1 and swath of 600 km. This antenna has been designed by TICRA; it achieves the swath on the Earth equal to 600 km, assuming the satellite altitude above the Earth of 817 km and the incidence angle of 53°. This antenna should operate at C-band (6.9 GHz), X-band (10.65 GHz) and Ku-band (18.7 GHz) with bandwidth 300 MHz, 100 MHz and 200 MHz, respectively. The analysis in this paper is performed at X-band only.

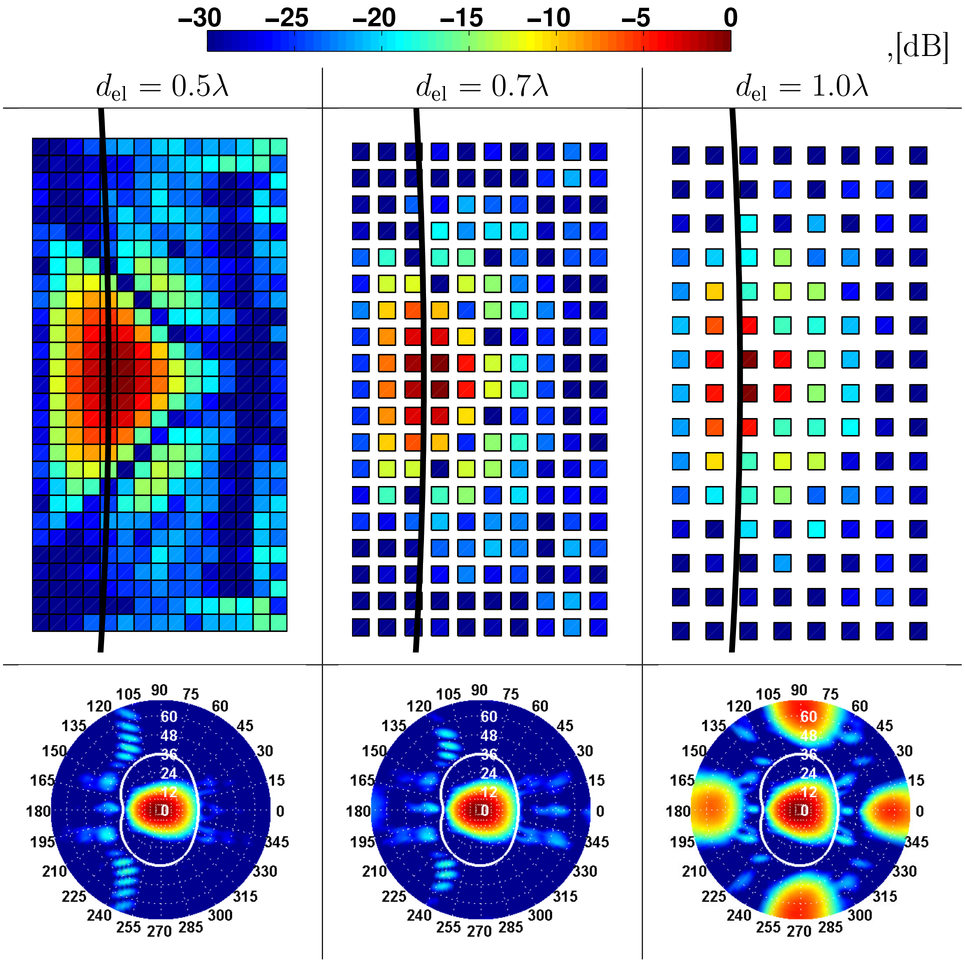

Figure 2: Effect of the inter-element separation distance d_{el} on (top) the optimized amplitude weights of the FPA sub-array elements for the centre beam, as determined for the customized beamformer maximizing the beam efficiency (@−20 dB) with constraints on the side-lobe and cross-polarization levels towards the Earth, and (bottom) the resultant illumination patterns of the reflector antenna. The array size is fixed to $L_{\mathrm{x}} \times L_{\mathrm{y}} = 7\lambda \times 14\lambda$.

3 FPA-system design

3.1 Antenna array model

As a starting point of the design procedure, we have considered a sub-array for the centre beam. The selected initial model of this sub-array represents a dual-polarized antenna array consisting of $15 \times 29 \times 2$ interconnected tapered-slot antenna elements with the inter-element distance varying from 0.5λ to 1.0λ. This model is based on the MoM-CBFM model of the $8 \times 9 \times 2$ element array in [4]. To reduce the computational time for our parametric studies, we have simplified this original model by assuming that all embedded element patterns are identical to that of the central element of the finite array. The sub-array embedded element patterns have been imported into the reflector antenna software GRASP10 to compute the secondary embedded element patterns (after reflection from the dish), which, in turn, have been used to simulate the overall receiving system (according to the procedure in [4]), and to optimize its beamforming weights. It is worth mentioning that this analysis and optimization procedure accounts for the effects of the array mutual coupling, elements loading, as well as the signal and noise properties of the terminating amplifiers. The later effects have not been considered yet and are left for the future work.

3.2 Beamforming algorithms

For this study, we have implemented two types of signal-processing beamforming algorithms: (i) standard maximum directivity beamformer (see Eq.3 in [4]), which is equivalent (under certain conditions) to the Conjugate Field Matching (CFM) beamformer, as commonly applied to conventional FPAs of horns; and (ii) customized beamformer that has been formulated so as to maximize the beam efficiency (within the -20dB area), subject to constraints on the total radiated power towards the coastal region. The latter approach is expected to lead to the optimal radiometer performance in terms of the minimum distance to land, minimum cross-polarization and side-lobe levels, and thus improved resistance to RFI.

Figure 3 illustrates the examples of the optimized weight coefficients for the sub-array elements for the CFM and constrained beamformers, where the corresponding aperture-field distributions and footprint patterns of the antenna are presented below. As expected, the CFM beamformer leads to the highest directivity (the larger area of the reflector aperture that is illuminated efficiently), as compared to that of the constrained beamformer. On the other hand, the latter has a significantly improved shape of the footprint and much lower side-lobe level.

3.3 Parametric study

The analysis of the weighting coefficients on Fig. 3 shows that many elements are weakly excited, so the size of the initially selected sub-array can be reduced along x-direction. Note that in y-direction, the sub-array cannot be smaller, since these elements will be used to form the scanning beams. We have, therefore, performed a parametric study by looking into the smaller arrays sizes, as well as different values of the element separation distances.

Inter-element separation distance

Fig. 2 and Fig. 4 present the first set of the results obtained for the array $7\lambda \times 14\lambda$ and constrained beamformer – that illustrate the effect of the element separation distance d_{el} on the optimized weights and corresponding aperture-field distribution of the reflector. As observed, the most dense FPA provides a very fine sampling of

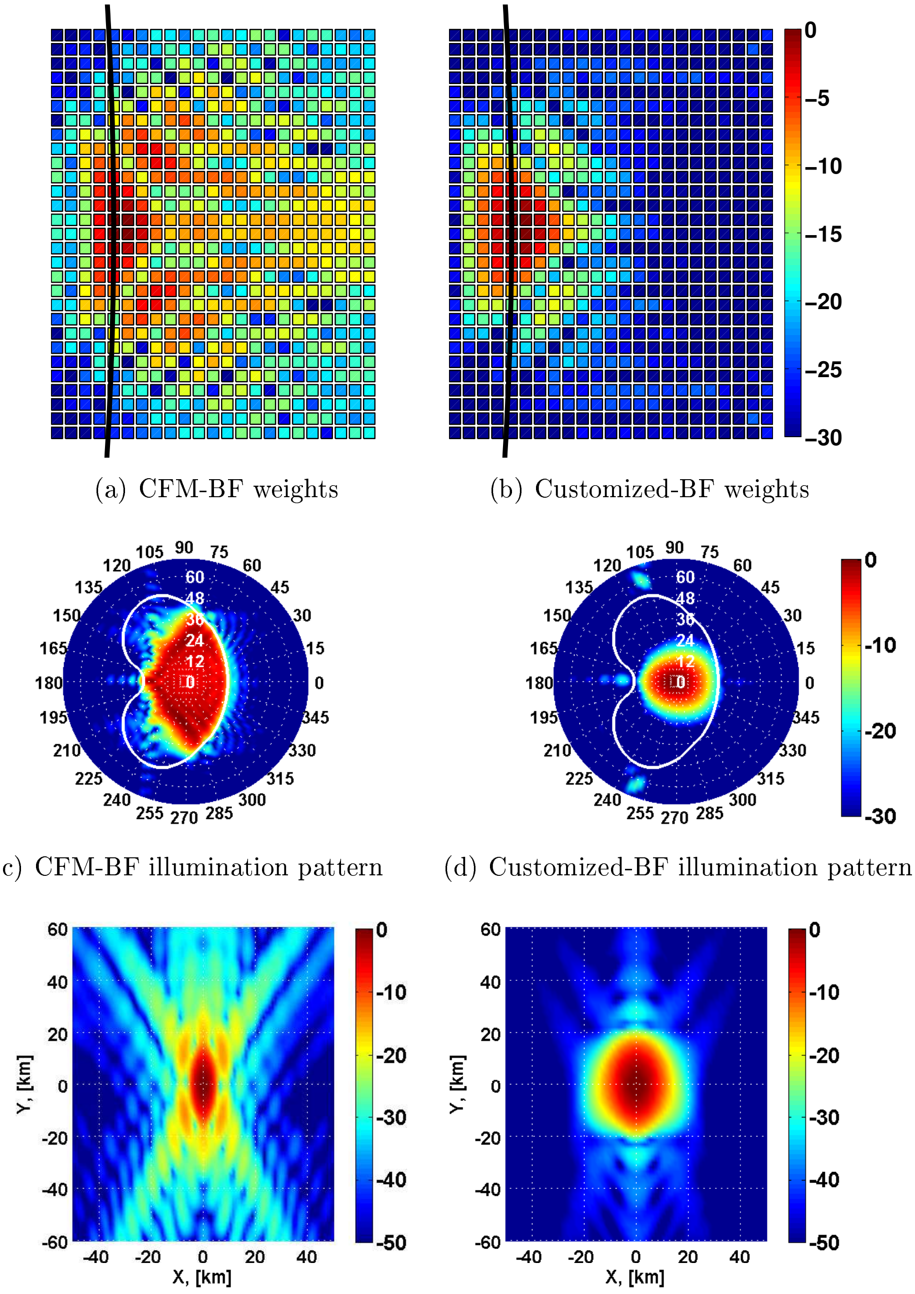

(a) CFM-BF weights (b) Customized-BF weights

(c) CFM-BF illumination pattern (d) Customized-BF illumination pattern

(e) CFM-BF footprint (f) Customized-BF footprint

Figure 3: Comparison of two beamforming algorithms for the FPA sub-array for the centre beam: (a, b) the array element amplitude weight coefficients for the CFM beamformer (CFM-BF) and customized beamformer (Customized-BF), where each block represents an element and the black line shows the focal line of the torus reflector, and the the corresponding (c, d) reflector aperture illumination patterns and (e, f) footprint patterns on the sea-surface.

the array aperture field, resulting in the well-behaved illumination of the reflector, whereas the field produced by the most sparse array with 1λ-spaced elements exhibits

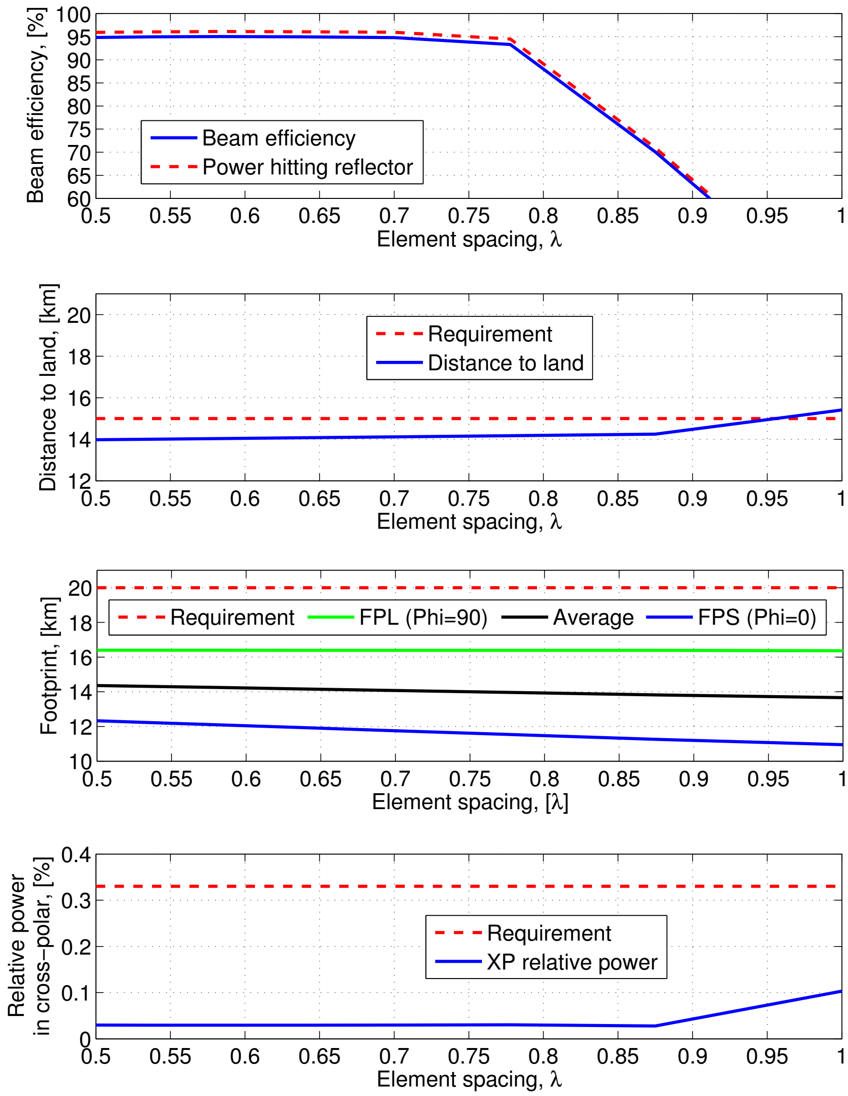

Figure 4: Radiometer characteristics as function of the FPA element spacing (d_{el}) for the case of $L_{\text{x}} = 7\lambda$, including (from top to bottom) the antenna beam efficiency (defined within the -20 dB region), distance to land at which the radiometer should stop working correctly, averaged footprint and relative cross-polarization power loss in the entire region.

the grating lobes. The importance of the array density can be also seen from the computed radiometer parameters that are shown on Fig. 4 as function of d_{el}. It is interesting to see that the beam efficiency and cross-polarization power are affected most when the array becomes sparse ($d_{\text{el}} > 0.7\lambda$) – because the array aperture field gets under-sampled and the grating lobes start to appear –, while the minimum distance from land remains small almost over the entire region of d_{el} (and within the required value of 15 km) thanks to the low side-lobes in the coastal region that are forced by the beamformer.

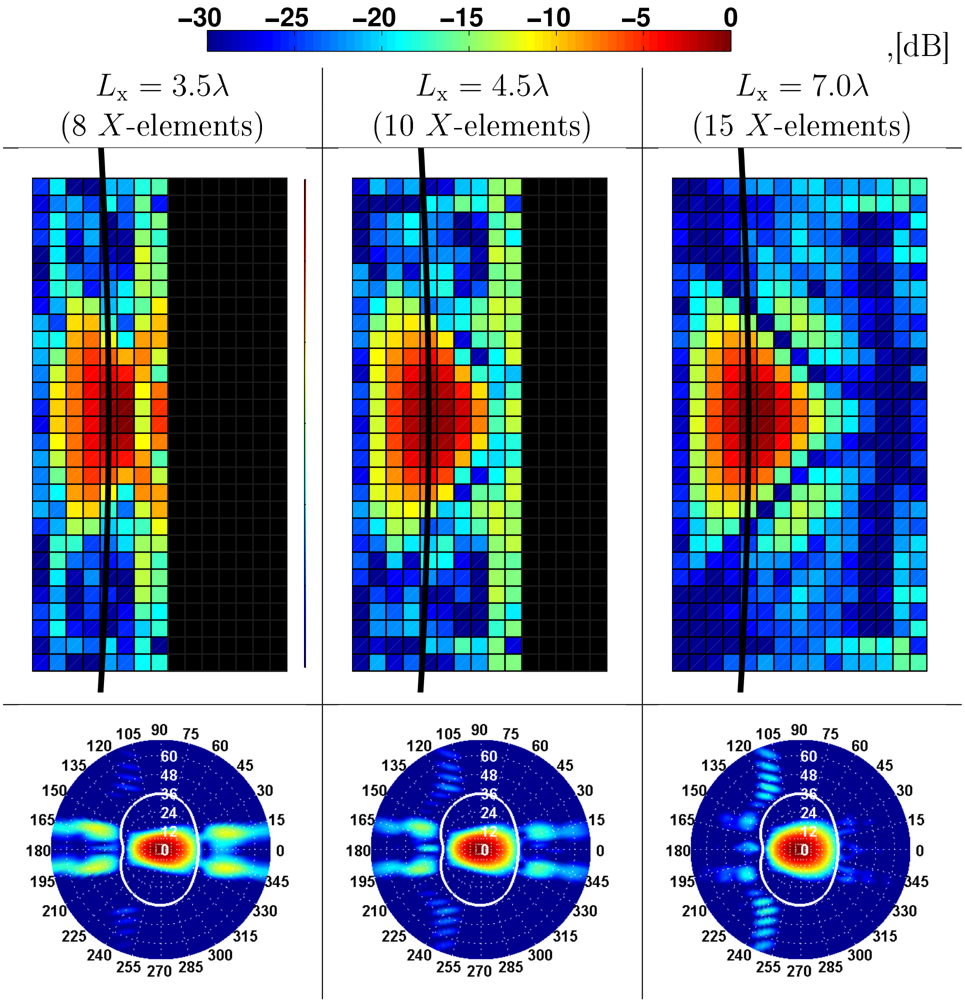

Figure 5: Effect of the array size L_x on (top) the optimized amplitude weights of the FPA sub-array elements for the centre beam, as determined for the customized beamformer maximizing the beam efficiency (@-20 dB) with constraints on the side-lobe and cross-polarization levels towards the coastal region, and (bottom) the resultant illumination patterns of the reflector antenna. The distance between the array elements is fixed to $d_{el} = 0.5\lambda$.

Array size

The second set of the parametric study results is illustrated on Fig. 5 and Fig. 6, that show the effect of the sub-array size along x-direction, for the case of $d_{el} = 0.5\lambda$. These results demonstrate that all the radiometer parameters are sensitive to change of the array size, and their values degrade when it becomes smaller. This observation is expected, since the larger arrays have more degrees of freedom that the smaller ones. In general, the minimum size of the array along x-direction should be $\sim 4.9\lambda$ to realize the beam efficiency higher than $\sim 91\%$ with the distance to coast according to the requirements. For $d_{el} = 0.7\lambda$, this would corresponds to $8 \times 21 \times 2$ elements in total for the center sub-array. Interestingly enough, the beam efficiency of twice

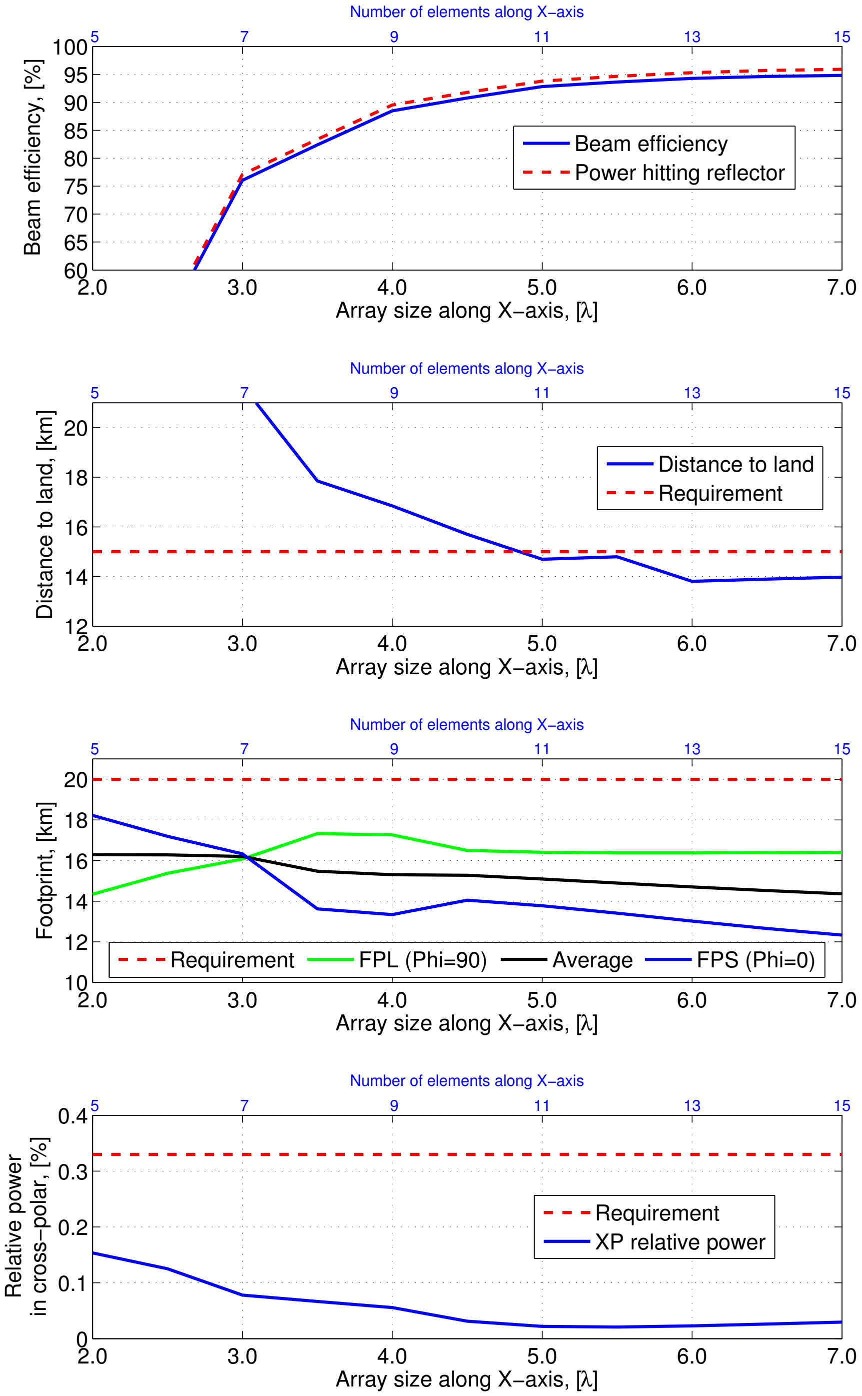

Figure 6: Radiometer characteristics as function of the number of elements (array size) alone X-axis for the case of $d_{\mathrm{el}} = 0.5\lambda$, including (from top to bottom) the antenna beam efficiency (defined within the -20 dB region), distance to land at which the radiometer should stop working correctly, averaged footprint and relative cross-polarization power loss in the entire Earth region.

larger sub-array ($L_x = 9\lambda$) would be only a few percent higher ($\sim 96\%$) with the similar values of other considered radiometer parameters.

4 Conclusions

Table 1: Radiometer characteristics for different FPAs

	Gauss. feed model	**FPA with CFM-BF** $15 \times 29 \times 2$ **elem.** $d_{el} = 0.5\lambda$	**FPA with Cust-BF** $15 \times 29 \times 2$ **elem.** $d_{el} = 0.5\lambda$	**FPA with Cust-BF** $8 \times 21 \times 2$ **elem.** $d_{el} = 0.7\lambda$
Beam efficiency [%]	84.2	85.1	94.9	92.0
XP-power, [%] (<0.33% is req.)	0.39	1.01	0.03	0.02
Dist. to land, [km] (<15 km is req.)	87.8	116.6	14.0	15.9
Beam width, [deg]	0.600	0.351	0.512	0.538
Footprint (FP), [km] (<20 km is req.)	16.9	10.5	14.4	14.9
FP ellipticity	1.38	2.14	1.33	1.22

Table 1 summarizes the X-band performance parameters of the pushbroom radiometer that employs a torus reflector antenna with the 5-m diameter projected aperture for different types of FPAs (i.e conventional FPAs of horns in one-horn-per-beam-configuration that are herein represented by Gaussian beams, and dense FPAs of tapered-slot antenna elements with different beamforming scenarios). As expected, dense FPAs have obvious benefits in achieving the required minimum distance to coast and footprint roundness, while meeting all other radiometer requirements. The minimum size of the FPA sub-array has been found to be 8×21 elements (for each polarization) with the inter-element separation distance in the order of $d_{el} = 0.7\lambda$, for the considered initial model of the array.

5 Acknowledgment

The present work has been carried out in the framework of the "Advanced Multi-Beam Radiometers" project that is a collaborative effort between TICRA, DTU-Space (Denmark), HPS (Germany) and Chalmers, funded by European Space Agency (ESA). The toroidal push-broom reflector antenna used for our study has been designed by TICRA. The authors would like to acknowledge the Swedish Research Council for providing partial support to this work through the VR project grant.

References

[1] (2013, Sep.). [Online]. Available: http://earthobservatory.nasa.gov/Features/EO1/eo1_2.php

[2] P. Nielsen, K. Pontoppidan, J. Heeboell, and B. L. Stradic, “Design, manufacture and test of a pushbroom radiometer,” in *Antennas and Propagation, 1989. ICAP 89., Sixth International Conference on (Conf. Publ. No.301)*, Coventry, United Kingdom, Apr. 1989, pp. 126–130.

[3] R. Hoferer and Y. Rahmat-Samii, “RF characterization of an inflatable parabolic torus reflector antenna for space-borne applications,” *IEEE Trans. Antennas Propag.*, vol. 46, no. 10, pp. 1449–1457, Oct. 1998.

[4] M. V. Ivashina, O. Iupikov, R. Maaskant, W. A. van Cappellen, and T. Oosterloo, “An optimal beamforming strategy for wide-field surveys with phased-array-fed reflector antennas,” *IEEE Trans. Antennas Propag.*, vol. 59, no. 6, pp. 1864–1875, Jun. 2011.

[5] W. A. van Cappellen and L. Bakker, “APERTIF: Phased array feeds for the Westerbork synthesis radio telescope,” in *IEEE International Symposium on Proc. Phased Array Systems and Technology (ARRAY)*, Boston, Oct. 2010, pp. 640–647.

[6] K. F. Warnick, “High efficiency phased array feed antennas for large radio telescopes and small satellite communication terminals,” in *Proc. European Conference on Antennas and Propag. (EuCAP)*, Gothenburg, Sweden, Apr. 2013, pp. 448–449.

[7] S. G. Hay, J. D. O’Sullivan, J. S. Kot, C. Granet, A. Grancea, A. R. Forsyth, and D. H. Hayman, “Focal plane array development for ASKAP (australian SKA pathfinder),” in *Proc. European Conference on Antennas and Propag. (EuCAP)*, Edinburgh, UK, Nov. 2007, pp. 1–5.

[8] C. Cappellin, K. Pontoppidan, P. Nielsen, N. Skou, S. S. Søbjærg, A. Ihle, D. Hartmann, M. Ivashina, O.Iupikov, and K. v. t Klooster, “Novel multi-beam radiometers for accurate ocean surveillance,” in *Proc. European Conference on Antennas and Propag. (EuCAP)*, The Hague, The Netherlands, Apr. 2014, pp. 1–4.

[9] C. Kidd, “Radio frequency interference at passive microwave earth observation frequencies,” *Int. Journal of Remote Sensing*, vol. 27, no. 18, pp. 3853–3865, Sep. 2006.

Paper F

Improving the Calibration Efficiency of an Array Fed Reflector Antenna Through Constrained Beamforming

A. Young; M. V. Ivashina; R. Maaskant; O. A. Iupikov and D. B. Davidson

IEEE Transactions on Antennas and Propagation, vol.61, no.7, 2013

The layout of this paper has been revised in order to comply with the rest of the thesis.

Improving the Calibration Efficiency of an Array Fed Reflector Antenna Through Constrained Beamforming

A. Young; M. V. Ivashina; R. Maaskant; O. A. Iupikov and D. B. Davidson

Abstract

Calibrating for the radiation pattern of a multi-beam Phased Array Feed (*PAF*) based radio telescope largely depends on the accuracy of the pattern model, and the availability of suitable reference sources to solve for the unknown parameters in the pattern model. It is shown how the efficiency of this pattern calibration for PAF antennas can be improved by conforming the beamformed far field patterns to a two-parameter physics-based analytic reference model through the use of a Linearly Constrained Minimum Variance (*LCMV*) beamformer. Through this approach, which requires only a few calibration measurements, an accurate and simple pattern model is obtained. The effects of the model parameters on the directivity and sidelobe levels of multiple scanned beams are investigated, and these results are used in an example PAF beamformer design for the proposed MeerKAT antenna. Compared to a typically used Maximum Directivity (*MaxDir*) beamformer, the proposed constrained beamforming method is able to produce beam patterns over a wide Field-of-View (*FoV*) that are modeled with a higher degree of accuracy and result in a significant reduction in pattern calibration complexity.

1 Introduction

Calibration of radio telescopes requires accurate models of the instrumental parameters and propagation conditions that affect the reception of radio waves [1]. These effects vary over time and the model parameters have to be determined at the time of observation through a number of calibration measurements. Furthermore, the calibration measurements should complete in a relatively short time and may be repeated often over the course of an observation during which the instrumental and atmospheric conditions can change significantly. One of the instrumental parameters that needs accurate characterization is the radiation pattern of the antenna, which is especially challenging in the arena of future array based multiple beam radio telescopes [2–4], both due to the complexity of these instruments, as well as the increased size of the Field-of-View (*FoV*). Above the requirement that the radiation pattern should be accurately known, currently developed techniques for the pattern calibration of these devices also emphasize the need for beams[1] over the FoV that are similar in shape, and that each beam varies smoothly with time, frequency, and over the main beam angular region [5]. Such beams can be described by simpler models, which reduce the number of pattern model parameters that need to be solved for, and also simplify the complexity of direction dependent calibration which is vitally important for future radio telescopes [6–10]. However, achieving patterns exhibiting these qualities, while also meeting the already stringent sensitivity requirements, presents a difficult task.

Previously, beamforming techniques have been used to create similarly shaped beams over the FoV by conforming them to an elliptical reference pattern, but at the cost of a significant loss in sensitivity [6] (up to 25%). An initial study has shown that this loss can be reduced by applying the same beamforming technique, but using a reference pattern that more closely matches the natural radiation characteristics of large aperture antennas [11]. Therein, the first term of the Jacobi-Bessel (*JB*) series solution of reflector antenna far field patterns [12, 13] was used as a reference pattern to define directional constraints in a Linearly Constrained Minimum Variance (*LCMV*) beamforming Phased Array Feed (*PAF*). It was found that this first JB-term is sufficient to model the patterns of a prime focus single reflector antenna over a wide FoV of up to 5 beamwidths, over which the sensitivity reduction was less than 10%. However, when considering a larger scan range, phase aberration effects cause deformation of the radiation patterns to such an extent that this beam model is no longer accurate. Furthermore, when applying this model to an offset reflector antenna for which the asymmetric geometry exacerbates the deformation of scanned patterns [14, *cf.* Figs. 1 and 3], the inclusion of more physics-based information is necessary.

Here, the reference pattern of [11] is extended to model the widening of the scanned beam as well as the change in the phase distribution for an offset dual-reflector antenna by introducing two additional model parameters. It will be shown that this model allows for the accurate characterization of multiple beams over a wide FoV without the need to perform additional calibration measurements. The effects of the model parameters on the directivity and sidelobe levels are investigated for a proposed design of the MeerKAT radio telescope reflector antenna [15]. An LCMV beamformer is designed based on the results of this study, and its performance evaluated through comparison with a Maximum Directivity (*MaxDir*) beamformer.

[1] Often referred to as the *direction-dependent gain* or *primary beam* in the radio interferometer community.

2 Antenna Pattern Model

The reference pattern employed in [11] to constrain the main beam shape of a scanned reflector is based on the JB-series solution for modeling reflector antenna far field patterns. The first term in this series is the near-boresight approximation of the co-polarized far field pattern radiated by a circular aperture with a uniform amplitude and phase distribution [16], i.e.,

$$F_A(\theta,\phi) \propto \frac{J_1(ka\sin\theta)}{ka\sin\theta} \equiv \mathrm{jinc}(ka\sin\theta) \tag{1}$$

where a is the aperture radius, k is the free space wavenumber, and J_1 is the Bessel function of the first kind of order one. Patterns radiated by more general aperture field distributions, including off-axis patterns of a scanned reflector are represented as a sum of (possibly) many more JB-terms. However, the first term in the series is still dominant over an angular region around the beam maximum. To obtain a pattern function that applies to more general aperture field distributions, certain modifications to the reference pattern (1) are required as detailed below.

In order to control the beamwidth of the pattern model, an angular scaling parameter s is introduced by letting $a \to sa$, which enables accounting for widening of the beam due to under-illumination of the reflector aperture or coma aberration when scanning [17,18][2]. In this sense a distinction can be made between the *physical* aperture radius a, and an *effective* aperture radius sa, where $s \lesssim 1$.

Another limitation of (1) is that it assumes a constant phase distribution of the beam pattern. This implies that the phase reference of the pattern coincides with the phase center of the antenna, defined here for a small angular region of the far field around the main beam center. Whereas this condition is easily satisfied for an on-axis beam of a prime focus reflector, the proper choice for the phase reference is not straightforward for scanned beams. In the latter case it is more convenient to keep the phase reference fixed at the center of the projected aperture and to account for a phase variation over the main beam through multiplying the pattern model by

$$F_\psi(\theta,\phi) = \exp\left(j\Psi\sin\theta\cos(\phi-\phi_0)\right) \tag{2}$$

in which Ψ is a constant that determines the phase gradient, and ϕ_0 defines the direction of the phase center shift. The value of ϕ_0 can be determined by noting that for a scanned beam the phase center shift is in the scan plane. It can be shown that the value of Ψ is proportional to the phase center shift projected orthogonally to the direction of observation [19].

[2]The pattern deformations for off-axis scanning are known to be asymmetrical, and since the analytic model is used here to constrain the pattern shape so that it is easily modeled, we elect to use a circularly symmetric pattern model.

Combining (1) and (2) gives the extended reference pattern model[3]

$$F(s, \Psi; \theta, \phi) = \mathrm{jinc}(ksa \sin\theta) e^{j\Psi \sin\theta \cos(\phi - \phi_0)} \tag{3}$$

in which the the amplitude and phase distributions of the reference pattern are controlled independently by the parameters s and Ψ, respectively. Note that (3) will serve as a *reference pattern* for deriving the directional constraints in an LCMV beamformer, as well as a pattern *calibration model* to describe the realized beamformed pattern.

3 Beamforming Strategy

An LCMV beamformer is implemented which minimizes the power received by the antenna due to noise subject to linear constraints that conform the co-polarized pattern shape to the reference pattern in (3). The beamformer weights applied to the elements of the PAF are calculated according to [20] [21, p. 526]

$$\mathbf{w}_{\mathrm{LCMV}}^{H} = \mathbf{g}^{H} \left[\mathbf{G}^{H} \mathbf{C}^{-1} \mathbf{G} \right]^{-1} \mathbf{G}^{H} \mathbf{C}^{-1} \tag{4}$$

in which $\mathbf{x}^H$ means the complex conjugate transpose of $\mathbf{x}$, $\mathbf{C}$ is the noise covariance matrix, $\mathbf{g}$ is the constraints vector, and $\mathbf{G}$ is the directional constraint matrix. For L elements in the array and constraints enforced in the K different directions $\{\Omega_1, \Omega_2, \ldots, \Omega_K\}$, $\mathbf{G}$ is an $L \times K$ matrix in which the ith column contains the signal response vector of the array due to a plane wave incident from direction Ω_i, and the corresponding element g_i in the vector $\mathbf{g}$ is the constraint value enforced on the pattern in that direction. The choice of these constraint parameters is discussed in the following subsections.

In this study the performance of the LCMV beamformer is compared to that for the standard MaxSNR beamformer (no directional constraints). In this case the beamformer weights are calculated according to [22] [21, p. 450]

$$\mathbf{w}_{\mathrm{MaxSNR}} = \mathbf{C}^{-1} \mathbf{v} \tag{5}$$

where $\mathbf{v}$ is the signal response vector of the array due to a plane wave incident from the direction of interest. In this study a noiseless system is assumed which means that the noise correlation matrix $\mathbf{C}$ can be taken equal to the identity matrix, and therefore the weights in (5) maximize the received signal power. It can be shown that this is approximately equivalent to maximizing the directivity, if the antenna exhibits low loss and low scattering, as is the case for the PAF used herein. Therefore the beamformer using the weights in (5) shall hereafter be referred to as a *MaxDir* (Maximum Directivity) beamformer.

[3]Henceforth we assume that (θ, ϕ) are defined in a local coordinate system for each beam in which the maximum is at $\theta = 0$.

3.1 Number of Constraints and Pattern Calibration Measurements

Each of the weights applied to the PAF elements presents a complex Degree of Freedom (*DoF*) available for optimizing the beamformed pattern, and for each constraint enforced on the pattern shape the number of DoFs available to maximize the directivity is reduced. The implication of this is that constraints should be selected carefully to obtain the desired pattern shape while retaining enough freedom in the system to achieve a sufficiently high directivity.

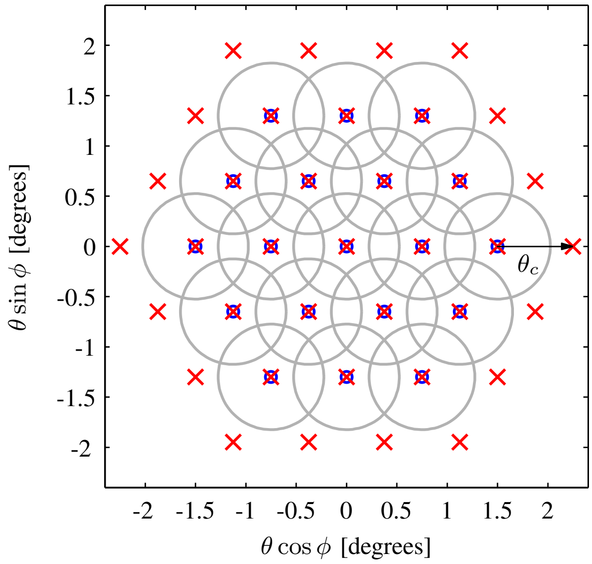

Figure 1: Beams arranged over the FoV to enable reuse of constraint directions between adjacent beams. Nominal half-power contours (HPBW = 1°) and constraint positions of each beam shown as solid lines and crosses, respectively.

Furthermore, the number of constraints has an impact on the calibration efficiency because a pattern calibration measurement is required for each constraint direction to determine the signal response vector of the PAF [22]. Since these measurements can become time consuming, we need to minimize the number of constraint directions to ensure that the system parameters do not drift significantly during this procedure. It is worth pointing out that since both the amplitude and phase of the signal response vectors are needed, this may require the use of an auxiliary antenna to recover the phase information in addition to a natural celestial calibration source [23].

3.2 Constraint Positions

We aim to conform the beam to the reference pattern down to a certain level below the beam maximum, so we choose to position the constraints within the corresponding angular region. Also, the total required number of pattern calibration measurements may be reduced by positioning the constraint directions at the centers of adjacent beams, as shown in Fig. 1. This allows the reuse of measurement data between multiple beams which is readily available in this type of measurement. In this example six constraints are enforced in a circularly symmetric fashion around, and an angular distance θ_c from the beam center for each beam. This arrangement results in a fine enough sampling of the FoV since the half-power beams overlap [22], and the constraints are enforced around the -8 to -5 dB level. In this case only 37 pattern calibration measurements are needed to realize a total of 19 constrained beams over the FoV, which is a minor increase over that for unconstrained beamforming as in (5). The 18 additional measurements are necessary for the constraints enforced around the edge of the FoV.

3.3 Constraints Vector

The constraints vector $\mathbf{g}$ in (4) is formed by evaluating the reference pattern in (3) at the beam center and the directions of constraints $\Omega_i = \{\theta_c, \phi_i\}$, i.e.,

$$g_i = \begin{cases} F(s, \Psi; 0, 0) & \text{for } i = 1 \\ F(s, \Psi; \theta_c, \phi_i) & \text{for } i = 2, 3, \ldots, 7, \end{cases} \tag{6}$$

where the selection of the model parameters s and Ψ has to be made for each scan direction to account for the beam widening and the increasing phase gradient over the main lobe region. In order not to compromise the beam sensitivity too much, it is natural to derive the initial physics-based values $s = s_0$ and $\Psi = \Psi_0$ from the reference patterns realized by the MaxDir beamformer, i.e.,

$$s_0 = \frac{a_{\text{eff,MaxDir}}}{a} = \frac{\lambda\sqrt{D_{\text{MaxDir}}}}{2\pi a} \tag{7a}$$

$$\Psi_0 = \left.\frac{\partial \psi_{\text{MaxDir}}}{\partial \theta}\right|_{\theta=0,\phi=\phi_0} \tag{7b}$$

where $a_{\text{eff,MaxDir}}$ is the effective aperture radius, and D_{MaxDir} and ψ_{MaxDir} are the directivity and phase pattern over the main lobe region, respectively, of the MaxDir beam. Using thus obtained values for the parameters s and Ψ result in rotationally symmetric beams that have sensitivities close to the MaxDir beams. However, this choice leads to a sidelobe level (SLL) that can be relatively high for certain (off-axis) beams. Hence, the optimum values for s and Ψ may be slightly different from s_0 and Ψ_0 depending upon the required antenna beam performance, such as minimum beam sensitivity and maximum allowable SLL, as explained below for a numerical example.

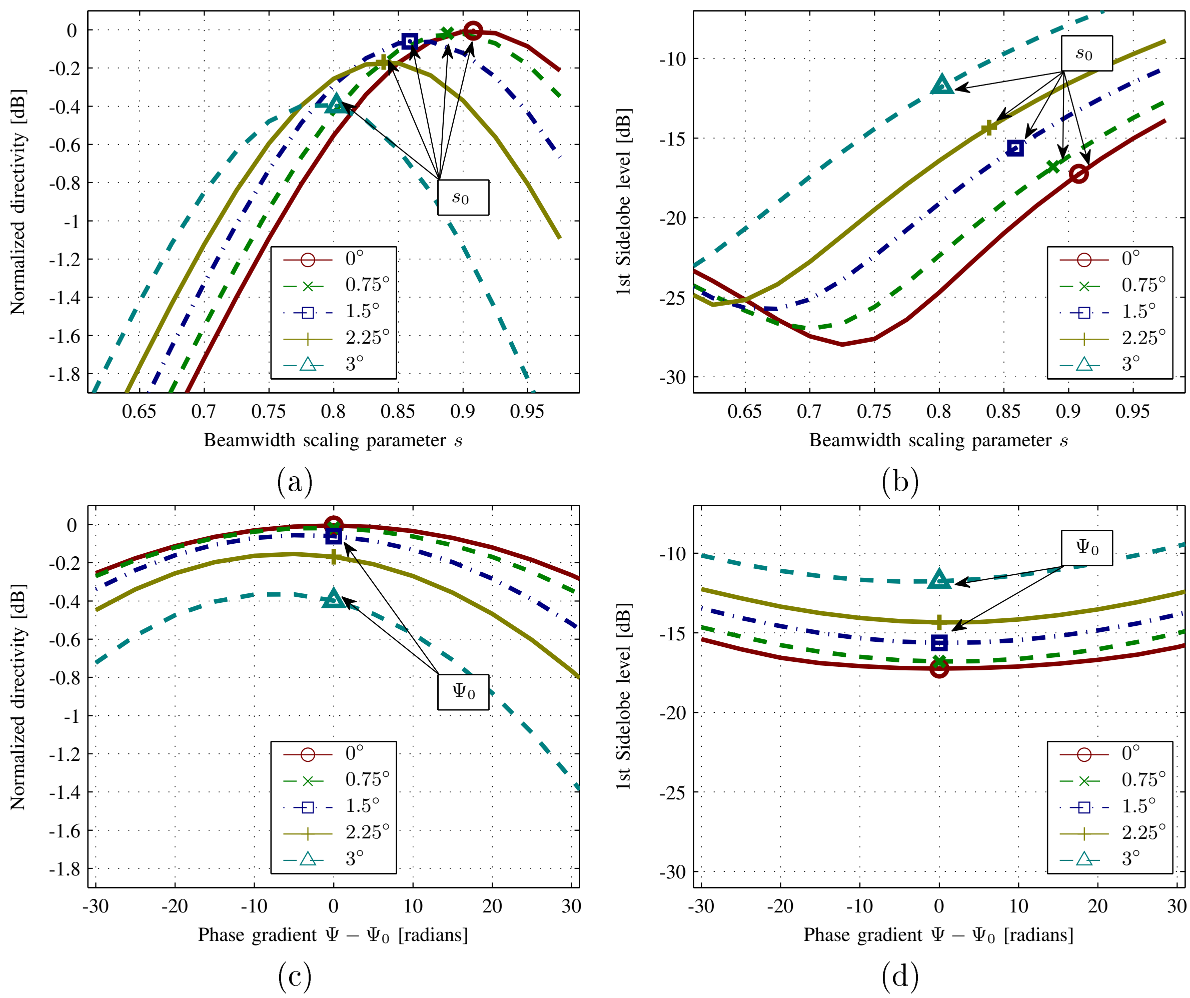

Figure 2: Effect of model parameters on beam pattern performance. (a) and (c) show the directivity of scanned LCMV patterns relative to that of the on-axis MaxDir pattern for various values of s and Ψ, respectively; (b) and (d) show the highest SLL of scanned LCMV patterns for various values of s and Ψ, respectively. Markers indicate the results for $s = s_0$ and $\Psi = \Psi_0$ for each scan direction.

4 Numerical Results

In this section we investigate the trade-off effects of the beam model parameters s and Ψ on the directivity and SLL. After choosing s and Ψ, the beam model accuracy is examined as the difference between the resulting LCMV-beamformed pattern and the reference beam. As a numerical example, we present results for an offset Gregorian geometry based on the MeerKAT radio telescope reflector antenna [15] by employing simulated primary far-field patterns of the APERTIF PAF [6]. The reflector has a projected diameter of 13.5 m (64λ at 1.42 GHz) and an equivalent focal length to diameter ratio (F/D) of 0.55. The APERTIF PAF is a dual-polarized array composed of 121 tapered slot antenna elements. Here all elements in the array (both polarizations) are employed to produce patterns on the sky for each nominal polarization (as opposed to a bi-scalar beamfomer wherein only elements of one polarization are used, *cf.* [24]). Results presented here are for only one nominal polarization, as the results for either polarization are very similar. The numerical results are shown for the operating frequency of 1.42 GHz at which the half-power beamwidth (HPBW) is approximately 1°, and results were obtained using a toolbox interface [22] to the GRASP software.

4.1 Beam Directivity and Side Lobe Levels

Fig. 2(a) shows the directivity of the LCMV-scanned patterns relative to the corresponding MaxDir patterns as a function of s (with $\Psi = \Psi_0$) over a scan range of 3 beamwidths in the symmetry plane[4]. Markers indicate the results for the initial values $s = s_0$ that were derived from the MaxDir beams. As expected, the highest directivity is achieved if s is close to s_0, except for far off-axis patterns where it occurs for slightly smaller values of s. This is attributed to the fact that the computation of s_0 is based solely on the directivity of the MaxDir elliptically-shaped pattern, while s_0 is applied to rotationally symmetric patterns pertaining to the same effective aperture size. It is also observed that when choosing $s = s_0$, the loss incurred by constrained beamforming is relatively small (< 0.4 dB) over the entire FoV. Letting $s \to 1$ results in the edge illumination taper approaching 0 dB as the primary (feed) pattern widens, and a subsequent decrease in directivity due to increasing spillover loss.

The effect of s on the 1st SLL performance of the LCMV patterns is shown in Fig. 2(b). As one can see, the choice of $s = s_0$ leads to a significant variation of the SLLs of the scanned beams where the minimum (for the on-axis direction) and maximum (for a scan angle of 3 beamwidths) are around -17 dB and -12 dB, respectively. Decreasing the value of s improves the SLL, albeit at a moderate cost of a reduction in directivity. This is in accordance with the familiar trade-off between directivity and SLL for reflector antennas. The 2nd SLL is affected similarly to the 1st SLL when s is varied, and these results are therefore not shown.

The effects of Ψ on the relative directivity and SLL of the LCMV beamformed patterns were also investigated and the results are shown in Figs. 2(c) and (d). In these figures, the abscissae represent the difference $\Psi - \Psi_0$ calculated for each scan direction. Over the FoV, the value of Ψ_0 decreases monotonically from 0 rad for the on-axis pattern to -33 rad for the farthest off-axis scanned pattern, indicating a steady shift of the antenna phase center from the phase reference point. Choosing Ψ close to Ψ_0 – as opposed to setting it to zero, thereby effectively reducing the pattern model to (1) – resulted in a significant improvement in directivity of far off-axis scanned

[4]Although results are only shown for scanning in a single plane, the conclusions are valid for scanning in all ϕ-directions.

patterns. This underlines the importance of using a proper reference pattern function such as (3) which represents a more accurate description of the (off-axis) radiation characteristics of the antenna. The effect of small variations of Ψ around the value Ψ_0 on the relative directivity and SLLs was found to be less pronounced than the effect of parameter s, so that, generally, the choice $\Psi = \Psi_0$ yielded the best results.

4.2 Calibration Performance

A deviation of the actual beam shape from the one predicted through calibration measurements sets constraints on the dynamic range of the mosaicked images. Although the relationship between the desired dynamic range and pattern calibration error is very complex (and typically requires the analysis of the error propagation effects in the image plane [25,26]), the required accuracy of the pattern model can be approximately derived from the required image fidelity [27] which is limited by the maximum error present in the beam model. In this section we will therefore use the maximum normalized error in the complex voltage pattern within the 10 dB region when approximating realized beam patterns with (3) as a measure of beamshape calibratibility.

The effect of s on the calibratibility of LCMV beamformed patterns is shown in Fig. 3(a). Using the MaxDir equivalent value $s = s_0$ the maximum error ranges from 0.7 % for on-axis up to 4 % for the widest scan angle. Decreasing the parameter over the range $s \lesssim s_0$ is seen to slowly increase the model error, whereas increasing $s > s_0$ is seen to have a more dramatic effect on the model accuracy for wider scan directions due to the increase of the 1st SLL above the 10 dB level. In Fig. 3(b) the effect of Ψ on the calibratibility is shown and for this figure of merit the optimal choice for the phase gradient is as before $\Psi = \Psi_0$.

Since the constrained beamformer ensures that the realized beam conforms exactly to (3) at the constraint positions the model error is smallest in the vicinity of these points and the placement of constraints may be optimized to minimize this error within a certain angular region. The effect of θ_c on the pattern calibratibility is shown in Fig. 3(c). Markers indicate the power level relative to pattern maximum that correspond to the values of θ_c. The optimal placement of constraints is seen to be around the -5 dB to -7 dB level.

Furthermore, to examine how the technique performs over a range of frequencies we repeated the above described analysis at several frequencies within the antenna array operation band from 1 to 1.75 GHz. In this study, frequency-dependent parameters were scaled for each of these frequencies (scan directions, positions of constraints for LCMV beamforming, etc.). The results obtained have shown that at the lower frequencies the FoV is limited by the size of the array (that is the case for any type of the PAF beamformers), although the results for the on-axis and closer scanned directions are similar to those at 1.42 GHz. Hence, the advantages of using the proposed

LCMV-based beamforming are also applicable at lower frequencies over a relatively smaller FoV. For higher frequencies, the results for all scan directions (within the FoV of ± 3 beamwidths) are very similar to those at 1.42 GHz. Based on these observations, we can conclude that the proposed beamforming technique ensures the smooth characteristics of the resulting FoV calibration over a wide frequency band, and does not require additional constraints due to frequency variation.

4.3 Comparison of MaxDir and LCMV beamformers

Using the results from Section 4.1, an LCMV beamformer was implemented to produce a number of beams over a dense grid within an angular region $\theta < 3°$. For each LCMV beam the value of s was chosen such that the 1st SLL is below -17 dB, and $\Psi = \Psi_0$ as calculated from a MaxDir beam towards the same scan direction. The performance of the MaxDir and LCMV produced beams were then compared for every scan direction within the angular region of interest.

In Fig. 4(a) the aperture efficiencies achieved with the respective beamformers are shown as a function of scan direction. The asymmetry of the results over the FoV is a consequence of the offset geometry and wide scanning towards $\phi = 0°$ is seen to result in the largest reduction in efficiency. A FoV was defined for each beamformer as the region within which the aperture efficiency is greater than 70%, the size of which was 23.6 and 19.3 square degrees for the MaxDir and LCMV beamformers, respectively. The boundary of each FoV is indicated on the plots in Fig. 4 as a solid black line, and the results presented below were calculated within the respective regions for the two beamformers.

The beamformers were compared by considering the maximum pattern calibration model error for each of the defined beams over the FoV, which is shown in Fig. 4(b). For the MaxDir beamformer this error ranges from 1.6% up to 10.4%, whereas for the LCMV beamformer the same error ranges from 0.5% up to 4.3% and presents a considerable improvement in accuracy. One prominent factor contributing to the relatively large model error for MaxDir beams, especially at wider scan angles, is the asymmetry of these patterns. As a comparison, the aspect ratio of the half-power contours of the MaxDir beams may be as high as 1.15:1, whereas for the LCMV beams this ratio is less than 1.01:1 for all scan directions. The symmetry of constrained beams therefore also present a significant advantage in terms of reducing the complexity of direction-dependent calibration [6].

Finally, the maximum 1st and 2nd SLLs are shown as a function of scan direction in Figs. 4(c) and (d), respectively. Compared to the MaxDir beams, the LCMV beams have 1st SLLs that are 0.8 dB lower and 2nd SLLs that are 1.0 dB lower, on average over the FoV. The 2nd SLL is of particular interest in the case of MeerKAT, for which the maximum is specified as -23 dB (L-band). The LCMV beamformer meets this specification over most of the FoV (except for wide scanning in the $\phi \approx 135°$, $225°$

directions), whereas the MaxDir beams exceed this limit over a much larger region. In order to quantify the trade-off in sensitivity for this reduction in sidelobes through constrained beamforming, LCMV beams were also realized to yield 1st SLLs within 0.2 dB of that for the MaxDir beams. Following this approach the size of the FoV could be increased by 4.6% to 20.2 square degrees.

5 Conclusions and Recommendations

A constrained beamforming technique that conforms multiple patterns on the sky to a physics-based analytic far field function was presented as a method to improve the calibration efficiency of an array fed reflector antenna. The effects of the two parameters in the analytic model on the pattern performance were investigated, and a procedure by which these parameters could be optimized was proposed. This beamforming approach was shown to have several performance benefits including circularly symmetric scanned beams over a wide FoV, even for non-symmetric reflector antennas. For the example of the MeerKAT offset Gregorian antenna, this strategy resulted in multiple beams with aperture efficiency above 70% that could be approximated down to the 10 dB level as a single analytic function with an error of less than 5%. In comparison with a conventional MaxDir beamformer, this would reduce the average pattern calibration model error by more than 50%. Finally, the proposed beamforming strategy was found to be effective across a wide frequency band by simply scaling all frequency dependent parameters.

Future work will include the assessment of the proposed beamforming in the presence of external and internal noise sources, as well as experimental demonstration for a practical system.

References

[1] O. Smirnov, "Revisiting the radio interferometer measurement equation. ii. calibration and direction-dependent effects," *Astronomy and Astrophysics*, vol. 527, Feb. 2011. [Online]. Available: http://arxiv.org/pdf/1101.1765v3.pdf

[2] S. Ellingson, T. Clarke, A. Cohen, J. Craig, N. Kassim, Y. Pihlstrom, L. Rickard, and G. Taylor, "The long wavelength array," *IEEE Trans. Antennas Propag.*, vol. 97, no. 8, pp. 1421–1430, Aug. 2009.

[3] M. D. Vos, A. Gunst, and R. Nijboer, "The lofar telescope: System architecture and signal processing," *IEEE Trans. Antennas Propag.*, vol. 97, no. 8, pp. 1431–1437, Aug. 2009.

[4] The SKA website. [Online]. Available: http://www.skatelescope.org/

[5] O. M. Smirnov, B. S. Frank, I. P. Theron, and I. Heywood, "Understanding the impact of beamshapes on radio interferometer imaging performance," in *Proc. Int. Conf. on Electromagn. in Adv. Applicat. (ICEAA)*, Cape Town, Sep. 2012, pp. 586–590.

[6] O. A. Iupikov, M. V. Ivashina, and O. M. Smirnov, "Reducing the complexity of the beam calibration models of phased-array radio telescopes," in *Proc. European Conference on Antennas and Propag. (EuCAP)*, Rome, Italy, Apr. 2011, pp. 930–933.

[7] B. D. Jeffs, K. F. Warnick, J. Landon, J. Waldron, D. Jones, J. R. Fisher, and R. Norrod, "Signal processing for phased array feeds in radio astronomical telescopes," *IEEE J. Selected Topics in Signal Processing*, vol. 2, no. 5, pp. 635–646, Oct. 2008.

[8] M. Elmer, B. Jeffs, K. F. Warnick, J. Fisher, and R. Norrod, "Beamformer design methods for radio astronomical phased array feeds," *IEEE Trans. Antennas Propag.*, vol. 60, no. 2, pp. 930–914, Feb. 2012.

[9] S. G. Hay, "SKA field of view de-rotation using connected array beam scanning with constant beam shape," in *Proc. 25th Asia-Pacific Microwave Conference*, Melbourne, Dec. 2011, pp. 1174–1177.

[10] S. J. Wijnholds, K. J. B. Grainge, and R. Nijboer, "Report on calibration and imaging working group activities," Calibration and Imaging Working Group, Technical Report, 2012.

[11] A. Young, R. Maaskant, M. V. Ivashina, and D. B. Davidson, "Performance evaluation of far field paterns for radio astronomy application through the use of the Jacobi-Bessel series," in *Proc. Int. Conf. on Electromagn. in Adv. Applicat. (ICEAA)*, Cape Town, Sep. 2012, pp. 884–887.

[12] V. Galindo-Israel and R. Mittra, "A new series representation for the radiation integral with application to reflector antennas," *IEEE Trans. Antennas Propag.*, vol. 55, no. 5, pp. 631–641, Sep. 1977.

[13] Y. Rahmat-Samii and V. Galindo-Israel, "Shaped reflector antenna analysis using the Jacobi-Bessel series," *IEEE Trans. Antennas Propag.*, vol. 28, no. 4, pp. 425–435, Jul. 1980.

[14] M. V. Ivashina and C. G. M. van't Klooster, "Focal fields in reflector antennas and associated array feed synthesis for high efficiency multi-beam performances," in *Proc. 25th ESA Workshop on Satellite Antenna Technologies*, Noordwijk, The Netherlands, Sep. 2002, pp. 339–346.

[15] I. Theron, R. Lehmensiek, and D. de Villiers, "The design of the meerkat dish optics," in *Proc. Int. Conf. on Electromagn. in Adv. Applicat. (ICEAA)*, Cape Town, Sep. 2012, pp. 539–542.

[16] R. C. Hansen, "A one-parameter circular aperture distribution with narrow beamwidth and low sidelobes," *IEEE Trans. Antennas Propag.*, vol. 24, no. 4, pp. 477–480, Jul. 1976.

[17] J. Ruze, "Lateral-feed displacement in a paraboloid," *IEEE Trans. Antennas Propag.*, vol. 13, no. 5, pp. 660–665, Sep. 1965.

[18] W. A. Imbriale, P. G. Ingerson, , and W. C. Wong, "Large lateral feed displacements in a parabolic reflector," *IEEE Trans. Antennas Propag.*, vol. 22, no. 6, pp. 742–745, Nov. 1974.

[19] Y. Y. Hu, "A method of determining phase centers and its application to electromagnetic horns," J. Franklin Inst., Technical Report, Jan. 1966.

[20] O. I. Frost, "An algorithm for linearly constrained adaptive array processing," *Proceedings of the IEEE*, vol. 60, no. 8, pp. 926–935, Aug. 1972.

[21] H. L. van Trees, *Optimum Array Processing – Part IV of Detection, Estimation, and Modulation Theory.* New York: Wiley, 2002.

[22] M. V. Ivashina, O. Iupikov, R. Maaskant, W. A. van Cappellen, and T. Oosterloo, "An optimal beamforming strategy for wide-field surveys with phased-array-fed reflector antennas," *IEEE Trans. Antennas Propag.*, vol. 59, no. 6, pp. 1864–1875, Jun. 2011.

[23] P. G. Smith, "Measurement of the complete far-field pattern of large antennas by radio-star sources," *IEEE Trans. Antennas Propag.*, vol. 14, no. 1, pp. 6–16, Jan. 1966.

[24] W. van Cappellen, S. Wijnholds, and L. Bakker, "Experimental evaluation of polarimetric beamformers for an l-band phased array feed," in *Proc. European Conference on Antennas and Propag. (EuCAP)*, Prague, Czech Republic, Mar. 2012, pp. 634–637.

[25] S. J. Wijnholds, "Calculating beam pattern inaccuracies and their implications," in *in* 3GC-II Workshop, Albufeira, Portugal, Sep. 2011.

[26] O. M. Smirnov and M. V. Ivashina, "Element gain drifts as an imaging dynamic range limitation in PAF-based interferometers," in *General Assembly and Scientific Symposium, 2011 XXXth URSI*, Istanbul, Turkey, Aug. 2011, pp. 1–4.

[27] G. Harp, R. F. Ackermann, Z. J. Nadler, S. Blair, M. Davis, M. C. H. Wright, J. R. Forster, D. DeBoer, W. J. Welch, S. Atkinson, D. Backer, P. R. Backus, W. Barott, A. Bauermeister, L. Blitz, D. C. J. Bock, G. Bower, T. Bradford, C. Cheng, S. Croft, M. Dexter, J. Dreher, G. Engargiola, E. D. Fields, C. Heiles, T. Helfer, J. Jordan, S. Jorgensen, T. Kilsdonk, C. Gutierrez-Kraybill, G. Keating, C. Law, J. Lugten, D. H. E. MacMahon, P. McMahon, O. Milgrome, A. Siemion, K. Smolek, D. Thornton, T. Pierson, K. Randall, J. Ross, S. Shostak, J. Tarter, L. Urry, D. Werthimer, P. Williams, and D. Whysong, "Primary beam and dish surface characterization at the Allen telescope array by radio holography," *IEEE Trans. Antennas Propag.*, vol. 59, no. 6, pp. 2004–2021, Jun. 2011.

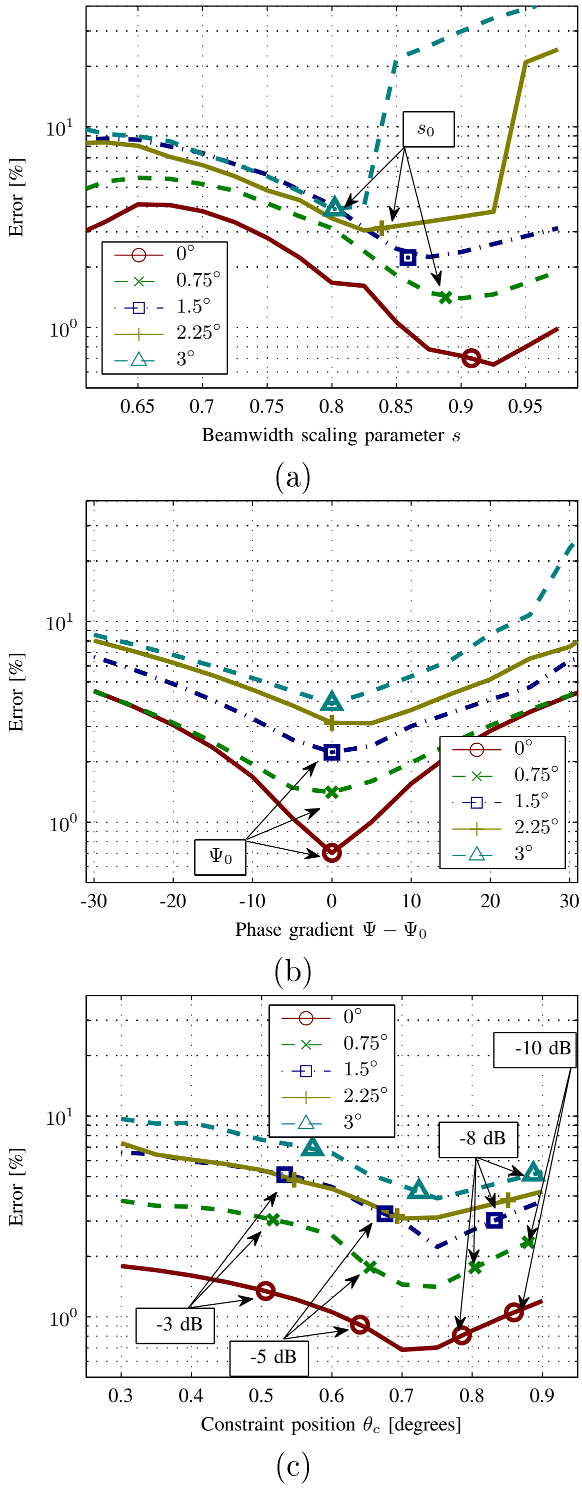

Figure 3: Maximum normalized error over the 10 dB beamwidth of the LCMV beamformed patterns when approximated by the analytical function (3), and using the same parameter values as was used to define directional constraints. The error is shown as a function of the parameter (a) s, (b) $\Psi - \Psi_0$, and (c) θ_c. Default values for these parameters are $s = s_0$, $\Psi = \Psi_0$, and $\theta_c = 0.75°$.

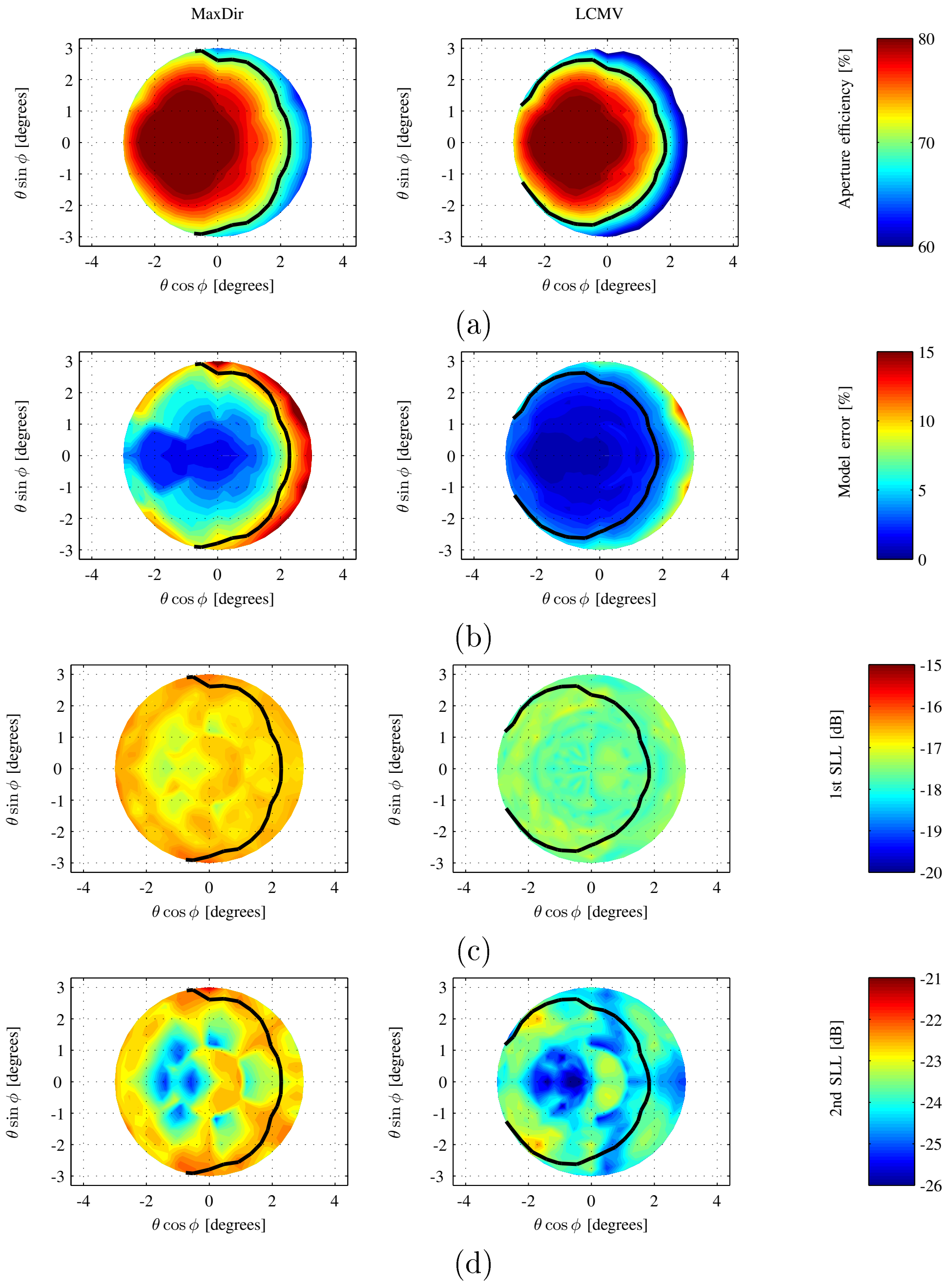

Figure 4: Comparison of LCMV and MaxDir beamformers over a $\theta \leq 3°$ angular region based on (a) aperture efficiency, (b) maximum beam model error, (c) 1st SLL, and (d) 2nd SLL. Figures of merit are shown as functions of beam steering direction over the FoV. Solid lines on all plots indicate the FoV within which aperture efficiency is above 70% for each beamformer. The asymmetry in the results is due to the offset geometry of the antenna.

Paper G

Domain-Decomposition Approach to Krylov Subspace Iteration

O. A. Iupikov; C. Craeye; R. Maaskant and M. V. Ivashina

EEE Antennas and Wireless Propagation Letters, vol. 15, 2016

The layout of this paper has been revised in order to comply with the rest of the thesis.

Domain-Decomposition Approach to Krylov Subspace Iteration

O. A. Iupikov; C. Craeye; R. Maaskant and M. V. Ivashina

Abstract

Krylov subspace iterative techniques consist of finding the solution of a scattering problem as a linear combination of "generating vectors" obtained through successive matrix-vector multiplications. This paper extends this approach to domain-decomposition. Here, on each subdomain a subspace is obtained by constructing the segments of each generating vector associated with the subdomain, and by weighting these segments independently, which provides more degrees of freedom. The method is tested for scattering by a sphere and a rectangular plate, as well as radiation from connected arrays with strongly coupled antenna elements. It is shown that substantial computational savings can be obtained for the sphere and the array. This opens up new perspectives for faster solutions of multi-scaled problems.

1 Introduction

Conventional iterative techniques, such as the Full Orthogonalization Method (FOM) or the Generalized Minimal Residual Method (GMRES) [1], have proved their capability and efficiency to solve large-scale electromagnetic problems. They define a set of current distributions on the whole domain through successive matrix-vector multiplications (mat-vecs) and then solve for their expansion coefficients in an iterative manner. However, these methods become computationally expensive for a large number of generating vectors. To avoid this, a restart procedure is often used, which in addition helps to improve the condition number of the generated system of equations, thereby improving the accuracy of the method.

Many improvements on the GMRES method can be found in the literature. For example, in [2] an adaptive deflation strategy is proposed, which retains useful information at the time of a restart to avoid stagnation and improve the convergence rate.

The generating vectors in GMRES can also be seen as Macro Basis Functions (MBFs) [3, 4]. A similar approach is used in domain-decomposition methods like the Characteristic Basis Functions Method (CBFM) [5] and the Synthetic Functions method (SFX) [6]. A major difference between them is that MBFs in GMRES (or

FOM) are defined on the whole computational domain and belong to a Krylov subspace, while CBFM-like techniques split the structure into subdomains and analyze them in isolation through the definition of set of independent MBFs on each subdomain, obtained by exciting the subdomain in various ways[1]. Assuming that MBFs are obtained using a multiple-scattering (between subdomains) methodology, a "rule of thumb" is proposed in [7] stating that both FOM and CBFM provide a similar accuracy when the number of iterations in FOM is equal to the average number of MBFs per subdomain in CBFM. However, in some cases, the CBFM yields better accuracy, owing to the fact that it provides more degrees of freedom (DoFs).

In this paper we propose a domain-decomposition approach to Krylov subspace iteration, where MBFs (or CBFs) on each subdomain are naturally constructed from the different segments of the generating vectors.

The paper is organized as follows. In Sec. 2 we formulate a reduced system of equations built from segments of the generating vectors as MBFs, while avoiding extra mat-vecs. Next, an algorithm for the restart procedure is described in Sec. 3. The proposed approach is validated in Sec. 4 for the case of a perfectly conducting sphere, a rectangular plate, and an array of electrically connected and disconnected tapered-slot antennas. A discussion about complexity and accuracy of the approach follows in Sec. 5 and conclusions are drawn in Sec. 6.

2 Segmented Krylov subspace as MBFs

Consider the Method of Moments (MoM) matrix equation:

$$\mathbf{Z}\mathbf{I} = \mathbf{e}, \tag{1}$$

where $\mathbf{Z}$ is the $N \times N$ MoM matrix; $\mathbf{e}$ is the $N \times 1$ excitation vector and $\mathbf{I}$ is a vector containing the expansion coefficients for the elementary basis functions. Accordingly, the reduced CBFM system of equations can be written as

$$\tilde{\mathbf{Z}}\tilde{\mathbf{I}} = \tilde{\mathbf{e}}, \tag{2a}$$

$$\tilde{\mathbf{Z}}_{i,j} = \mathbf{K}_i^H \mathbf{Z}_{i,j} \mathbf{K}_j, \tag{2b}$$

$$\tilde{\mathbf{e}}_i = \mathbf{K}_i^H \mathbf{e}_i, \tag{2c}$$

where $i, j = 1 \dots M$ are sub-domain indices; H is the Hermitian operator and $\mathbf{K}_i$ is the set of MBFs. The method proposed here consists of selecting as MBFs on a given subdomain the corresponding segments of the generating vectors. Those

[1]More about the relationship between CBFM-like approaches and Krylov subspace iterative methods can be found in [7].

segments correspond to entries associated to basis functions defined on the subdomain of interest. Hence, the newly proposed MBF selection reads:

$$\mathbf{K}_i = \left[\mathbf{k}_i^{(1)} = \mathbf{e}_i \mid \mathbf{k}_i^{(2)} \mid \ldots \mid \mathbf{k}_i^{(P)}\right], \tag{3}$$

in which generating vector $\mathbf{k}$ is formed iteratively as

$$\mathbf{k}^{(p+1)} = \mathbf{Z}\mathbf{k}^{(p)} \quad \text{for} \quad p = 1 \ldots P-1, \tag{4}$$

where index i refers to the MBF vector entries related to subdomain i.

It is important to point out that the most computationally expensive part of the MoM matrix reduction (2b), namely the matrix-matrix product $\mathbf{Z}_{i,j}\mathbf{K}_j$, can be carried out during the subspace construction (4). For this purpose, (4) is built from M^2 smaller matrix-vector products resulting in the M^2 vectors $\mathbf{v}_{i,j}^{(p)}$, expressed as

$$\mathbf{v}_{i,j}^{(p)} = \mathbf{Z}_{i,j}\mathbf{k}_j^{(p)}. \tag{5}$$

Segment i of the vector $\mathbf{k}^{(p+1)}$ (at the next iteration) is obtained by a simple summation of vectors $\mathbf{v}_{i,j}^{(p)}$ as

$$\mathbf{k}_i^{(p+1)} = \sum_j \mathbf{v}_{i,j}^{(p)}. \tag{6}$$

If the vectors $\mathbf{v}_{i,j}^{(p)}$ are concatenated in a matrix $\mathbf{Q}$ as

$$\mathbf{Q}_{i,j} = \left[\mathbf{v}_{i,j}^{(1)} \mid \mathbf{v}_{i,j}^{(2)} \mid \ldots \mid \mathbf{v}_{i,j}^{(p)}\right], \tag{7}$$

then the MoM matrix reduction (2b) can be rewritten as

$$\tilde{\mathbf{Z}}_{i,j} = \mathbf{K}_i^H \mathbf{Z}_{i,j}\mathbf{K}_j = \mathbf{K}_i^H \mathbf{Q}_{i,j}, \tag{8}$$

which allows one to reduce by a factor close to two the time involved in (2)-(4), as compared to a straight-forward implementation. The appendix explains how (8) can be modified when the set of MBFs needs to be orthogonalized.

3 CBFM with restarts

The accuracy of the CBFM method can be significantly improved down to machine precision by introducing a restart procedure similar to that used in a restarted GMRES method [1]:

- Step 1. Initialize the final solution $\mathbf{I}_{\text{fin}} = \mathbf{0}$.
- Step 2. Set the excitation vector $\mathbf{e}$ in (2c) to the initial excitation vector $\mathbf{e}_0$.

- Step 3. Build and solve the reduced system of equations (2a), compute the solution $\mathbf{I}_j = \mathbf{K}_j \tilde{\mathbf{I}}_j$ for $j = 1, \dots, M$. Note that the reduced system of equations can be built progressively, similar to the internal iterations in GMRES.
- Step 4. Add the result to the final solution, $\mathbf{I}_{\text{fin}} = \mathbf{I}_{\text{fin}} + \mathbf{I}$.
- Step 5. Compute the residue $\mathbf{r} = \mathbf{e}_0 - \mathbf{Z}\mathbf{I}_{\text{fin}}$.
- Step 6. Set the excitation vector $\mathbf{e}$ to the residue $\mathbf{r}$ and go to Step 3 until the required residue is reached.

The main difference with GMRES is that the subspace is restarted on every subdomain.

4 Numerical results

In this section the proposed approach is compared to the GMRES algorithm in terms of an error in surface current versus the solving complexity. The complexity is defined herein as the number of elementary operations "$ab+$" (floating point product of complex scalar numbers and summation with another complex number), required to solve the problem, while the relative error in the surface current is computed as

$$\epsilon = 20 \log_{10} \left(\sqrt{\sum_n |I_n^{\text{approx}} - I_n^{\text{ref}}|^2} \Big/ \sqrt{\sum_n |I_n^{\text{ref}}|^2} \right), \tag{9}$$

where $\mathbf{I}^{\text{approx}}$ is the current expansion coefficient vector, obtained using the proposed approach or restarted GMRES; and $\mathbf{I}^{\text{ref}}$ is the reference solution, obtained by direct solution of the MoM matrix equation (1).

The structures considered hereafter are subdivided into subdomains to have nearly equal and compact surfaces; for antenna arrays each subdomain is chosen to be a single antenna element. One possible way to improve the division into subdomains is through the so-called graph-partitioning technique (see e.g. [8]).

The system of equations (1) is assumed to be preconditioned for both CBFM and GMRES using the preconditioner described in [9], during which auxiliary subdomains are considered [7] in order to deal with the nearest interactions. Furthermore, a simplified version of GMRES is used [10], which implements the Gram-Schmidt orthogonalization of the vectors in the Krylov sub-space instead of using the Arnoldi iteration. This approach has a similar complexity as the original GMRES algorithm, while it is structurally closer to the CBFM.

For each geometry considered below a series of simulations have been performed for different numbers of CBFM-"generating vectors" and different numbers of internal iterations (between restarts) for GMRES, and the best convergence curves of both

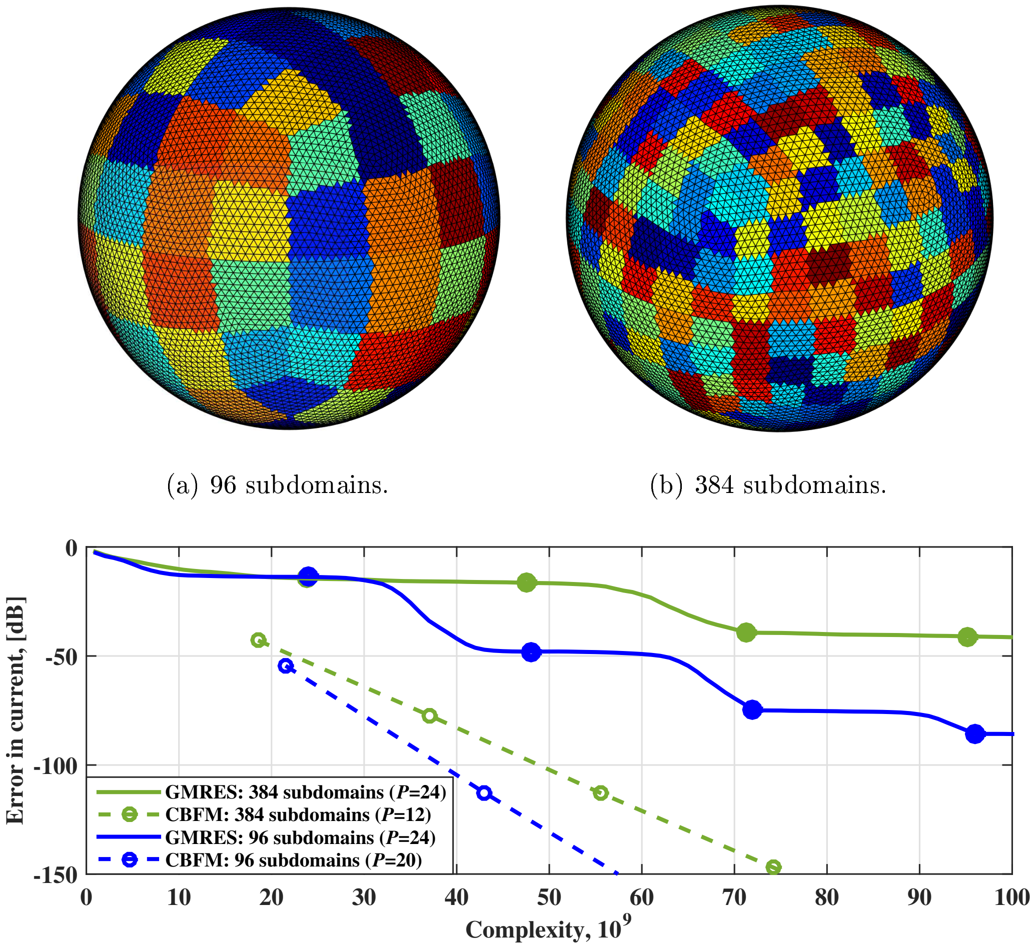

(c) GMRES and CBFM convergence.

Figure 1: Numerical example 1: A sphere with radius 1.58λ, divided into (a) 96 subdomains and (b) 384 subdomains, and excited by an incident plane wave. Subfigure (c) compares the convergence rates of restarted GMRES and CBFM. The restart positions are indicated with circles.

methods are compared. Under "an iteration" for CBFM approach we understand hereafter a procedure consisting of (i) building the reduced system of equations of size $PM \times PM$, which involves P mat-vecs, and (ii) solving this system.

Three geometries are considered:

- (Fig. 1) A sphere with radius 1.58λ, divided into $M = 96$ or $M = 384$ subdomains. The number of elementary basis functions (RWG) is $N = 30720$. The sphere is excited by a plane wave.

- (Fig. 2) A rectangular plate with size 12λ, divided into $M = 144$ or $M = 256$ subdomains. The number of RWG basis functions is $N = 42960$. The plate is excited by a plane wave under 45 degrees incidence.

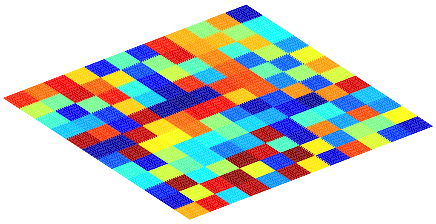

(a) 144 subdomains.

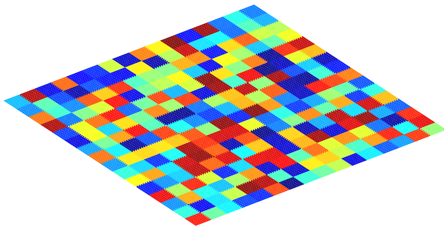

(b) 256 subdomains.

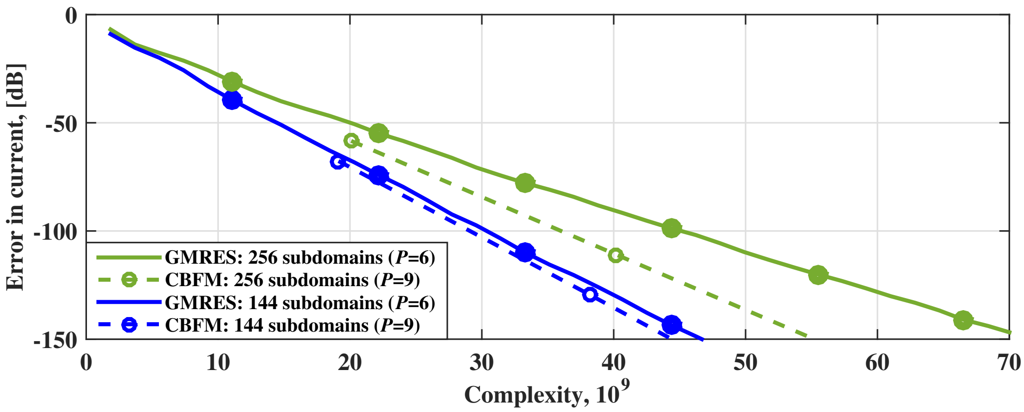

(c) GMRES and CBFM convergence.

Figure 2: Numerical example 2: A rectangular plate with size 12λ, divided into (a) 144 subdomains and (b) 256 subdomains, and excited by a plane wave under 45 deg incidence. Subfigure (c) compares the convergence rates of restarted GMRES and CBFM. The restart positions are indicated with circles.

- (Fig. 3) A 121-element dual-polarized array of both connected and disconnected Vivaldi tapered slot antennas. The numbers of RWG basis functions are $N = 41975$ and $N = 39325$ respectively. The array is uniformly excited by delta-gap voltage sources at each antenna element. The connected Vivaldi array has been designed by ASTRON [11].

Fig. 1 demonstrates the convergence rate of the newly defined iterative CBFM and GMRES for the sphere. If one aims at an accuracy in the surface current of e.g. 50 dB, the domain-decomposition approach is more than twice faster than GMRES, i.e. with twice smaller operations count. The convergence in case of 96 subdomains is faster for both methods, and this can be explained by the influence of the preconditioner, which accounts for all adjacent neighbours of each subdomain. This is true as long as the solution time of the reduced system of equations is small compared to the matrix-vector product needed to produce that system of equations. As explained in Section 5, this supposes that the number of subdomains M remains small compared to F^2, where $F > 1$ is the DoF reduction factor[2], which is satisfied in all numerical

[2] $F = N_{sd}/P$ is average ratio between numbers of elementary basis functions and MBFs on each

examples considered here.

Similar observations are made for the square plate shown in Fig. 2. However, the advantage of using the iterative CBFM is not significant in this case as compared to the more strongly coupled subdomains in the other examples.

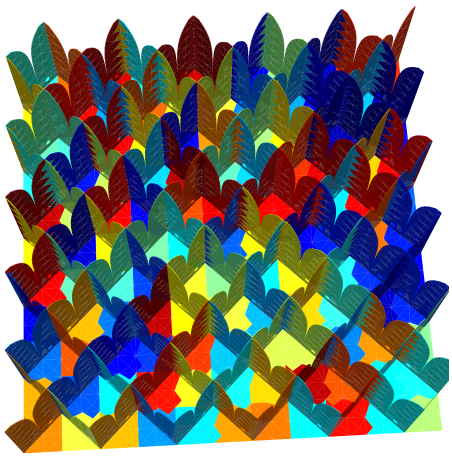

(a) connected array.

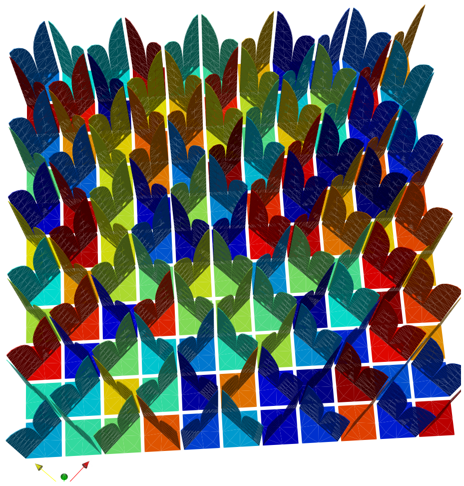

(b) disconnected array.

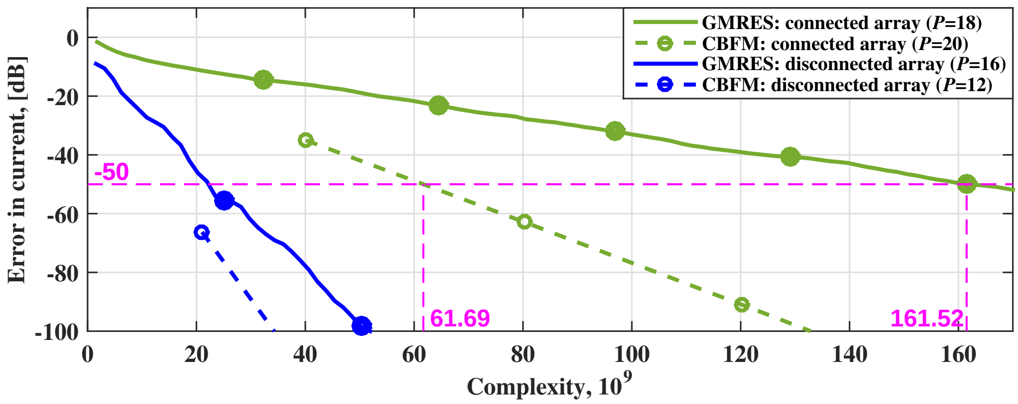

(c) GMRES and CBFM convergence.

Figure 3: Numerical example 3: (a) A connected and (b) disconnected 121-element dual-polarized Vivaldi array, divided into 121 subdomains, and excited by a delta-gap voltage sources at each antenna element. Subfigure (c) compares the convergence rates of restarted GMRES and CBFM. The restart positions are indicated with circles.

The more complicated Vivaldi array case is demonstrated in Fig. 3. As expected, the disconnected array is a much easier case for numerical analysis, since no current can physically flow from one subdomain to another, which reduces mutual coupling, such that the convergence is much faster. The figure also shows that for the connected

---

subdomain

array the proposed domain-decomposition approach is more than a factor two faster, as compared to a conventional GMRES approach.

In all numerical examples the CBFM reaches an accuracy better than −50 dB in only 1 to 2 iterations (for 0 to 1 restarts), with the number of mat-vecs per iteration equal to P as indicated in the legends of Figs. 1–3. GMRES requires 1 to 5 restarts to achieve similar accuracy levels.

It worth noting that we used an integral error in the surface current as a main figure of merit in this study. However, antenna characteristics, such as the antenna impedance and radiation pattern, are most commonly used by antenna designers. The relation between respective errors is not straightforward, however it can be assumed that the error in surface current and the error in antenna characteristics are of same order (see e.g. the approximation error analysis in [12], where different reflector antenna feeds are considered).

5 Discussion

When well preconditioned, GMRES converges very rapidly (i.e. within a few tens of iterations), almost irrespective of the number of unknowns. As explained in [10], GMRES amounts to solving a reduced system of equations, whose size (i.e. number of DoFs), corresponds to the number of iterations. For large problems, this solution takes a negligible time as compared to that involved in the mat-vec operations. This means that, without significant increase in the computation time, one can afford more DoFs, as is the case with the approach proposed here, since the number of DoFs now corresponds to the number of mat-vecs P multiplied by the number of subdomains. Without any specific matrix-vector multiplication, solving the reduced system of equations has a complexity $(PM)^3$ (here it is worth to mention that there are methods to reduce this exponent, see e.g. [13]), while the complexity of mat-vecs is PN^2. The increase of computational time is hence small as long as $P^2M \ll N_{sd}^2$, where N_{sd}^2 is the average number of elementary basis functions per subdomain.

It is pointed out that the gained accuracy does not seem to be commensurate with the increase of the degrees of freedom. More precisely, the achieved accuracy is not as good as that we may expect from GMRES when the number of iterations equals the total number of CBFs in the problem (in that case GMRES exploits the same number of DoF, at the expense of an excessive number of mat-vecs). This is probably due to the possible slight discontinuity between current distributions on contiguous subdomains; part of the newly generated DoFs may actually be needed to correct this deficiency.

In the very worst case, i.e., when the iterative CBF approach essentially provides the same accuracy as GMRES, one has two methods, one based on GMRES and one based on CBFs, with comparable accuracies when the number of iterations in the former is equal to the number of CBFs per subdomains in the latter. That equality is obtained by construction of the proposed method, since one new CBF per segment from the new generating vector is created at every iteration. It is interesting to notice that this equality precisely corresponds to the rule of thumb delineated from numerical experiments in [7] where MBFs (or CBFs) were created in a multiple-scattering fashion, and it is shown here that this rule of thumb constitutes a lower bound for the capabilities of the iterative CBF (or MBF) approach.

It appears that a clear advantage beyond this rule is obtained with CBFs when – as proposed here – the CBFs on a given subdomain are simply taken as the segments of the generating vectors (which correspond to the subdomain of interest). Other (either purely algebraic or more physical) ways of creating the CBFs may allow us to further benefit from the larger number of DoFs created through the subdomain-based approach.

6 Conclusions

This work has introduced a domain-decomposition technique into Krylov subspace iteration, such as in GMRES for instance. This method is similar to the CBFM, here the MBFs are generated by simple segmentation of the pre-computed vectors of the Krylov subspace. The achieved convergence is faster than with GMRES by a factor ranging from 1.05 (the rectangular plate with large subdomains) to 2.6 (the connected Vivaldi array) while keeping the same accuracy. This opens new perspectives for the solution of multi-scaled radiation and scattering problems.

Appendix

To keep a well-conditioned reduced system of equations, the set $\mathbf{K}$ of MBFs should be orthogonalized by means of, e.g., a QR-decomposition. This slightly complicates the acceleration technique described in the Sec. 2. The updated acceleration can be carried out in the following way.

Let us denote the orthogonalized matrix $\mathbf{K}$ as $\mathbf{K}^{\mathrm{o}}$, then (2b) becomes

$$\tilde{\mathbf{Z}}_{i,j} = \mathbf{K}_i^{\mathrm{o}H} \mathbf{Z}_{i,j} \mathbf{K}_j^{\mathrm{o}}. \tag{10}$$

After performing the QR-decomposition for each sub-domain j, $\mathbf{K}_j = \mathbf{K}_j^{\mathrm{o}} \mathbf{R}_j$, Eq. (10) can be rewritten as

$$\tilde{\mathbf{Z}}_{i,j} = \mathbf{K}_i^{\mathrm{o}H} \mathbf{Z}_{i,j} \mathbf{K}_j \mathbf{R}_j^{-1} = \mathbf{K}_i^{\mathrm{o}H} \mathbf{Q}_{i,j} \mathbf{R}_j^{-1}, \tag{11}$$

which only involves small matrices, and based on (7), is the final expression of the (i, j) block of the reduced MoM matrix.

References

[1] Y. Saad and M. H. Schultz, “GMRES: a generalized minimal residual algorithm for solving nonsymmetric linear systems,” *SIAM Journal on Scientific and Statistical Computing*, vol. 7, no. 3, pp. 856–869, Jul. 1986.

[2] D. N. Wakam, J. Erhel, and W. D. Gropp, “Parallel adaptive deflated GMRES,” in *The 20th International Conference on Domain Decomposition Methods*, UC San Diego, in La Jolla, California, Feb. 2011, pp. 631–638.

[3] E. Suter and J. R. Mosig, “A subdomain multilevel approach for the efficient MoM analysis of large planar antennas,” *Micr. Opt. Technol.*, vol. 26, no. 4, pp. 270–277, Aug. 2000.

[4] I. Stevanovic and J. R. Mosig, “Subdomain multilevel approach with fast MBF interactions,” in *Proc. IEEE AP-S International Symposium*, Monterey, California, Jun. 2004, pp. 367–370.

[5] V. Prakash and R. Mittra, “Characteristic basis function method: A new technique for efficient solution of method of moments matrix equations,” *Micr. Opt. Technol.*, vol. 36, no. 2, pp. 95–100, Jan. 2003.

[6] L. Matekovits, G. Vecchi, G. Dassano, and M. Orefice, “Synthetic function analysis of large printed structures: the solution space sampling approach,” in *Proc. IEEE AP-S International Symposium*, vol. 2, Boston, Massachusetts, Jul. 2001, pp. 568–571.

[7] N. Ozdemir, D. Gonzalez-Ovejero, and C. Craeye, “On the relationship between multiple-scattering Macro Basis Functions and Krylov subspace iterative methods,” *IEEE Trans. Antennas Propag.*, vol. 61, no. 4, pp. 2088–2098, Apr. 2013.

[8] R. Mitharwal and F. P. Andriulli, “On the multiplicative regularization of graph laplacians on closed and open structures with applications to spectral partitioning,” *IEEE Access*, vol. 2, pp. 788–796, 2014.

[9] N. Ozdemir, D. Gonzalez-Ovejero, and C. Craeye, “A near-field preconditioner preserving the low-rank representation of method of moments interaction matrices,” in *Proc. Int. Conf. on Electromagn. in Adv. Applicat. (ICEAA)*, Torino, Italy, Sep. 2013, pp. 133–136.

[10] C. Craeye, J. Laviada, R. Maaskant, and R. Mittra, “Macro Basis Function framework for solving Maxwell’s equations in surface integral equation form,” *The FERMAT Journal*, vol. 3, pp. 1–16, 2014.

[11] M. Arts, M. Ivashina, O. Iupikov, L. Bakker, and R. van den Brink, "Design of a low-loss low-noise tapered slot phased array feed for reflector antennas," in *Proc. European Conference on Antennas and Propag. (EuCAP)*, Barcelona, Spain, Apr. 2010, pp. 1–5.

[12] O. A. Iupikov, R. Maaskant, M. Ivashina, A. Young, and P. Kildal, "Fast and accurate analysis of reflector antennas with phased array feeds including multiple reflections between feed and reflector," *IEEE Trans. Antennas Propag.*, vol. 62, no. 7, Jul. 2014.

[13] A. Bojańczyk, "Complexity of solving linear systems in different models of computation," *SIAM Journal on Numerical Analysis*, vol. 21, no. 3, pp. 591–603, Jun. 1984.

Paper H

Design of a push-broom multi-beam radiometer for future ocean observations

C. Cappellin, K. Pontoppidan, P. H. Nielsen, N. Skou, S. S. Søbjærg, A. Ihle, M. V. Ivashina, O. A. Iupikov, and K. v. 't Klooster

in *Proceedings of the 9th European Conference on Antennas and Propagation, EUCAP 2015,* Lisbon, Portugal, April 2015.

The layout of this paper has been revised in order to comply with the rest of the thesis.

Design of a push-broom multi-beam radiometer for future ocean observations

C. Cappellin, K. Pontoppidan, P. H. Nielsen, N. Skou, S. S. Søbjærg, A. Ihle, M. V. Ivashina, O. A. Iupikov, and K. v. 't Klooster

Abstract

The design of a push-broom multi-beam radiometer for future ocean observations is described. Such a radiometer has the big advantage of being fully stationary on the platform and provides a sensitivity one order of magnitude higher than a traditional conical scanning radiometer. Thanks to a dense focal plane array and a dedicated optimization procedure, the radiometric performance can be optimized and the instrument can accurately measure in C, X and Ku band and as close as 15 km from the coast line.

1 Introduction

The oceanographic community has strong interest in high spatial resolution. Current microwave radiometers in space operating at C-band (6.9 GHz) or at higher frequency provide a spatial resolution of around 50 km, whereas less than 20 km is desirable. Current capabilities provide measurements not closer than around 100 km from the shore-line, because of the signal contamination by the antenna side-lobes illuminating the land. There is a strong desire to reduce this distance to 5-15 km.

The instrument requirements for future radiometers measuring sea surface temperature (SST) and ocean vector wind (OVW) are summarized in Table 1. The instrument shall operate in three well separated bands, C-band (6.9 GHz), X-band (10.65 GHz) and Ku-band (18.7 GHz). The required 20 km resolution, i.e. 3 dB footprint, at C-band leads to a large antenna aperture of around 5 m in diameter. This is considerably larger than any radiometer system antenna flown hitherto.

The conical scanning antenna rotates around a vertical axis, and the coverage of the Earth is obtained partly by the movement of the satellite and partly by the rotation. For the push-broom system there are no moving parts but the antenna radiates as many beams as required to cover the swath. The push-broom system achieves very high sensitivity since all across track footprints are measured simultaneously. The antenna has the clear advantage of being stationary, but the number of beams and receivers is very high.

Table 1: Radiometer characteristics for the conical scan antenna at C-, X- and Ku-band.

Freq., [GHz]	**Bandwidth, [MHz]**	**Polarization**	**Sensitivity, [K]**	**Accuracy, [K]**	**Resolution, [km]**	**Dist. to coast, [km]**
6.9	300	V, H	0.30	0.25	20	5-15
10.65	100	V, H	0.22	0.25	20	5-15
		S_3, S_4	0.22	0.25	20	5-15
18.7	200	V, H	0.25	0.25	10	5-15
		S_3, S_4	0.25	0.25	10	5-15

The trade-off between a conical scanning and a pushbroom scanning relative to reflector optics and feed array design was described in [1], and indicated the push-broom antenna as the most promising candidate.

The purpose of the present paper is to focus on the detailed design of the push-broom antenna radiometer.

The paper is organized as follows: in Sec. 2 the antenna requirements are summarized, in Sec. 3 the geometry of the push-broom antenna and its focal plane array are described. The principles behind the optimization of the focal plane array are given in Sec. 4, while the detailed RF performances of the antenna are given in Sec. 5. Finally, Sec. 6 describes the mechanical realization of the push-broom reflector and Sec. 7 summarizes important results on the feeding network and the necessary power.

2 Antenna requirements

The requirements for the radiometer antenna can be derived from the radiometric requirements of Table 1.

One requirement concerns the cross-polarization of the antenna. The radiometer shall measure brightness temperatures in two linear polarizations, vertical and horizontal, and with an accuracy of 0.25K. It can be demonstrated [1] that this will be fulfilled when the cross-polar power received from the Earth does not exceed 0.33% of the total power coming from the Earth for that polarization state.

The instrument must be able to measure as close as 5-15 km from the coast. The brightness temperature of the sea is between 75 and 150K, whereas the land is 250K. The power in the pattern over the land shall be sufficiently small. It can be found [1] that the required accuracy is obtained when the coast line is located outside a cone around the main beam containing 99.72% of the total power on the Earth. In order to obtain a small distance to coast it is therefore of interest to reduce this cone.

The satellite height above the Earth and the incidence angle are assumed equal to 817 km and 53°, respectively. The required swath width was initially set to 1500 km. It was however realized very early in the study that, as far as push-broom systems are concerned, this will lead to a very large antenna. It was therefore decided to reduce

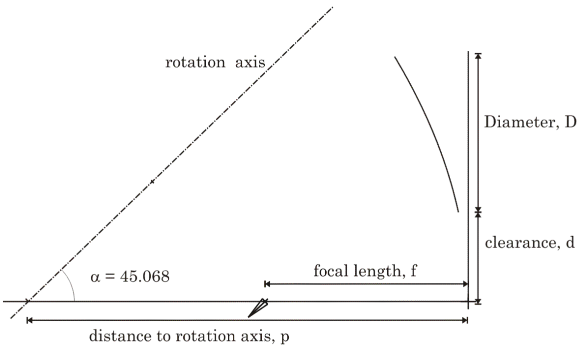

Figure 1: Push-broom torus design.

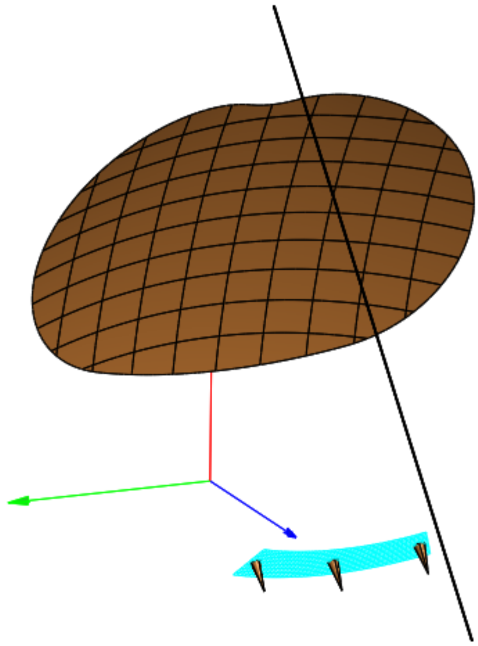

Figure 2: Torus push-broom antenna with projected aperture D and focal length f of 5 m. The three feed positions represent scan directions of 0° and ±20°. The feed array is shown in blue.

the swath width to 600 km. Even with this reduction the radiometer will represent a major advancement in the study of the oceans.

3 Push-broom antenna

3.1 Antenna geometry

For the push-broom system a torus reflector has been considered with projected aperture D of 5 m. The torus surface is obtained by rotating a section of a parabolic arc around a rotation axis, as shown in Fig. 1. The focal length f of the parabolic generator has been selected as 5 m. The angle α between the rotation axis and the parabola axis is connected to the orbit geometry, including the satellite height and the required incidence angle on ground. The distance p from the parabola vertex to the rotation axis is a function of f and α. The feed axis is selected parallel to the rotation axis, implying that all feed element axes are parallel and orthogonal to the focal plane. The feed array becomes therefore planar, simplifying the mechanical and electrical design. The reflector rim is found by intersecting the torus surface by the feed cone up to the outmost scan positions.

The antenna shall be able to provide a scan of ±20° corresponding to a swath width of 600 km. The final design is shown in Fig. 2, where the projected reflector aperture is 5 m by 7.5 m.

3.2 Feed array

The sensitivity provided by the torus push-broom is always one degree of magnitude better than the one provided by the conical scanner. This is at the expenses of a very large number of beams, and correspondingly large number of receivers. For a swath of 600 km we need:

- 58 beams across track at 6.9 GHz;
- 89 beams across track at 10.65 GHz;
- 156 beams across track at 18.7 GHz.

The array elements are arranged in a $\rho\phi$-grid around the rotation axis. The distance between the elements is approximately the same in the ρ-direction and in the ϕ-direction, and set equal to 0.75 wavelength. This distance was proven to be the optimal distance. For analysis purposes the array elements are assumed to be half-wave dipoles located a quarter of a wavelength above an infinite ground plane. Each element consists of both an x- and a y-directed dipole with separate ports. They only radiate in the upper half space above the ground plane.

4 Feed array design principles

Two different methods have been applied in order to determine the excitation coefficients of the feed array: the Conjugate Field Matching (CFM) and a direct optimization of the distance to coast.

It was realized early in the project that a traditional one beam-per-feed arrangement was not possible and a dense focal plane array was needed. This means that many array elements take part in the formation of one beam and the same array element takes part in the formation of many beams. The composite feed array must be excited by a multi-mode beam-forming network.

The feed array design was investigated almost independently by both TICRA and Chalmers. Initially, TICRA used the Conjugate Field Matching method to determine the feed element excitations. It turned out that this approach was too restrictive and gave rise to a number of feed elements larger than the one obtained by Chalmers [1] with a dedicated optimization procedure.

Since behind each feed element sit two receivers for the respective orthogonal polarization states, it is of high importance to reduce the number of receivers to the minimum necessary, in order to minimize the power consumption and the complexity of the feed array. An alternative technique was thus developed by TICRA, by which the array excitations are obtained by directly minimizing the distance to coast. It turns out that the optimization can be formulated as an eigenvalue problem, where the eigenvalue represents the maximum radiated power inside a given cone and the eigenvector holds the excitations to generate this field. The number of elements along the ρ and ϕ direction must be given as input to the algorithm.

The optimization method used by TICRA is similar to the one developed by Chalmers [2]. The difference lies in the way the cost function is defined: it is the ratio of the power inside and outside the angular cone for TICRA; while it is the ratio of the power inside a specified small region to the noise power outside this region for Chalmers. The radiometric performances obtained by the two algorithms are very similar.

5 RF performance results

5.1 Central beam at Ku band

The reflector surface is not a paraboloid and the performances are therefore expected to be most critical at the highest frequency. In this section the central beam at Ku-band, 18.7 GHz, is thus presented.

The feed array has 8 elements in the ρ-direction and 21 elements in the ϕ-direction, as indicated by Chalmers. The total number of array elements to generate the central beam is therefore 168. The element excitations are determined by TICRA's optimization approach described earlier and the result shows that 99.72% of the power from the antenna is contained inside a cone with half angle 0.5°. The synthesized excitation coefficients in amplitude are shown in Fig. 3 and the far field from the feed array at 18.7 GHz is shown in Fig. 4. It is seen that the radiation outside the reflector rim is very low leading to a spill-over of only 0.05%. The far-field pattern of the antenna is depicted in Fig. 5. It is evident that this pattern is not rotationally symmetric and one could therefore get the impression that the actual orientation of the coast line would be very important for the instrument performance quality. When the -30 dB contour is plotted, one can find that it is nearly a circle with radius 0.5°. This circle contains 99.72% of the power and the coast line can therefore be located anywhere outside this circle and its orientation is not important.

The radiometer characteristics are shown in Table 2 and include not only the centre frequency but also the two band ends in order to demonstrate that the performance is almost constant across the entire band. It is noticed that the distance to coast at Ku-band is only 7 km.

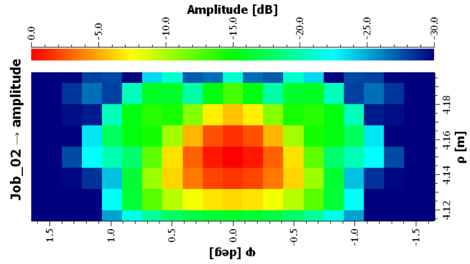

Figure 3: Excitation coefficients for the centre beam for minimum distance to coast.

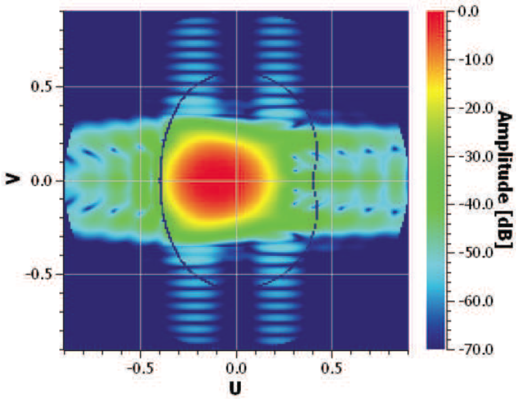

Figure 4: Far-field radiation pattern of the feed array for the centre beam.

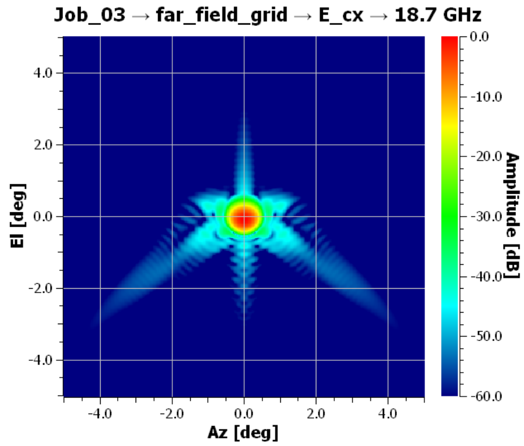

Figure 5: Image plot of the co-polar far field of the centre beam for the push-broom antenna optimised for low distance to coast.

Table 2: Radiometer characteristics for the central ku-band beam for the push-broom antenna optimized for low distance to coast.

Frequency, [GHz]	Cx-power], [%]	Footprint, [km]	Dist. to coast, [km]
18.6	0.15	10.34	7.16
18.7	0.14	10.32	7.08
18.8	0.14	10.31	7.02

5.2 Reduction of feed array rows along ϕ

It was demonstrated in the previous section that a feed array with 8 rows along ϕ gives a distance to coast of 7 km which is actually better than the required 15 km. It was investigated if it is possible to reduce the number of feed array rows to 7 or 6 and still maintain an acceptable performance.

The excitations are determined such that 99.72% of the power is contained in the smallest possible cone around the beam peak. Using a smaller number of rows generates a more elliptical illumination on the reflector and a more elliptical far-field beam. The radiometer characteristics are summarized in Table 3 where it is seen that with 6 rows the footprint is slightly larger than 10 km and the distance to coast is smaller than 10 km, thus acceptable.

Table 3: Radiometer characteristics for the central ku-band beam for different number of feed array rows along ϕ.

Feed array rows along phi	**Number of active elements**		**Cx-power, [%]**	**Footprint, [km]**	**Dist. to coast, [km]**
	x-dir	y-dir			
8 rows	168	0	0.14	10.34	7.16
7 rows	147	0	0.11	10.32	7.08
6 rows	126	0	0.08	10.31	7.02

5.3 Total feed arrays for C-, X- and Ku-band

It was demonstrated in the previous section that acceptable performance for the centre beam at Ku-band can be achieved with a feed array containing 6 elements in the ρ-direction and 21 elements in the ϕ-direction.

We will use the same principles as for Ku-band to design the feed arrays for the centre beams for C- and X-band, still using 6×21 elements. The element excitations are determined by optimizing the distance to coast and the calculated results are summarized in Table 4. It is seen that the footprint size is slightly too large at C- and Ku-band and the distance to coast exceeds slightly the required 15 km at C-band.

Table 4: Radiometer characteristics for the centre beam at C-, X- and Ku-band.

Frequency, [GHz]	**Cx-power], [%]**	**Footprint, [km]**	**Dist. to coast, [km]**
C-band	0.20	23.26	16.41
X-band	0.14	16.53	12.28
Ku-band	0.08	10.86	9.19

Having determined the feed array for the centre beam the complete feed array can be readily designed. The Ku-band feeds are located close to the focal circle of the push-broom torus and the feed arrays for C- and X-band are located on either side of the Ku-band array. The three feed arrays are shown in Fig. 6. The total number of array elements is 1284, 1956 and 3156 for C-, X- and Ku-band, respectively. If 8 rows along ϕ instead of 6 were used the number of elements becomes 1616, 2480 and 4320. (The latter numbers are used for the power estimates in Sec. 7.) These numbers clearly show that the number of rows along ϕ is an important design parameter for the push-broom system.

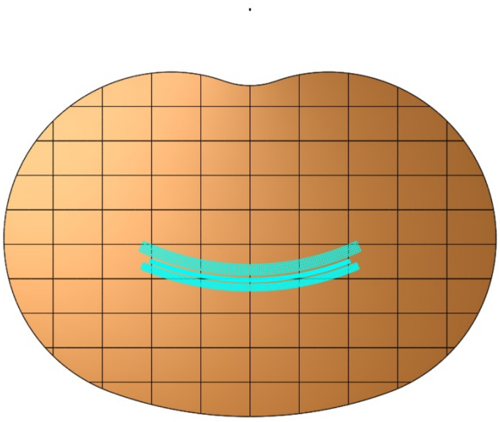

Figure 6: Feed arrays for C-, X- and Ku-band.

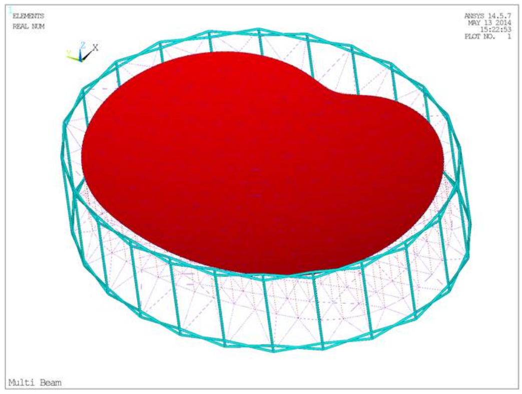

Figure 7: Mechanical realization of the torus push-broom reflector dish.

5.4 Additional performance checks

A number of different detailed investigations were carried out. The results can be summarized as follows:

Scan performance. The antenna is able to scan up to 20° to both sides without any severe scan degradations. It was found that the excitations are practically identical for all the beams but shifted in the ϕ-direction according to the actual scan direction.

Bandwidth investigations. The required bandwidth is 300, 100 and 200 MHz at C-, X- and Ku-band, respectively. The radiometer performance is almost constant over the bands.

Sensitivity to excitation inaccuracies. The feed element excitations can only be realized to certain accuracy. Two types of excitation errors were investigated. It was found that excitation errors up to 10% for each separate element and up to 3% of the largest excitation are acceptable. This is very well in line with another observation, namely that it is acceptable to discard all elements with an amplitude lower than 30 dB below the strongest excited element.

Redundancy aspects. It was finally demonstrated that it is possible to re-optimize the excitation coefficients in case of a receiver failure and in this way remedy the consequences of the failure.

6 Mechanical design of the push-broom torus antenna

The mechanical realization of the torus reflector proposed by HPS consists of a double layer pantograph and two triangular wire-band nets, one in the front and one in the back. The corners of the triangles of the two nets are connected by adjustment wires, as shown in Fig. 7. The front net forms the support of the reflector.

Initially it was assumed that the front net would be covered with a knitted metal mesh in order to provide the necessary RF reflection. It was realized, however, that the triangular facets would generate high and unacceptable grating lobes unless the triangles were made very small, i.e. 100 mm size. Consequently, it was proposed to construct the reflector as a doubly curved CFRS (Carbon Fibre Reinforced Silicon) surface. The triangular net is maintained to support the CFRS but the size of the triangles can be much larger, around 400 mm.

7 Feeding network and receiver issues

In this section the receiver resource demands, especially concerning power consumption, will be evaluated, first using existing state-of-the-art components, and second using values that can be realistically expected within a 5 years' time frame.

7.1 Existing state-of-the-art components

As illustrated in Fig. 8, each feed array element is assumed to be connected to a direct detection circuit, one for each polarization channel and assigned its own receiver and A/D converter. Hence, the total number of components in a single receiver must be multiplied onto the number of feed array elements and polarization, and a major concern is the total number of components in the system, with respect to mass, size and especially power consumption.

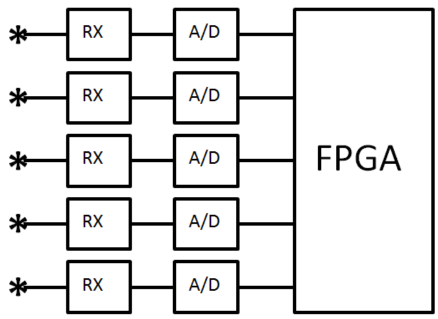

Figure 8: Dense feed array receiver system.

The A to D converter is the most critical component, as it is traditionally the largest and by far the most power consuming. However, over the past decade technology has developed rapidly. Most components are wideband, or similar between the three frequency bands of interest, and thus a common overview has been made for the different component types included in each receiver. The result of this shows that a realistic power budget based on state-of-the-art components will result in a power consumption of approximately 850 mW per receiver at X-band and 1100 mW at Ku-band and C-band. The total power budget is dominated by X- and Ku-band due to the many receivers at these frequencies, and for global power budget estimates we can assume 1 W per receiver. Adding also power for the beam forming network and RFI processor we end up with 1.38 W per receiver. With 8416 elements this gives a total power of 11.6 kW, which is not realistic now or in the near future.

7.2 Realistic components within a 5 years time frame

Already now A/D converters able to sub-sample signals up to X-band are available in research labs and within very few years Ku-band is also served. The development concerning amplifiers is also impressive, especially when it comes to noise figure at high frequencies and power consumption. For global power budget estimates we can within a few years assume 49 mW per receiver, including beam forming network and RFI processor. This amounts to a total power consumption of 8416×49 mW = 412 W, which is certainly realistic.

References

[1] C. Cappellin, K. Pontoppidan, P. Nielsen, N. Skou, S. S. Søbjærg, A. Ihle, D. Hartmann, M. Ivashina, O.Iupikov, and K. v. t Klooster, "Novel multi-beam radiometers for accurate ocean surveillance," in *Proc. European Conference on Antennas and Propag. (EuCAP)*, The Hague, The Netherlands, Apr. 2014, pp. 1–4.

[2] O. A. Iupikov, M. V. Ivashina, K. Pontoppidan, P. H. Nielsen, C. Cappellin, N. Skou, S. S. Søbjærg, A. Ihle, D. Hartmann, and K. v. t Klooster, "An optimal beamforming algorithm for phased-array antennas used in multi-beam spaceborne radiometers," in *Proc. European Conference on Antennas and Propag. (EuCAP)*, Lisbon, Portugal, Apr. 2015, pp. 1–5.

Paper I

An Optimal Beamforming Algorithm for Phased-Array Antennas Used in Multi-Beam Spaceborne Radiometers

O. A. Iupikov, M. V. Ivashina, K. Pontoppidan, P. H. Nielsen, C. Cappellin, N. Skou, S. S. Søbjærg, A. Ihle, D. Hartmann, K. v. 't Klooster

in *Proceedings of the 9th European Conference on Antennas and Propagation, EUCAP 2015,* Lisbon, Portugal, April 2015.

The layout of this paper has been revised in order to comply with the rest of the thesis.

An Optimal Beamforming Algorithm for Phased-Array Antennas Used in Multi-Beam Spaceborne Radiometers

O. A. Iupikov, M. V. Ivashina, K. Pontoppidan, P. H. Nielsen, C. Cappellin, N. Skou, S. S. Søbjærg, A. Ihle, D. Hartmann, K. v. 't Klooster

Abstract

Strict requirements for future spaceborne ocean missions using multi-beam radiometers call for new antenna technologies, such as digital beamforming phased arrays. In this paper, we present an optimal beamforming algorithm for phased-array antenna systems designed to operate as focal plane arrays (FPA) in push-broom radiometers. This algorithm is formulated as an optimization procedure that maximizes the beam efficiency, while minimizing the side-lobe and cross-polarization power in the area of Earth, subject to a constraint on the beamformer dynamic range. The proposed algorithm is applied to a FPA feeding a torus reflector antenna (designed under the contract with the European Space Agency) and tested for multiple beams. The results demonstrate an improved performance in terms of the optimized beam characteristics, yielding much higher spatial and radiometric resolution as well as much closer distance to coast, as compared to the present-day systems.

1 Introduction

Recent advances in phased-array antenna technologies and low-cost active electronic components open up new possibilities for designing Earth observation instruments. One example of such technologies is digital beamforming phased-array feeds (PAFs) (often referred to as dense focal plane arrays [1]). Using PAFs is especially attractive in spaceborne radiometers in so-called push-broom configuration [2], where a large number of beams cover a wide region (swath) of the Earth simultaneously to achieve high sensitivity. For such radiometers, various optics concepts have been investigated [3], and the optimum solution has been found to be an offset toroidal single reflector antenna. This reflector structure is rotationally symmetric around its vertical axis, and thus is able to cover a wide swath range. However, its aperture field exhibits significant phase errors due to the non-ideal (parabolic) surface of the reflector that lead to the beam deformation. Accurate compensation for these effects requires the use of a moon-shaped PAF (as shown on fig.1) as well as dedicated beamforming algorithms. Development of such an optimal algorithm is the objective of this paper.

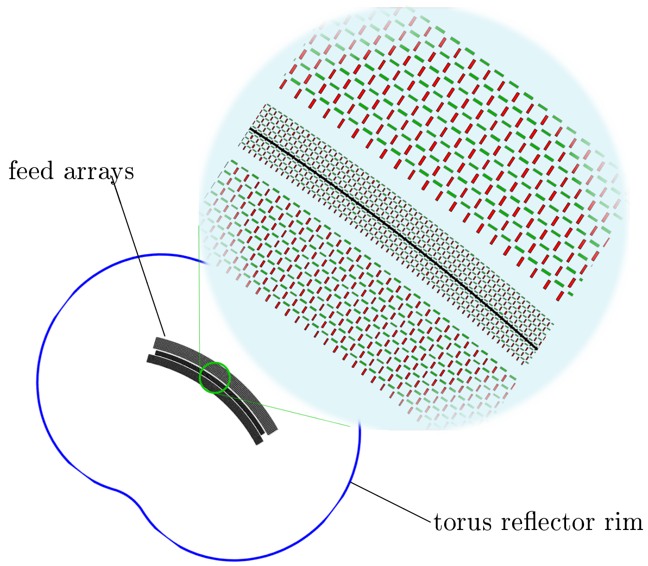

Figure 1: A schematic layout of the moon-shaped phased-array feeds for X-, Ku- and C-bands that are located in the focal field region of the torus reflector. The arrays comprise dual-polarized dipole antenna elements, denoted by the red and green lines. The black curve denotes the focal arc of the torus reflector.

2 Array design

An initial design of the PAF has been reported in [4]; where the array elements are arranged on the rectangular grid. For the current study, we have re-arranged the element positions along the focal-field arc of the torus reflector (see Fig. 1). This re-arrangement has led to the moon-shaped layout of the present PAF enabling similar focal-field distributions that are resulted from different incident directions upon the apertures of the corresponding sub-arrays. Thanks to this advantageous property, optimization of the beamformer weights for multiple beams reduces to the optimization of a single set of weights for one beam only, and most importantly, to the virtually identical beam shapes over the wide observation range. Furthermore, the new design consists of dual-polarized 0.5λ-dipole antennas, having higher polarization purity, as compared to the tapered-slot antenna elements used in the array in [4].

To simplify the modeling of the array for this study, we have made the following assumptions: (i) all array elements have the same radiation patterns; (ii) no mutual coupling and edge truncation effects are accounted for the array, and; (iii) the dipoles are located above an infinite ground plane. In the future studies, these simplifications will be eliminated.

3 Optimal beamforming algorithm

3.1 Generic formulation

The proposed optimization algorithm is formulated as the maximum Signal-To-Noise beamformer (MaxSNR) [5], where the antenna efficiency - defined for a given direction of observation corresponding to the beam center - is maximized, while minimizing the power received from the other directions. The weight vector for this beamformer can be written as

$$\mathbf{w}_{\mathrm{MaxSNR}} = \mathbf{C}^{-1}\mathbf{e}, \text{ with SNR} = \mathbf{e}^{H}\mathbf{w}_{\mathrm{MaxSNR}}, \tag{1}$$

where the vector $\mathbf{e} = [e_1, \ldots, e_N]^T$ holds the signal-wave amplitudes at the receiver outputs and arises due to an externally applied electromagnetic plane wave $\boldsymbol{E}_{\mathrm{i}}$; and $\mathbf{C}$ is a Hermitian spectral noise-wave correlation matrix holding the correlation coefficients between the outputs of the array receiving system.

If we assume a noiseless receiver system, the matrix $\mathbf{C}$ represents the antenna noise correlation matrix, which contains the noise correlation coefficients due to external noise sources (that are present in the region of observation on the Earth as well as outside). The elements of $\mathbf{C}$ can be calculated through the pattern-overlap integrals between $\boldsymbol{f}_n(\Omega)$ and $\boldsymbol{f}_m(\Omega)$, which are the nth and mth embedded element pattern (EEP) of the array (defined after the reflection from the dish), respectively [6], i.e.,

$$C_{mn} = \int T_{\mathrm{ext}}(\Omega)[\boldsymbol{f}_m(\Omega) \cdot \boldsymbol{f}_n^*(\Omega)]\,\mathrm{d}\Omega, \tag{2}$$

where $T_{\mathrm{ext}}(\Omega)$ is the brightness temperature distribution of the environment. To meet the radiometer requirements [2], the function $T_{\mathrm{ext}}(\Omega)$ is chosen such that it has low temperature values in the region of the expected main lobe (down to -20 dB level) and high values outside of this region. In this way, we realize the maximization of the beam efficiency – defined at the -20 dB level – while minimizing the side-lobe and cross-polarization power outside of this region, as required for the radiometers.

3.2 Computation acceleration

When constructing matrix $\mathbf{C}$, one should realize that its filling can be an extremely time-consuming procedure as it requires computation of all secondary EEPs over the entire sphere and evaluation of the pattern overlap integral (2) for all combinations of EEPs (see Tabl. 1). In order to speed-up the computational process, we have therefore represented the matrix $\mathbf{C}$ as a sum of two contributions, matrices $\mathbf{C}_1$ and $\mathbf{C}_2$ that

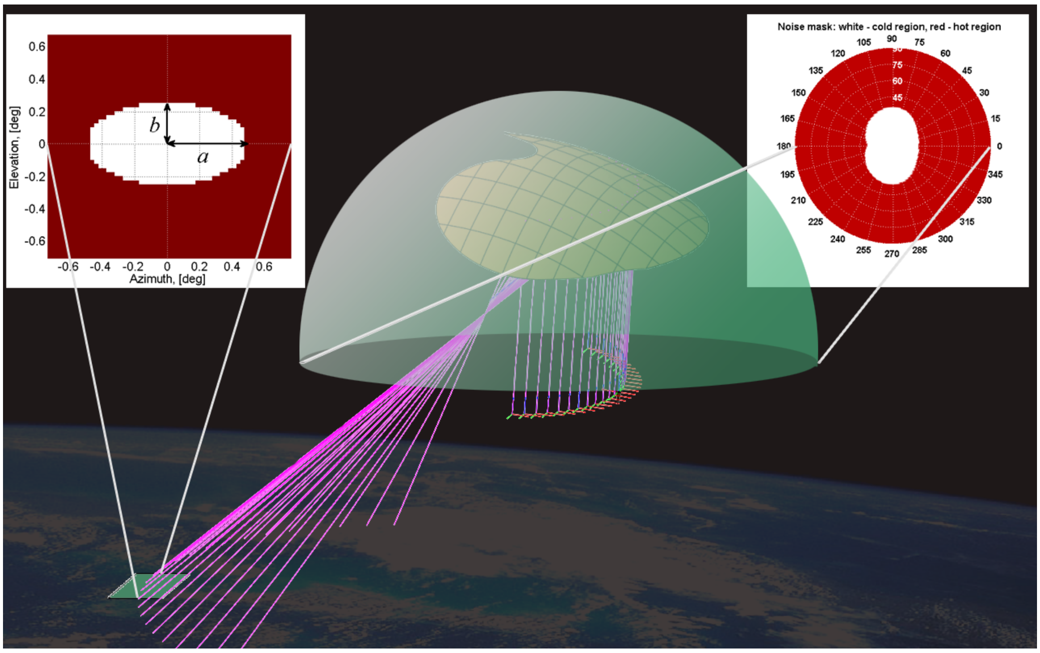

Figure 2: The T_{ext} mask-constrained functions defined for the calculation of the antenna noise correlation matrices $\mathbf{C}_1$ due to the noise sources in the Earth region (see the inset in the left upper corner) and $\mathbf{C}_2$ due to the noise sources in the sky region (see the inset in the right upper corner). The toroidal reflector fed with a PAF is in the middle of the illustration, where the multiple beams point to the Earth.

can be calculated relatively fast. The first matrix is obtained by using the secondary EEPs computed in a limited angular range around the main lobe region, while the second matrix is used for correcting for the spillover effects and evaluated through the primary feed patterns. The brightness temperature distribution functions $T_{\mathrm{ext}}(\Omega)$ corresponding to $\mathbf{C}_1$ and $\mathbf{C}_2$ are illustratively shown in the insets of Fig. 2.

The table below cross-compares the computational time at Ku band that is needed for the simulations (using GRASP) of the secondary patterns over the entire sphere (when computing the matrix $\mathbf{C}$ through the brute-force approach) and over the reduced region with the post-correction for the spillover effect (when computing the matrices $\mathbf{C}_1$ and $\mathbf{C}_2$ through the proposed approach). There is obvious advantage in using the latter approach, especially for the systems with a large number of beams and high operational frequencies.

Table 1: Computational time of the matrix $\mathbf{C}$ at Ku-band (18.7 GHz)

Brute-force approach		**Proposed approach**	
Computing sec. EEPs	Computing $\mathbf{C}$	Computing sec. EEPs	Computing $\mathbf{C}_1$ and $\mathbf{C}_2$
$\sim$ 9 months	*no data*	3 hours	5 min/beam

3.3 Iterative procedure for constraints on the dynamic range of the weights

The proposed beamformer, as described in sub-section III.A, has been extended so as to include constraints on the dynamic range of the weights that should not exceed a certain value. For this purpose, we have implemented an iterative procedure that modifies the reference weighting coefficients (as determined by the MaxSNR beamformer), while aiming to maintain the shape of the PAF pattern as close as possible to the reference one. This ensures that the radiometer parameters are as similar as possible to those obtained with the reference set of weights. The corresponding algorithm is listed as follows:

- At the first iteration ($q = 1$) the reference weight vector $\mathbf{w}^{(1)}$ is calculated using (1) with the initial noise-wave correlation matrix $\mathbf{C}^{(1)}$.

- At iteration $q = 2, 3 \ldots$ a new weight vector $\mathbf{w}^{(q)}$ is computed using the noise covariance matrix $\mathbf{C}^{(q)}$, diagonal elements of which are a function of the weight vector $\mathbf{w}^{(q-1)}$ obtained after the previous iteration, i.e.,

$$C_{nn}^{(q)} = C_{nn}^{(q-1)} f(|w_n^{(q-1)}|) \tag{3}$$

  where f is a receiver function that needs to be provided as an input to the algorithm; it should have such a behaviour that the lower the weight of the array antenna element, the higher the function value is (which physically corresponds to an increase in the noise temperature of the corresponding receiver channel). In the numerical results presented hereafter, a filter function is used whose values are close to zero when the weights magnitude $|w_i|$ are higher than w_{constr}, and which has a sharp linear increase near w_{constr}. In this way, f is similar to the inverse step function near w_{constr} (Fig. 3). Here, w_{constr} is the value of the amplitude weight constraint, which is typically in the order of -30 dB or -40 dB.

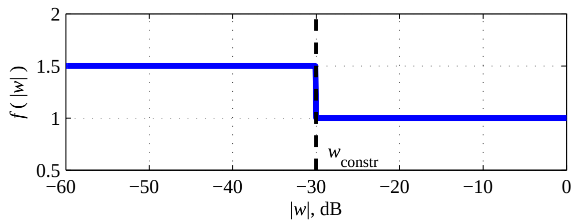

Figure 3: The function f used in the iterative procedure described in section III.C.

- Check whether all the weights are higher than w_{constr}, or negligibly low (i.e. -80 dB in this work). If this condition is satisfied, the iterative procedure is terminated. The channels with negligible weights are switched-off, while the resulting set of weight coefficients is considered to be the final one.

In order to use the beamformer for scanned beams, the noise temperature distribution function $T_{\text{ext}}(\Omega)$ must be provided for each of them and the matrix $\mathbf{C}$ needs to be recomputed.

More detailed on the formulation and implementation of the beamformer can be found in [7].

4 Parametric studies

4.1 Beamformer

The proposed beamformer has two parameters for defining the "cold" ellipse of the mask-constrained function $T_{\text{ext}}(\Omega)$ that are used for the computation of $\mathbf{C}_1$: the ellipse major semi-axis a and the axis ratio a/b (see Fig. 2, top-left inset). Since the area of the ellipse is related to the area of the main lobe over which the received power is maximized, and the size of the foot print is known from specifications, the range of practical values for a and the axis ratio a/b is relatively small, and hence the parametric study to find the optimal values is not time-consuming.

The considered radiometer characteristics [2] as functions of these parameters have been computed and the most critical ones, i.e. the distance-to-land and footprint size, are shown in Fig. 4. As a trade-off between the required values of the distance-to-land (< 15 km) and the footprint size (< 10 km), the following best values have been chosen: $a = 0.535$ and $a/b = 1.3$.

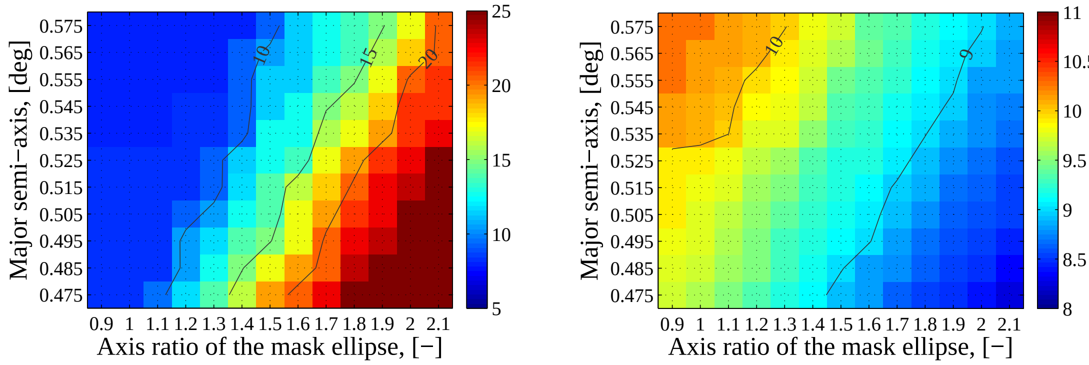

(a) (b)

Figure 4: (a) Distance-to-land, [km]; and, (b) footprint size, [km], as functions of a and a/b used for the definition of the mask-constrained function $T_{\text{ext}}(\Omega)$ as shown on Fig. 2.

4.2 PAF size and final radiometer characteristics

For the beamformer with the parameters as obtained above, we have studied a range of PAF designs which have a number of rows varying from 5 to 8. The computed radiometer characteristics for the range of rows are shown in Fig. 5. As one can see, to satisfy all radiometer requirements, the minimum number of rows in the PAF must be equal to 6.

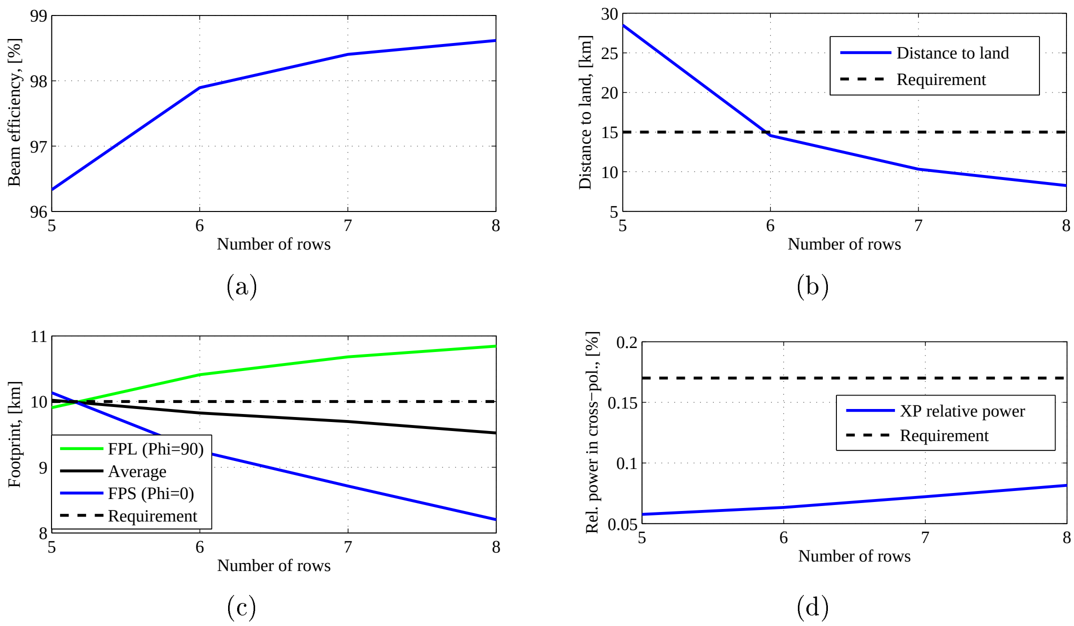

Figure 5: Radiometer characteristics, including the beam efficiency, distance to land, footprint and relative cross-polarization power, vs. the number of rows in the PAF.

Table 2: Final radiometer characteristics at Ku-band (18.7 GHz)

Radiometer characteristic	**Requirement**	**Gaussian feed**	**PAF** $6 \times 19 \times 2$ **elem.** $d_{\mathrm{el}} = 0.75\lambda$
Beam efficiency [%]		73.9	97.9
XP-power, [%]	0.34	0.38	0.06
Dist. to land, [km]	15	90.8	14.6
Beam width, [deg]		0.38	0.357
Footprint (FP), [km]	10	10.5	9.8
FP ellipticity		1.13	1.12

The optimized set of weight coefficients are shown in Fig. 6. The corresponding pattern of the phased-array feed and the pattern of the entire reflector antenna system for the on-axis beam are shown in Fig. 7. We can observe the very fine shape of the illumination pattern across the reflector aperture, and well-behaved final beam with the minimized side-lobe levels. The levels of the side lobes are different, though, over the angular region; that results in the angular dependence of the distance-to-land parameter, which becomes a function of the coast line position. Since the footprint on the Earth resulted from this beam, is not symmetric either, we have investigated whether the “distance-to-land” requirement is satisfied for all possible locations on

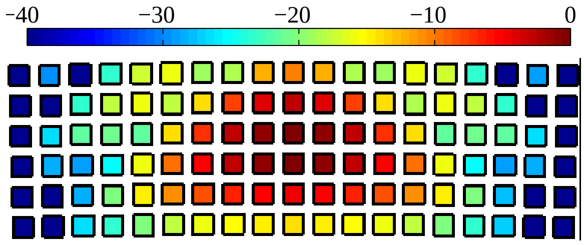

Figure 6: The array element amplitude weight coefficients, [dB], as obtained with the proposed beamforming algorithm. Each block represents an element of the array.

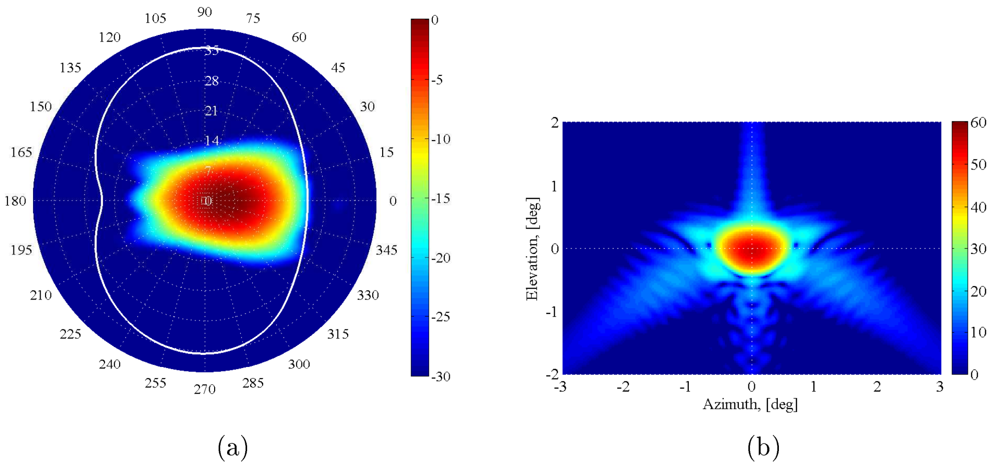

Figure 7: (a) The optimized pattern of the PAF when illuminating the aperture of the torus reflector, [dB], and (b) the corresponding final beam of the entire reflector antenna system for the case of the center beam, [dBi].

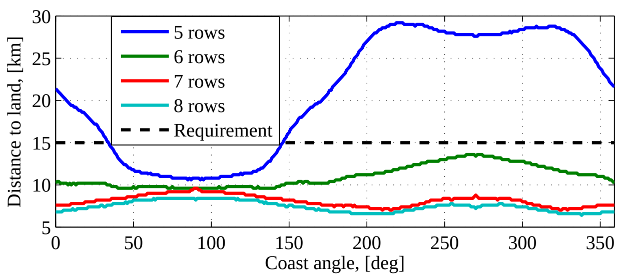

Figure 8: Distance-to-land as a function of angle at which the coast line is approached by the beam for different array sizes.

the land line with respect to the beam footprint. As the data on Fig. 8 show, the PAF with 6 rows satisfies this criterion for all possible positions.

The corresponding radiometer characteristics for the on-axis beam are summarized in Table 2. Thanks to the rotational symmetry of the reflector and the moon-shaped array layout, the scanned beams will have similar characteristics.

5 Conclusion

An optimal beamforming algorithm for phased-array antennas, such as considered for the next generation multi-beam radiometers, has been presented and evaluated for a currently designed prototype system. It yields well behaved multiple beams which satisfy strick requirements to the footprint on the Earth, minimized power in the side-lobes and cross-polarization as well as the distance-to-coast. The proposed algorithm is formulated in a closed form and enables different performance trade-offs.

References

[1] M. Ivashina and J. Bregman, "A way to improve the field of view of the radio telescope with a dense focal plane array," in *Proc. of the Int. conf. on Microwave and Telecommunication Technology*, Sevastopol, Ukraine, Sep. 2002.

[2] C. Cappellin, K. Pontoppidan, P. Nielsen, N. Skou, S. S. Søbjærg, A. Ihle, D. Hartmann, M. Ivashina, O.Iupikov, and K. v. t Klooster, "Novel multi-beam radiometers for accurate ocean surveillance," in *Proc. European Conference on Antennas and Propag. (EuCAP)*, The Hague, The Netherlands, Apr. 2014, pp. 1–4.

[3] P. Nielsen, K. Pontoppidan, J. Heeboell, and B. L. Stradic, "Design, manufacture and test of a pushbroom radiometer," in *Antennas and Propagation, 1989. ICAP 89., Sixth International Conference on (Conf. Publ. No.301)*, Coventry, United Kingdom, Apr. 1989, pp. 126–130.

[4] O. A. Iupikov, M. V. Ivashina, K. Pontoppidan, P. H. Nielsen, C. Cappellin, N. Skou, S. S. Søbjærg, A. Ihle, D. Hartmann, and K. v. t Klooster, "Dense focal plane arrays for pushbroom satellite radiometers," in *Proc. European Conference on Antennas and Propag. (EuCAP)*, Hague, The Netherlands, Apr. 2014, pp. 1–5.

[5] H. L. van Trees, *Optimum Array Processing – Part IV of Detection, Estimation, and Modulation Theory.* New York: Wiley, 2002.

[6] M. V. Ivashina, O. Iupikov, R. Maaskant, W. A. van Cappellen, and T. Oosterloo, "An optimal beamforming strategy for wide-field surveys with phased-array-fed reflector antennas," *IEEE Trans. Antennas Propag.*, vol. 59, no. 6, pp. 1864–1875, Jun. 2011.

[7] O. Iupikov, "Phased-array-fed reflector antenna systems for radio astronomy and Earth observations," Licentiate Thesis, Institutionen för signaler och system, Antenner, Chalmers tekniska högskola, Göteborg, Oct. 2014. [Online]. Available: http://publications.lib.chalmers.se/records/fulltext/206295/206295.pdf

Paper J

Enabling High-sensitivity Near-land Radiometric Measurements With Multi-beam Conical Scanners Employing Phased Arrays

M. V. Ivashina, O. A. Iupikov, C. Cappellin, K. Pontoppidan,
P. H. Nielsen, N. Skou, S. S. Søbjærg, B. Fiorelli

in *Proceedings of 36th ESA Antenna Workshop on Antennas and RF Systems for Space Science,* ESA/ESTEC, The Netherlands, 6-9 October 2015

The layout of this paper has been revised in order to comply with the rest of the thesis.

Enabling High-sensitivity Near-land Radiometric Measurements With Multi-beam Conical Scanners Employing Phased Arrays

M. V. Ivashina, O. A. Iupikov, C. Cappellin, K. Pontoppidan, P. H. Nielsen, N. Skou, S. S. Søbjærg, B. Fiorelli

Abstract

In the recent study, carried out under the ESA contract 4000107369/12/NL/MH "Study on Advanced Multiple-Beam Radiometers", we investigated the use of "dense" phased arrays feeds (dPAFs) for conical scan and push-broom radiometer configurations. It has been found that such systems can satisfy all the challenging requirements for the future Earth observation missions, but need large arrays with many antenna elements. To determine the minimum number of elements and their excitations, we have developed a dedicated optimization procedure and applied it to the dPAFs for the push-broom case. This procedure is based on the beamforming approach that jointly optimizes for the maximum beam efficiency (or the maximum beam sensitivity) and minimum distance-to-land. The goal of this work is to repeat the same procedure for the conical-scan radiometer, for which we initially used a simplified Conjugate Field Matching based beamforming approach.

1 Introduction

Existing spaceborne microwave radiometers typically use conical-scan (CS) reflector antennas with horn feeds. Such systems, operating at C-band (6.9 GHz) or at higher frequency, provide a spatial resolution of around 50 km, whereas less than 20 km is desirable [1, 2]. Furthermore, accurate radiometric measurements are currently possible at not closer than around 100 km from the shore-line, because of the signal contamination by the antenna side-lobes illuminating the land (see Table 1). There is a strong desire to reduce it to 5-15 km.

The required 20 km resolution, i.e. 3-dB footprint, at C-band leads to a large antenna aperture of around 5 m in diameter that is considerably larger than any radiometer system antenna flown hitherto. Moreover, the required short distance-to-land (i.e. 5-15 km) can only be achieved by replacing the conventional feed technology with novel "dense" phased arrays feeds (dPAFs), which are capable of producing many simultaneously-formed and closely-spaced beams. A feasibility study of dPFAs was

Table 1: Characteristics of the existing radiometers (ANSR-E and WindSat). The desired values for future observation missions are shown in parentheses.

Band	Footprint, [km]	Sensitivity, [K]	Dist.to coast, [km]
C	55 (20)	0.3 (0.30)	100 (5-15)
X	35 (20)	0.5 (0.22)	100 (5-15)
Ku	20 (10)	0.5 (0.22)	100 (5-15)

conducted by the authors (in collaboration with HPS, Germany), where dPAFs were investigated in both CS and more advanced push-broom configurations. This study has demonstrated that with dPFAs we could satisfy all the challenging radiometric requirements, but at the expenses of a large number of array elements [3,4]. To determine the optimum number of elements and their excitations, we developed a dedicated procedure maximizing the beam efficiency or the beam sensitivity (as formulated by TICRA and CHALMERS, respectively), while minimizing the distance-to-land [5,6]. First, this procedure was applied to reduce the number of elements in the dPAFs for the push-broom antenna, while for the conical scanner – which needs relatively smaller array feeds – we used a simplified Conjugate Field Matching (CFM) based approach. In this paper, we apply this dedicated procedure to the conical-scan case and show its advantages.

2 Limitations of horn feeds

Horn antenna feeds used in radiometer systems are typically designed to produce an illumination pattern with strong taper toward the edge of the reflector to trade high beam efficiency, and low cross-polarization power against low side lobes, to achieve a short distance to land. Figures 1(b-h) show typical antenna patterns as well as radiometer parameters at C-band, which were obtained for the conical scanner (see the description of antenna geometry in [3]). The antenna is a paraboloid with circular projected aperture, and it has the projected aperture diameter of 5 m, clearance of 1 m and focal length of 3 m. The antenna was analyzed with the Gaussian beam model of the feed having a varying illumination taper and aperture diameter of the corresponding horn antenna [7,8]. The positions and aperture diameters of the horns in the focal plane are depicted on Figure 1(a) by circles of different sizes corresponding to three taper values at C, X and Ku bands. As one can see, the horn feeds have large aperture diameter (> one wavelength), and thereby large offset positions with respect to the focal point, hence degradation in performance of such off-axis beams can be expected, especially at the C-band.

These simulations have been used as the starting point of our research on dPAFs in order to quantitatively illustrate fundamental limitations of conventional feed technologies. Indeed, as the results in Figures 1(e-h) show, the cross-polarization power

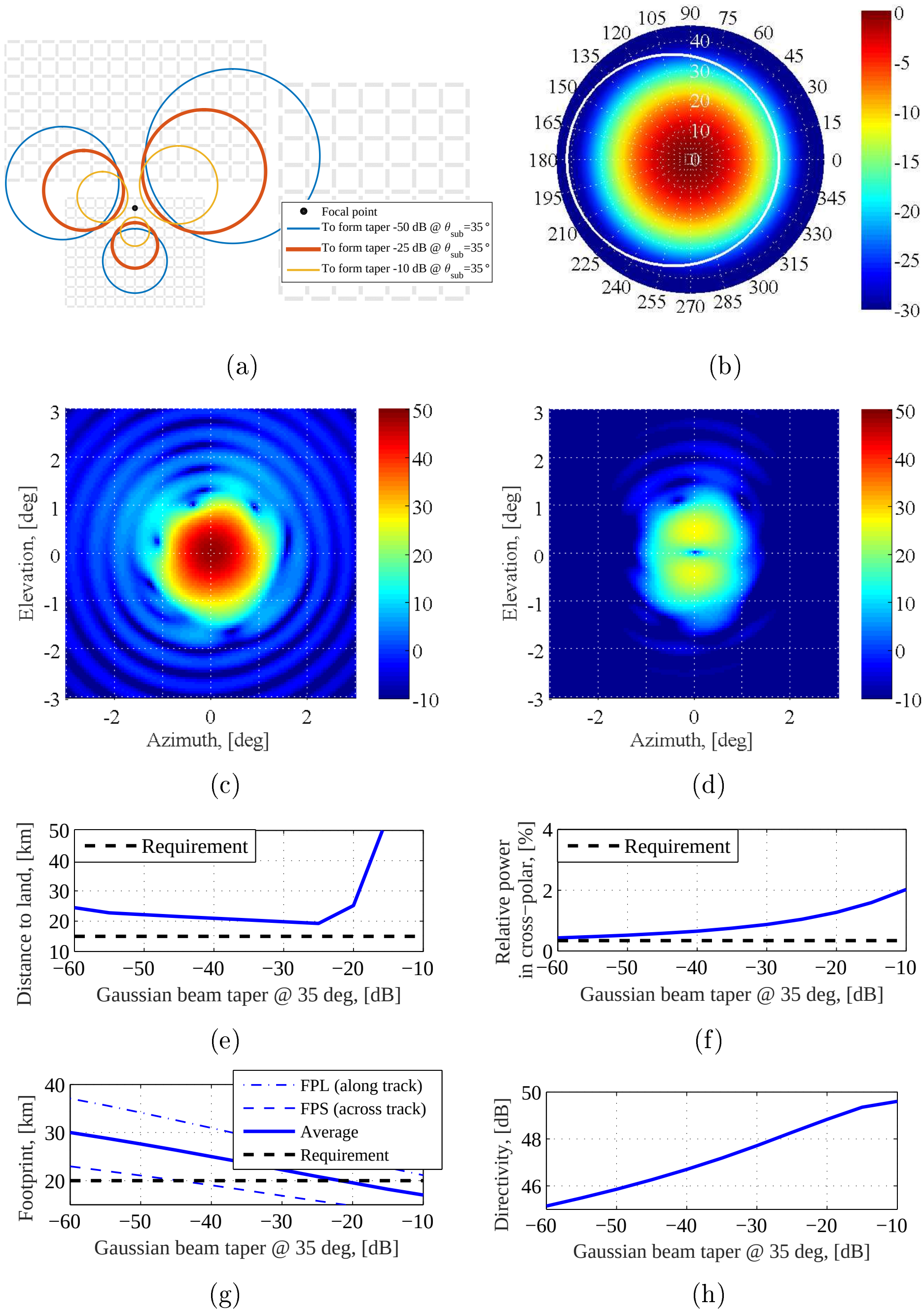

Figure 1: (b) Simulated locations and aperture diameters of the horn feeds at C, X and Ku frequency bands for three different values of the illumination taper; (b) Illumination pattern of the Gaussian feed with the optimal relative taper toward the edge of reflector of -25dB and (c-d) Co- and cross-polarization patterns of the reflector antenna. (e-h) Radiometer characteristics, i.e. the distance-to-land, relative cross-polarization power, footprint size and directivity as function of the illumination taper of the Gaussian feed.

for the conical-scan radiometer can only be minimized by strongly tapering the feed pattern, but this leads to the increase of the footprint size and distance-to-land, and hence the difficulties to satisfy the sensitivity requirements (more horn/receivers may be needed). The shortest distance-to-land that can be achieved with this tapering approach is $\sim$ 20 km for the taper value of -25dB, for which the realized cross-polarization power is at least 3 times higher than the desired 0.34%. The radiometer characteristics for the optimal taper value are also summarized in Table 3.

3 Arrays feeds: CFM beamforming

During the project 'Study on Advanced Multiple-Beam Radiometers" we found that in order to meet the sensitivity requirement for a swath of 1500 km, the conical-scan antenna needs 2 beams at C-band, 21 beams at X-band and 30 beams at Ku-band [3,9]. The layouts of the considered dPAFs along with their relative positions in the focal plane of the reflector are illustrated on Figure J.1(a) and their dimensions is summarized in Table 2.

Table 2: Number of antenna elements in the arrays

Band	Array size	Number of elements		
		X-orient.	Y-orient.	Total
C	$6.0 \times 5.3\lambda$	64	63	127
X	$6.0 \times 11.3\lambda$	128	135	263
Ku	$8.3 \times 10.5\lambda$	165	168	333

In the course of this study, some assumptions and simplifications were made in order to limit the complexity of the phased array feed. One of these assumption was that the array has identical embedded element patterns, which were modeled for the case for a half wavelength dipole antenna array with 0.75 wavelength inter-element separation distance, located above an infinite ground plane. Furthermore, for the conical scanner, a simple beamforming method was applied to determine the optimal excitation coefficients of the feed array elements. This method is based on the Conjugate Field Matching (CFM) approach that has been conventionally used as a feed synthesis technique for horn feeds [10]. The core of this approach is to analyze the focal region field of a reflector antenna (in the absence of the feed) for an incident plane wave (PW), and then calculate the desired size of the feed aperture, which should conjugately match the truncated reference focal-field distribution. One of the limitations of this CFM method is that the optimal taper of the incident plane wave (that is typically used to control side-lobe levels) is a priory not known, and – if not determined correctly – can yield an over-estimated feed size or unsatisfactory beam performance. This limitation can be critical, especially when applying CFM to

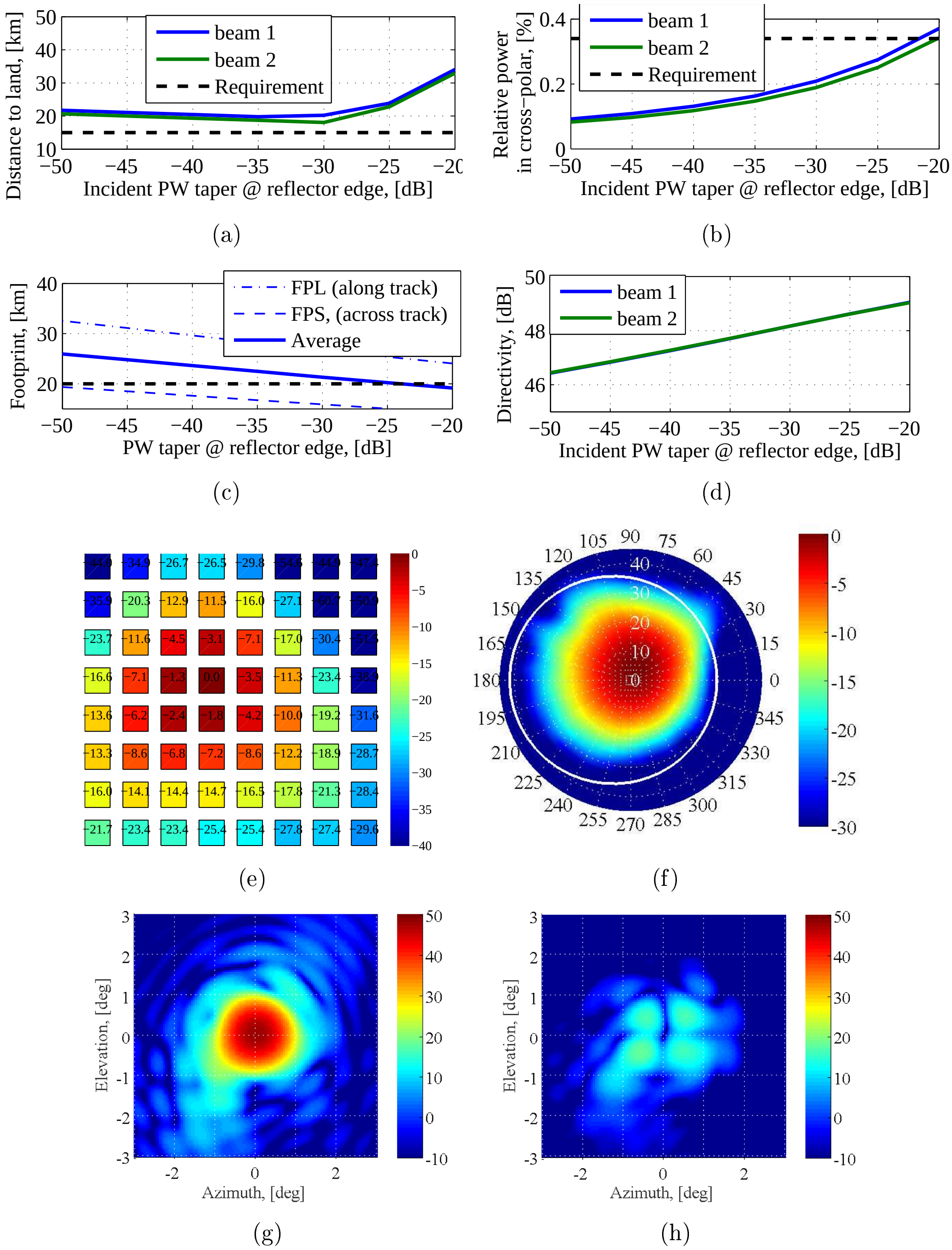

Figure 2: CFM beamforming approach: (a-d) Radiometer characteristics, i.e. the distance-to-land, relative cross-polarization power, footprint size and directivity as function of the incident plane wave taper; (e) Excitation coefficients of the PAF at C-band, dB, as obtained with the CFM approach for the plane wave taper of -30 dB as an example, (f) corresponding illumination pattern, (g-h) co- and cross-polarization patterns of the reflector antenna.

Table 3: Radiometer characteristics for different feeds

Radiometer characteristic	Require-ment	Horn feed	Array feed I, CFM beamformer		Array feed II, CFM beamformer		Array feed I, MSMDL beamf.	
			Beam 1	Beam 2	Beam 1	Beam 2	Beam 1	Beam 2
Number of antenna elements (2 polarizations)			$64 + 63 = 127$		$80 + 77 = 157$		$64 + 63 = 127$	
Distance to land, [km]	< 15	19	20	18	16	16	14	15
Rel. cross-pol. power, [%]	< 0.34	1.04	0.21	0.19	0.19	0.19	0.29	0.23
Beam efficiency, [%]		97	95	95	95	95	96	95
Footprint (average), [km]	< 20	21	21	21	21	21	20	20
Footprint ellipticity		1.6	1.7	1.7	1.7	1.7	1.4	1.4

design PAFs, which can have a large number of active antenna elements and exhibit strong mutual coupling effects.

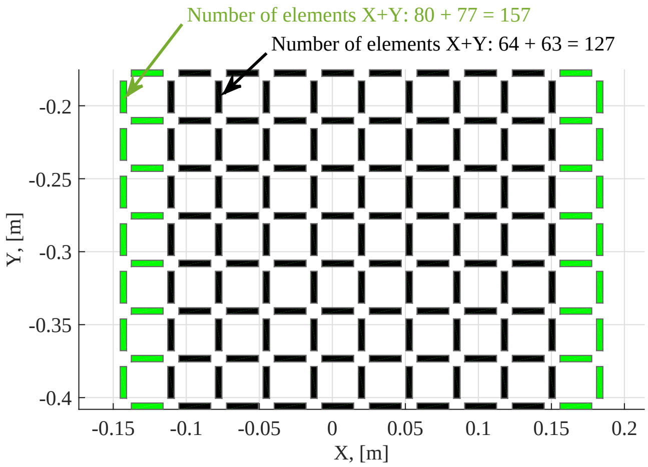

Figure 3: Original (black) and enlarged (green) dual-polarized phased array feeds for C-band.

Figure 2(a-d) presents the results of a parametric study aimed to determine the optimal value of the plane wave taper that could meet the performance specifications at C-band (see Array I in Table 3). As seen, with the given array size and utilized CFM optimization approach, the performance upper bound in terms of the distance-to-land is 18 and 20 km that is similar to that with the Gaussian feed, while the relative cross-polarization power is significantly better (0.20% vs. 1.04%). Figure 2(e-h) shows the element excitation coefficients and antenna patterns for the optimum PW taper value of -30dB.

As one can notice from the Figure 2(e), the excitation coefficients at the left edge of the array have relatively high amplitude values (> -14 dB). Therefore, an improvement in the radiometer performance can be expected by adding additional column of antenna elements. The enlarged in such way array is shown on Figure 3, where newly added elements are denoted by green color. The radiometer characteristics for this array (Array II) are also summarized in Table 3. A better performance is observed now, where most of the requirements are satisfied, though with the larger array of 30 more antenna elements.

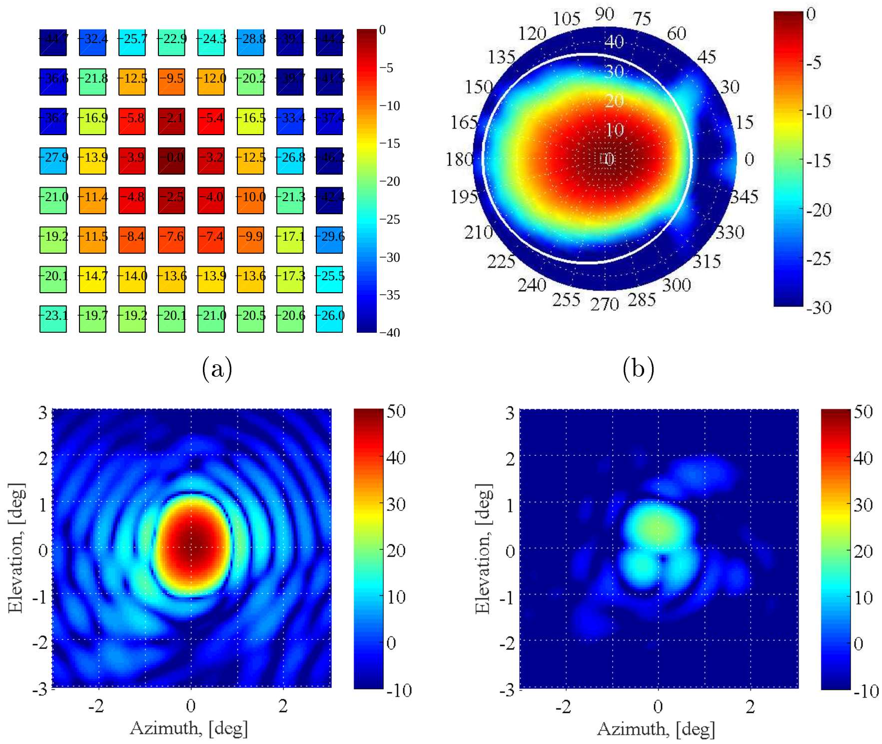

Figure 4: MSMDL beamforming approach: (a) Excitation coefficients of the PAF at C-band, (b) corresponding illumination pattern, (c-d) co- and cross-polarization patterns of the reflector antenna. All values are in dB.

4 Arrays feeds: Max. Sensitivity - Min. Distance-to-Land beamforming

In contrast to the traditional CFM beamforming, new approaches based on optimum array signal processing methods are more accurate, and capable of handling a large number of array elements, large number of beams and complex performance specifications. An example of such methods is a customized beamforming method that jointly optimizes for maximum sensitivity and minimum distance-to-land, which was proposed and applied to the push-broom radiometer concept [5, 6]. In this paper we apply this customized beamforming to the conical scanner and present obtained results.

The proposed optimization method is formulated as the maximum Signal-To-Noise beamformer (MaxSNR) [11], where the antenna sensitivity (or efficiency in the noise-less case) - defined for a given direction of observation corresponding to the beam center - is maximized, while minimizing the power received from the directions of side-lobes. The weight vector for this beamformer can be written as $\mathbf{w}_{\mathrm{MaxSNR}} =$

$\mathbf{C}^{-1}\mathbf{e}$ with with SNR $= \mathbf{e}^H \mathbf{w}_{\mathrm{MaxSNR}}$, where where the vector $\mathbf{e} = [e_1, \ldots, e_N]^T$ holds the signal-wave amplitudes at the receiver outputs and arises due to an externally applied electromagnetic plane wave $\boldsymbol{E}_{\mathrm{i}}$; and $\mathbf{C}$ is a Hermitian spectral noise-wave correlation matrix holding the correlation coefficients between the outputs of the array receiving system.

If we assume a noiseless receiver system, the matrix $\mathbf{C}$ represents the antenna noise correlation matrix. The elements of $\mathbf{C}$ can be calculated through the pattern-overlap integrals between $\boldsymbol{f}_n(\Omega)$ and $\boldsymbol{f}_m(\Omega)$, which are the nth and mth embedded element pattern of the array (defined after the reflection from the dish), respectively [12], i.e., $C_{mn} = \int T_{\mathrm{ext}}(\Omega)[\boldsymbol{f}_m(\Omega) \cdot \boldsymbol{f}_n^*(\Omega)]\, \mathrm{d}\Omega$, where $T_{\mathrm{ext}}(\Omega)$ is the brightness temperature distribution of the environment. To meet the radiometer requirements [3], the function $T_{\mathrm{ext}}(\Omega)$ is chosen such that it has low temperature values in the region of the expected main lobe and high values outside of this region. In this way, we realize the maximization of the beam efficiency, while minimizing the side-lobe and cross-polarization power outside of this region.

The resulting excitation coefficients and antenna patterns for the smaller array (Array I) are shown on Figure 4 and the radiometer characteristics are summarized in Table 3. These results clearly demonstrate the advantage of the MSMDL beamforming approach to determine the minimum number of antenna elements, as compared to the CFM approach. Further minor reduction in the array size could be possible for the MSMDL beamformer, but this has to be still studied.

5 Conclusions

An advantage of novel phased array feeds with respect to traditional single-horns is their capability of satisfying complex performance specifications by optimally beamforming the signals received by a large number of array elements. As shown in this paper, an optimal beamforming approach, such as the Maximum Sensitivity - Minimum Distance-to-Land approach – can lead to a major improvement in the performance of the present and flying technologies. For the conical-scan antenna, the distance to land of 15 km can be achieved with an array of 127 half-wavelength dipole antenna elements. For comparison, a beamforming method based on the conventional Conjugate Field Matching approach would provide similar performance with a larger array, in our case with 30 more elements. In future work we plan to re-evaluate the resultant radiometer characteristics with a more accurate array model accounting for the mutual coupling and edge truncation effects, as well as try to further minimize the number of antenna elements.

Acknowledgments

The authors acknowledge the Swedish Research Council for providing partial support to this work as well as Kees van 't Klooster for many fruitful discussions.

References

[1] P. W. Gaiser, "The WindSat spaceborne polarimetric microwave radiometer: Sensor description and early orbit performance," *IEEE Trans. Geo. Rem. Sensing*, vol. 42, no. 11, pp. 591–603, Nov. 2004.

[2] Amsr-e instrument description. [Online]. Available: http://nsidc.org/data/docs/daac/amsre_instrument.gd.html

[3] C. Cappellin, K. Pontoppidan, P. Nielsen, N. Skou, S. S. Søbjærg, A. Ihle, D. Hartmann, M. Ivashina, O.Iupikov, and K. v. t Klooster, "Novel multi-beam radiometers for accurate ocean surveillance," in *Proc. European Conference on Antennas and Propag. (EuCAP)*, The Hague, The Netherlands, Apr. 2014, pp. 1–4.

[4] O. A. Iupikov, M. V. Ivashina, K. Pontoppidan, P. H. Nielsen, C. Cappellin, N. Skou, S. S. Søbjærg, A. Ihle, D. Hartmann, and K. v. t Klooster, "Dense focal plane arrays for pushbroom satellite radiometers," in *Proc. European Conference on Antennas and Propag. (EuCAP)*, Hague, The Netherlands, Apr. 2014, pp. 1–5.

[5] C. Cappellin, K. Pontoppidan, P. H. Nielsen, N. Skou, S. S. Søbjærg, A. Ihle, M. V. Ivashina, O. A. Iupikov, and K. v. 't Klooster, "Design of a push-broom multi-beam radiometer for future ocean observations," in *Proc. European Conference on Antennas and Propag. (EuCAP)*, Lisbon, Portugal, Apr. 2015, pp. 1–5.

[6] O. A. Iupikov, M. V. Ivashina, K. Pontoppidan, P. H. Nielsen, C. Cappellin, N. Skou, S. S. Søbjærg, A. Ihle, D. Hartmann, and K. v. t Klooster, "An optimal beamforming algorithm for phased-array antennas used in multi-beam spaceborne radiometers," in *Proc. European Conference on Antennas and Propag. (EuCAP)*, Lisbon, Portugal, Apr. 2015, pp. 1–5.

[7] P.-S. Kildal, *Foundations of Antenna Engineering – A Unified Approach for Line-Of-Sight and Multipath*. Kildal Antenn AB, 2015.

[8] T. Teshirogi and T. Yoneyama, *Modern Millimeter-wave Technologies*. IOS Press, 2001.

[9] N. Skou, S. S. Søbjærg, S. S. Kristensen, C. Cappellin, K. Pontoppidan, M. Ivashina, A. Ihle, and K. v.'t Klooster, "Future spaceborne ocean missions using high sensitivity multiple-beam radiometers," in *IEEE International Geoscience and Remote Sensing Symposium (IGARSS)*, Québec City, Québec, Canada, Jul. 2014.

[10] M. V. Ivashina and C. G. M. van't Klooster, "Focal fields in reflector antennas and associated array feed synthesis for high efficiency multi-beam performances," in *Proc. 25th ESA Workshop on Satellite Antenna Technologies*, Noordwijk, The Netherlands, Sep. 2002, pp. 339–346.

[11] H. L. van Trees, *Optimum Array Processing – Part IV of Detection, Estimation, and Modulation Theory.* New York: Wiley, 2002.

[12] M. V. Ivashina, O. Iupikov, R. Maaskant, W. A. van Cappellen, and T. Oosterloo, "An optimal beamforming strategy for wide-field surveys with phased-array-fed reflector antennas," *IEEE Trans. Antennas Propag.*, vol. 59, no. 6, pp. 1864–1875, Jun. 2011.

Paper K

Multi-Beam Focal Plane Arrays with Digital Beamforming for High Precision Space-Borne Remote Sensing

O. A. Iupikov, M. V. Ivashina, N. Skou, C. Cappellin, K. Pontoppidan, K. v. 't Klooster

Under review for *IEEE Transactions on Antennas and Propagation,* 2017

The layout of this paper has been revised in order to comply with the rest of the thesis.

Multi-Beam Focal Plane Arrays with Digital Beamforming for High Precision Space-Borne Remote Sensing

O. A. Iupikov, M. V. Ivashina, N. Skou, C. Cappellin, K. Pontoppidan, K. v. 't Klooster

Abstract

The present-day ocean remote sensing instruments that operate at low microwave frequencies are limited in spatial resolution and do not allow for monitoring of the coastal waters. This is due the difficulties of employing a large reflector antenna on a satellite platform, and generating high-quality pencil beams at multiple frequencies. Recent advances in digital beamforming focal-plane-arrays (FPAs) have been exploited in the current work to overcome the above problems. A holistic design procedure for such novel multi-beam radiometers has been developed, where (i) the antenna system specifications are derived directly from the requirements to oceanographic surveys for future satellite missions; and (ii) the numbers of FPA elements/receivers are determined through a dedicated optimum beamforming procedure minimizing the distance to coast. This approach has been applied to synthesize FPAs for two alternative radiometer systems: a conical scanner with an off-set parabolic reflector, and stationary wide-scan torus reflector system; each operating at C, X and Ku bands. Numerical results predict excellent beam performance for both systems with as low as 0.14 % total received power over the land.

1 Introduction

Microwave radiometry is a highly versatile method of remote sensing, capable of delivering measurements of a variety of geophysical properties of the ocean and atmosphere, even through clouds. The retrieval methods distinguish the individual effects of different geophysical properties by using the frequency and polarization state of the microwave radiation detected by the antenna. Despite such versatility, the exploitation of microwave radiometry in Earth observation has been constrained by the difficulties of generating antenna beams with low side-lobes and cross-polarization, and accomodating several feeds operating at different frequencies, when deploying the antenna on a satellite platform [1]. In particular, for high resolutions demanded by oceanographers, the current antenna designs would need to be scaled up to a physical size that is too large to be achievable or affordable within typical Earth observation infrastructure budgets. For this reason, space agencies have been seeking solutions to overcome what seems at present to be an unpassable barrier to further significant improvement of a whole class of remote sensing methods.

The European Space Agency (ESA) is currently considering the ocean missions where extreme weather, climate variability, coastal and marginal-ice-zone studies are strong drivers [2, 3]. These studies require a very high radiometric resolution, i.e. around 0.25 Kelvin, and at the same time a high spatial resolution approaching 20 km at C and X bands and 10 km at Ku band (see Table 1) [4]. This desired performance represents a significant improvement compared with existing space-borne radiometer systems, such as AMSR-E and WindSat [5,6]. They feature spatial resolutions around 55 km, 35 km, and 20 km at the C, X, and Ku bands, and the radiometric resolution provided by AMSR-E is 0.3 K at C band and 0.6 K at X and Ku band, while for WindSat it is around 0.7 K. Moreover, future systems are required to provide valid observations up to very short distances from the coastline, i.e. 5-15 km, while the existing systems can observe only up to ~ 100 km.

It can be shown that the desired spatial resolution calls for a reflector antenna with ~ 5 m aperture diameter [7]; that is considerably larger than any radiometer antenna flown hitherto. On the other hand, for all three frequency bands the bandwidths are limited to a few hundreds of MHz, that makes it possible (at least in theory) to achieve very low noise temperatures of the receivers. However, even the most optimistic receiver noise properties cannot ensure the required radiometric resolution when considering a single beam scanning system (see Fig. 1(a)). For a scanner, the only solution is to employ several independent beams per frequency, and improve radiometric resolution by integrating several footprints. This calls for a large number of overlapping beams – in the present case up to 30 beams at Ku-band. An alternative is a push-broom system [8, 9], where many beams cover the swath simultaneously, as illustrated in Fig. 1(b). Using traditional feeds, each antenna beam is associated with its own receiver, and high radiometric resolution is achieved thanks to the fact that the signals associated with multiple across-track footprints do not have to be multiplexed through a single receiver. Radiometric resolution is no longer a problem, but a more complicated antenna design (a tilted parabolic torus reflector) is needed as well as many beams – for the present case up to 156 at Ku-band. Realizing these, while correcting for the antenna field distortions causing the well-known triangular footprints and their large separation on the Earth [8, 9], represents a great challenge. Also the implementation of this concept should be feasible regarding the resource requirements, i.e. the size, mass and power consumption.

As demonstrated in this study (see Sec. 4), the above radiometric requirements cannot be fulfilled by using traditional cluster feeds of horns (in one-horn-per-beam configuration), employed at such multi-frequency radiometer antennas. Recent studies supported by ESA [10–13] have identified a promising solution that originates from the field of radio astronomy [14–20], where instrument designs have evolved to meet the high-sensitivity and large-coverage requirements of ground based observatories exploring the universe without the above challenges. This solution is based on 'dense' focal plane arrays (FPAs), where many small antenna elements take part in the formation of each beam (so that each beam can be optimized for high performace, even far off-axis beams) and the same element takes part in the formation of multiple beams (so that the footprints overlap), thanks to digital beamforming. Although the basic principles of these systems are rather similar to those in radio astronomy, there are many differences, which are related to application specific requirements. These requirements will be discussed in Sec. 2, and transtated into antenna system specifications and beam characteristics to optimize for. The reflector antenna geometries used in this study are briefly described in Sec. 3. Section 5 will cover the synthesis of FPAs for such systems, and include the following original contributions: (i) a dedicated optimum-beamforming algorithm minimizing the distance to coast; (ii) optimized antenna patterns and radiometric parameters – as obtained for the half-wavelength dipole element FPAs – that fulfill all above requirements with almost twice less elements in comparison to the conventional conjugate-field-matching optimization approach [10]; and (iii) validation of the simplified array model with the assumed identical embeded element patterns [10, 12] across the full MoM model for the purpose of the FPA synthesis. Finally, digital receiver resource requirements will be considered in Sec. 6.

2 From oceonagraphic requirements to antenna system specifications

The requirements for future missions in Table 1 are defined in terms of performance metrics for oceanographic surveys, i.e. spatial resolution, radiometric resolution, bias and distance to coast. Since these terms are not commonly known by antenna designers, next we will summarize their definitions and use these to derive the antenna system specifications.

Table 1: Radiometric requirements for future ocean missions

Freq., [GHz]	Band width, [MHz]	Polarization	Radiometric resolution, [K]	Bias, [K]	Spatial resolution, [km]	Dist.to coast, [km]
6.9	300	V, H	0.30	0.25	20	5-15
10.65	100	V, H, S_3, S_4	0.22	0.25	20	5-15
18.7	200	V, H, S_3, S_4	0.25	0.25	10	5-15

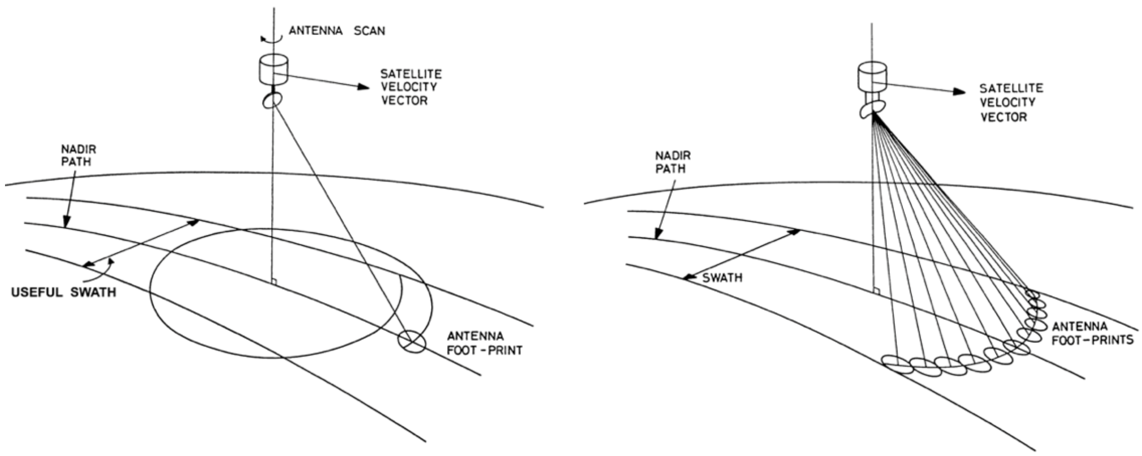

Figure 1: Operational principle of (left) the conical scan and (right) push-broom microwave radiometers for ocean remote sensing.

2.1 Spatial resolution (FP) ⇒ reflector diameter

The required spatial resolution in Table 1 is defined in terms of the footprint (FP) on the Earth's surface:

$$\mathrm{FP} = (Y \times \theta_{\mathrm{3dBT}} + Y \times \theta_{\mathrm{3dBL}}/\cos\nu)/2, \qquad (1)$$

where θ_{3dBL} and θ_{3dBT} are the half-power beamwidths of the antenna main beam along the elevation and azimuth directions, respectively, ν is the incidence angle as measured from the normal to the Earth's surface and Y is the distance from the satellite to the observation point on the Earth.

The FP is directly related to the antenna beamwidth, and hence determines its aperture diameter. This diameter should be at least 5 m for the present case ($\nu = 53°$ and $Y = 1243$ km) in order to realize the FP of 20 km at C-band. Since for the considered system, the same antenna is used at different bands, the same FP cannot be obtained at both C- and X-bands. The required FP shall therefore be considered a guideline and values both slightly above and below are acceptable. The important factor is that the beam crossover points should be at the -3 dB level. This means that if the FP is reduced, more beams are needed to cover a particular region on the Earth.

2.2 Bias (ΔT) ⇒ acceptable cross-polarization power

Bias is a systematic error of the measured brightness temperature of the sea. For full polarization radiometers, ΔT is typically driven by polarization leackage. The approximate values of the see temperature for the incidence angle 53° are $T_{\mathrm{v}} = 150$ K and $T_{\mathrm{h}} = 75$ K in vertical and horizontal polarizations, respectively. To measure

T_h, one can select the co-polar component as the horizontal polarization. The cross-polarization component of the pattern, however, will pick up the vertical component of the radiation from the sea, which has a temperature of 150 K. Using the assumption that the amount of radiation received from the sky is negligible, it is sufficient to consider the antenna pattern in the angular region covering the Earth only, and hence compute the total temperature as $T_\mathrm{b} = T_\mathrm{v} P_\mathrm{cross} + T_\mathrm{h} P_\mathrm{co}$, where P_co and P_cross are the co- and cross-polarization received powers in the angular region of the Earth. Then, $\Delta\mathrm{T}$ can be found as

$$\Delta\mathrm{T} = T_\mathrm{b} - T_\mathrm{h} = (T_\mathrm{v} - T_\mathrm{h}) P_\mathrm{cross}, \tag{2}$$

where P_cross is the acceptable relative cross-polarization power of the antenna pattern that coverers the Earth. Using (2), one can show that the requirement for the $\Delta T =$ 0.25 K can be satisfied only if P_cross does not exceed 0.34 %.

2.3 Distance to coast (D_c) ⇒ acceptable side lobes and cross-polarization power

Table 1 states that D_c should be 5-15 km, when measured from the FP. The reason behind this requirement is that the brightness temperature of the land is much higher than that of the sea. This means that the power in the antenna pattern over land must be sufficiently small. In order to assess the influence from the land the cross polarization can be neglected. The brightness temperature of the land surface is about $T_\mathrm{land} = 250$ K. Assuming the measurements at horizontal polarization, the sea temperature is around $T_\mathrm{h} = 75$ K. If there is no land below the satellite, the radiometer will receive an amount of power proportional to $T_\mathrm{h} P_\mathrm{co}$. If the satellite covers both the land and sea regions, the power from the sea is $T_\mathrm{h}(P_\mathrm{co} - P_\mathrm{land})$, where P_land is the relative co-polarization power in the land region. The signal from the land is $T_\mathrm{land} P_\mathrm{land}$. The measured temperature and $\Delta\mathrm{T}$ are therefore

$$T_\mathrm{b} = T_\mathrm{h} \frac{P_\mathrm{co} - P_\mathrm{land}}{P_\mathrm{co}} + T_\mathrm{land} \frac{P_\mathrm{land}}{P_\mathrm{co}}, \tag{3}$$

$$\Delta\mathrm{T} = T_\mathrm{b} - T_\mathrm{h} = (T_\mathrm{land} - T_\mathrm{h}) \frac{P_\mathrm{land}}{P_\mathrm{co}}. \tag{4}$$

We will now determine D_c by the help of Fig. 2, where we have assumed a straight coastline and a circular symmetric beam with the beamwidth of θ_3dB. The beam is located over the sea and the distance from the peak to the coast is indicated by the angle θ_c, while the power in the cone with semi-angle θ_c is denoted by P_c. The power outside this cone is $P_\mathrm{co} - P_\mathrm{c}$ and approximately half of this power will fall on the land, so we have $P_\mathrm{land} = (P_\mathrm{co} - P_\mathrm{c})/2$. Substituting this into (4) gives

$$\frac{P_\mathrm{c}}{P_\mathrm{co}} = 1 - \frac{2\Delta\mathrm{T}}{T_\mathrm{land} - T_\mathrm{h}}. \tag{5}$$

Inserting the required $\Delta\mathrm{T} \leq 0.25\mathrm{K}$ in (5) gives

$$\frac{P_{\mathrm{c}}}{P_{\mathrm{co}}} \geq 1 - \frac{2 \times 0.25}{T_{\mathrm{land}} - T_{\mathrm{h}}} = 0.9972. \tag{6}$$

This equation shows that the required accuracy is obtained when the coastline is located outside a cone around the main beam containing 99.72% of the total power on the Earth. Hence, in order to reduce D_{c}, one should minimize this cone. Then D_{c} can be defined as the angular difference $\theta_{\mathrm{c}} - \theta_{3\mathrm{dB}}$ projected on the Earth surface, i.e.,

$$D_{\mathrm{c}} = Y \sin\theta_{\mathrm{c}} - Y \sin\theta_{3\mathrm{dB}} \approx (\theta_{\mathrm{c}} - \theta_{3\mathrm{dB}})Y. \tag{7}$$

It should be noted that for non-symmetric patterns, the same procedure can be used, where the resulting distance to coast should be an average value for all antenna pattern cuts.

2.4 Radiometric resolution ($\Delta T_{\mathbf{min}}$) $\Rightarrow$ number of beams

Radiometric resolution is the smallest change in input brightness temperature that can be detected. For a full-polarization radiometer it can be found as

$$\Delta T_{\mathrm{min}} = \frac{T_{\mathrm{sys}}}{\sqrt{N_b B \tau}} = \frac{T_{\mathrm{rec}} + T_{\mathrm{b}}}{\sqrt{N_b B \tau}}, \tag{8}$$

where τ is the integration interval, B is the radiometer effective bandwidth, T_{rec} is the receiver noise temperature, and N_{b} is the number of beams. Since $T_{\mathrm{h}} \ll T_{\mathrm{v}}$, it is more affected by the erroneous power signal from land.

The required ΔT_{min} can be achieved by making a trade-off between N_{b} for a given reflector diameter, and complexity of the feed. For a conically scanning antenna, rotating at 11.5 RPM, N_{b} in the along-track direction is selected such to cover the same strip width on the Earth at each frequency band. To reach the required ΔT_{min} we need:

- 2 beams along track at 6.9 GHz
- 3 beams along track and 7 beams across track at 10.65 GHz
- 5 beams along track and 6 beams across track at 18.7 GHz

For a push-broom case, the antenna is stationary, and its ΔT_{min} is about one order of magnitude better than the one for the scanner. This is at the expense of a very large N_{b}, and correspondingly large number of receivers. For a swath of 600 km we need:

- 58 beams across track at 6.9 GHz

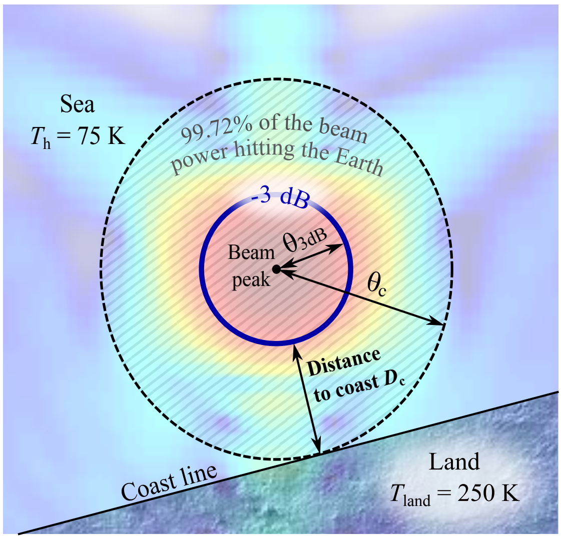

Figure 2: Footprint falling on the sea near a coast: illustration for the definition of the distance to coast D_c.

- 89 beams across track at 10.65 GHz
- 156 beams across track at 18.7 GHz

For both cases listed above, we have considered a FP overlap of $\sim$ 30% both along track and across track to assure accurate sampling of the temperature scene on-ground, and the values of B and T_{rec} as shown in the Table 1 and Table 2 [7].

Table 2: Assumed noise characteristics of the receiver

	Conical scanner		Push-broom	
	NF	T_{rec}	NF	T_{rec}
C band	2.5 dB	226 K	3.5 dB	359 K
X band	2.5 dB	226 K	3.5 dB	359 K
Ku band	3.0 dB	290 K	4.0 dB	438 K

3 Reflector antenna design

3.1 Reflector geometries

To find a suitable type of the antenna that is capable of fulfilling all performance requirements, while having as compact as possible design, we have investigated different reflector systems, including conventional off-set parabolic reflectors with circular and

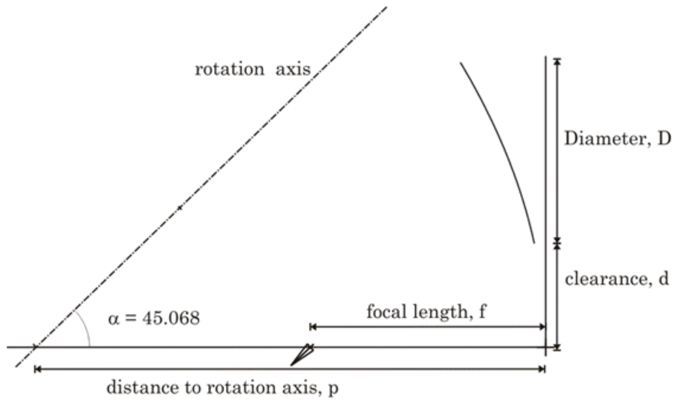

Figure 3: Obtaining a torus from a parabolic arc.

elliptical apertures as the conical scanner, and toroidal single- and dual-reflector antennas for the push-broom concept. The sections below describe the selected conical scanner and push-broom antenna implementations.

The conical scan antenna is a conventional offset paraboloid with projected aperture D of 5 m and circular rim. The clearance is set to 1 meter in order to provide space for the feed cluster and the focal length f is set to 3 m in order to make the design more compact.

The push-broom antenna is a torus reflector with projected aperture D of 5 m. The torus is obtained by rotating a section of a parabolic arc around a rotation axis. The focal length of the parabolic generator is also 5 m. A possible way of obtaining the torus is shown in Fig. 3: the feed axis is selected parallel to the rotation axis, implying that all feed element axes are parallel and orthogonal to the focal plane. The array feed becomes therefore planar, simplifying the mechanical and electrical design. The antenna shall be able to provide a scan of $\pm 20°$ corresponding to a swath width of 600 km. The reflector rim is found by intersecting the torus surface by the feed cone up to the out-most scan positions of 20° and $-20°$ (see Fig.3 in [10]). The antenna projected aperture is 5×7.5 m.

3.2 Reflector surface technology

The conical scan and push-broom antennas can be realized by a deployable double layer pantograph technology with two triangular wire-band curved nets, like in an AstroMesh reflector [21,22]. The corners of the triangles of the two nets are connected by adjustment wires. The front net forms the support of the reflector. Initially it was assumed that the front net would be covered with a knitted metal mesh in order to provide the necessary RF reflection. It was realized, however, that the triangular facets would generate high and unacceptable grating lobes which would deteriorate the beams and the short distance to coast unless the triangles were made very small,

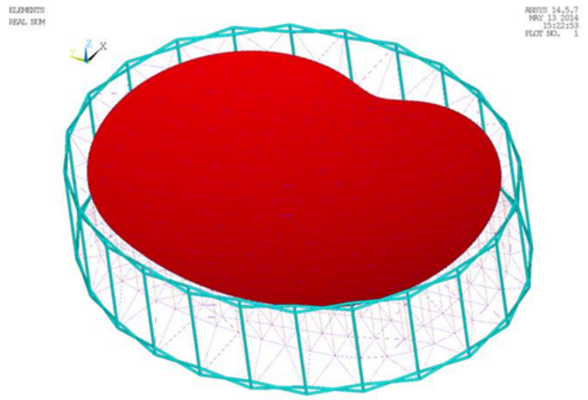

Figure 4: Mechanical realization of the torus push broom reflector dish.

i.e. 100 mm size. Consequently, it was proposed to construct the reflector as a doubly curved CFRS (Carbon Fibre Reinforced Silicon) surface (see Fig. 4.). The triangular net is maintained to support the CFRS but the size of the triangles can be much larger, around 400 mm.

4 Limitations of cluster feeds of horns

Cluster feeds for space-borne multi-frequency radiometers are typically designed to provide a strong illumination taper toward the edge of the reflector (when seen in transmit situation) in order to maximize the antenna beam efficiency and minimize the side-lobe and cross-polarization power [25]. This approach, however, leads to (i) the lower spatial resolution due to the widening of the footprint; and (ii) the difficulty to accommodate several feeds due to their large apertures, and hence several bands. Figs 5(a-c) and 5(d-f) illustrate these limitations for the considered scanner and push-broom systems, respectively. As seen, P_{cross} of the scanner can only be minimized by employing a feed with the aperture diameter larger than 5λ and illumination taper that is < 60 dB at $35°$. This gives FP > 30 km and $D_{\mathrm{c}} > 23$ km at C-band, while FP $= 20$ km and $D_{\mathrm{c}} = 5 - 15$ km are desired. The shortest D_{c} that can be achieved is ~ 20 km, for which the realized P_{cross} is at least 3 times higher than the desired 0.34%. At higher frequency bands, realizing the required D_{c} is not a problem, as the side-lobe levels can be significantly reduced (see Figs 6(c)) by under-illuminating the reflector aperture, while providing FP=10 km. However, the cross-polarization power is not acceptable.

For the push-broom system, the dependence of the radiometer characteristics from the illumination taper is similar to that of the scanner, and even larger feed apertures are needed due to the more shalow surface of the reflector. The main challenges for this system are attributed to the complex shape of the torus reflector, and, as the result, more complex focal field (compare Figs K.8(a) and K.8(b)). The

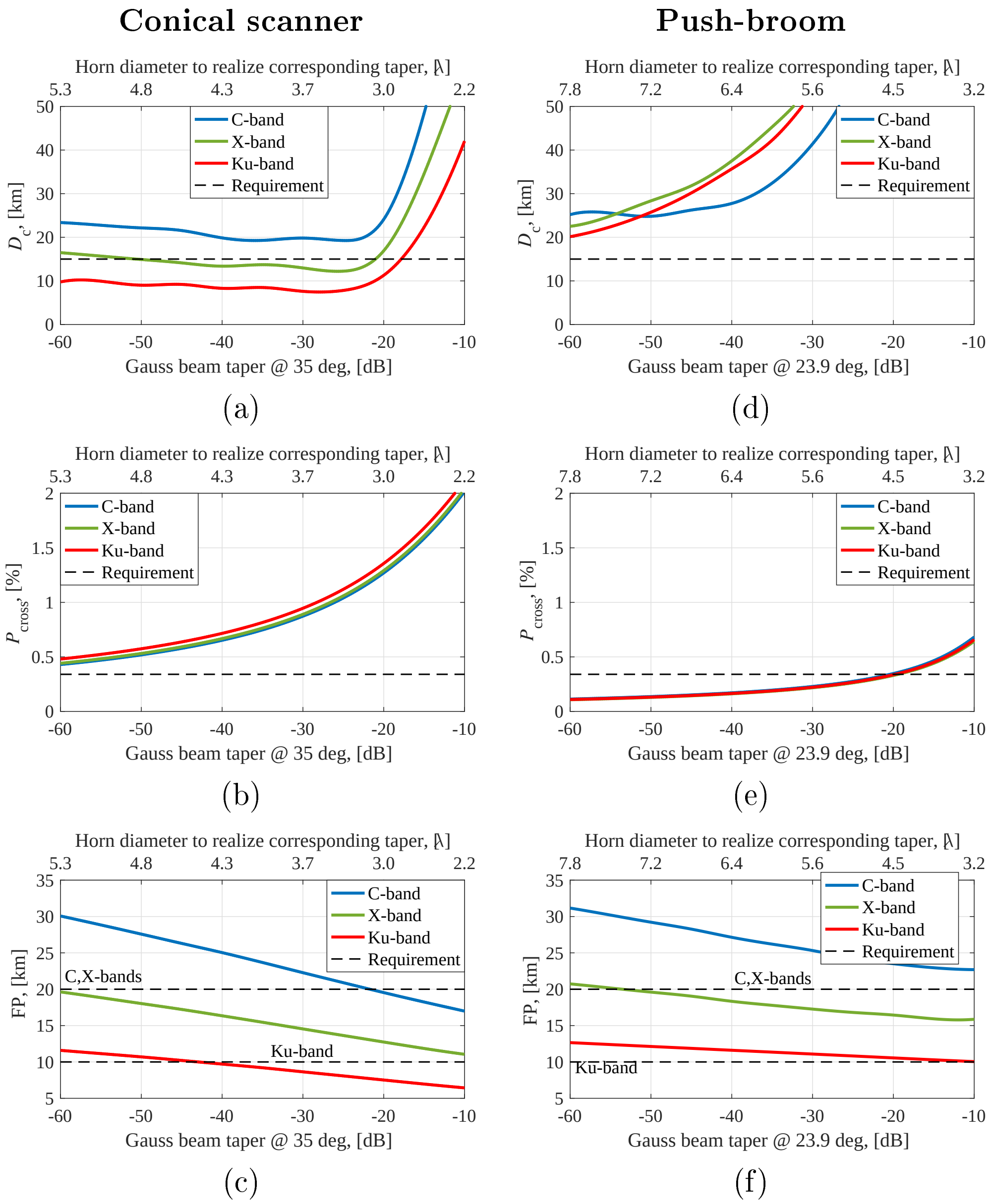

Figure 5: Radiometer characteristics, i.e. the distance-to-land, relative cross-polarization power and footprint size, as function of the illumination taper of the Gaussian feed for (a-c) the conical scanner and (d-f) push-broom antenna configuration. The corresponding aperture diameter of the optimal circular horn [23, 24] is shown on the top axis.

high coma-side lobes and non-circular main lobe of the focal field distribution of the torus reflector (see Fig. K.8(b)) cannot be accurately sampled by a single (horn) antenna feed; and this is the reason of the high side-lobe of the antenna far-field pattern (see Figs. 7(a-c)), and hence too large distance-to-coast. In contrast, dense FPAs are capable of handeling these complexities, as will be demonstrated in the following section.

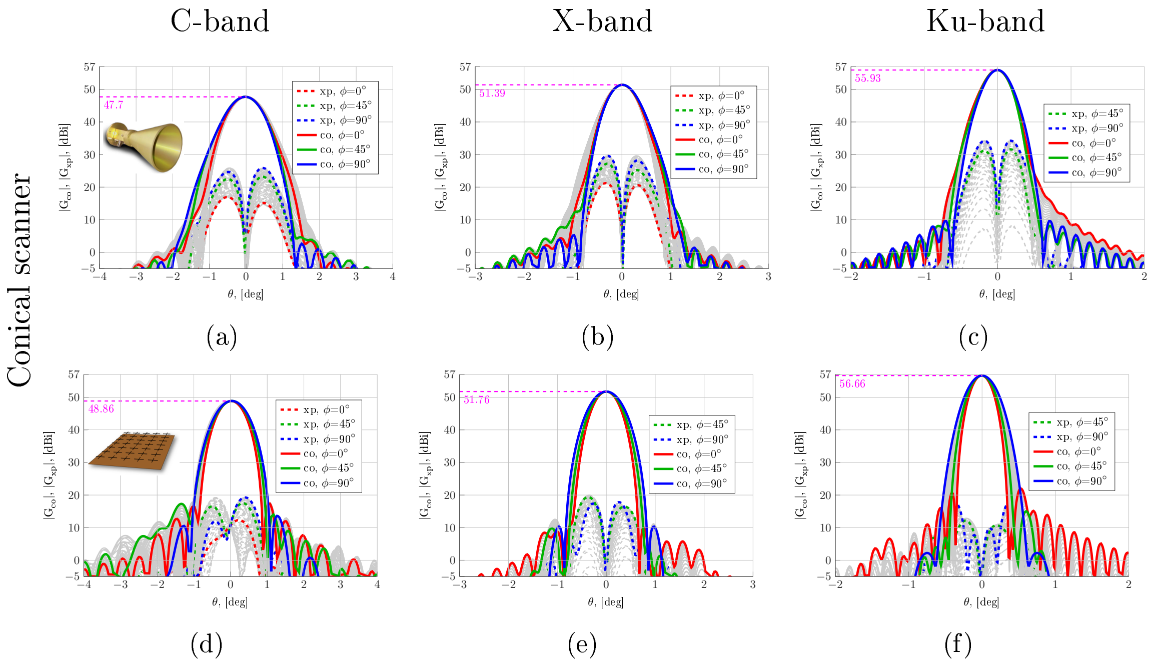

Figure 6: Far-field pattern cuts for the conical scanner antenna at (a,d) C-band, (b,e) X-band, and (c,f) Ku-band, when the feed is (a-c) the Gaussian horn feed illuminating the reflector edge with the taper -30 dB, and (d-e) FPA with the optimum beamforming.

5 Dense Focal Plane Arrays

5.1 Array models and configurations

Based on the requirements derived in Sec. 2, three FPAs of half-wavelength dipole antenna elements covering C-, X- and Ku-bands have been designed for each radiometer. First, we computed the focal fields of several plane waves corresponding to the desired beam directions, and then used these to derive the minimum aperture sizes of FPAs and their positions in the focal regions, as shown in Fig. 8. After that, a parametric study was carried out to determine the minimum needed N_{el} and the corresponding inter-element separation distance d_{el}. Note that to reduce the computational time, we have simplified the original MoM array model by assuming that all embedded element patterns (EEPs) are identical to that of the central element (the validity of this assumption will be confirmed in Sec. 5.3). The EEPs for each unique set of N_{el} and element positions were imported into the reflector antenna software GRASP10 to compute the secondary EEPs, which, in turn, were used to determine the optimum element excitation coefficients that will be discussed further. Table 3 summarizes the results of this parametric study. As one can see, for the conical scanner we need 127, 263 and 333 antenna elements for the C- X- and Ku-band, respectively, to provide 2, 21 and 30 beams. Since the radiometric resolution of the push-broom system is much higher (due to many more beams), as one can expect, this comes at the expenses

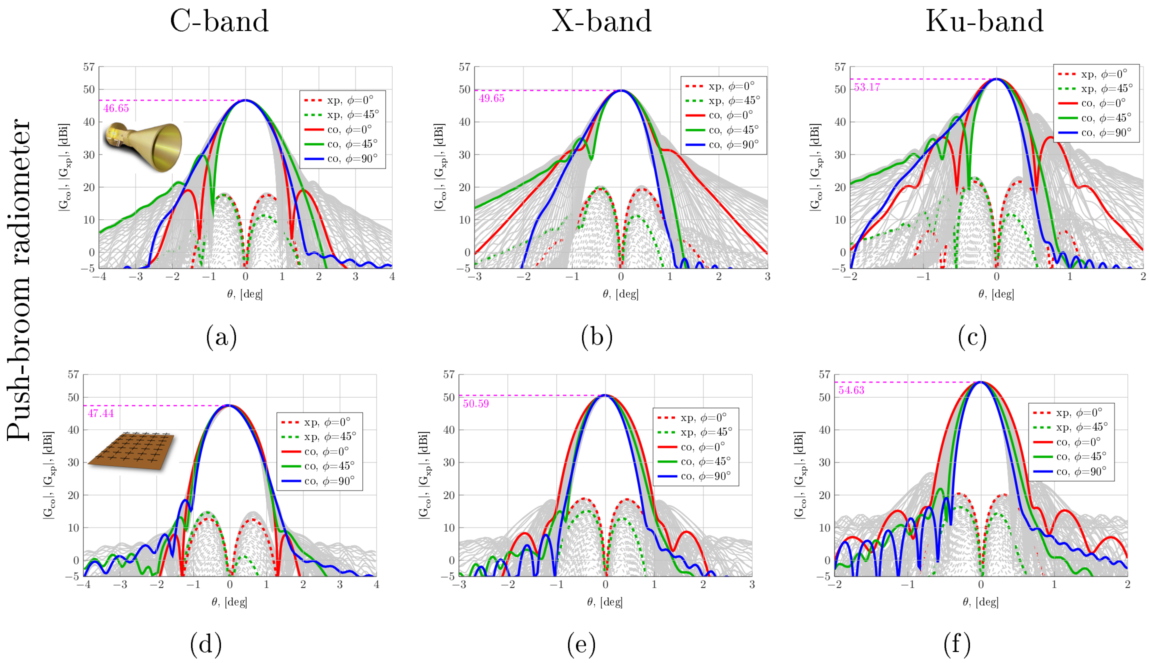

Figure 7: Far-field pattern cuts for the push-broom radiometer antenna at (a,d) C-band, (b,e) X-band, and (c,f) Ku-band, when the feed is (a-c) the Gaussian horn feed illuminating the reflector edge with the taper -30 dB, and (d-e) FPA with the optimum beamforming.

Table 3: Number of elements

	Conical scanner	**Push-broom**
Array grid	rectangular	polar
C band	$64 + 63 = 127$	$6 \times 111 \times 2 = 1332$
X band	$128 + 135 = 263$	$6 \times 153 \times 2 = 1836$
Ku band	$165 + 168 = 333$	$6 \times 255 \times 2 = 3060$

of more elements. It is important to note that the required numbers of elements, determined through this optimization procedure, are almost twice smaller than when applying a conventional conjugate-field-matching optimization approach (see Table 3 in [10]).

For both systems, the optimal $d_{\rm el}$ is near 0.75λ; this value satisfies the grating-lobe free condition [11] and also minimizes the active impedance variation of antenna elements due to their non-identical excitation [26, 27].

5.2 Optimization procedure for element excitation

In Sec. 2, it has been shown that the antenna far-field beam should contains 99.72% of the total power within a circular cone with half angle $\theta_{\rm c}$ to realize the desired $D_{\rm c}$. The goal is, therefore, to determine the excitation coefficients such that the angle $\theta_{\rm c}$

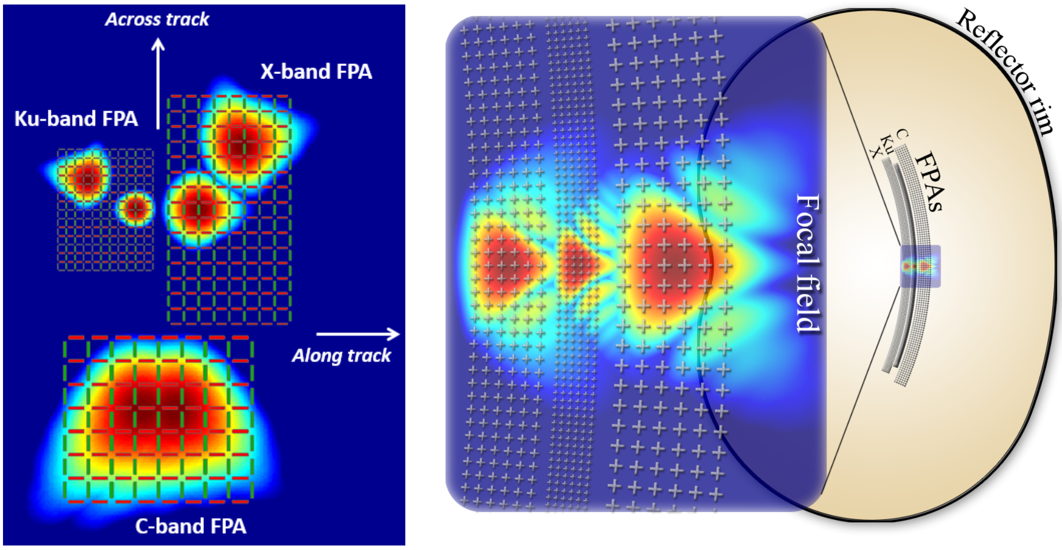

(a) (b)

Figure 8: Focal field distributions of multiple plane waves incident on (a) the conical scan reflector antenna and (b) torus reflector antenna at C-, X- and Ku-bands, as calculated using the Physical Optics software GRASP10. For each band, the field distributions are shown for two beam directions and overlaid with the array grids.

becomes as small as possible, i.e. D_{c} is minimized.

The far field from the reflector antenna can be written as

$$\boldsymbol{E}_{\mathrm{far}}(\theta,\phi) = \sum_{i=1}^{N_{\mathrm{el}}} \alpha_i \boldsymbol{E}_{\mathrm{far},i}(\theta,\phi), \tag{9}$$

where $\boldsymbol{E}_{\mathrm{far},i}$ is the field due to element i, N_{el} is the total number of elements; and α_i is the corresponding complex excitation coefficient. The radiated power within the cone of half-angle θ_{c} can be written as

$$P_{\mathrm{c}}(\theta_{\mathrm{c}}) = \int_0^{2\pi}\int_0^{\theta_{\mathrm{c}}} |\boldsymbol{E}_{\mathrm{far}}(\theta,\phi)|^2 \sin\theta \,\mathrm{d}\theta\,\mathrm{d}\phi, \tag{10}$$

If the expression (9) is inserted in (10) it is seen that it becomes a quadratic polynomial in the α_i variables and can be written in the form

$$P_{\mathrm{c}}(\theta_{\mathrm{c}}) = \boldsymbol{\alpha}^H \mathbf{A} \boldsymbol{\alpha}, \tag{11}$$

where $\boldsymbol{\alpha} = [\alpha_1, \alpha_2, \ldots, \alpha_N]^T$ and H is Hermitian operator. The matrix $\mathbf{A}$ is Hermitian of size $N_{\mathrm{el}} \times N_{\mathrm{el}}$ such that the expression in (11) becomes a real number. Note that the matrix $\mathbf{A}$ is a function of θ_{c}.

The power $P_{\mathrm{c}}(\theta_{\mathrm{c}})$ in (10) must be related to the total radiated power from the feed array. This power, P_{tot}, can be computed from the expression (10) if θ_{c} is replaced by $\pi/2$ and the reflector patterns $\boldsymbol{E}_{\text{far},i}$ are replaced by the array element patterns $\boldsymbol{E}_{\text{far,array},i}$. Again the power P_{tot} becomes a quadratic polynomial in the variables $\boldsymbol{\alpha}$ such that

$$P_{\text{tot}} = \boldsymbol{\alpha}^H \mathbf{C} \boldsymbol{\alpha}, \tag{12}$$

For a given value of θ_{c} it is thus desired to find the excitations $\boldsymbol{\alpha}$ that maximize the ratio

$$\frac{P_{\text{c}}(\theta_{\text{c}})}{P_{\text{tot}}} = \frac{\boldsymbol{\alpha}^H \mathbf{A} \boldsymbol{\alpha}}{\boldsymbol{\alpha}^H \mathbf{C} \boldsymbol{\alpha}}, \tag{13}$$

It can be shown that the maximum value of this ratio is the maximum eigenvalue λ of the expression

$$\mathbf{A}\boldsymbol{\alpha} = \lambda \mathbf{C} \boldsymbol{\alpha}, \tag{14}$$

and that the vector holding the complex excitation coefficients are given by the corresponding eigenvector.

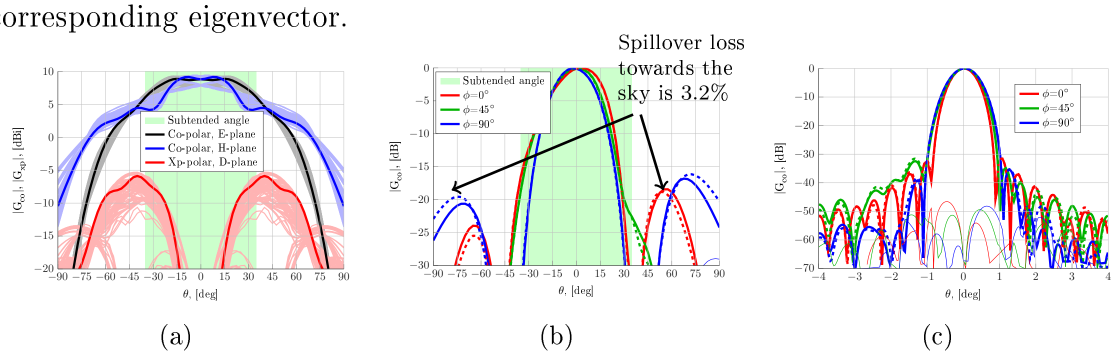

Figure 9: (a) All embedded element patterns of the C-band FPA for the conical scanner at E-, H- and D-planes, as obtained through the Method of Moments in CAESAR software [28], where the bold lines correspond to the central antenna element of the array; (b) beamformed far-field pattern cuts of the FPA within the reflector subtended angle region for the conical scan antenna, and (c) far-field pattern cuts of the reflector antenna for beam 1. The solid lines correspond to the MoM array model, dashed lines represent the model with the assumed identical embedded element patters of the array, and the thin solid lines show the relative normalized difference between the antenna patterns obtained with the above models.

The present optimisation method is similar to the one reported in [12] – which is based on a more general Signal-To-Noise-Ratio algorithm – but simpler to implement. Since for the considered application scenario, the optimization is strongly driven by the acceptable side-lobe and cross-polarization power of the antenna, the radiometric performances obtained by the two algorithms are very similar.

5.3 Antenna patterns and radiometric characteristics

Dense FPAs offer more degrees of freedom in beam-forming, as compared to conventional feeds, and thereby can provide highly optimized beams with more circular-symmetric main lobes and much lower cross polarization and side-lobe levels, as demonstrated in Figs 6(d-f) and 7(d-f). This results in significantly better radiometric characteristics for both systems. As one can see in Table 4, the realized D_c of the conical scanner is 6.6-14 km and P_{cross} is only 0.10-0.15% (i.e. about one order of magnitude better than the horn feed); for the push-broom radiometer, the respective quantities are less than 16 km (while the horn feed cannot fulfill this requirement) and 0.08-0.12% (i.e. 3 times better than the horn feed). Furthermore, the latter system has wide scan-range performance, where the characteristics of all multiple beams within the angular range of ±20 deg are virtually identical, thanks to the symmetry of the torus reflector in the azimuthal plane and the moon-like shape of the FPA that matches the focal line of the reflector (see Fig. 8(b)).

Table 4: Radiometric characteristics of the conical scanner and push-broom systems for the Gaussian horn and FPA. The values in brackets are for the full MoM array model, and the other values are when assuming identical embedded element patterns

Radiometer characteristic	**Requirement**	**Conical scanner**			**Push-broom**	
		Horn feed	**FPA**		**Horn feed**	**FPA**
			Beam 1	**Beam 2**		
C-band						
Distance to land, [km]	<15	19.2	14.2 (14.2)	14.2 (14.2)	41.4	16.1
Rel. cross-pol. power, [%]	<0.34	1.04	0.15 (0.06)	0.10 (0.07)	0.23	0.08
Beam efficiency, [%]		97.2	95.6 (96.0)	95.6 (96.0)	96.1	97.8
Footprint, [km]	<20	21	19.6 (19.6)	19.6 (19.6)	25.3	23.1
Footprint ellipticity		1.64	1.43 (1.44)	1.44 (1.44)	1.57	1.48
X-band						
Distance to land, [km]	<15	13.0	9.7	9.8	55.3	13.4
Rel. cross-pol. power, [%]	<0.34	0.89	0.10	0.10	0.22	0.12
Beam efficiency, [%]		97.7	98.2	97.4	95.0	98.4
Footprint, [km]	<20	14.5	14.2	14.2	17.3	15.9
Footprint ellipticity		1.64	1.32	1.38	1.48	1.21
Ku-band						
Distance to land, [km]	<15	7.6	6.6	6.6	53.2	13.4
Rel. cross-pol. power, [%]	<0.34	0.95	0.03	0.07	0.22	0.08
Beam efficiency, [%]		97.7	97.4	97.2	84.5	98.0
Footprint, [km]	<10	8.6	8.0	8.2	11.1	10.0
Footprint ellipticity		1.67	1.24	1.35	1.27	1.05

The accuracy of the above analysis (that is based on the assumption of identical array element patterns) has been evaluated by cross-comparing the antenna patterns and corresponding radiometric characteristics with those obtained through the full MoM model. Fig. 9 shows the results for C-band, as the worse case scenario among the considered ones. As seen, the relative difference between the far-field patterns obtained with the simplified and more rigorous FPA models is negligible, so as the difference between the corresponding sets of radiometric characteristics (see Table 4). This observation might appear count-intuitive, given a significant variation between the embedded element patterns (EEPs) of the array, as shown in Fig. K.9(a). However, one should realize that the optimal pattern of the feed leading to the minimum distance to land represents a combined effect of the EEPs and element excitation coefficients. Hence, when the optimization algorithm is applied to the set of non-identical EEPs, the excitation coefficients are modified with respect to that determined for the identical EEP case. For the considered arrays with more than 100 dipole antenna elements, the resultant optimal feed patterns have been found very similar for both array models (see the example for C-band in Fig. 9(b,c)). This observation, however, may not be valid for arrays with fewer and denser-spaced elements.

6 Receiver considerations

In this section, we briefly consider receiver resource requirements in order to see if implementation of the present antenna concept is feasible and realistic. We consider the receiver where the signals from different antenna elements contribute to more than one beam, and each antenna element is connected to its own receiver, followed by an A/D converter. The beam-forming process takes place in an Field Programmable Gate Array (FPGA), using complex digital multipliers and adders. Both the scanner and the push-broom system require a large number of elements to fulfill the radiometric requirements. Hence resource requirements concerning the size, mass and especially power consumption, is an important issue.

A study of state-of-the-art microwave components, assuming a super-heterodyne receiver (see Fig.7 in [29]), has been carried out. It has been found that at the considered frequency bands, most components are small and light weight, and thus volume and mass are not deemed to be a problematic issue. Power consumption has dropped dramatically over the past decade, and 1 W per receiver is now a realistic estimate. Furthermore, the output signals from FPA elements have to be optimally combined in a dedicated beamforming network to form the desired antenna beams. This involves a number of FPGAs and the average power consumption is estimated to be 0.24 W per receiver. Future radiometers must include intelligent RFI detection and mitigation processors. Based on a representative case study of such a processor [30], the power consumption can be estimated to be 0.14 W per receiver.

In summary, the power estimate is: $1 + 0.24 + 0.14 = 1.38$ W per receiver, using present state-of-the-art components. The total number of receivers is 6228 in the push-broom case. This results in a total power consumption of 8.6 kW, which is not realistic today. For the scanner with 723 receivers, the estimate is 1000 W – a large number, but feasible.

The present study is a preparation for the future, and it is of interest to base a power budget on realistic developments over a 5 years time frame. Already now, A/D converters able to sub-sample signals up to X-band are available in research labs, and within very few years Ku band is also possible. Thus we do not need the super-heterodyne layout, and the local oscillator and its power consumption, can be avoided. The new, fast A/D converters use very small signal levels typically around −35 dBm, and hence not much gain is needed in the receiver (also saving on power). The development concerning amplifier power consumption is also impressive. For global power budget estimates we can within a few years assume $\sim$ 35 mW per receiver. If we assume a similar reduction for processing circuitry, the result is 9 mW for the beam forming network, and 5 mW for the RFI processor, i.e. 49 mW per receiver. For the push-broom system this amounts to a total power consumption of 305 W, which is certainly realistic. For the scanner the estimate is about 35 W.

7 Conclusions

Existing space-borne microwave radiometers that are used for the assessment of ocean parameters like salinity, temperature, and wind can provide valid observations only up to $\sim$ 100 km from the coastline, and hence do not allow for monitoring of the coastal areas and ice-edge polar seas, and measuring under extreme wind and weather conditions. To achieve the desired precision, as required for future missions, we propose digitally-beamforming dense focal plane arrays (FPAs) – previously not used in space-borne applications, – employed either in a traditional conical-scan off-set parabolic reflector antenna or in a wide-scan torus reflector system.

When synthesized and excited according to the proposed optimum beamforming procedure – aiming to minimize the signal contamination given by the side-lobes and cross-polarization of antenna beams covering the land, – the number of the FPA antenna elements and associated receivers can be kept to minimum. In this procedure, the input parameters include the number of array elements, their positions and the secondary embedded element patterns (EEPs), which are computed after the illumination of the reflector antenna, and the output parameters are the optimal complex-valued element excitations. Although, the primary EEPs are generally not identical, due to the array antenna mutual coupling and edge truncation effects, for the considered FPAs with more than 100 dipole antenna elements and inter-element spacing of 0.75λ, it has been found sufficient to use a single primary EEP, i.e. the one for a central element of the array, as the source of the secondary EEPs for all elements in order to accurately predict the achievable radiometric characteristics.

For both types of radiometers, the realized resolutions are at least twice higher than the values provided by the current systems, and the distance to coastline is as short as 6-15 km. This excellent performance was shown to be impossible with traditional multi-frequency FPAs of horns in one-horn-per-beam configuration, as these cannot compensate for the high cross-polarization of off-axis beams in conical-scanners, and produce unacceptably high side-lobes due to severe focal-field under-sampling effects in torus reflector systems.

Our analysis of realistic developments of digital processors predicts acceptable receiver resources budget for such multi-beam radiometers within a 5 years time frame.

References

[1] C. Prigent, F. Aires, F. Bernardo, J.-C. Orlhac, J.-M. Goutoule, H. Roquet, and C. Donlon, “Analysis of the potential and limitations of microwave radiometry for the retrieval of sea surface temperature: Definition of MICROWAT, a new mission concept,” *Geophys. Res. Oceans*, vol. 118, pp. 3074–3086, Jun. 2013.

[2] E. V. Zabolotskikh, L. M. Mitnik, and B. Chapron, “New approach for severe marine weather study using satellite passive microwave sensing,” *Geophys. Res. Lett.*, vol. 40, pp. 3347–3350, Jul. 2013.

[3] N. Reul, B. Chapron, T. Lee, C. Donlon, J. Boutin, and G. Alory, “Sea surface salinity structure of the meandering Gulf stream revealed by SMOS sensor,” *Geophys. Res. Lett.*, vol. 41, pp. 3141–3148, May 2014.

[4] STSE-high resolution microwave wind and temperature (MICROWAT). [Online]. Available: https://www.yumpu.com/en/document/view/10779401/download-document-microwat

[5] P. W. Gaiser, “The WindSat spaceborne polarimetric microwave radiometer: Sensor description and early orbit performance,” *IEEE Trans. Geo. Rem. Sensing*, vol. 42, no. 11, pp. 591–603, Nov. 2004.

[6] Amsr-e instrument description. [Online]. Available: http://nsidc.org/data/docs/daac/amsre_instrument.gd.html

[7] N. Skou and D. L. Vine, *Microwave Radiometer Systems: Design & Analysis*. Artech House, 2006.

[8] R. Hoferer and Y. Rahmat-Samii, “RF characterization of an inflatable parabolic torus reflector antenna for space-borne applications,” *IEEE Trans. Antennas Propag.*, vol. 46, no. 10, pp. 1449–1457, Oct. 1998.

[9] P. Nielsen, K. Pontoppidan, J. Heeboell, and B. L. Stradic, “Design, manufacture and test of a pushbroom radiometer,” in *Antennas and Propagation, 1989. ICAP 89., Sixth International Conference on (Conf. Publ. No.301)*, Coventry, United Kingdom, Apr. 1989, pp. 126–130.

[10] C. Cappellin, K. Pontoppidan, P. Nielsen, N. Skou, S. S. Søbjærg, A. Ihle, D. Hartmann, M. Ivashina, O.Iupikov, and K. v. t Klooster, “Novel multi-beam radiometers for accurate ocean surveillance,” in *Proc. European Conference on Antennas and Propag. (EuCAP)*, The Hague, The Netherlands, Apr. 2014, pp. 1–4.

[11] O. A. Iupikov, M. V. Ivashina, K. Pontoppidan, P. H. Nielsen, C. Cappellin, N. Skou, S. S. Søbjærg, A. Ihle, D. Hartmann, and K. v. t Klooster, “Dense focal plane arrays for pushbroom satellite radiometers,” in *Proc. European Conference on Antennas and Propag. (EuCAP)*, Hague, The Netherlands, Apr. 2014, pp. 1–5.

[12] ——, “An optimal beamforming algorithm for phased-array antennas used in multi-beam spaceborne radiometers,” in *Proc. European Conference on Antennas and Propag. (EuCAP)*, Lisbon, Portugal, Apr. 2015, pp. 1–5.

[13] C. Cappellin, K. Pontoppidan, P. H. Nielsen, N. Skou, S. S. Søbjærg, A. Ihle, M. V. Ivashina, O. A. Iupikov, and K. v. ’t Klooster, “Design of a push-broom multi-beam radiometer for future ocean observations,” in *Proc. European Conference on Antennas and Propag. (EuCAP)*, Lisbon, Portugal, Apr. 2015, pp. 1–5.

[14] J. Fisher and R. Bradley, “Full-sampling array feeds for radio telescopes,” in *Proc. SPIE, Radio Telescopes*, vol. 4015, Munich, Germany, Jul. 2000, pp. 308–318.

[15] K. F. Warnick, D. Carter, T. Webb, B. D. Jeffs, J. Landon, V. Asthana, M. Elmer, R. Norrod, D. A. Roshi, and J. R. Fisher, “Towards a high sensitivity cryogenic phased array feed antenna for the Green Bank Telescope,” in *XXXth URSI General Assembly and Scientific Symposium*, Istanbul, Turkey, Aug. 2011, pp. 1–4.

[16] D. R. DeBoer, R. G. Gough, J. D. Bunton, T. J. Cornwell, R. J. Beresford, S. Johnston, I. J. Feain, A. E. Schinckel, C. A. Jackson, M. J. Kesteven, A. Chippendale, G. A. Hampson, J. D. O’Sullivan, S. G. Hay, C. E. Jacka, T. W. Sweetnam, M. C. Storey, L. Ball, and B. J. Boyle, “Australian SKA pathfinder: A high-dynamic range wide-field of view survey telescope,” *Proc. IEEE*, vol. 97, no. 8, pp. 1507–1521, Aug. 2009.

[17] B. Veidt, T. Burgess, R. Messing, G. Hovey, and R. Smegal, “The DRAO phased array feed demonstrator: Recent results,” in *13th Int. Symp. on Antenna Technology and Applied Electromagnetics and the Canadian Radio Science Meeting, ANTEM/URSI 2009*, Banff, Canada, Feb. 2009, pp. 1–4.

[18] M. V. Ivashina, O. Iupikov, R. Maaskant, W. A. van Cappellen, and T. Oosterloo, “An optimal beamforming strategy for wide-field surveys with phased-array-fed reflector antennas,” *IEEE Trans. Antennas Propag.*, vol. 59, no. 6, pp. 1864–1875, Jun. 2011.

[19] Y. Wu, X. Zhang, B. Du, C. Jin, L. Zhang, and K. Zhu, “Design of antenna array for the L-band phased array feed for FAST,” in *Antennas Propagation (ISAP),*

2013 Proceedings of the International Symposium on, Nanjing, China, Oct. 2013, pp. 11–13.

[20] K. F. Warnick, R. Maaskant, M. V. Ivashina, D. B. Davidson, and B. D. Jeffs, "High-sensitivity phased array receivers for radio astronomy," *Proceedings of the IEEE*, vol. 104, no. 3, pp. 607–622, Mar. 2016.

[21] M. W. Thomson, "The AstroMesh deployable reflector," in *Antennas and Propagation Society International Symposium, 1999. IEEE*, vol. 3, Orlando, Florida, Jul. 1999, pp. 1516–1519.

[22] K. van't Klooster, E. Medzmariashvili, S. Tserodze, L. Datashvili, and N. Tsignadze, "Large deployable reflector configuration for spacebased applications in telecommunications, science, and remote sensing," in *International Scientific Conference on Advanced Lightweight Structures and Reflector Antennas*, Tbilisi, Georgien, Oct. 2009, pp. 75–82.

[23] T. Teshirogi and T. Yoneyama, *Modern Millimeter-wave Technologies.* IOS Press, 2001.

[24] P.-S. Kildal, *Foundations of Antenna Engineering – A Unified Approach for Line-Of-Sight and Multipath.* Kildal Antenn AB, 2015.

[25] S. Contu and F. M. Marinelli, "The antenna system for the multi-frequency imaging microwave radiometer: M.I.M.R," in *Antennas and Propagation Society International Symposium, 1994. AP-S. Digest*, vol. 3, Seattle, WA, USA, Jun. 1994, pp. 2054–2057.

[26] M. Arts, M. Ivashina, O. Iupikov, L. Bakker, and R. van den Brink, "Design of a low-loss low-noise tapered slot phased array feed for reflector antennas," in *Proc. European Conference on Antennas and Propag. (EuCAP)*, Barcelona, Spain, Apr. 2010, pp. 1–5.

[27] K. F. Warnick, D. Carter, T. Webb, J. Landon, M. Elmer, and B. D. Jeffs, "Design and characterization of an active impedance matched low-noise phased array feed," *IEEE Trans. Antennas Propag.*, vol. 59, no. 6, pp. 1876–1885, Jun. 2011.

[28] R. Maaskant, "Analysis of large antenna systems," Ph.D. dissertation, Electrical engineering, Eindhoven University of Technology, Eindhoven, 2010. [Online]. Available: http://alexandria.tue.nl/extra2/201010409.pdf

[29] N. Skou, S. S. Søbjærg, S. S. Kristensen, C. Cappellin, K. Pontoppidan, M. Ivashina, A. Ihle, and K. v.'t Klooster, "Future spaceborne ocean missions using high sensitivity multiple-beam radiometers," in *IEEE International*

Geoscience and Remote Sensing Symposium (IGARSS), Québec City, Québec, Canada, Jul. 2014.

[30] N. Skou, S. Kristensen, A. Kovanen, and J. Lahtinen, "Processor breadboard for on-board RFI detection and mitigation in MetOp-SG radiometers," in *Geoscience and Remote Sensing Symposium (IGARSS), 2015 IEEE International*, Milan, Italy, Jul. 2015, pp. 1445–1448.

Paper L

Prediction of Far-Field Pattern Characteristics of Phased Array Fed Reflector Antennas by Modeling Only a Small Part of the Array – Case Study of Spaceborne Radiometer Antennas

O. A. Iupikov, A. A. Roev, M. V. Ivashina

in *Proceedings of the 11^{th} European Conference on Antennas and Propagation, EUCAP 2017,* Paris, France, April 2017.

The layout of this paper has been revised in order to comply with the rest of the thesis.

Prediction of Far-Field Pattern Characteristics of Phased Array Fed Reflector Antennas by Modeling Only a Small Part of the Array – Case Study of Spaceborne Radiometer Antennas

O. A. Iupikov, A. A. Roev, M. V. Ivashina

Abstract

In this work we present an approach for the prediction of far-field pattern characteristics of phased array fed reflector antennas by modeling only a small part of the array. In this approach, the simulated EEPs of the FPA are modeled as the phase-shifted versions of the simulated embedded element pattern (EEP) of the central element, and thereafter combined with the optimum weighting coefficients in order to find the total pattern of the feed. Although, the EEPs of dense array antennas are generally not identical (due to the array antenna mutual coupling and edge truncation effects), for typical FPA excitation scenarios, where the array edge elements have relatively low weights to produce the desired illumination of the reflector, this simplified approach has been found sufficiently accurate.

1 Introduction

Recent advances in radio-frequency and digital electronics have allowed for the design of novel antenna systems, which have superior beamforming capabilities. Examples of such systems are spaceborne antennas for ocean surveillance and satellite communication; these systems are capable to provide multiple high-efficiency beams (with extremely low side-lobes or cross-polarization) and operate at several frequency bands (typically L-, C-, X and Ku-bands), while having a compact single-antenna design. These challenging requirements can be met by using dense focal plane arrays (FPAs) feeding a reflector (or a lens), or directly-radiating sparse irregular arrays [1,2]. However, there are common problems with such large and multi-scale antenna designs, including fast and accurate electromagnetic analysis as well as cost-efficient prototype development. Different approaches have been proposed to overcome these problems for the sparse arrays, where performance of the whole antenna system is evaluated through the analysis of a small part of it (e.g. [1,2]).

In this work we address this problem for the case of FPA systems, and in particular present a validated simplified approach where a reduced-size FPA simulations are used to predict the performance of the whole array feeding the reflector antenna.

2 Antenna geometry and specifications

To demonstrate the proposed approach we have considered a conical-scan offset parabolic reflector antenna (projected aperture diameter is 5 m, focal length is 3 m and clearance is 1 m) with the 67-element array feed. This antenna system is currently being considered for potential future ocean missions by ESA [3]. The requirements for this mission are given in Table 1, [4], in terms of standard performance metrics for oceanographic surveys. For the given satellite altitude and incidence angle, the radiometric requirements can be transfered [5] to the antenna system specifications as shown in Table 2.

Table 1: Radiometric requirements for future ocean missions

Freq., [GHz]	Band width, [MHz]	Polari-zation	Radiometric resolution, [K]	Bias, [K]	Spatial resolution, [km]	Dist.to coast, [km]
L-band: 1.404 – 1.423	19	V, H	0.15	0.25	100	50-100
C-band: 6.8 – 7.0 7.2 – 7.4	200	V, H	0.30	0.25	20	15-20

Table 2: Antenna requirements

Antenna characteristic	**L-band**	**C-band**
Number of beams	4	2
Cross-polar. power over the Earth	< 0.34 %	
Power over the land	< 0.28 %	
Projected aperture diameter of the reflector	5 m	

In previous *system-level* studies, we have applied this simplified approach to cross-compare different radiometer system concepts, i.e. a traditional conical-scan off-set parabolic reflector antenna vs. a wide-scan torus reflector system [6, 7], as well as to perform parametric studies for the FPAs to define the optimal number of antenna elements, inter element spacing, and the arrangement of FPAs operating at different bands [6, 8, 9]. In the current work, we validate this approach for the case of a wide-band Vivaldi antenna element FPA feeding the conical-scan reflector antenna, and use for this purpose the requirements in Table 1. To simplify the prototyping phase, our focus will be on the high frequency performance only (C-band), for which the small-size array demonstrator has only 24 elements, while the operational bandwidth of the designed full-scale array covers both L- and C-bands.

3 Array antenna design

The Vivaldi antenna element in [10], which most closely meets the wide-band requirements of the project, was chosen as a reference: it has the relative bandwidth greater than 6:1 over wide scan range (±45 deg). Since the geometry of the referred TSA in [10] is for the frequency band of 0.4–1.6 GHz, we have scaled up this design with some modifications related to the following practical implementation aspects:

- to improve the mechanical stability;
- to improve the matching for the reference impedance of 50 Ohm (in opposite to the original design, where 70 Ohm LNAs are used).

Thus a new element geometry of a dual-polarized phased array has been optimized and analyzed with the aid of periodic boundary conditions. The slotline width, rate of exponential slotline, cavity length, stub radius and stripline width were chosen as variable parameters. The main goal was to achieve the impedance matching condition with magnitude of the active reflection coefficient less than −10 dB within ±45 deg scan range. The optimization have been performed with the commercially available EM software HFSS and CST.

The final antenna and feed geometries with dimensions are shown in Fig. L.1(a) and L.1(b), respectively. Tapered slot profile is determined by curve:

$$y = C_1 e^{Rx} + C_2, \tag{1}$$

where R is the rate of exponential slotline, and coefficients C_1 and C_2 are defined as

$$C_1 = \frac{y_2 - y_1}{e^{Rx_2} - e^{Rx_1}} \tag{2}$$

$$C_2 = \frac{y_1 e^{Rx_2} - y_2 e^{Rx_1}}{e^{Rx_2} - e^{Rx_1}}, \tag{3}$$

where points (x_1, y_1) and (x_2, y_2) determine a slot width in the excitation region and the aperture, respectively.

Based on the simulations, a prototype of the small-scale dual-polarized array, comprising 24 elements, was designed and manufactured (Fig. 2). The array antenna structure consists of 4 orthogonally placed brass sheets with 3 TSA elements per polarization. All elements are mounted on the 250x250 mm aluminum ground plane. Each element is excited directly by a PCB feed with the SMA connector located under the ground plane.

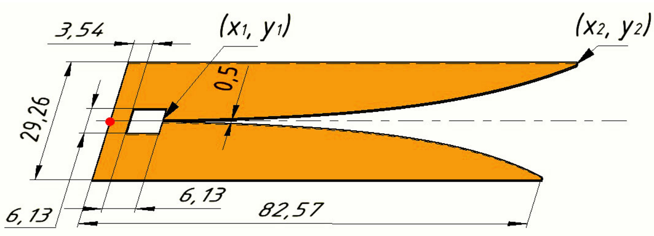

(a)

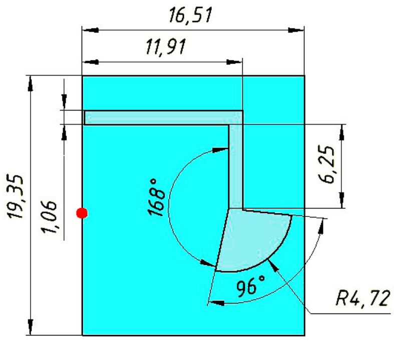

(b)

x_1	y_1	x_2	y_2	R
13.21	0.25	82.57	13.92	0.04

Figure 1: Geometrical dimensions of (a) the proposed TSA element and (b) feeding plate. All dimensions are given in [mm].

4 Analysis methodology and numerical results

For typical FPA excitation scenarios, the antenna elements at the edge of the array have significantly (-5...-15 dB) lower weighting coefficients relatively to the elements in the center. This implies that the differences in the embedded element pattern shapes, introduced by the edge effects, will have relatively weak contribution to the total compound beam of the array when all elements are excited. This motivates our assumption on the identical EEPs that can be taken to be the same as the pattern of an element in the center. Such approach can greatly speed up the numerical analysis of a reflector antenna system, which is very important for optimization.

The antenna specifications (see Table 2) define the required array layout and aperture area, which are shown in Fig. L.3(a). In order to validate the proposed analysis approach, we have used the full-wave simulation results for this array as the reference for the following simplified models:

1. Simplified model I, where FPA EEPs are phase-shifted versions of the EEP of the central element (element No.18), which was obtained for the full-scale array;

2. Simplified model II, where FPA EEPs are phase-shifted versions of the EEP of the central element (element No.5), which was obtained for the small-sized array, shown in Fig. L.3(b).

Figure 4 shows the EEPs for all these cases.

Figure L.3(c) shows the weighting coefficients for Simplified models I and II have been found through the dedicated optimum beamforming procedure detailed in [11] that aims to satisfy the radiometric requirements. The coefficients for the small-sized

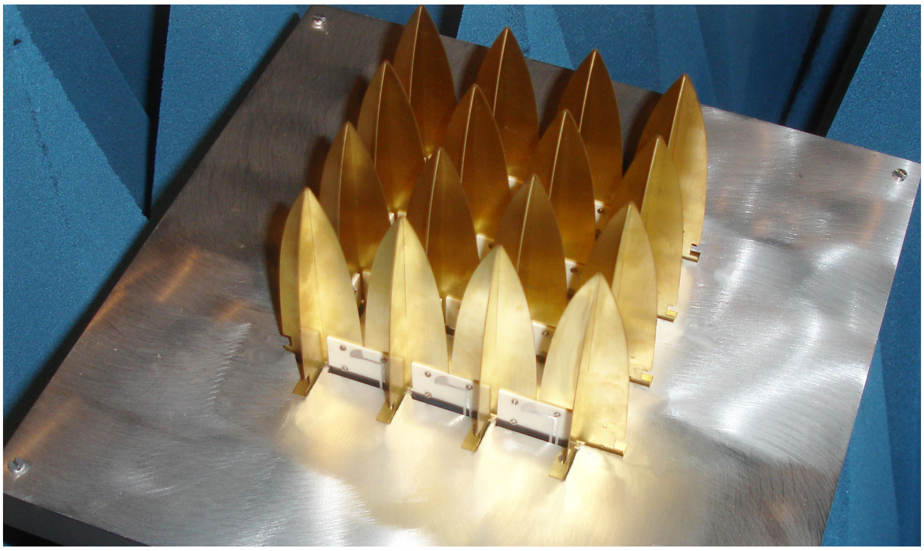

Figure 2: Photo of the manufactured reduced prototype.

array have been chosen to be a sub-set of the calculated coefficients that correspond to the most strongly excited elements; they are shown in Fig. L.3(d).

To cross-compare the array performances, we have used the active reflection coefficient [12] of the central element, when all antenna elements are excited with a certain complex-valued weight, as well as the radiometric characteristics specified in Table 3.

The full-sized and small-scaled arrays have been modeled using a full-wave approach and the active reflection coefficient of the most excited elements are shown in Fig. 5. The red curve (a) corresponds to the fully-excited full-sized array; dashed curve (b) is for the same array when only 24 elements (highlighted in Fig. L.3(a)) are active; and the blue curve (c) corresponds to the most excited element of the small array, when the same weight coefficients are used as for the previous case.

As one can see, the curves (a) and (b) are nearly identical. This is expected, since they are for the same EM model of the full-sized array, and the array elements outside the highlighted area are weakly excited, so they have negligible effect on the central element active reflection coefficient. The result (c) differs from (b) since the edge truncation effects are stronger in the smaller array. Nevertheless, the overall prediction of the reference reflection coefficient (a) is good enough for such a strongly-coupled antenna array.

The total primary- and secondary patterns of the array, i.e. the pattern before and after reflection from the dish) are cross-compared for the above cases in Fig. 6 and Fig. 7, respectively.

One can see the overall shape of the co-polar pattern of the reference full-wave array model has been predicted rather well with both simplified models, however the cross-polar components obtained with the latter appear to be higher. Similar obser-

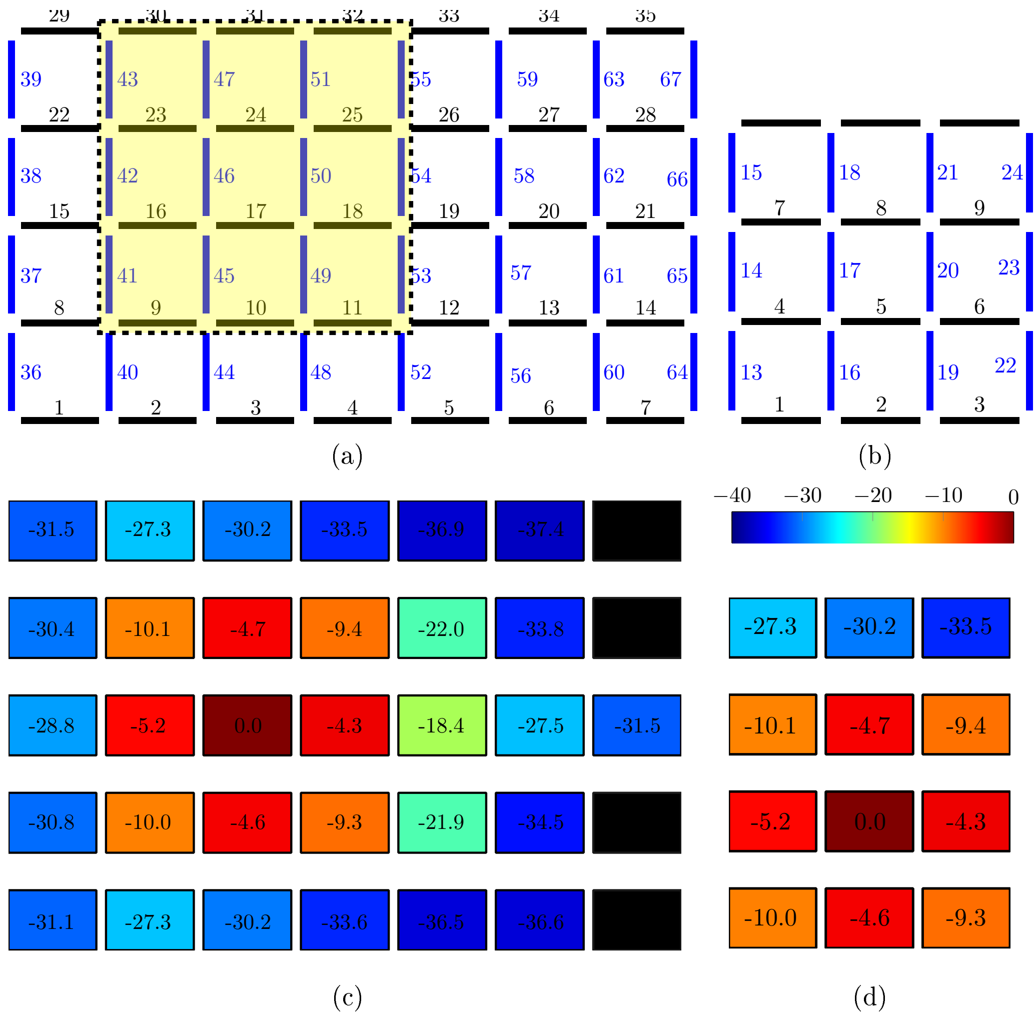

Figure 3: (a,c) Full-size array and (b,d) small-sized array layouts, and the corresponding weighting coefficients of the horizontally-polarized elements at 6.9 GHz (weighting coefficients of the orthogonally-polarized elements are not shown due to their low values), in [dB]

vations can be made for the radiometric characteristics, cross-compared in Table 3, where the distance to coast, beam width, footprint size and beam efficiencies have very similar values for all models, while the cross-polarization powers are a bit pessimistic for Simplified models I and II. More close investigation of the latter effects indicates the sensitivity of the presently used optimum beamforming approach to the variations and asymmetries of the cross-polarization patterns. This will be studied in our future work.

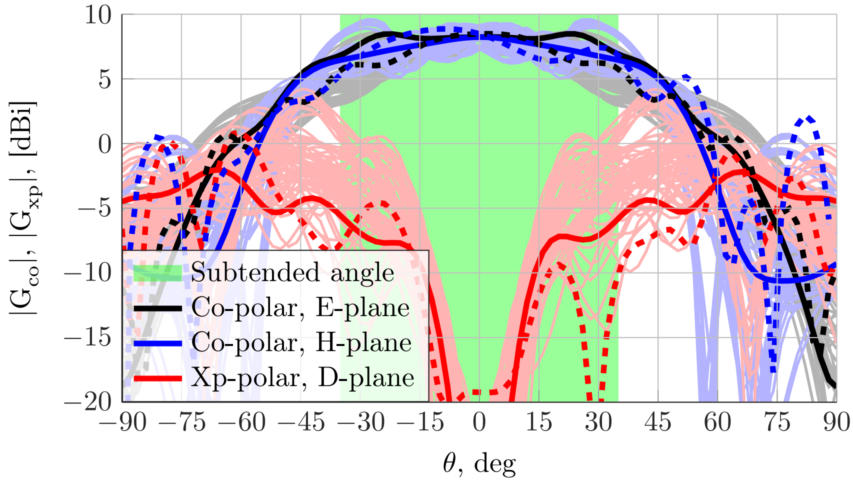

Figure 4: (solid lines) The E-, H- and D-plane embedded element pattern (EEP) cuts of the 67-element array at C-band, simulated with the finite element method in HFSS software (reference case), where the bold lines denote the EEP of the central element (no. 18) of the full-size array, used for Simplified model I; and the dashed lines denote the EEP of the central element (no. 5) in the small-sized array, used for Simplified model II.

Table 3: Final radiometer characteristics at C-band (6.9 GHz)

Radiometer characteristic	**Requirement**	**Reference model**	**Simplified model I**	**Simplified model II**
Beam efficiency [%]		96.6	97.8	96.5
Cross-polar. power, [%]	< 0.34	0.19	0.34	0.71
Distance to coast, [km]	≤ 15	11.4	14.5	13.6
Beam width, [deg]		0.648	0.664	0.647
Average footprint, [km]	20	18.8	19.5	18.6
Footprint ellipticity		1.69	1.91	1.60

5 Conclusions

The simplified modeling approach – assuming identical embedded element patterns of the phased array feed illuminating a large reflector – has been validated for the case of a conical scan radiometer antenna fed with a strongly coupled Vivaldi antenna element array. It has been shown that rather significant differences between the embedded element patterns, introduced by the edge truncation effects, have relatively weak contribution to the total compound beam of the array, when all elements are excited to provide optimum illumination. As the result, radiometer characteristics derived from the antenna far-field pattern, such as the beam efficiency, footprint, and distance to coast can be predicted almost as equally well as with the full-wave array model – that is important for the antenna system optimization and array prototype development phase. When applying this approach to applications with stringent requirements on the cross-polarization, one could expect pessimistic estimation of its

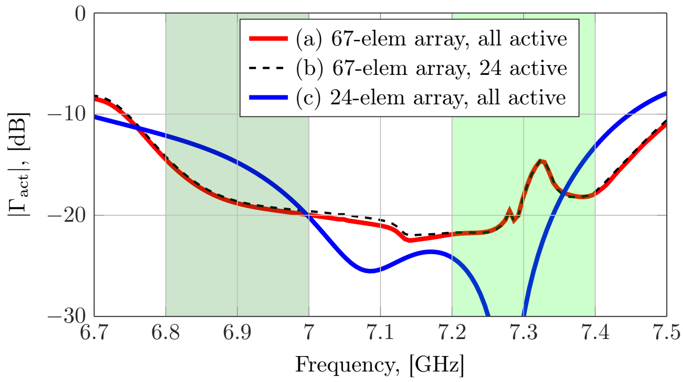

Figure 5: Central active reflection coefficient for (a) full-size array, when all elements are excited to form the optimum beam; (b) full-size array, when only 24 most strongly excited elements are used in the calcultion; and (c) 24-element array with the same weight coefficients as for the previous case. The operating frequency bands are shown as green strips.

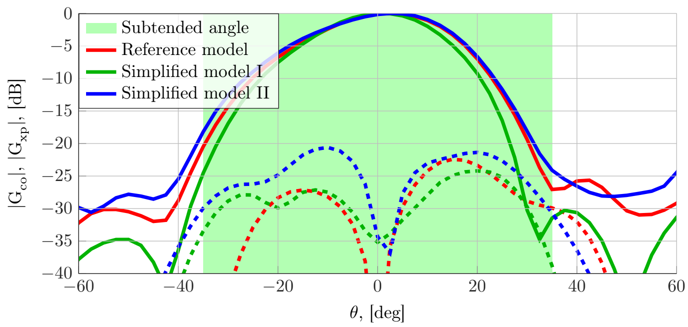

Figure 6: Comparison of the total *primary* patterns obtained for the reference full-wave array model and Simplified models I and II. Solid and dashed lines show the co-polarized (at $\phi = 0°$) and cross-polarized (at $\phi = 45°$) field components, respectively.

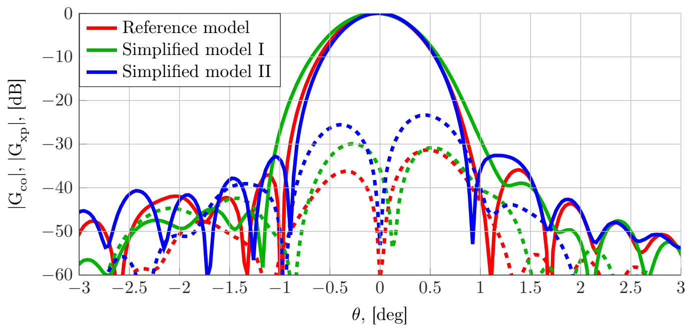

Figure 7: Comparison of the total *secondary* patterns obtained for the reference full-wave array model and Simplified models I and II. Solid and dashed lines show the co-polarized (at $\phi = 0°$) and cross-polarized (at $\phi = 45°$) field components, respectively.

levels and the sensitivity to the optimum element excitation choice.

Acknowledgment

The present work has been funded by the Swedish National Space Board. The radiometer requirements have been derived by the team consisting of TICRA and DTU-Space (Denmark).

References

[1] C. Bencivenni, M. Ivashina, R. Maaskant, and J. Wettergren, "Synthesis of maximally sparse arrays using compressive-sensing and full-wave analysis for global earth coverage," *IEEE Trans. Antennas Propag.*, vol. PP, no. 99, pp. 1–6, 2016.

[2] L. Poli, P. Rocca, G. Gottardi, and A. Massa, "Design of simplified large array structures for preliminary experimental validation," in *10th European Conference on Antennas and Propagation (EuCAP)*, Davos, Switzerland, Apr. 2016, pp. 1–4.

[3] (2015) Earth Explorer Mission EE-9. [Online]. Available: http://explorercall.esa.int/index.php/15-mission-ee9

[4] F. Collard *et al.*, "Sea surface temperature, wind and salinity (TWIST)," proposal for the Earth Explorer Mission EE-9, Unpublished.

[5] N. Skou and D. L. Vine, *Microwave Radiometer Systems: Design & Analysis.* Artech House, 2006.

[6] C. Cappellin, K. Pontoppidan, P. Nielsen, N. Skou, S. S. Søbjærg, A. Ihle, D. Hartmann, M. Ivashina, O.Iupikov, and K. v. t Klooster, "Novel multi-beam radiometers for accurate ocean surveillance," in *Proc. European Conference on Antennas and Propag. (EuCAP)*, The Hague, The Netherlands, Apr. 2014, pp. 1–4.

[7] O. A. Iupikov, M. V. Ivashina, C. Cappellin, and N. Skou, "Digital-beamforming array antenna technologies for future ocean-observing satellite missions," in *Proc. IEEE AP-S International Symposium*, Fajardo PR, Jul. 2016, pp. 1–2.

[8] O. A. Iupikov, M. V. Ivashina, K. Pontoppidan, P. H. Nielsen, C. Cappellin, N. Skou, S. S. Søbjærg, A. Ihle, D. Hartmann, and K. v. t Klooster, "Dense focal plane arrays for pushbroom satellite radiometers," in *Proc. European Conference on Antennas and Propag. (EuCAP)*, Hague, The Netherlands, Apr. 2014, pp. 1–5.

[9] C. Cappellin, K. Pontoppidan, P. H. Nielsen, N. Skou, S. S. Søbjærg, A. Ihle, M. V. Ivashina, O. A. Iupikov, and K. v. 't Klooster, "Design of a push-broom

multi-beam radiometer for future ocean observations," in *Proc. European Conference on Antennas and Propag. (EuCAP)*, Lisbon, Portugal, Apr. 2015, pp. 1–5.

[10] G. W. Kant, P. D. Patel, S. J. Wijnholds, M. Ruiter, and E. van der Wal, "EMBRACE: A multi-beam 20,000-element radio astronomical phased array antenna demonstrator," *IEEE Trans. Antennas Propag.*, vol. 59, no. 6, pp. 1990–2003, Jun. 2011.

[11] O. A. Iupikov, M. V. Ivashina, K. Pontoppidan, P. H. Nielsen, C. Cappellin, N. Skou, S. S. Søbjærg, A. Ihle, D. Hartmann, and K. v. t Klooster, "An optimal beamforming algorithm for phased-array antennas used in multi-beam spaceborne radiometers," in *Proc. European Conference on Antennas and Propag. (EuCAP)*, Lisbon, Portugal, Apr. 2015, pp. 1–5.

[12] M. V. Ivashina, R. Maaskant, and B. Woestenburg, "Equivalent system representation to model the beam sensitivity of receiving antenna arrays," *IEEE Antennas Wireless Propag. Lett.*, vol. 7, no. 1, pp. 733–737, Jan. 2008.